

UC Davis

UC Davis Electronic Theses and Dissertations

Title

Evaluating the Stability and Catalytic Reactivity of Molybdenum Chalcogenides: Towards the Design of Earth-Abundant Hydrogen Evolution and Carbon Dioxide Reduction Electrocatalysts

Permalink

<https://escholarship.org/uc/item/443623fx>

Author

Perryman, Joseph

Publication Date

2021

Peer reviewed|Thesis/dissertation

**Evaluating the Stability and Catalytic Reactivity of Binary and Ternary
Molybdenum Chalcogenides: Towards the Design of Earth-Abundant
Hydrogen Evolution and Carbon Dioxide Reduction Electrocatalysts**

By

JOSEPH TERRY PERRYMAN

DISSERTATION

Submitted in partial satisfaction of the requirements for the degree of

DOCTOR OF PHILOSOPHY

In

Chemistry

In the

OFFICE OF GRADUATE STUDIES

of the

UNIVERSITY OF CALIFORNIA

DAVIS

Approved:

Jesús M. Velázquez, Chair

Susan M. Kauzlarich

Frank E. Osterloh

Committee in Charge

2021

Dedication

I would like to dedicate this work to my family and friends that have supported me in my life and in this journey: To my family Darrah, Randy, Sherry, Paul, Tyler, Ashton, and Sam. To my friends Collin, Kaylee, Abby, Dave, Jessica, Dwayne, and Johnson. To my partner Nina, thank you for bringing light into my life and for taking on this first of many adventures with me.



In Loving Memory of Barbara Perryman

Acknowledgements

I would first like to express my deepest gratitude to my Ph.D. advisor Professor Jesús Velázquez for his exceptional support and dedication throughout my graduate studies. His mentorship, passion for scientific discovery, and undying optimism have all been paramount to my success in traversing the world of inorganic chemistry, electrochemistry, and materials science. I will forever value our work together and will always strive to be the force for positive change in the world that he continues to exemplify.

I would also like to thank my dissertation committee members Prof. Susan Kauzlarich and Prof. Frank Osterloh for their insightful discussions, both during the process of writing my dissertation and throughout my time as a graduate student at UC Davis. They are both beacons of inspiration in the field of inorganic chemistry, and both give me hope that our efforts to advance the frontiers of physical science research can truly impact our world for the better.

I also acknowledge Professors Liz Atkinson, Tom Reinert, and Brian Gilbert at Linfield College for their dedicated support of my education, research, and personal development as a scientist. Finally—for their tremendous contributions to my early education and for advocating my pursuit of higher education—I am eternally indebted to Brian and Cindy Gunn. I would like to thank them both for initiating my academic journey, for their generosity, and for their genuine devotion to the success of their students.

I am deeply grateful to have received financial support from a number of generous institutions and fellowships during my time as a graduate student at UC Davis, including from Chevron Corporation, the Bradford Borge Fellowship, the Fred P. Corson/Dow Chemical Fellowship, the Ernest E. Hill Memorial Fellowship, and the Susan M. Kauzlarich Fellowship.

I would also like to thank Prof. Charles Musgrave, Prof. Ambar Kulkarni, Prof. Christopher Patridge, and Prof. Alexandra Navrotsky for their engaging and productive collaborations, as well as the many scientists at Stanford Linear Accelerator Center and specifically at Stanford Synchrotron Radiation Lightsource for their support.

Finally, I would like to thank my colleagues in the Velázquez research group for their constant support in research and in life. This has been an unforgettable journey and I could not have asked for a better group of people to be a part of it.

Evaluating the Stability and Catalytic Reactivity of Binary and Ternary Molybdenum Chalcogenides: Towards the Design of Earth-Abundant Hydrogen Evolution and Carbon Dioxide Reduction Electrocatalysts

Abstract

Sustainable terawatt-scale energy solutions for a constantly evolving energy landscape necessitate the rapid development of transformative materials that facilitate energy conversion reactions that can power industrial, commercial, and even residential sectors without further accelerating anthropogenic climate change. Transitioning from a highly pollutive fossil-fuel based energy economy to a carbon-neutral or even carbon-negative one could require massive infrastructural changes in energy production and distribution at both the national and global scales if this transition were to be achieved by complete removal of the liquid fuels currently afforded by crude oil refining. However, drop-in replacements for these fossil fuels that include short-chain hydrocarbons and oxygenates like methane, ethylene, methanol, and ethanol—maintain desirable energy densities and are synthesizable via electrochemical methods that can be readily coupled to renewable sources of electricity—namely, intermittent wind and solar electricity. The conversion of vastly abundant yet intermittent solar energy into easily storable fuels such as hydrocarbons and alcohols represents one of the defining challenges of our time. Hence, the onus of proof is ours as researchers to verify the existence of rational design principles for novel catalyst materials that can facilitate chemical transformations of abundant feedstocks such as atmospheric CO₂ and water to viable fuels using sunlight as the only energy source. Such catalysts will not only provide a means of storing solar power but will also precipitate a paradigm shift within the chemical industry from reliance on petroleum feedstocks to the largescale utilization of CO₂ as the primary carbon source. The design of novel catalytic materials is subject to a stringent set of criteria—the materials need to be constituted from inexpensive and earth-abundant elements, exhibit high activity and selectivity in terms of chemical transformations, and be stable over long periods of operation. This dissertation details an iterative research effort that includes the synthesis and

stability analysis of new catalyst compositions, characterization of their local and electronic structures, as well as evaluation of their catalytic reactivity for foundational energy conversion reactions like H^+ reduction, CO reduction (COR), and CO_2 reduction (CO_2R).

The development of precisely tailored catalyst materials is predicated on a fundamental understanding of their composition-structure-function relationships. Hence, efforts here were focused on investigating dimensionally controlled binary and ternary chalcogenide materials wherein compositional and structural variations give rise to tunable charge transport dynamics, interfacial reaction kinetics, as well as bulk and surface energetics. These studies span synthetic materials chemistry, synchrotron X-ray spectroscopy analysis of electronic and atomistic structure, CO_2 reduction and hydrogen evolution electrocatalysis, as well as computational modeling, all in order to develop foundational materials design principles, where the evolution of electrochemical reactivity is evaluated in order to gain fundamental insights into energy conversion and storage.

Chapter 1 provides a review of the state-of-the art in CO_2 reduction and hydrogen evolution electrocatalysis, including fundamental principles that will be discussed in this work related to the interplay between physicochemical properties of catalyst materials and their surface reactivity. Also included in this chapter is a review of gaps in the current understanding of design principles for multinary chalcogenide-based electrocatalysts, as well as the route toward establishing such design principles that is highlighted in this dissertation. Foundational information relevant for synthetic and characterization techniques discussed through out the dissertation is also provided.

Chapter 2 outlines the development of rapid, microwave-assisted solid-state synthetic methods for promising binary and ternary chalcogenides in the pseudo-molecular Chevrel-phase sulfide, selenide, and telluride electrocatalyst families of composition $M_yMo_6X_8$ (M = metal intercalant; X = S, Se, Te; y = 0-4) which enable significant compositional and structural flexibility which is critical for developing the aforementioned composition-structure-function relationship. Our focus is on establishing synthetic accessibility based upon the thermodynamic stability of the target phases compared to other binary and

ternary chalcogenide phases with competitive stability at intermediate (300-700°C) and high (>700°C) reaction temperatures.

Chapter 3 elucidates the structural and electronic structure features of promising binary and ternary Chevrel-phase sulfide electrocatalysts using synchrotron-based X-ray spectroscopic methods. These studies highlight potential electronic signatures that can be used as proxies for electrochemical CO₂R, COR, and HER reactivity, and offer glimpses into a new avenue of *operando* interfacial spectroscopic evaluation for these materials of interest. Observed spectral features in the S K-edge X-ray Absorption Near-Edge Structure (XANES) indicate that the increased population of frontier S 3p orbitals upon ternary intercalation into binary Chevrel-phase frameworks leads to a reactive Mo-S active site that is more conducive to mediating requisite proton-coupled electron-transfer steps in the CO₂ and CO reduction pathways to liquid methanol. Additionally, the effect of composition and structure on thermodynamic stability is discussed through the lens of synergistically incorporating insights from experiment and theory to accelerate the discovery of new energy materials.

Chapter 4 highlights an investigation into the effects of dimensional modification in the ternary molybdenum sulfide composition space wherein chalcogen-deficient 1-dimensional pseudo-Chevrel-phase (PCP) sulfide nanorods of composition (M₂Mo₆S₆) are directly synthesized for the first time through solid-state methodologies. A nucleation mechanism is proposed based on computational surface modeling, and a series of alkali metal-intercalated PCP phases are evaluated electrochemically to elucidate interfacial charge-transport dynamics.

Contents

Dedication	ii
Acknowledgements.....	iii
Contents.....	viii
List of Abbreviations	x
List of Figures and Tables.....	xii
1. Chapter 1: Introduction	1
Introduction	1
Earth-Abundant Electrocatalyst Design:	2
Chevrel-Phase and Pseudo-Chevrel-Phase Molybdenum Chalcogenide Compositions Spaces ..	5
Composition-Structure-Function Relationships in Chevrel and Pseudo-Chevrel Phases	6
X-Ray Absorption Spectroscopy	9
Rapid Microwave-Assisted Solid-State Synthesis	11
References	13
2. Chapter 2: Metal-Promoted Mo ₆ S ₈ Clusters: A Platform for Probing Ensemble Effects on the Electrochemical Conversion of CO ₂ and CO to Methanol.....	17
Abstract	17
Introduction	17
Experimental Methods	20
Results and Discussion	26
Conclusions	41
Acknowledgements	43
Publication Information, Copyright, and Author Acknowledgements	44
References	44
Supporting Information	48
3. Chapter 3: Spectroscopic, Calorimetric, and Computational Study of the Electronic Structure, Local Coordination, and Thermodynamic Stability of 1 st Row Transition Metal-Intercalated Chevrel-Phase Sulfides.....	71
Abstract	71
Introduction	72
Experimental Methods	74
Results and Discussion	79
Conclusions	94

Acknowledgments	95
Publication Information, Copyright, and Author Acknowledgements	95
References	96
Supporting Information	99
4. Chapter 4: Direct Solid-State Nucleation and Charge Transport Dynamics of Alkali Metal- Intercalated $M_2Mo_6S_6$ (M = K, Rb, Cs) Nanorods	117
Abstract	117
Introduction	117
Experimental Methods	119
Results and Discussion	123
Conclusions	132
Acknowledgments	133
Publication Information, Copyright, and Author Acknowledgements	133
References	133
Supporting Information	136

List of Abbreviations

CA	chronoamperometry
CO ₂ R	carbon dioxide reduction
CO ₂ RR	carbon dioxide reduction reaction
COR	carbon monoxide reduction
CORR	carbon monoxide reduction reaction
CP	Chevrel-phase
CPE	controlled potential electrolysis
CV	cyclic voltammetry
DFT	density functional theory
EDX	energy dispersive X-ray spectroscopy
EXAFS	extended X-ray absorption fine structure
FE	Faradaic efficiency
HER	hydrogen evolution reaction
HOMO	highest occupied molecular orbital
LSV	linear sweep voltammetry
LUMO	lowest unoccupied molecular orbital
OCV	open circuit voltage
PBE	Perdew-Burke-Ernzerhof
PCP	pseudo Chevrel-phase
PEIS	potentiostatic electrochemical impedance spectroscopy
PTFE	polytetrafluoroethylene
PXRD	powder X-ray diffraction
SEM	scanning electron microscopy
SSRL	Stanford Synchrotron Radiation Lightsource

TEM	transmission electron microscopy
VASP	Vienna ab-initio simulation package
XANES	X-ray absorption near-edge structure
XAS	X-ray absorption spectroscopy
XPS	X-ray photoelectron spectroscopy

List of Figures and Tables

Figure 1.1 Diagram illustrating a net carbon neutral or negative energy cycle driven by renewable electricity and electrochemical conversion of atmospheric greenhouse molecules into value-added products.	2
Figure 1.2. Schematic showing generic CP and PCP compositions as well as ternary and quaternary substitutions that are all synthesizable via rapid, high-temperature microwave assisted synthesis.	6
Figure 1.3. Schematic illustrating the principles of bond formation between adsorbate valence states and surface s and d states. Bond strength according to this model is dependent on the population of metal-adsorbate antibonding states, which depends on the position of the surface d-band center relative to its Fermi level. Figure adapted from Ref 49.	7
Figure 1.4. (a) Electron density (qualitatively represented here by transparent spheres) within the Mo ₆ core (blue) of the CP structure can be changed via implantation of increasingly electron-withdrawing (yellow spheres representing S) or electron-donating (pink spheres representing Te) chalcogen species, thereby controlling the formal Mo ₆ valence electron count which can range from 20-24 e ⁻ for stable CP compositions, depending on chalcogen and intercalant composition. In (a), solid spheres represent ionic radii of Mo ²⁺ , S ²⁻ , and Te ²⁻ of 83 pm, 172 pm, and 207 pm, respectively. (b) Illustration that electron donation from M into the binary Mo ₆ S ₈ cluster can be directed by careful selection of metallic precursors. This panel illustrates the phenomenon that charge-transfer to the cluster, specifically to the chalcogen cage as is discussed further in Chapters 2 and 3, from the intercalant increases as the electronegativity decreases (in this example from 4.48 eV for Cu in its neutral state to 2.42 eV for K in its neutral state ⁵¹). For clarity, all solid spheres in (b) represent Van der Waals radii similar to those expected for each species in its elemental form, and the increase in the size of the transparent spheres around S indicates an increase in electron density.	8
Figure 1.5. Diagram of core-level electron ejection processes analyzed with XAS, including the origin of pre-edge spectral signatures that arise due to mixing between metal and chalcogen frontier orbitals, as is the case in many of the materials of interest in this work. Figure from Ref 52.	10
Figure 1.6. Illustration of the microwave-assisted heating technique used to synthesize materials throughout this work. Inset captures the commonly observed case where resistive heating is coupled to heating from arcing phenomena wherein electrical charge jumps from solid structure to solid structure.	12
Figure 2.1. Hypothetical depiction of CO hydrogenation over a purely metallic surface (top), compared to a “promoted” metal chalcogenide surface (bottom) where synergistic chalcogen (X=S, Se, Te)(yellow) and intercalant (grey) inclusion at CO ₂ RR active Mo sites (blue) can hypothetically encourage a unique intermediate binding geometry. Simplified Coulombic stabilization is included for clarity and is represented by the dashed line connecting partially negatively charged (O) and partially/formally positively charged (M) species.	19
Table 2.1. Reagent masses used to obtain 500 mg precursor mixtures for microwave heating.	20
Figure 2.2. Fitted XRD patterns for Mo ₆ S ₈ (a), Cr _{1.73} Mo ₆ S ₈ (b), Ni ₂ Mo ₆ S ₈ (c), and Cu ₂ Mo ₆ S ₈ (d), showing difference (gray) between experimental data (black) and calculated curve (red). Insets are provided for each panel to illustrate the characteristic asymmetry of the <101> peak at around 13.8°. Extracted lattice parameters are given in Table S2.1 and compared to expected values.	22

Figure 2.3. Computationally confirmed interaction between CO and a ternary CP active site ensemble (a). This illustrates that preferential binding of CO on a $\text{Cu}_2\text{Mo}_6\text{S}_8$ CP surface occurs at Mo (blue) active sites, while the proximity of Cu (brown) to S sites (yellow) encourages promoter-to-chalcogen charge transfer. Scanning electron micrograph detailing the faceted morphology of polycrystalline $\text{Cu}_2\text{Mo}_6\text{S}_8$ (b). 27

Figure 2.4. EDX spectra for $\text{Cu}_2\text{Mo}_6\text{S}_8$ (a), and Mo_6S_8 (b) indicating that copper has been removed from the bulk $\text{Cu}_2\text{Mo}_6\text{S}_8$ structure upon chemical etching. Signal at ~ 1 keV represents the Cu L edge, and is unlabeled because it was not required for quantification. Label for oxygen was included to illustrate lack of bulk oxidation in the samples. 28

Figure 2.5. K-edge XANES for Cu in $\text{Cu}_2\text{Mo}_6\text{S}_8$ with a Cu^0 foil for reference (a), K-edge XANES for Mo in $\text{Cu}_2\text{Mo}_6\text{S}_8$ and Mo_6S_8 , with a Mo^0 foil for reference (b), and K-edge XANES for S in $\text{Cu}_2\text{Mo}_6\text{S}_8$ and Mo_6S_8 (c). A reference scan using $\text{Na}_2\text{S}_2\text{O}_3$ is shown in Fig. S2.12 of the SI. 29

Figure 2.6. High-resolution XPS spectra for Cu (a), Mo (b), and S (c) before electrolysis (black) which are in reasonable agreement with expected oxidation states in $\text{Cu}_2\text{Mo}_6\text{S}_8$ of +1, +2.33, and -2, respectively, and after electrolysis (red) which indicates slight oxidation of Cu and Mo as a result of exposure to moisture and oxygen following electrolysis. It is not expected that either species is oxidized during electrolysis. Values were determined using the Perkin-Elmer handbook of XPS. 30

Figure 2.7. Processed EXAFS information plotted in magnitude and in real space for Cu in $\text{Cu}_2\text{Mo}_6\text{S}_8$ (a), Mo in Mo_6S_8 (b), Mo in $\text{Cu}_2\text{Mo}_6\text{S}_8$ (c), and for Mo in $\text{Cu}_2\text{Mo}_6\text{S}_8$ overlaid with Mo in Mo_6S_8 to compare Mo-S and Mo-Mo signals (d). Qualitative differences in local Mo coordination as presented here are discussed quantitatively in the results and discussion sections. 31

Figure 2.8. NMR signals for formate at 8.45 ppm (a)-(c) and for methanol at 3.36 ppm (d)-(e) detected after electrolysis under CO_2 (a),(d), CO (b), (e), and N_2 (c),(f). Signals at 3.00 ppm and 7.92 ppm both correspond to the internal standard, N,N-dimethylformamide. All displayed NMR spectra are the result of electrolysis at -1.0 V vs RHE in either 0.1M Na_2CO_3 purged with CO_2 or N_2 or 0.1M NaHCO_3 purged with CO 32

Figure 2.9. Potential-dependent geometric current density after electrolysis for CO_2 reduction products (a), for hydrogen evolution under CO_2 headspace (b), for CO reduction products (c), and for hydrogen evolution under CO headspace (d). Experiments for (a) and (b) were carried out in a pH 6.8 electrolyte where 0.1 M Na_2CO_3 was purged for 1 hr with CO_2 , while experiments for (c) and (d) were carried out in pH 6.8 electrolyte where 0.1 M NaHCO_3 was purged for 1 hr with CO . Current densities were calculated using the product of the Faradaic efficiency (Fig. S2.9) and the steady-state geometric current density (Fig S2.13) during electrolysis at each potential, and standard deviations are shown. Note that connecting lines are included to aid in the visualization of partial current density trends, although these plots represent a collection of discrete fixed-potential experiments at -0.4 V, -0.6 V, -0.8 V, and -1.0V. Representative CPE data can be found in Fig. S2.13. 33

Figure 2.10. Plot of the open circuit potential over time with $\text{Cu}_2\text{Mo}_6\text{S}_8$ as a working electrode in 0.1 M Na_2CO_3 , purged with CO_2 to achieve neutral pH (a); NMR spectrum showing absence of methanol production, with a DMF standard signal at 3.00 ppm (b); NMR spectrum showing absence of formate production, with a DMF standard signal at 7.92 ppm (c). 34

Figure 2.11. Density of states for Mo_6S_8 (a) and $\text{Cu}_2\text{Mo}_6\text{S}_8$ (b) calculated using the HSE06 functional. A noticeable DOS increase at more negative energies indicates charge transfer to the S atoms as evidenced by XAS. The grey region shows the d10 electronic configuration of Cu(I). Respective structures are represented above where Mo are blue spheres, S are yellow spheres, and Cu are red spheres.

Further confirmation of charge transfer to S atoms can be seen in Fig. S2.17 which shows the result of Bader charge analysis.	35
Figure 2.12. NMR spectra showing production of formate (8.45 ppm) (a) and methanol (3.36 ppm) (b) on $\text{Cr}_{1.73}\text{Mo}_6\text{S}_8$ as well as formate (8.45 ppm) (c) and methanol (3.36 ppm) (d) on $\text{Ni}_2\text{Mo}_6\text{S}_8$. Both formate and methanol were produced in significant quantities over $\text{Ni}_2\text{Mo}_6\text{S}_8$, while methanol was only produced in trace levels over $\text{Cr}_{1.73}\text{Mo}_6\text{S}_8$ while formate was the dominant CO_2 RR liquid product. Raw data from CPE experiments for these phases is included in Fig. S2.18	37
Figure 2.13. ^1H NMR spectra showing signals for methanol at 3.36ppm before electrolysis over a $\text{Mo}_6\text{S}_8@\text{C}$ working electrode (a) after electrolysis at 50 coulombs over the same $\text{Mo}_6\text{S}_8@\text{C}$ electrode (b), before electrolysis of PTFE@C working electrode (c), and after electrolysis at 50 coulombs over the same PTFE@C working electrode (d). Experiments were performed in CO_2 -saturated 0.1M Na_2CO_3 electrolyte at -0.8V vs RHE. We observe the evolution of a signal for methanol only when Mo_6S_8 is present on the electrode, indicating that the intrinsic activity of Mo_6S_8 yields methanol from CO_2 in aqueous environments. The same experiments also yield formate when Mo_6S_8 is present, where observed faradaic efficiencies for methanol and formate are 0.09% and 0.05%, respectively.	39
Figure 2.14. Proposed reaction pathway over a simplified CP surface for the carbophilic reduction of CO_2 to methanol (highlighted in green), with as well as the competitive oxophilic reaction pathway leading to formate (highlighted in red).....	40
Figure S2.1. Diagram showing experimental set-up for microwave-assisted synthesis method (a) and Crystal structure for $\text{Cu}_2\text{Mo}_6\text{S}_8$ (b) where Cu = red spheres*, Mo = blue spheres, and S = yellow spheres.	48
Figure S2.2. Indexed PXRD pattern for as-synthesized $\text{Cu}_2\text{Mo}_6\text{S}_8$ (red) overlaid with pattern expected from literature (black).....	49
Figure S2.3. Images depicting a custom-blown H-cell configured electrolysis cell with working, reference, and counter electrodes sealed under CO_2 by precision seal rubber septa (a) and a piece of as-synthesized CP prior to electrolysis (b).....	50
Figure S2.4. Experimental validation that carbonate electrolyte bulk pH is reduced to near-neutral values over the course of CO_2 sparging (a) and that bulk pH does not increase significantly in the static cells implemented in this study over the course of electrolysis where 50 coulombs of charge are passed through a $\text{Cu}_2\text{Mo}_6\text{S}_8$ working electrode.	51
Figure S2.5. Monitoring pH over time for a CO -purged 0.1M NaHCO_3 electrolyte, showing slight increases to bulk electrolyte pH of less than one pH unit. Effects of increasing bulk pH do not necessarily reflect inherently high pH at the electrode-electrolyte interface, and as such the effect of bulk pH increase over time on CO_2 reduction catalysis are not systematically studied here.	52
Figure S2.6. Current stability over the course of electrolysis at -1.0 V vs RHE and pH 6.8 in a 0.1 M Na_2CO_3 electrolyte purged with CO_2 (a). Linear sweep voltammograms in pH 6.8 electrolytes at constant scan rates of 50 mV/sec, showing an identical onset potential for reductive current under both CO_2 (black) and N_2 (red) (b). This indicates that HER dominates observed current densities and there is no observable contribution to current density from CO_2 reduction, as confirmed by the values seen in Figure S2.9. Linear sweep voltammograms were observed for pellets of identical exposed surface area.	53
Figure S2.7. Complete NMR spectrum after electrolysis at -1.002V vs RHE at $\text{Cu}_2\text{Mo}_6\text{S}_8$ showing a large, suppressed H_2O signal at ~ 4.7 ppm (a)*, and NMR inset showing the peak at 1.90 ppm that corresponds	

to acetate in both the electrolysis product aliquot, as well as in a blank prior to electrolysis (b). Acetate was not observed as a product at any point in this study. 54

Figure S2.8. GC-TCD chromatographs illustrating the test injections used for calibration of H₂, CO, and CH₄ (a-b) as well as test injections to ensure sufficient detection of C₂H₄. 100% C₂H₄ resulted in fronting of the eluent, and the detection limit on the order of 0.01% percent was sufficient in detecting trace quantities of ethylene given the electrochemical cell construct implemented in this study. Methane and ethylene were undetected in all electrolysis experiments involving M_xMo₆S₈ catalysts. 55

Figure S2.9. Potential-dependent Faradaic efficiency for CO₂ reduction products (a), for hydrogen evolution under CO₂ headspace (b), for CO reduction products (c), and for hydrogen evolution under CO headspace (d). Experiments for (a) and (b) were carried out in a pH 6.8 electrolyte where 0.1 M Na₂CO₃ was purged for 1 hr with CO₂, while experiments for (c) and (d) were carried out in pH 6.8 electrolyte where 0.1 M NaHCO₃ was purged for 1 hr with CO. Error bars reflect one standard deviation. 56

Figure S2.10. Most stable binding geometry for CO on Mo₆S₈. Multiple CO binding configurations at the Mo and atoms were explored and binding to Mo was determined to be most favorable in all cases. CO binding results in a stable octahedral coordination of the active Mo atom. 57

Figure S2.11. Calculated binding energies for CO at relevant binding sites in Mo₆S₈ (a), and at the most favorable Cu and Mo sites in Cu₂Mo₆S₈ (b). S interactions are not presented for Cu₂Mo₆S₈ because only very weak VdW forces were calculated, as was the case for Mo₆S₈. 58

Figure S2.12. Full XAS spectra for (a) Cu-CP with a Cu⁰ foil reference; (b) Cu-CP and bare-CP with a Mo⁰ foil reference; (c) Cu-CP and bare-CP with a Na₂S₂O₃ reference. Scans for the Na₂S₂O₃ reference (black) in (c) were only carried out in the immediate energy range around the S K-edge because reference spectra were not collected simultaneously with CP spectra, as was the case for CPs. 59

Figure S2.13. Raw data from controlled potential electrolysis experiments that show steady-state reduction currents over Cu₂Mo₆S₈ that were then normalized with respect to electrode surface area and then multiplied by Faradaic efficiency for each product that was detected via NMR and GC following each experiment in order to obtain partial current density values presented in Figure 2.9. These scans are representative of the raw current over time for each of the four potentials tested in this work (-0.4 V vs RHE (red), -0.6 V vs RHE (blue), -0.8 V vs RHE (pink), and -1.0 V vs RHE (green)), and are therefore not shown in their surface-area normalized forms. A notable increase in noise due to vigorous formation of H₂ under stirring is observable for the -1.0 V experiments in panels (b) and (d). All experiments were performed in CO₂-saturated 0.1M Na₂CO₃ at pH 6.8 under vigorous magnetic stirring. 60

Figure S2.14. Mo 3d XPS spectra for Cu₂Mo₆S₈ catalyst before electrolysis (a), and after electrolysis (b), indicating slight oxidation of Mo following exposure to moisture and oxygen. It is not believed that catalyst oxidation occurs during electrolysis. 61

Figure S2.15. XPS survey scan of Cu₂Mo₆S₈ CP both before (black) and after (red) electrolysis. Peaks to note are the O1s and C1s signals that arise from a native oxide layer as well as surface carbon. Both species diminished over the course of successive surface-sputtering depth-profile scans, hence the only signal that evolved as the result of electrolysis is that of Na, a principle electrolyte component. 62

Figure S2.16. Mass-spectrum following injection of the cell headspace following electrolysis over Cu₂Mo₆S₈ at -1.0 V vs RHE in a 0.1M Na₂C O₃ electrolyte saturated with CO₂ at 1 atm. Prominent signals for N₂ and O₂ resulted from the ambient gas in the needle of the injection syringe. 63

Figure S2.17. Results of Bader charge analysis for Mo₆S₈, CuMo₆S₈ and Cu₂Mo₆S₈ which shows a notable increase in electron localization on S atoms upon introduction of Cu. Bader charge analysis operates on the principle that atoms within a structure can be divided based upon their charge density according to

discreet volumes that form from zero-flux surfaces that are two-dimensional planes on which charge density for an atom is at a minimum perpendicular to the plane. Hence charge density within the volume made up by these zero-flux surfaces is a good approximation of the relative charge each atom within a structure.⁶⁰ 64

Figure S2.18. Raw data from controlled potential electrolysis experiments that show steady-state reduction currents over $\text{Cr}_{1.73}\text{Mo}_6\text{S}_8$ (black) and $\text{Ni}_2\text{Mo}_6\text{S}_8$ (red) that yielded the product distributions shown in Fig. 2.12. These experiments were performed in aqueous CO_2 -saturated 0.1 M Na_2CO_3 electrolyte at pH 6.8 at -0.8 V vs RHE under vigorous mechanical stirring. 65

Figure S2.19. XRD patterns overlaid with published patterns for $\text{Cr}_{1.73}\text{Mo}_6\text{S}_8$ (a) and $\text{Ni}_2\text{Mo}_6\text{S}_8$ (b) that were used in control experiments. 66

Table S2.1 Result of Pawley refinement for all Chevrel-phase structures studied in this work. 67

Table S2.2 Fitting parameters for Mo K-edge of $\text{Cu}_2\text{Mo}_6\text{S}_8$ 69

Table S2.3 Fitting parameters for Mo K-edge of Mo_6S_8 69

Table S2.4 Fitting parameters for Cu K-edge of $\text{Cu}_2\text{Mo}_6\text{S}_8$ 69

Table S2.5 Extracted bond lengths from EXAFS fittings..... 70

Figure 3.1. Crystal structure showing connectivity in $\text{Cu}_2\text{Mo}_6\text{S}_8$ where Cu ions (red) are found inside the cavity formed by adjacent Mo_6S_8 units (a), and an Mo_6S_8 cluster unit showing six additional axial bonds between Mo (blue) and S (yellow) that link adjacent clusters together (b). 72

Table 3.1. Reagent masses used to obtain 500 mg precursor mixtures for microwave heating. 75

Figure 3.2. Indexed PXRD pattern for as-synthesized $\text{Cu}_2\text{Mo}_6\text{S}_8$ overlaid with an ICSD reference pattern (a) and a scanning electron micrograph showing faceted $\text{Cu}_2\text{Mo}_6\text{S}_8$ crystal which forms under microwave irradiation (b). 76

Figure 3.3. Mo L_2 -edge XANES for $\text{M}_2\text{Mo}_6\text{S}_8$ (M = Fe, Ni, Cu) (a) and for $\text{Fe}_x\text{Mo}_6\text{S}_8$ (x = 0-2) (b) showing consistent edge overlap irrespective of transition metal identity or stoichiometry. This overlap indicates consistent oxidation state between Mo in different CP species. Overlaid spectra are insets of normalized S K-edge EXAFS regions where the Mo L-edges arise and are therefore not normalized for the Mo L_2 -region. Fe, S, and Mo K-edge XAS spectra in their entirety can be found in Fig. S3.4-S3.6. 80

Figure 3.4. Mo 3p (a) and 3d (b) XPS spectra overlaid for all CPs studied, detailing similar oxidation states and chemical environments for Mo in each CP species. 81

Figure 3.5. Overlaid S K-edge XAS spectra for $\text{M}_2\text{Mo}_6\text{S}_8$ (M = Fe, Ni, Cu) (a) and the corresponding 1st derivative plot for the same scans (b), along with overlaid S K-edge XAS spectra for $\text{Fe}_x\text{Mo}_6\text{S}_8$ (x = 0-2) (c) and the corresponding 1st derivative plot for the same scans (d). Notably, the pre-edge centroid overlaps at 2471 eV for all phases, with a slight (<~0.25 eV) shift in the white line position..... 81

Figure 3.6. Fe 2p XPS spectra overlaid for FeMo_6S_8 and $\text{Fe}_2\text{Mo}_6\text{S}_8$, illustrating a red-shift in the onset energy of photoelectron ejection from a moderately less oxidized Fe species in $\text{Fe}_2\text{Mo}_6\text{S}_8$ 83

Figure 3.7. Processed EXAFS information plotted in magnitude (top line) and in real space (bottom line) for un-promoted Mo_6S_8 (a), $\text{Ni}_2\text{Mo}_6\text{S}_8$ (b), and $\text{Cu}_2\text{Mo}_6\text{S}_8$ (c), qualitatively indicating different local Mo coordination in the three CP structures. EXAFS fitting parameters can be found in Tables S3.3-S3.5. 84

Figure 3.8. Relevant fragments of the CP structure including all scattering paths as discussed in Table 3.2, numbered as follows: intracluster Mo-Mo paths (1, 2), axial Mo-S path (3), and intracluster Mo-S paths (4-7). Intuitively, in a distorted octahedron with 2 distinct Mo-Mo scattering paths for a given Mo absorber, each path (1 and 2) will have a degeneracy (N) of 2 which indicates that two of each such paths exist for each Mo absorber. 85

Table 3.2. Results of EXAFS fittings sorted by structure, absorbing atom, and scattering atom. 86

Table 3.3. Drop solution enthalpies of the binary and ternary sulfides, enthalpies of formation calculated from reactions (3.1) and (3.2) and enthalpies of formation from elements.	88
Figure 3.9. Experimental and computation enthalpies of formation from elements for $M_yMo_6S_8$ and MoS_2 , illustrating good agreement in the stability trend within the propagated error of the experimental enthalpy measurements.	89
Table 3.4. Computational bond distances, component charges, integrated COOP, and Madelung Energies for $M_yMo_6S_8$ ($M = Fe, Ni, Cu; y = 0-2$) and MoS_2	90
Figure 3.10. Total density of states (DOS, black line) and crystal orbital overlap population (COOP, red line) of Mo and S atoms for the five Chevrel structures and MoS_2 . Positive COOP values indicate covalent bonding states and negative values indicate covalent anti-bonding states. Σ is the energy integrated COOP from -14 eV to the Fermi level (dashed line) which indicates the net covalent bonding between Mo and S in these structures.	92
Figure 3.11. Reductive effects of M species intercalation into Mo_6S_8 decreases the covalency of the Mo-S interactions observed in binary Mo_6S_8 , and increases the relative charge on Mo and S to yield a net increase in ionic bonding character within the structure.	93
Figure 3.12. Orientation of lined Chevrel-Phase clusters showing the rhombohedral axis along which they possess three-fold rotation symmetry, and away from which clusters tilt in triclinic $Fe_2Mo_6S_8$	93
Figure S3.1. Graphic representation of the principle of core-shell electron ejection, followed by relaxation of outer-shell electrons to yield fluorescent radiation. Fluorescence signal was acquired in all of the experiments presented in this work. The diagram to the right represents a generalized view of S K-shell ejection mechanisms that would result in the evolution of a pre-edge feature (Laporte forbidden), as well as the excitations that result in the main edge (Laporte allowed). States higher in energy than the LUMO positions constitute the continuum.	99
Figure S3.2. Schematic illustrating the experimental set-up adapted from ref. 28 implemented for microwave-assisted solid-state synthesis of Chevrel-phase materials.	100
Figure S3.3. Powder XRD patterns for synthesized $M_xMo_6S_8$ ($M = Fe, Ni; x = 0-2$) with major peaks indexed, showing ICSD reference patterns and collection codes, along with corresponding SEM images listed immediately below each pattern overlay.	101
Figure S3.4. Overlaid raw XAS spectra showing raw fluorescence signal starting at the S K-edge (a) and the Mo K-edge (b) for all CPs studied.	102
Figure S3.5. Raw XAS spectra for all metal intercalant K-edges, including raw fluorescence signal for the Fe K-edge in $Fe_2Mo_6S_8$ (black) and $FeMo_6S_8$ (red) (a), for the Ni K-edge in $Ni_2Mo_6S_8$ (b), and for the Cu K-edge in $Cu_2Mo_6S_8$ (c).	103
Figure S3.6. Zoomed and overlaid XAS spectra showing fluorescence signal for all Chevrel-phase S (a) and Mo (b) K-edge XANES regions.	104
Figure S3.7. Spin-polarized densities of state calculated for Mo and S in Mo_6S_8	105
Figure S3.8. Spin-polarized densities of state calculated for Fe, Mo, and S in $FeMo_6S_8$, indicative of a d6 Fe(II) iron species.	106
Figure S3.9. Spin-polarized densities of state calculated for $Fe_2Mo_6S_8$, indicative that the triclinic Fe-promoted CP may exhibit semiconducting properties.	107
Figure S3.10. Spin-polarized densities of state calculated for Ni, Mo, and S in $Ni_2Mo_6S_8$, indicative of a d8 Ni(II) iron species.	108
Figure S3.11. Spin-polarized densities of state calculated for Cu, Mo, and S in $Cu_2Mo_6S_8$, indicative of a d10 Cu(I) species.	109

Figure S3.12. Zoomed and overlaid Chevrel-phase and reference foil XAS spectra, showing fluorescence signal for metal intercalant K-edges that include Fe (a), Ni (b), and Cu (c).	110
Figure S3.13. Wireframe representation of the triclinic $\text{Fe}_2\text{Mo}_6\text{S}_8$ crystal structure where Fe atoms (orange) reside in exactly two cavity positions.....	111
Figure S3.14. Processed EXAFS information plotted in k-space for un-promoted (a), Ni-promoted (b), and Cu-promoted (c) CPs. As is reflected by extracted scattering paths, oscillation magnitudes for both Ni and Cu-promoted Mo_6S_8 differ similarly from 6-9 wavenumbers in comparison to un-promoted Mo_6S_8 where weighted oscillation is comparatively more uniform. This qualitatively indicates that the changes in local coordination of Mo upon metal promotion are similar in nature, as is quantitatively observed following further processing of experimental data.	112
Table S3.1 Results of Pawley refinements on each Chevrel-phase investigated.....	113
Table S3.2 Results of Bader Charge analysis for $\text{Fe}_y\text{Mo}_6\text{S}_8$ ($y = 0-2$).	113
Table S3.3 Fitting parameters for the Mo K-edge of Mo_6S_8	114
Table S3.4 Fitting parameters for the Mo K-edge of $\text{Ni}_2\text{Mo}_6\text{S}_8$	114
Table S3.5 Fitting parameters for the Mo K-edge of $\text{Cu}_2\text{Mo}_6\text{S}_8$	115
Table S3.6. Thermodynamic cycles used to calculate the enthalpy of formation of $\text{Me}_y\text{Mo}_6\text{S}_8$ from Me and Mo_6X_8 (Me = Fe, Ni, Cu).	115
Table S3.7. Thermodynamic cycles used to calculate the enthalpy of formation from elements of Mo_6S_8 and $\text{Me}_y\text{Mo}_6\text{S}_8$ (Me = Fe, Ni, Cu).	116
Table S3.8. Computational enthalpies of formation from elements, from intercalation of M_y into Mo_6S_8 , and from synthetic conditions for $\text{Me}_y\text{Mo}_6\text{S}_8$ (Me = Fe, Ni, Cu).	116
Figure 4.1. (A) 1-dimensional structure of $\text{M}_2\text{Mo}_6\text{S}_6$ (Alkali = Purple, Mo = Blue, S = Yellow) as viewed perpendicular to the principle hexagonal axis with alkali intercalants surrounding Mo_6S_6 wires, (B) Mo_6S_6 wire as viewed along the hexagonal axis, and (C) crystal structure representations of the Chevrel parent phase where Mo_6 clusters are significantly separated via S_8 encapsulation, while Mo_6 units form a continuous chain surrounded by an S_6 "sleeve" in the PCP framework.....	118
Table 4.1. Reagent masses used to obtain 250 mg precursor mixtures for microwave heating.	120
Figure 4.2. Schematic representation of the H-shaped three-electrode configuration that was implemented in all electrochemical experiments.	122
Figure 4.3. (A)-(C) SEM images for as-synthesized K-PCP (A), Rb-PCP (B), and Cs-PCP (C), (D)-(F) Indexed PXRD patterns overlaid with literature patterns from the International Crystal Structure Database (ICSD) for K-PCP (D), Rb-PCP (E), and Cs-PCP (C).	124
Table 4.2 Results of computational surface energy modeling for K_2 -PCP $\langle 010 \rangle$, $\langle 110 \rangle$, and $\langle 001 \rangle$ surfaces.	124
Figure 4.4. Crystal structure representations for each surface for which computational free energies were determined, illustrating an increasing number of broken bonds in moving from (A) $\langle 010 \rangle$, to (B) $\langle 110 \rangle$, and finally to (C) $\langle 001 \rangle$. In each case, the compass shows that the unit cell is oriented such that the lattice plane is parallel to the viewing perspective.	125
Figure 4.5. Scan-rate dependent cyclic voltammograms performed in 0.5M H_2SO_4 for (A) a blank ink without PCP, (B) K-PCP, (C) Rb-PCP, and (D) Cs-PCP. Voltammograms were collected in a region +/- 0.1V from each electrode's open circuit potential, as this region is generally non-Faradaic and therefore measured currents accurately represent purely capacitive charging. To ensure reliable statistics, CVs similar to the ones shown here were repeated for at least 6 electrodes of each ink.	126

Figure 4.6. Examples of oxidative and reductive charging currents for (A) PCP-free blank ink, (B) K-PCP, (C) Rb-PCP, and (D) Cs-PCP. Capacitance is taken as the average of the absolute value for both positive and negative slopes in each case. In some experiments, 200mV/sec scans resulted in a large amount of noise, and are excluded on a case by case basis. Average capacitance values shown here represent the values for these specific scans, and are not the average values following replicated scans as reported in the main text. Average values for double layer capacitance are reported in Figure S3.11. 127

Figure 4.7. (A) Specific capacitance per gram of M_2 PCP, calculated using double layer capacitance and known mass loading onto a conductive carbon substrate, (B) Resistance to electron-transfer of M_2 PCP inks in a 0.5M H_2SO_4 solution under multiple applied potentials vs RHE, (C) Polarization curves obtained via linear sweep voltammetry for M_2 PCP inks as well as for a blank ink, all submerged in 0.5M H_2SO_4 , and (D) Tafel plots for M_2 PCP inks along with a blank ink for reference, further illustrating the current-potential response of each ink acting as a catalyst for the Hydrogen Evolution Reaction (HER). 128

Figure 4.8. Phase angle response during potential-dependent EIS experiments for (A) PCP-free blank ink, (B) K-PCP, (C) Rb-PCP, and (D) Cs-PCP where ω is the AC bias frequency. 130

Figure 4.9. Impedance modulus response during potential-dependent EIS experiments for (A) PCP-free blank ink, (B) K-PCP, (C) Rb-PCP, and (D) Cs-PCP where ω is the AC bias frequency. Low frequency regions in all cases exhibit potential-dependent diffusion control, evidenced by the ~ 45 degree response of the impedance modulus..... 131

Figure S4.1. Schematic illustration of the synthetic method wherein the fused quartz reaction vessel is packed tightly with microfibrinous Al_2O_3 and a layer of sacrificial graphite in order to isolate compressed pellets with $M_2Mo_6S_6$ stoichiometry under an inert atmosphere during heating. The entirety of the far-right figure is placed in a microwave chamber under continuous flow of Ar. 136

Figure S4.2. PXRD patterns used for Pawley refinement (black dots), along with their calculated patterns (red line) and the difference curve (grey line) for all three PCPs studied. Insets in each case contain the characteristic (010) peak of the PCP crystal system illustrating a relatively large degree of asymmetry, consistent with many low-angle diffraction peaks. 137

Figure S4.3. Lattice-resolved TEM images for Rb-PCP and Cs-PCP that illustrate the (010) and (110) directions, respectively. K-PCP was omitted owing to the thickness of K-PCP rods preventing required levels of transmission for lattice imaging. 138

Figure S4.4. EDX spectra for (A) K-PCP, (B) Rb-PCP, and (C) Cs-PCP, illustrating no bulk elemental impurities for the rods synthesized here, and no significant evidence of bulk oxidation as might be expected from a nano-scale chalcogenide. Average alkali metal atomic percent compositions for each M_2 -PCP are listed and are in good agreement with expected values within the error of EDX quantification, although Mo/S composition is omitted owing to strong overlap between Mo L α 1 and S K α 1 lines which convolutes their quantification. 139

Figure S4.5. Result of EDX mapping of an individual K-PCP nanorod, performed with an accelerating voltage of 10keV and beam current of 3.2nA, illustrating uniform elemental distribution throughout the entirety of the rod. The corresponding line scan is shown in Figure S4.6. 140

Figure S4.6. EDX line scan for the isolated K-PCP nanorod shown in Figure S4.5. Constituent element signals scale with sample thickness under the electron beam, and is uniform along the length of the rod. The scan position represented by a yellow line in the corresponding SEM (A) has been aligned to scale with the position axis in (B)..... 141

Figure S4.7. Result of EDX mapping of an individual Rb-PCP nanorod, performed with an accelerating voltage of 10keV and beam current of 3.2nA, illustrating uniform elemental distribution throughout the entirety of the rod. The corresponding line scan is shown in Figure S4.8. 142

Figure S4.8. EDX line scan for the isolated Rb-PCP nanorod shown in Figure S4.7. Constituent element signals scale with sample thickness under the electron beam, and is uniform along the length of the rod. The scan position represented by a yellow line in the corresponding SEM (A) has been aligned to scale with the position axis in (B)..... 143

Figure S4.9. Result of EDX mapping of an individual Cs-PCP nanorod, performed with an accelerating voltage of 10keV and beam current of 3.2nA, illustrating uniform elemental distribution throughout the entirety of the rod. The corresponding line scan is shown in Figure S4.10. 144

Figure S4.10. EDX line scan for the isolated Cs-PCP nanorod shown in Figure S4.9. Constituent element signals scale together with sample thickness under the electron beam. Intensity of each component decreases from $\sim 0.6\mu\text{m}$ onward owing to decreased thickness of the rod. The scan position represented by a yellow line in the corresponding SEM (A) has been aligned to scale with the position axis in (B)... 145

Figure S4.11. Double layer capacitance for each of the inks studied herein, taken as the average slope of all repeated current versus scan-rate plots. 146

Figure S4.12. Examples of Nyquist plots for (A) PCP-free blank ink, (B) K-PCP, (C) Rb-PCP, and (D) Cs-PCP that were used to determine interfacial charge transfer resistance. Using a Randle circuit, resistance to charge transfer is taken as the difference between extrapolated x-intercepts at low AC frequency (right side) and at high frequency (left side). 147

Figure S4.13. (A) Average overpotential required to achieve a current density of $10\text{mA}/\text{cm}^2$ for all four inks, and (B) Average Tafel slope calculated for all four inks. In both figures, error bars represent a single standard deviation. 148

Table S4.1 Compiled lattice parameters extracted via Pawley refinement for $\text{M}_2\text{Mo}_6\text{S}_6$, compared with literature values. 149

1. Chapter 1 Introduction

Introduction

Sustainable terawatt-scale energy solutions for a constantly evolving energy landscape necessitate the rapid development of transformative materials that facilitate energy conversion reactions that can power industrial, commercial, and even residential sectors without further accelerating anthropogenic climate change. Transitioning from a highly pollutive fossil-fuel based energy economy to a carbon-neutral or even carbon-negative one could require massive infrastructural changes in energy production and distribution at both the national and global scales if this transition were to be achieved by complete removal of the liquid fuels currently afforded by crude oil refining. However, drop-in replacements for these fossil fuels that include short-chain hydrocarbons and oxygenates like methane, ethylene, methanol, and ethanol—maintain desirable energy densities and are synthesizable via electrochemical methods that can be readily coupled to renewable sources of electricity—namely, intermittent wind and solar electricity. The conversion of vastly abundant yet intermittent solar energy into easily storable fuels such as hydrocarbons and alcohols represents one of the defining challenges of our time. The rational design of novel catalyst materials that can facilitate chemical transformations of abundant feedstocks such as atmospheric CO₂ and water to viable fuels using sunlight as the only energy source is an urgent imperative. Such catalysts will not only provide a means of storing solar power but will also precipitate a paradigm shift within the chemical industry from reliance on petroleum feedstocks to the largescale utilization of CO₂ as the primary carbon source. The design of novel catalytic materials is subject to a stringent set of criteria—the materials need to be constituted from inexpensive and earth-abundant elements, exhibit high activity and selectivity in terms of chemical transformations, and be stable over long periods of operation. With the example of solar-to-fuels technology, materials must be designed that convert solar electricity directly to fuels (photoelectrochemical processes)^{1,2} or that convert solar-sourced electricity to fuels in a tandem photovoltaic—electrolyzer (PV-

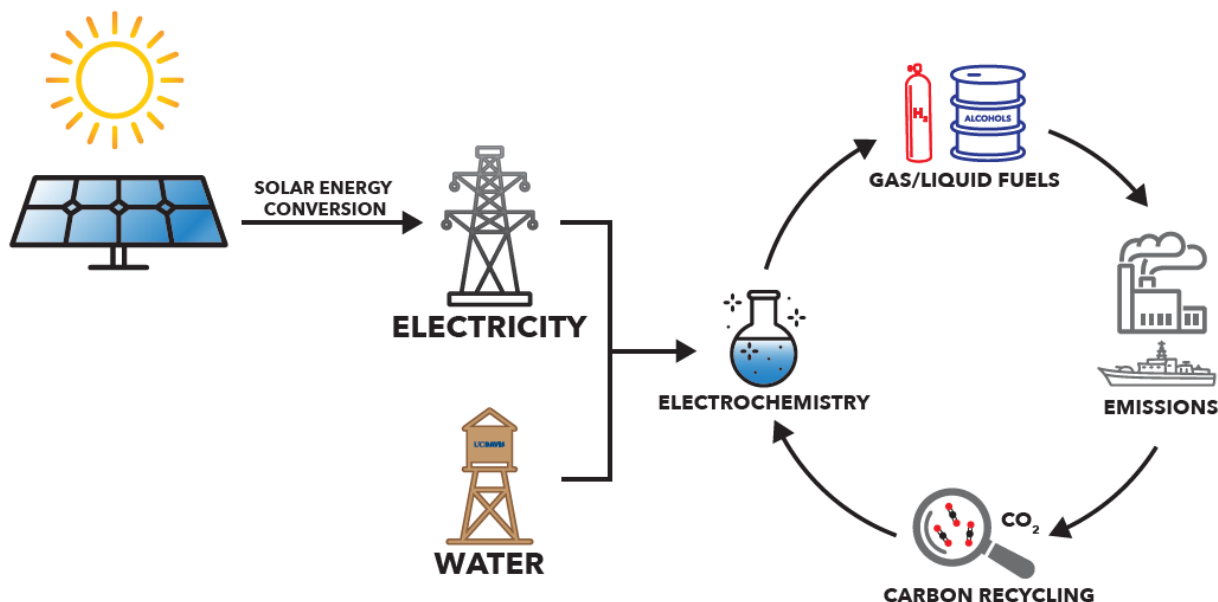


Figure 1.1 Diagram illustrating a net carbon neutral or negative energy cycle driven by renewable electricity and electrochemical conversion of atmospheric greenhouse molecules into value-added products.

electrolyzer) construct (see **Fig. 1.1**).³⁻⁵ Material performance considerations associated with either task are plentiful. Perhaps most importantly, functional material compositions are ones that most effectively reduce energy penalties for the desired chemical conversion process, like the hydrogen evolution reaction (HER) with the balanced half reaction shown in **eq. 1.1**.



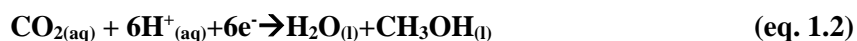
An unfortunate reality is that the most efficient (i.e. low energy penalties and high rates of fuel production) catalytic acceleration of reactions like the HER have required non-abundant elements like Pt, Ru, and Ir that engender prohibitively expensive material costs for large scale deployment.⁶⁻⁸

Earth-Abundant Electrocatalyst Design:

An increasingly popular strategy for mitigating the aforementioned composition-based limitation is the design of entirely Earth-abundant materials that *also* mediate desirable energy conversion reaction such as the aforementioned HER (to generate hydrogen gas for combustion or for use in fuel cells),⁹⁻¹¹ the CO₂ reduction (CO₂R) reaction (to form oxygenate and hydrocarbon fuels),^{12, 13} oxygen evolution reaction

(OER) (to balance cathodic reactions like HER and CO₂R),^{14, 15} and the oxygen reduction reaction (ORR) (for fuel cell applications and peroxide synthesis).^{16, 17}

Of these reactions, the electrochemical small-molecule transformations of particular interest in this body of work are the CO₂ reduction reaction (CO₂RR) and CO reduction reaction (CORR) wherein chemical bonds of dissolved CO₂ and CO, respectively, are manipulated in the presence of hydrogen (i.e. protons from aqueous electrolyte) and electrons from a surface under applied bias in order to yield hydrocarbons (e.g. methane, ethane, ethylene, propane etc.) and oxygenates (e.g. methanol, formic acid, ethanol, acetate etc.). Balanced reactions in the case of CO₂R to methanol and COR to methanol are given in **eq. 1.2** and **eq. 1.3**, respectively:



Intuitively, mediating either of these multi-proton and multi-electron transfer reactions through electrocatalysis requires an electrode surface that facilitates the complex reaction kinetics of multi-step pathways toward liquid fuels. Hence active catalyst surfaces must stabilize a series of adsorbed intermediate species while simultaneously minimizing activation barriers for proton and electron transfer steps, bond cleavage steps, and association/dissociation steps.¹⁸ This requirement is further complicated by the presence of a slew of competitive reactions that include undesirable pathways hydrocarbon and oxygenate products, and that include the ubiquitous HER which presents an existential challenge to CO₂ and CO conversion electrochemistry.^{19, 20} Hence it remains highly desirable to develop a system that can facilitate either the CO₂RR or the CORR selectively to a single liquid-phase product, with at most a single gas-phase product—ideally hydrogen gas which can be further integrated into functional energy systems.^{21, 22} To date, only metallic copper electrocatalysts have been championed for their ability to yield value-added products from CO₂ and CO with an appreciable Faradaic efficiency.^{13, 23, 24} That is, the majority of electrons passing through a biased copper surface are indeed coupled to the CO₂ or CO target molecule to produce desirable

chemicals, rather than being coupled to other species (e.g. H^+) present in solution to yield undesirable side-products. The problem with all known unary CO_2RR and $CORR$ electrocatalysts lies in their poor selectivity, their poor intrinsic reactivity, or a combination of the two.²⁵ Hence it is of great importance that new catalytically reactive systems are developed that incorporate multiple elements at their active sites in order to provide unique binding environments for adsorbate intermediates of the aforementioned conversion reactions. This strategy may prove efficacious in steering reaction trajectories selectively to specific liquid phase CO_2R and COR products, while simultaneously affording multiple levers of control over reaction efficiencies.²⁶

Studies of molybdenum chalcogenide-based CO_2 reduction catalysis have been largely focused on evaluating the basal plane and edge-site reactivity of MoS_2 , where reactivity has been evaluated in both aqueous²⁷ and ionic liquid conditions.²⁸ In aqueous electrolyte, it has been shown that basal planes of MoS_2 which have been traditionally considered inert for electrocatalysis, can in fact mediate the reduction of CO_2 to C_{2+} alcohols that include n-propanol which is an exceptionally promising value-added product. It was observed in this work by Francis and Velázquez et al²⁷ that the source of this interesting reactivity was the presence of sulfur vacancies on MoS_2 basal planes that have since been shown to encourage the generation of formaldehyde intermediates which are key in the formation of higher alcohols like ethanol and methanol.^{29,30} Additionally, a significant body of work has been dedicated to computational analysis of transition metal-doped MoS_2 where systems doped with Ni and Nb encourage adsorption $COOH^*$ and CHO^* at bridging S sites while favorably adsorbing CO^* at the metal dopant site, thereby breaking the reactivity-limiting intermediate scaling relations that plague metallic electrocatalysts.³¹ Experimentally, such doping strategies have proven successful in increasing turnover frequencies for the reduction of CO_2 to CO in ionic liquid electrolytes,³² and this mechanism of intermediate stabilization by incorporation of ternary species into molybdenum sulfides motivates the current body of work on underexplored ternary Mo-based systems with the goal of catalyzing CO_2 reduction to liquid fuels like methanol. In addition to Mo-based sulfide electrocatalysts, sulfide-derived $Cu_2S@Cu$ core shell architectures have shown relatively

high efficiencies for the formation of C_{2+} products, albeit at total Faradaic efficiencies under 35%.³³ Additionally, S-modified Sn catalysts have recently been shown to increase formate production current densities by as much as four-fold compared to their metallic analogues,³⁴ further highlighting the potential for chalcogen inclusion at catalytically active sites to encourage CO_2R reactivity. However, selective formation of fuels remains a challenge for heterogenous systems.

Chevrel-Phase and Pseudo-Chevrel-Phase Molybdenum Chalcogenide Compositions Spaces

In expanding our search for catalytically reactive materials to multinary spaces, we introduce a broad landscape of physicochemical properties that change as the compositions, structures, and dimensionality of materials change—dramatically complicating the search for viable solutions to our energy needs. However, with these multinary systems we simultaneously unlock near-infinite control with which we can leverage those very same composition-dependent variables (crystallinity, dimensionality, electronic structure, etc....) that initially appear to complicate our search for viable energy materials. As a result, we must be diligent and well-guided by chemical intuition in our extraction of meaningful properties that allow for the construction of informative composition-structure-function relationships.

One multinary family with profound energy applications that is well-suited to the pursuit of composition-structure-function relationships is the expansive metal-chalcogenide (S, Se, and Te) composition space where functionality,^{35,36} stability,³⁷ material cost, and even large-scale processability^{38,39} can be controlled via careful selection and arrangement of constituent elements. In this body of work, promising functionality is observed in pseudo-molecular and dimensionally controlled multinary chalcogenides within the Chevrel-Phase (CP) $M_yMo_6X_8$ (M = alkali, alkaline, transition, post transition metal; y = 0-4; X = S, Se, Te) and Pseudo-Chevrel-Phase (PCP) $M_2Mo_6S_6$ (M = K, Rb, Cs) families that exhibit tremendous potential for compositional modification, as illustrated in **Fig. 1.2** where experimentally verified substitution modalities are depicted. In addition, the foundations of design strategies for chalcogenide-based frameworks that have applications in energy conversion technologies like electro- and

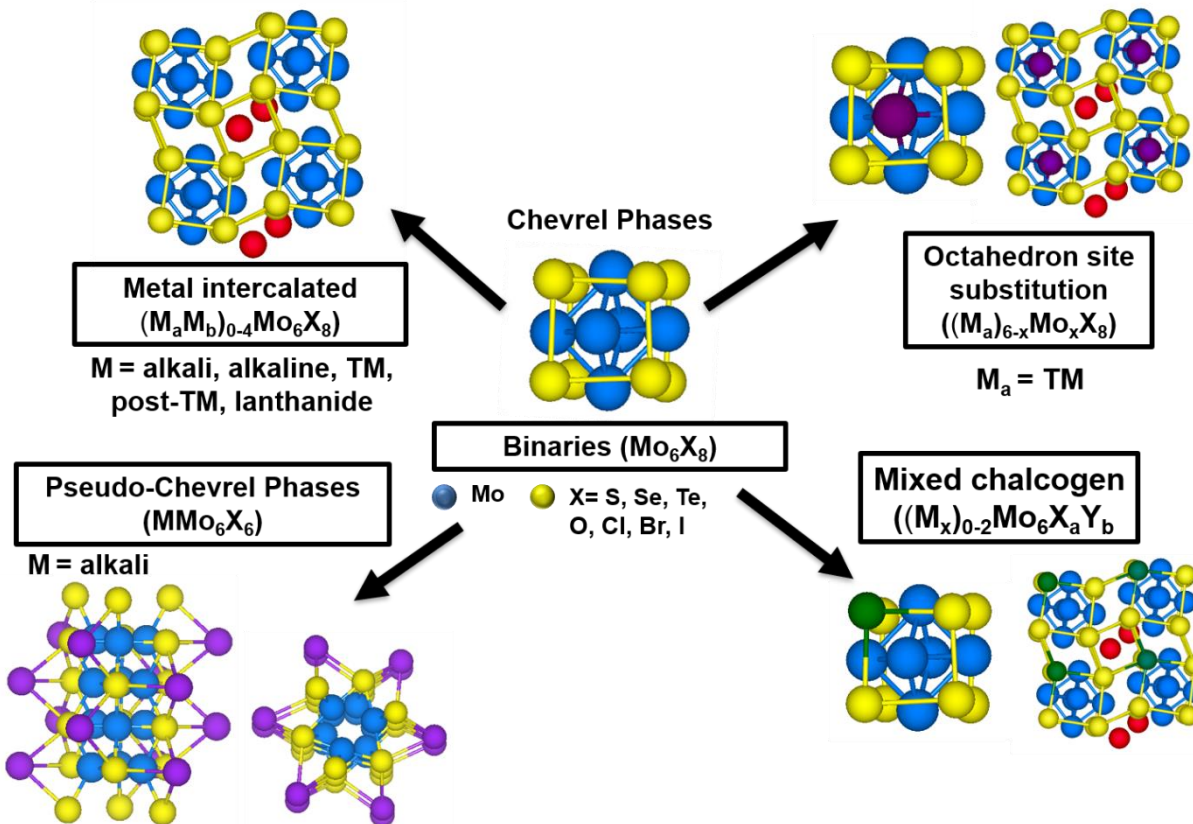


Figure 1.2. Schematic showing generic CP and PCP compositions as well as ternary and quaternary substitutions that are all synthesizable via rapid, high-temperature microwave assisted synthesis.

photoelectrocatalysis are outlined. Integrated experimental and computational approaches to chalcogenide design have already been established in some areas including adsorption affinity during electrochemical reactions as well as thermodynamic stability of frameworks as a function of composition, and we expect that future developments in functionality for these highly flexible materials will be necessarily borne out of synergistic efforts by experimentalists and theoreticians.

Composition-Structure-Function Relationships in Chevrel and Pseudo-Chevrel Phases

Important considerations when evaluating the performance of any material depend very obviously on the desired application. However, for the sake of highlighting energy applications for the flexible chalcogenide spaces of interest in this body of work, we consider properties related to local coordination and electronic structure. It is well understood that interfacial catalytic reactivity (i.e. reaction rate and selectivity) depends strongly on local coordination of reaction intermediate adsorbates at active sites.^{40, 41} In multinary

chalcogenides as with any system, these active site configurations drive reactivity through an “ensemble effect”⁴² wherein implantation of unique elements in the proximity of the adsorption site, either via structural incorporation,^{43, 44} or even by electrostatic attraction to a charged species from an electrolyte (in the case of electrocatalysis)⁴⁵ will directly affect the local electric field experienced by the adsorbate. Moreover, this implantation can affect formal coordination to molecular domains of intermediate species, as was computationally evaluated in the Chevrel phase system by Liu and White et al. for a series of cation-“promoted” Mo₆S₈ structures.^{44, 46} Intuitively, the evolution of formal bonding between catalysts and reaction intermediates depends on the orbital landscape of the systems involved. This phenomenon has been previously coined as the “ligand effect” to denote electronic contributions from surrounding species to adsorbate binding at catalytically active sites (an important consideration in coordination complexes and extended solids alike).^{42, 47} Hence, we consider the argument for using the incredibly informative and, historically, readily computed d-band center model (**Fig. 1.3**) for explaining and predicting reactivity of electrocatalysts.^{48, 49}

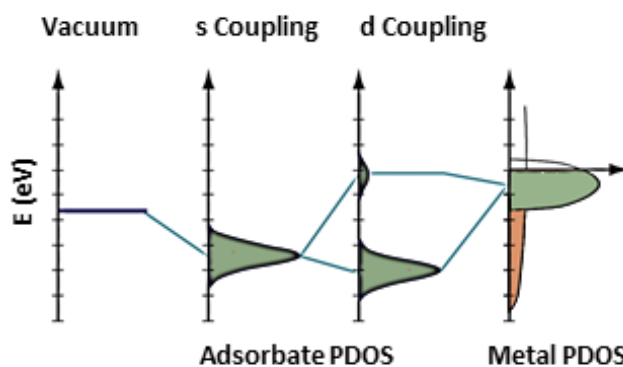


Figure 1.3. Schematic illustrating the principles of bond formation between adsorbate valence states and surface s and d states. Bond strength according to this model is dependent on the population of metal-adsorbate antibonding states, which depends on the position of the surface d-band center relative to its Fermi level. Figure adapted from Ref 49.

This descriptor is necessarily composition dependent and has proven useful for explaining the reactivity of metallic catalyst systems on the basis of bonding versus antibonding orbital population, but we must also acknowledge the severe convolution of the frontier orbital landscape within p-block systems like the chalcogenides of interest here. By introducing non-metal species into multinary chalcogenides, we obviate

a potentially straightforward mechanism for predicting reactivity like simply observing d-band characteristics. Ostensibly, more complex electronic structure-based metrics for quantifying chalcogenide reactivity must then be addressed such as the interplay between d-band *and* p-band positions or perhaps even the total density of p-states and/or d-states under the fermi level, as these electronic structure descriptors can directly inform models, for example, of adsorbate binding in interfacial catalysis, as was shown by Ortiz-Rodríguez et al. for a series of chalcogen-substituted Mo_6X_8 catalysts.⁵⁰ To advance our understanding regarding the interplay between composition, electronic structure (as detailed in **Fig. 1.4**),

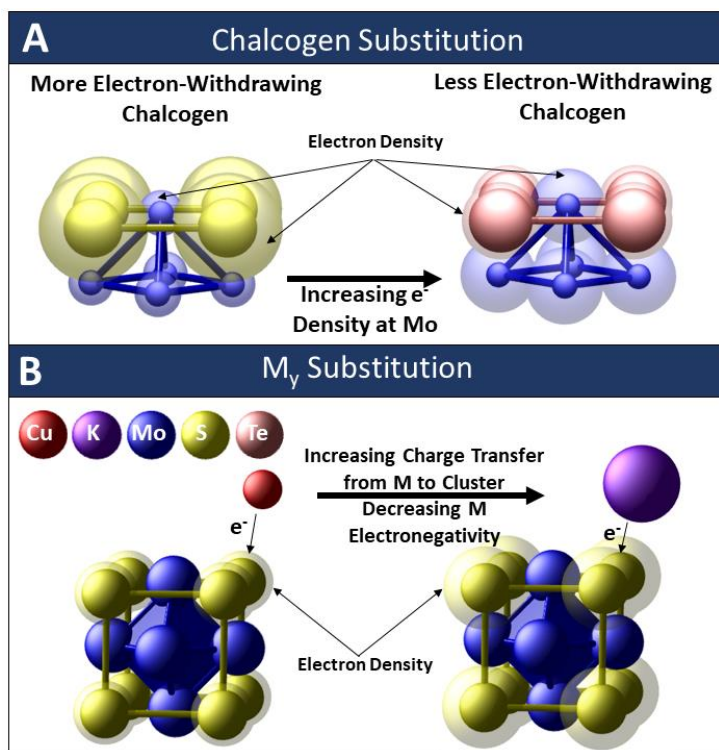


Figure 1.4. (a) Electron density within the Mo core (solid blue spheres) of the CP structure can be changed via implantation of increasingly electron-withdrawing (solid yellow spheres representing S) or electron-donating (solid pink spheres representing Te) chalcogen species, thereby controlling the formal Mo_6 valence electron count which can range from 20-24 e^- for stable CP compositions, depending on chalcogen and intercalant composition. In (a), solid spheres represent ionic radii of Mo^{2+} , S^{2-} , and Te^{2-} of 83 pm, 172 pm, and 207 pm, respectively. (b) Illustration that electron donation from M into the binary Mo_6S_8 cluster can be directed by careful selection of metallic precursors. This panel illustrates the phenomenon that charge-transfer to the cluster, specifically to the chalcogen cage as is discussed further in Chapters 2 and 3, from the intercalant increases as the electronegativity decreases (in this example electronegativity decreases from 4.48 eV for Cu in its neutral state to 2.42 eV for K in its neutral state⁵¹). All solid spheres in (b) represent Van der Waals radii similar to those expected for each species in its elemental form, and the increase in the size of the transparent spheres around S indicates an increase in electron density. In both (a) and (b) the size of transparent spheres represents the relative amount of electron density around the atom compared to its analogue in the structure to its right or left (i.e. more Mo electron density in the right structure of (a) than in the left).

local coordination, and electrocatalytic functionality in binary and ternary CPs, in Chapters 2 and 3 we evaluate the effect of compositional modification in CPs on local Mo-X coordination and on frontier electronic structure, observing the effects on catalytic CO₂R reactivity in Chapter 3 and on HER in Chapter 4. To facilitate the conceptualization of composition effects on surface reactivity, CP electronic structure and trends in intermediate adsorption will be framed in the context of electron localization (charge density) which in part motivates language from Hard-Soft Acid Base (HSAB) theory. In line with this discussion of how charge density affects local coordination and electronic structure, **Fig 1.4b** illustrates the phenomenon confirmed by Liu et al⁴⁶ in Chevrel-Phases where less electronegative and more polarizable (lower charge density) intercalants like K are more likely to undergo full charge transfer (to form their monovalent cationic species) to clusters in comparison to more electronegative and less polarizable (higher charge density) intercalants like Cu which are less likely to undergo full charge transfer to clusters. This is represented in **Fig 1.4b** by the smaller red species and larger purple species that are illustrative of the Van der Waals radii of relatively electronegative Cu and relatively electropositive K intercalants (91 pm and 152 pm, respectively). As discussed in Ref 46, this decrease in electronegativity results in increased charge transfer from M to S, which scales well with trends in decreasing reduction potentials (e.g. 0.52 V vs SHE and -2.92 V vs SHE for Cu and K, respectively), lower first ionization potentials I (e.g. 7.73 eV and 4.34 eV for Cu and K, respectively), lower electron affinities A (e.g. 1.23 eV and 0.50 eV for Cu and K, respectively), and lower absolute hardness values μ (e.g. 3.25 eV and 1.92 eV, respectively).⁵¹ These parameters, along the mulliken electronegativities χ given by the relationship $\chi = (I+A)/2$ can serve as good predictors for the tendency of an intercalant to donate electron density to a CP cluster.

X-Ray Absorption Spectroscopy

In this work we employ informative and element-specific spectroscopic techniques based on synchrotron radiation wherein core-shell electron ejection events and the relaxation and scattering events that follow are evaluated to form the basis of our understanding of the structural and electronic properties of materials. Owing to the unique nuclear charge of any given element on the periodic table, core-level electrons of an

atom within any structure are bound with some quantized attracting force. This attractive force dictates the energy required for an incident source of photons to eject electrons from within a shell of principle quantum number n ($n = 1, 2, 3, \dots$) to either the lowest unoccupied electronic state in the case of X-ray absorption near-edge structure (XANES) analysis, or to the continuum in the case of extended X-ray absorption fine structure (EXAFS) analysis, as depicted graphically in **Fig. 1.5**.

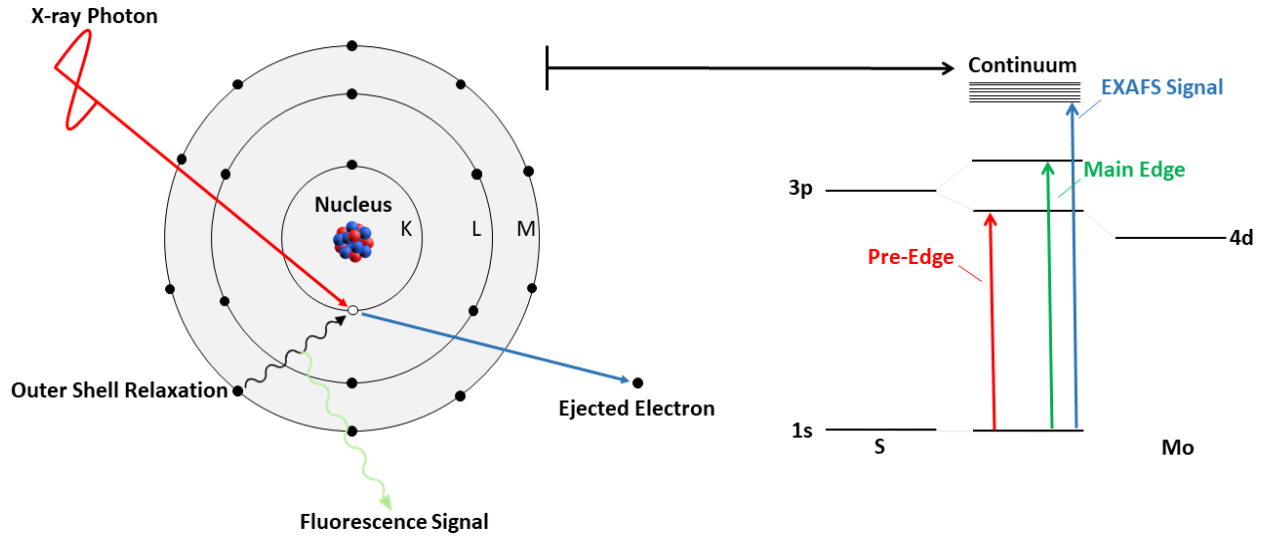


Figure 1.5. Diagram of core-level electron ejection processes analyzed with XAS, including the origin of pre-edge spectral signatures that arise due to mixing between metal and chalcogen frontier orbitals, as is the case in many of the materials of interest in this work. Figure from Ref 52.

To extract structural information from EXAFS analysis, we leverage known photoelectron scattering properties of neighboring atoms according to the EXAFS equation (eq. 1.4):

$$\chi(k) \sim S_0^2 \sum_j N_j \frac{f_j(k)}{kR_j^2} e^{-2R/\lambda(k)} e^{-2k^2\sigma_j^2} \sin[2kR_j + \delta_j(k)] \quad (\text{eq. 1.4})$$

to analyze the scattering distance to that nearest neighbor, its coordination number, and the degeneracy of the scattering paths between absorbers and nearest neighbors. In this expression, k is the wavenumber, $f(k)$ is the scattering amplitude and $\delta(k)$ is the phase-shift which both depend on the atomic number Z of the scattering species as well as the incident X-ray energy, R is the distance to the neighboring scatterer, N is its coordination number, and σ^2 is the mean-square disorder for the scattering distance. $\lambda(k)$ is the mean free path of the ejected photoelectron, and S_0^2 is the amplitude reduction factor. Holistically this equation can be used to model and predict constructive and destructive interference when the wavefunction of X-

ray-generated photoelectrons overlaps with the wavefunction of nearest-neighbor electron wavefunctions—thereby enabling element and local coordination-specific analysis within solid structures.

These complimentary XAS analysis techniques afford a slew of electronic and structural details for molecules and extended structures alike, including oxidation state,^{53, 54} orbital symmetry,⁵⁵ and electronic state population⁵⁶ in the case of XANES, as well as local coordination and nearest neighbor composition in the case of EXAFS.^{57, 58} In Chapters 2 and 3, we explore the effect of binary and ternary composition within the CP framework on the electronic make-up of constituent Mo and S species within the pseudo-molecular networks of interest, and work toward developing chemically sound correlations to electrocatalytic functionality that can be fed into iterative mechanisms for discovering novel functional materials.

Rapid Microwave-Assisted Solid-State Synthesis

The integration of microwave suscepting materials into conventional chambers that irradiate radiation at a frequency around 2.45 GHz is quite common in the food industry and in household heating applications. The mechanisms by which oscillating electromagnetic (EM) fields are converted into thermal energy depend on the nature of the absorbing species, although traditionally, as is the case with most susceptor materials, vibrational and/or rotational modes are excited by the rapidly oscillating incident EM fields to induce an overall increase in the average kinetic energy of the system; in other words, generating a temperature increase. One can alternatively introduce so called “high-temperature” susceptor materials that mediate energy transfer from electromagnetic to thermal via Joule heating (i.e. “resistive” or “resistance” heating). The efficiency with which a material can mediate this energy conversion depends on its electric and magnetic permittivities ϵ' and μ' (ability to store electric and magnetic energy) and its dielectric and magnetic losses ϵ'' and μ'' (ability to convert electrical and magnetic energy to heat), and the heating power in a susceptor-based resistive heating mechanism is directly proportional to the product of the material's electrical resistance R and the square of its electrical current I . In solid structures like graphitic carbon where conjugated pi-electron networks predominate, electrons can easily flow within layers comprised of interconnected sp^2 -hybridized carbon atoms, and impingement of an excitation source like microwave

radiation is sufficient in encouraging Joule heating that can rapidly produce temperatures well in excess of 1000°C.⁵⁹ The rapid nature of this dissipation of thermal energy depends on both the heating induced by both the electric and magnetic fields according to the expression:

$$Q_{MW} = \pi f e_0 e_r'' |E|^2 + \pi f \mu_0 \mu_r'' |H|^2 \quad (\text{eq. 1.5})$$

where Q_{MW} is the heat generation per unit volume for a given material and the $|E|$ and $|H|$ terms represent heating from the induced electric and magnetic fields, respectively.⁵⁹ In short, through appropriate selection of a susceptor with amenable dielectric properties for a given microwave frequency, coupling the susceptor material to conventional microwave reactors represents a highly effective strategy for initiating bulk nucleation of crystalline materials, as shown by successful synthesis of other multinary chalcogenides like CuTi_2S_4 , FeS_2 , and CoS_2 ,⁶⁰ as well as chalcopyrites like CuInS_2 and CuInSe_2 .^{61, 62} The implementation of this synthetic strategy, as depicted in **Fig 1.6**, is discussed for the materials synthesized in Chapters 2, 3, and 4. This rapid high-temperature modality may serve as a strong driving force for increasing the throughput with which we can synthesize and characterize novel catalyst compositions within material families that have controllable thermodynamic stability.

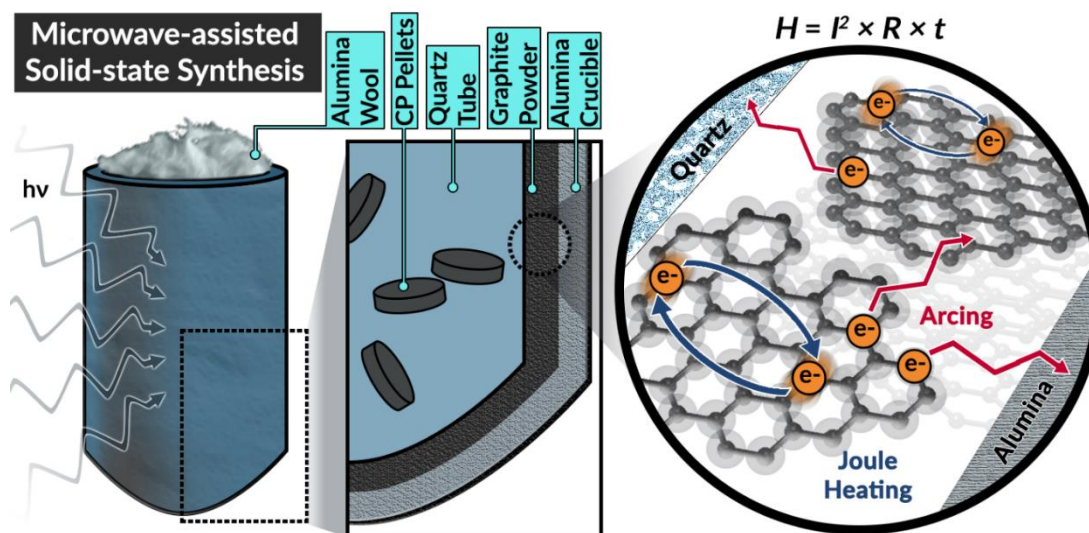


Figure 1.6. Illustration of the microwave-assisted heating technique used to synthesize materials throughout this work. Inset captures the commonly observed case where resistive heating is coupled to heating from arcing phenomena wherein electrical charge jumps from solid structure to solid structure.

References

1. V. Kumaravel, J. Bartlett and S. C. Pillai, *ACS Energy Letters*, 2020, **5**, 486-519.
2. S. W. Boettcher, E. L. Warren, M. C. Putnam, E. A. Santori, D. Turner-Evans, M. D. Kelzenberg, M. G. Walter, J. R. McKone, B. S. Brunschwig, H. A. Atwater and N. S. Lewis, *Journal of the American Chemical Society*, 2011, **133**, 1216-1219.
3. U. Banin, N. Waiskopf, L. Hammarström, G. Boschloo, M. Freitag, E. M. J. Johansson, J. Sá, H. Tian, M. B. Johnston, L. M. Herz, R. L. Milot, M. G. Kanatzidis, W. Ke, I. Spanopoulos, K. L. Kohlstedt, G. C. Schatz, N. Lewis, T. Meyer, A. J. Nozik, M. C. Beard, F. Armstrong, C. F. Megarity, C. A. Schmuttenmaer, V. S. Batista and G. W. Brudvig, *Nanotechnology*, 2020, **32**, 042003.
4. R. E. Clarke, S. Giddey, F. T. Ciacchi, S. P. S. Badwal, B. Paul and J. Andrews, *International Journal of Hydrogen Energy*, 2009, **34**, 2531-2542.
5. N. S. Lewis, *Science*, 2016, **351**.
6. C. Li and J.-B. Baek, *ACS Omega*, 2020, **5**, 31-40.
7. R. Yukesh Kannah, S. Kavitha, Preethi, O. Parthiba Karthikeyan, G. Kumar, N. V. Dai-Viet and J. Rajesh Banu, *Bioresource Technology*, 2021, **319**, 124175.
8. M. R. Shaner, H. A. Atwater, N. S. Lewis and E. W. McFarland, *Energy & Environmental Science*, 2016, **9**, 2354-2371.
9. X. Xie, C. He, B. Li, Y. He, D. A. Cullen, E. C. Wegener, A. J. Kropf, U. Martinez, Y. Cheng, M. H. Engelhard, M. E. Bowden, M. Song, T. Lemmon, X. S. Li, Z. Nie, J. Liu, D. J. Myers, P. Zelenay, G. Wang, G. Wu, V. Ramani and Y. Shao, *Nature Catalysis*, 2020, **3**, 1044-1054.
10. I. Roger, M. A. Shipman and M. D. Symes, *Nature Reviews Chemistry*, 2017, **1**, 0003.
11. J. Kibsgaard and T. F. Jaramillo, *Angewandte Chemie International Edition*, 2014, **53**, 14433-14437.
12. L. Ji, L. Chang, Y. Zhang, S. Mou, T. Wang, Y. Luo, Z. Wang and X. Sun, *ACS Catalysis*, 2019, **9**, 9721-9725.
13. J. Resasco and A. T. Bell, *Trends in Chemistry*, 2020, **2**, 825-836.
14. M. Huynh, T. Ozel, C. Liu, E. C. Lau and D. G. Nocera, *Chemical Science*, 2017, **8**, 4779-4794.
15. C. C. L. McCrory, S. Jung, I. M. Ferrer, S. M. Chatman, J. C. Peters and T. F. Jaramillo, *Journal of the American Chemical Society*, 2015, **137**, 4347-4357.
16. H. Sheng, E. D. Hermes, X. Yang, D. Ying, A. N. Janes, W. Li, J. R. Schmidt and S. Jin, *ACS Catalysis*, 2019, **9**, 8433-8442.
17. A. A. Gewirth, J. A. Varnell and A. M. DiAscro, *Chemical Reviews*, 2018, **118**, 2313-2339.

18. T. K. Todorova, M. W. Schreiber and M. Fontecave, *ACS Catalysis*, 2020, **10**, 1754-1768.
19. A. Goyal, G. Marcandalli, V. A. Mints and M. T. M. Koper, *Journal of the American Chemical Society*, 2020, **142**, 4154-4161.
20. E. R. Cave, C. Shi, K. P. Kuhl, T. Hatsukade, D. N. Abram, C. Hahn, K. Chan and T. F. Jaramillo, *ACS Catalysis*, 2018, **8**, 3035-3040.
21. D. Ferrero, M. Gamba, A. Lanzini and M. Santarelli, *Energy Procedia*, 2016, **101**, 50-57.
22. F. Mueller-Langer, E. Tzimas, M. Kaltschmitt and S. Peteves, *International Journal of Hydrogen Energy*, 2007, **32**, 3797-3810.
23. C. Yang, Y. Wang, L. Qian, A. M. Al-Enizi, L. Zhang and G. Zheng, *ACS Applied Energy Materials*, 2021, **4**, 1034-1044.
24. K. P. Kuhl, E. R. Cave, D. N. Abram and T. F. Jaramillo, *Energy & Environmental Science*, 2012, **5**, 7050-7059.
25. B. Khezri, A. C. Fisher and M. Pumera, *Journal of Materials Chemistry A*, 2017, **5**, 8230-8246.
26. Z. Sun, T. Ma, H. Tao, Q. Fan and B. Han, *Chem*, 2017, **3**, 560-587.
27. S. Francis, J. M. Velázquez, I. M. Ferrer, D. A. Torrel, D. Guevarra, M. T. McDowell, K. Sun, X. Zhou, F. H. Saadi, J. John, M. H. Richter, F. P. Hyler, K. M. Papadantonakis, B. S. Brunschwig and N. S. Lewis, *Chemistry of Materials*, 2018, **30**, 4902-4908.
28. M. Asadi, B. Kumar, A. Behranginia, B. A. Rosen, A. Baskin, N. Reppin, D. Pisasale, P. Phillips, W. Zhu, R. Haasch, R. F. Klie, P. Kral, J. Abiade and A. Salehi-Khojin, *Nature Communications*, 2014, **5**, 4470.
29. S. Kang, S. Han and Y. Kang, *ChemSusChem*, 2019, **12**, 2671-2678.
30. D. Le, T. B. Rawal and T. S. Rahman, *The Journal of Physical Chemistry C*, 2014, **118**, 5346-5351.
31. K. Chan, C. Tsai, H. A. Hansen and J. K. Nørskov, *ChemCatChem*, 2014, **6**, 1899-1905.
32. P. Abbasi, M. Asadi, C. Liu, S. Sharifi-Asl, B. Sayahpour, A. Behranginia, P. Zapol, R. Shahbazian-Yassar, L. A. Curtiss and A. Salehi-Khojin, *ACS Nano*, 2017, **11**, 453-460.
33. T. T. Zhuang, Z. Q. Liang, A. Seifitokaldani, Y. Li, P. De Luna, T. Burdyny, F. Che, F. Meng, Y. Min, R. Quintero-Bermudez, C. T. Dinh, Y. Pang, M. Zhong, B. Zhang, J. Li, P. N. Chen, X. L. Zheng, H. Liang, W. N. Ge, B. J. Ye, D. Sinton, S. H. Yu and E. H. Sargent, *Nature Catalysis*, 2018, **1**, 421-428.
34. X. Zheng, P. De Luna, F. P. Garcia de Arquer, B. Zhang, N. Becknell, M. B. Ross, Y. Li, M. N. Banis, Y. Li, M. Liu, O. Voznyy, C. T. Dinh, T. Zhuang, P. Stadler, Y. Cui, X. Du, P. Yang and E. H. Sargent, *Joule*, 2017, **1**, 794-805.
35. J. Bonde, P. G. Moses, T. F. Jaramillo, J. K. Nørskov and I. Chorkendorff, *Faraday Discussions*, 2009, **140**, 219-231.

36. A. A. Tedstone, D. J. Lewis and P. O'Brien, *Chemistry of Materials*, 2016, **28**, 1965-1974.
37. K. Lilova, J. T. Perryman, N. R. Singstock, M. Abramchuk, T. Subramani, A. Lam, R. Yoo, J. C. Ortiz-Rodríguez, C. B. Musgrave, A. Navrotsky and J. M. Velázquez, *Chemistry of Materials*, 2020, **32**, 7044-7051.
38. F. Murgia, P. Antitomaso, L. Stievano, L. Monconduit and R. Berthelot, *Journal of Solid State Chemistry*, 2016, **242**, 151-154.
39. X. Li, X. Lv, N. Li, J. Wu, Y.-Z. Zheng and X. Tao, *Applied Catalysis B: Environmental*, 2019, **243**, 76-85.
40. D. D. Zhu, J. L. Liu and S. Z. Qiao, *Advanced Materials*, 2016, **28**, 3423-3452.
41. Z. W. Seh, J. Kibsgaard, C. F. Dickens, I. Chorkendorff, J. K. Nørskov and T. F. Jaramillo, *Science*, 2017, **355**.
42. P. Liu and J. K. Nørskov, *Physical Chemistry Chemical Physics*, 2001, **3**, 3814-3818.
43. X. Hong, K. Chan, C. Tsai and J. K. Nørskov, *ACS Catalysis*, 2016, **6**, 4428-4437.
44. P. Liu, Y. Choi, Y. Yang and M. G. White, *J Phys Chem A*, 2010, **114**, 3888-3895.
45. J. Resasco, L. D. Chen, E. Clark, C. Tsai, C. Hahn, T. F. Jaramillo, K. Chan and A. T. Bell, *Journal of the American Chemical Society*, 2017, **139**, 11277-11287.
46. C. Liu and P. Liu, *ACS Catalysis*, 2015, **5**, 1004-1012.
47. B. Hammer and J. K. Nørskov, *Surface Science*, 1995, **343**, 211-220.
48. S. Bhattacharjee, U. V. Waghmare and S.-C. Lee, *Scientific Reports*, 2016, **6**, 35916.
49. J. K. Nørskov, F. Abild-Pederson, F. Studt, T. Bligaard, *PNAS*, 2011, **3**, 937-943.
50. J. C. Ortiz-Rodríguez, N. R. Singstock, J. T. Perryman, F. P. Hyler, S. J. Jones, A. M. Holder, C. B. Musgrave and J. M. Velázquez, *ACS Applied Materials & Interfaces*, 2020, **12**, 35995-36003.
51. R. G. Pearson, *Inorganic Chemistry*, 1988, **27**, 734-740.
52. J. T. Perryman, F. P. Hyler, J. C. Ortiz-Rodríguez, A. Mehta, A. R. Kulkarni and J. M. Velázquez, *Journal of Coordination Chemistry*, 2019, **72**, 1322-1335.
53. M. Kubin, M. Guo, T. Kroll, H. Löchel, E. Källman, M. L. Baker, R. Mitzner, S. Gul, J. Kern, A. Föhlisch, A. Erko, U. Bergmann, V. Yachandra, J. Yano, M. Lundberg and P. Wernet, *Chemical Science*, 2018, **9**, 6813-6829.
54. V. Kunzl, *Collection of Czechoslovak Chemical Communications*, 1932, **4**, 213-224.
55. J. M. Velázquez, C. Jaye, D. A. Fischer and S. Banerjee, *The Journal of Physical Chemistry C*, 2009, **113**, 7639-7645.
56. A. Nilsson and N. Mårtensson, *Physica B: Condensed Matter*, 1995, **208-209**, 19-22.

57. P. A. O'Day, J. J. Rehr, S. I. Zabinsky and G. E. Brown, Jr., *Journal of the American Chemical Society*, 1994, **116**, 2938-2949.
58. A. I. Frenkel, *Chemical Society Reviews*, 2012, **41**, 8163-8178.
59. M. Bhattacharya and T. Basak, *Energy*, 2016, **97**, 306-338.
60. M. M. Butala, M. A. Perez, S. Arnon, C. Gobel, M. B. Preefer and R. Seshadri, *Solid State Sciences*, 2017, **74**, 8-12.
61. C. C. Landry and A. R. Barron, *Science*, 1993, **260**, 1653-1655.
62. C. C. Landry, J. Lockwood and A. R. Barron, *Chemistry of Materials*, **7**, 699-706.

2. Chapter 2: Metal-Promoted Mo₆S₈ Clusters: A Platform for Probing Ensemble Effects on the Electrochemical Conversion of CO₂ and CO to Methanol

Abstract

Presented herein is an investigation of a promising ternary metal sulfide catalyst that is capable of electrochemically converting CO₂ to liquid and gas fuels such as methanol and hydrogen. When promoted by copper, an extended structure of Chevrel-phase Mo₆S₈ clusters is capable of reducing CO₂ and CO to methanol in aqueous conditions with an overpotential of -0.4 V vs RHE. H₂ gas is simultaneously and preferentially evolved during this process, contributing to total current densities as high as 35 mA/cm² at a potential of -1.0V vs RHE. It has been observed that Cu₂Mo₆S₈ displays unique catalytic activity among other Mo-based chalcogenides in terms of product selectivity, and we attribute this activity to molybdenum sulfide cluster units based on the results of structural, electronic, and electroanalytical characterization. Also discussed is the formulation of an interesting electronic structure-function correlation founded on the basis of X-ray absorption spectroscopic analyses and corroborated by the results of electroanalytical evaluation, where it has been observed that introduction of metal promoting species into the Chevrel-phase framework encourages charge transfer into cluster chalcogen sites.

Introduction

Growing interest in the fields of energy conversion and storage involves developing materials and methods that can facilitate production of liquid fuel products which can easily be incorporated into modern petroleum-based infrastructures.^{1,2} In certain difficult-to-decarbonize energy services such as long-distance shipping, aviation, and production of materials like steel and cement—which combined contribute to over 9.2 Gt of CO₂ emissions per year—implementation of alternative energy sources based on hydrogen or solar energy is infeasible owing to necessarily high gravimetric and volumetric energy densities.³ However, it is immediately apparent that continued production and subsequent combustion of fossil fuels may

exacerbate detrimental anthropogenic effects on both public and environmental health. Hence it will be desirable for future methods of fuel production to utilize abundant feedstocks such as solar energy and water, as well as captured and/or atmospheric CO₂.³ This will ensure that future energy cycles are effectively carbon-neutral and based on converted renewable energy.⁴ One potential route towards realizing carbon-neutrality is electrochemical reduction of captured CO₂ to liquid fuels; this process will need to be facilitated by an earth-abundant, selective and efficient catalyst material that is stable under aqueous, near-neutral operating conditions.⁵ Unfortunately, highly selective CO₂ and CO reduction to energy-dense hydrocarbons and oxygenates in water remains a challenge for all known heterogeneous catalysts.⁶

Transition metal chalcogenides are capable of withstanding reductive potentials over wide pH ranges,⁷ and are among the best earth-abundant hydrogen evolution catalysts under extreme pH conditions.⁸ Moreover, transition metal chalcogenide materials have been studied for decades, owing to their tunable electronic, structural, and catalytic properties.¹⁰⁻¹⁴ Chevrel-phase (CP) sulfides with formula M_xMo₆S₈ (M = transition metal, alkali metal, x = 0-4) have been the subject of much study due to their high-temperature superconducting behavior as well as their reputation as the first functional multivalent battery cathode materials.¹⁵⁻¹⁷ To the best of our knowledge, despite numerous studies evaluating their performance as hydrodesulfurization, hydrogen evolution, oxygen reduction, and oxygen evolution catalysts, no experimental work has elucidated the ability of Chevrel-phase materials to reduce CO₂.^{8, 14, 18-20} The chemical composition of catalytically active sites for small-molecule electroreduction is known to have a direct effect on the adsorption strength of reaction intermediates, largely stemming from modulation of electronic structure and subtle alterations in the geometry of binding sites.²¹⁻²⁴ In the context of heterogeneous catalyst surfaces, the former is known as the “ligand effect,” and often, changes to electronic structure through compositional modification lead to accompanying effects associated with unique active-site “ensembles,” wherein neighboring atoms at catalytically active binding sites afford unique coordination interactions (**Fig 2.1**) for intermediate species with varying energetic favorability.^{25, 26} In other words, the presence of multiple elements at an active binding site can afford a distribution of diverse and distinctive coordination environments for reaction intermediates—effectively allowing for independent variation of

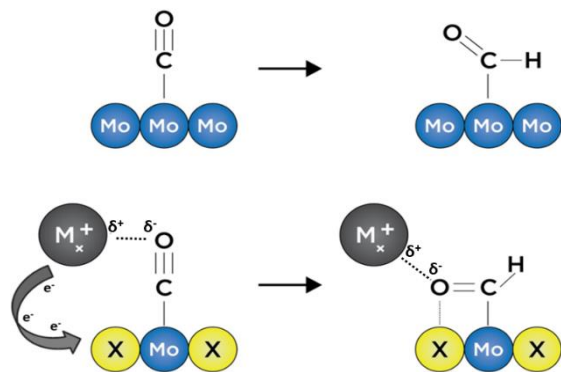


Figure 2.1. Hypothetical depiction of CO hydrogenation over a purely metallic surface (top), compared to a “promoted” metal chalcogenide surface (bottom) where synergistic chalcogen (X=S, Se, Te)(yellow) and intercalant (grey) inclusion at CO₂RR active Mo sites (blue) can hypothetically encourage a unique intermediate binding geometry. Simplified Coulombic stabilization is included for clarity and is represented by the dashed line connecting partially negatively charged (O) and partially/formally positively charged (M) species.

binding strength for preceding and succeeding adsorbates with relevance in a given catalytic reaction. These phenomena are illustrated graphically in **Fig. 2.1** where intermediate binding over a metallic surface is compared to binding over a surface with a ternary active-site ensemble. Recent computational studies by Liu *et al* suggest that CP sulfides may be promising candidates as selective catalysts for the formation of methanol, both from CO₂ and from syngas (CO and H₂).^{26, 27} Specifics of a potential reaction mechanism are discussed later in this work, although it is noteworthy that key intermediate species in the CO₂ reduction reaction (CO₂RR) such as CO* and HCO* are thought to be stabilized at Mo binding sites by cationic promoting species, while adjacent S atoms facilitate sequential hydrogenation toward an energy-dense product.^{26, 28} Binding strengths to these two intermediates in particular are often key factors in the rate of CO₂ reduction to liquid fuels; hence it is critical that materials which promote favorable binding are investigated.²⁵

In this work, the catalytic ability of the Cu₂Mo₆S₈ CP is reported to reduce both CO₂ and CO to methanol without also producing a myriad of other CO₂RR products, and a rationale for such behavior is provided through interpretation of complimentary electronic and local structure analysis.

Experimental Methods

Chemicals and Materials:

MoS₂ powder (99%, ~325 mesh), Cu powder (99.995%, ~100 mesh), Ni powder (99.8%, ~325 mesh), Cr powder (99.85%, ~100 mesh), and Pt mesh (99.99%) were used as purchased from Alfa Aesar. Mo powder (99.99%, ~100 mesh), Na₂CO₃ (99.999% trace metals basis), and NaHCO₃ (>99.5%) were used as purchased from Sigma Aldrich. Na₂CO₃ electrolyte solutions were prepared with 18.2 MΩ/cm water from a Thermo-Fisher Barnstead E-pure® purification system and did not require any pre-electrolysis treatment. Research-grade CO₂ (99.999%) and CO (99.999%) were used as purchased from Matheson Gas. Ag/AgCl reference electrodes were purchased through ALS Japan. Selemion® anion exchange membrane was purchased from AGC Engineering and stored in ultra-pure deionized water prior to use in electrochemical experiments.

Catalyst Synthesis:

CP catalysts were prepared by a direct microwave assisted solid-state synthesis method adapted from literature methods.²⁹ To obtain the desired CP, an appropriate metal powder (e.g. Cu, Cr, Ni), Mo powder, and MoS₂ powder were mixed under N₂ atmosphere in stoichiometric ratios to within +/- 0.0002 g of their target masses, according to the reaction $M_x + 2Mo + 4MoS_2 \rightarrow M_xMo_6S_8$ to obtain 500 mg of precursor in total (see **Table 2.1** for corresponding reagent masses).

Table 2.1. Reagent masses used to obtain 500 mg precursor mixtures for microwave heating.

Composition	Molar Mass (g/mol)	M _x Mass (g)	Mo Mass (g)	MoS ₂ Mass (g)
Cr _{1.73} Mo ₆ S ₈	922.181	0.0488	0.1040	0.3472
Ni ₂ Mo ₆ S ₈	949.614	0.0618	0.1010	0.3372
Cu ₂ Mo ₆ S ₈	959.320	0.0662	0.1000	0.3337

Precursors were then ball-milled for 24 hrs under N₂ and pressed under 25 metric tons over a 20 mm surface area. Compressed powders were transferred to fused quartz tubes, and Al₂O₃ wool was tightly packed above the pellet under +5.0 mbar partial pressure of N₂ as shown in **Fig. S2.1**. This reaction vessel was then transferred to a bath of ~325 mesh graphite powder in a conventional microwave that had been

purged with Ar and irradiated with microwaves at a power of 1000 W for 10 minutes. In this process, graphite acts as a microwave susceptor and radiates heat to generate reaction temperatures $>900^{\circ}\text{C}$ after less than one minute of irradiation. After allowing full phase-conversion over the course of a 10 minute reaction time, the quartz tube was removed from the graphite bath and immediately cooled in a room-temperature water bath. In order to obtain bare Mo_6S_8 , Cu was chemically etched from a $\text{Cu}_2\text{Mo}_6\text{S}_8$ pellet according to literature methods which involved bubbling O_2 gas into a 6.0 M HCl solution overnight.³⁰ The synthesized binary product was isolated from the leachate by vacuum filtration followed by 5 sequential washes with ~ 10 mL of ultra-pure de-ionized (UPDI) water to ensure complete removal of residual acid and CuCl_4^{2-} complex that was formed through the leaching process.

Structural and Electronic Characterization:

Crystal structures and phase purity of as-synthesized CPs were analyzed via powder X-ray diffraction (PXRD) using a Bruker D8 Advance diffractometer with Cu K-alpha radiation (1.5406 \AA) as well as at Stanford Synchrotron Radiation Lightsource (SSRL) beamline (BL) 2-1 (0.728068 \AA). PXRD experiments at BL 2-1 were performed under He atmosphere with a 1.3 Tesla bend magnet and a Si (111) monochromator giving an energy resolution ($\Delta E/E$) of 5×10^{-4} . Powder pattern indexing (**Fig. S2.2**) and full-pattern refinement as shown in **Fig. 2.2** was performed using the TOPAS analysis software by Bruker.

Catalyst morphology and composition were analyzed before and after electrolysis using an FEI (Hillsboro, OR) 430 Nano Scanning Electron Microscope (SEM) and an FEI Scios DualBeam SEM with an Oxford Energy Dispersive X-ray (EDX) detector, respectively. Further elemental analysis was completed using a PHI Versaprobe 3 X-ray photoelectron spectrometer (XPS) to determine catalyst surface composition and oxidation state before and after electrolysis. Additional structural and electronic information was acquired through ex-situ XAS at SSRL beam lines 4-1 and 4-3 using hard and soft/tender X-rays, respectively, in order to acquire X-ray Absorption Near-Edge Structures (XANES) and Extended X-ray Absorption Fine Structure (EXAFS) information for Cu, Mo, and S.

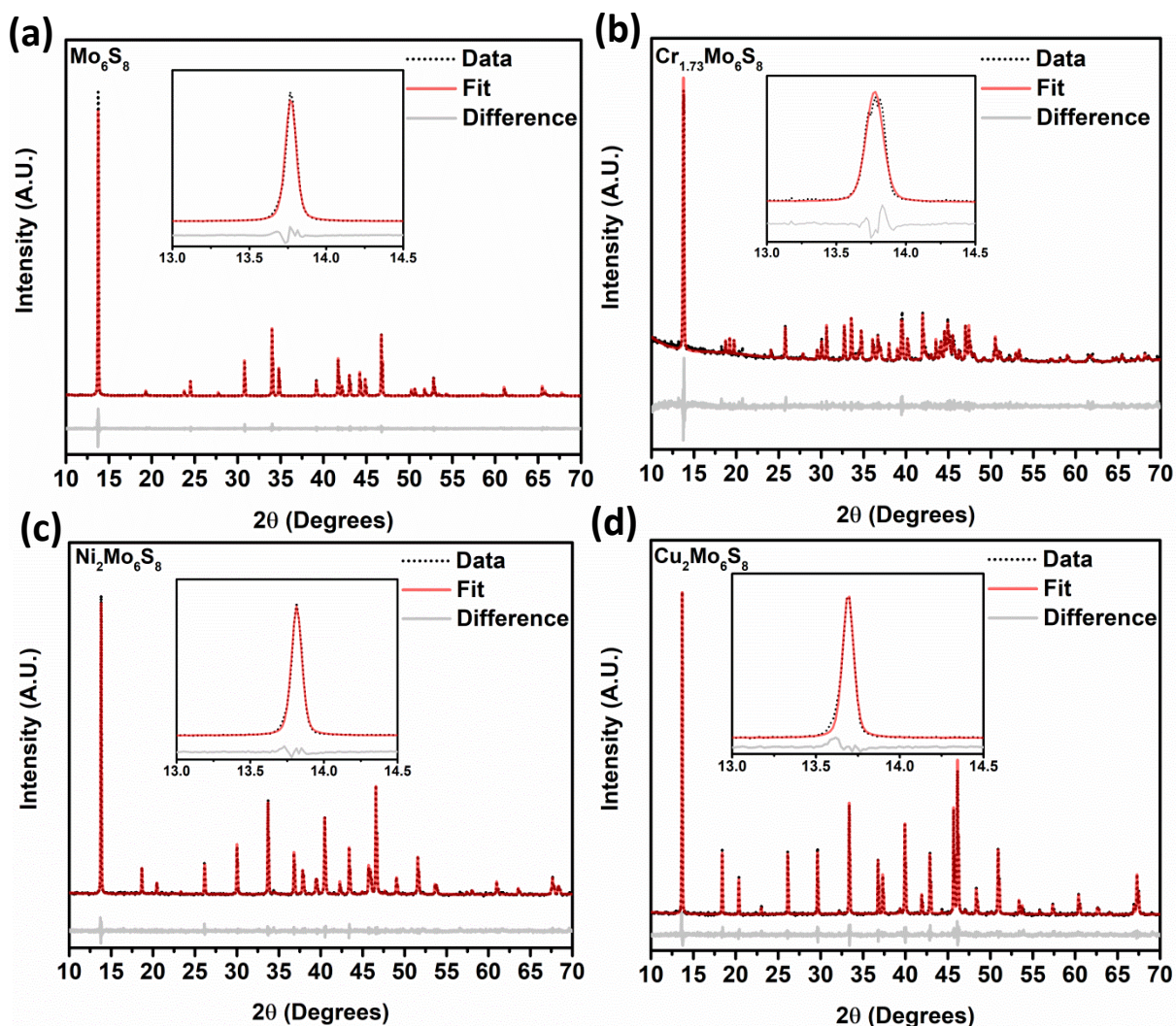


Figure 2.2. Fitted XRD patterns for Mo_6S_8 (a), $\text{Cr}_{1.73}\text{Mo}_6\text{S}_8$ (b), $\text{Ni}_2\text{Mo}_6\text{S}_8$ (c), and $\text{Cu}_2\text{Mo}_6\text{S}_8$ (d), showing difference (gray) between experimental data (black) and calculated curve (red). Insets are provided for each panel to illustrate the characteristic asymmetry of the $\langle 101 \rangle$ peak at around 13.8° . Extracted lattice parameters are given in Table S2.1 and compared to expected values.

X-ray Absorption Spectroscopy and Data Analysis:

Near-edge (XANES) and fine structure (EXAFS) information was collected SSRL BL 4-1 (molybdenum K-edge and copper K-edge) and BL 4-3 (sulfur K-edge). All samples were collected at room temperature (25°C). BL 4-1 operates with a 20 pole 2.0-Tesla wiggler station and uses a liquid N_2 -cooled double-crystal Si (220) monochromator giving an energy resolution ($\Delta E/E$) of 1×10^{-4} and flux of 2×10^{12} . BL 4-3 monochromator uses the Si (111) giving similar resolution and flux. Samples were collected in fluorescence and transmission with foil standards (Mo and Cu) collected simultaneously for calibration, while sodium

thiosulfate was measured separately as a calibration standard for sulfur K-edge measurements. Data was calibrated for energy by comparing the first derivative of sample spectrum with that of the respective elemental reference. Scans were performed in triplicate and merged to reduce noise at high k values. Processing was done using Athena and AUTOBK algorithm under the Demeter package.³¹ EXAFS modeling (Mo K and Cu K-edge) was done using Artemis in the Demeter package. Theoretical EXAFS was calculated based on previous refinement for Cu₂Mo₆S₈ from literature.³¹⁻³³ Mo K-edge data was fit in R-space using Hanning window and multiple k-weight (1, 2, and 3) using a reciprocal space range of 2.0 Å⁻¹ – 12.5 Å⁻¹ and a real space range of 1.0 Å – 3.2 Å. The scattering paths were calculated using feff 6.³¹ Dominant scattering paths for the Mo K-edge data, Mo – S (4 paths), Mo – Mo (4 paths), and Mo – Cu (2 paths) were fit using a single energy parameter (E₀), a passive reduction factor (S₀²) set to 0.83 for Mo K found by fitting the Mo foil standard, bond length shift parameters (drS1, drS2, drMo1, drCu1), and Debye-Waller thermal parameter (ssS, ssMo, and ssCu) giving a total of 8 parameters in the fit. The un-promoted Mo₆S₈ CP was fit with the same scheme without Cu scattering paths. The Cu K-edge data was fit using the data range of 2.0 Å⁻¹ – 12.0 Å⁻¹ in k space and 1.3 Å – 4.2 Å in real space. No Cu-Cu scattering paths appeared to contribute significantly to the EXAFS signal and therefore only Cu – S (2 paths), and Cu – Mo (4 paths) were given parameters of E₀, drS1, drS2, drMo1, ssS, and ssMo. The passive reduction factor (S₀²) was set to 0.82, found by fitting the Cu foil standard. Theoretical XANES were calculated with Feff9.05 using full multiple scattering.³⁴

Electrode Preparation and Electrochemical Analysis:

Electrodes in all catalysis studies presented here were comprised of as-synthesized CP pellets in the case of metal-promoted Cr, Ni, and Cu CPs, while un-promoted Mo₆S₈ was deposited on conductive carbon paper using a PTFE binder to improve structural integrity. CP samples were integrated as working electrodes into a custom three-electrode cell as shown in **Fig. S2.3** where the working and counter electrode compartments were separated by a Selemion® anion-exchange membrane. The working, reference (Ag/AgCl), and counter (Pt mesh) electrodes were submerged in 0.1 M Na₂CO₃ solution that had been sparged with ultra-pure CO₂ for 1 hr—this long purge time ensure complete removal of O₂ and N₂ from the

electrolyte as well as the cell headspace. This CO₂ sparging process simultaneously shifted the electrolyte to a near-neutral pH as shown in **Fig. S2.4**, while experiments utilizing CO as the target molecule required a 0.1 M NaHCO₃ electrolyte in order to maintain near-neutral pH. As a result of the water-gas shift reaction which causes continual loss of CO₂ and resultant equilibria shifting toward CO₃²⁻ the pH of CO-saturated NaHCO₃ electrolyte increased over the course of bulk electrolysis, as shown in **Fig. S2.5**, although the final pH was still less than 8.5 after electrolysis in all cases, therefore no additional adjustments were made to maintain near-neutral pH. Magnetic stirring was implemented to ensure homogenization of the electrolyte throughout the course of reaction and to mitigate issues associated with CO₂ mass transport. All electrochemical experiments were carried out using a Bio-Logic VSP-300 multichannel potentiostat and potentials were converted to RHE scale using **Eq. 2.1**.

$$E_{\text{RHE}} = E_{(\text{Ag}/\text{AgCl})} + 0.195 + 0.059 \times \text{pH} \quad (\text{Eq. 2.1})$$

Electrochemical activity was evaluated potentiostatically via linear sweep voltammetry under N₂ and under CO₂ atmosphere as shown in **Fig. S2.6** as well as by controlled-potential electrolysis (CPE) at fixed potentials with 50 coulombs of charge passing through the system in all electrolysis experiments. Chronoamperometry experiments performed under CO₂ and CO atmosphere were repeated under N₂ atmosphere to ensure electrolyte reduction was not the source of product formation. Further, catalyst stability was determined via open circuit voltammetry for 12 hrs under CO₂ atmosphere where Nuclear Magnetic Resonance (NMR) product quantification was performed before and after each experiment to ensure catalyst degradation does not contribute to observed product distributions, as is discussed later.

Product Analysis:

To detect liquid products of CPE experiments, electrolyte aliquots were analyzed using a 400 MHz Bruker NMR spectrometer using a water pre-saturation program with a DMF internal standard and D₂O as the lock target (see **Fig. S2.7** for a full NMR spectrum that details the result of water suppression). Faradaic efficiencies for liquid products was calculated according to **Eq. 2.2**.

$$FE(\%) = \frac{nFCV}{Q_{tot}} \quad (\text{Eq. 2.2})$$

where n = # of electrons transferred per product molecule

F = Faraday's constant

C = Product concentration in electrolyte solution

V = Volume of electrolyte solution

Q_{tot} = Total charge passed

For the detection of gas-phase products such as H₂ and CO, methane and ethylene, gas chromatography with thermal conductivity detection (GC–TCD) was implemented as is illustrated in **Fig. S2.8** with a Thermo-Fisher GC equipped with a Carboxen® 1010 Porous Layer Open Tubular (PLOT) fused silica column (30m x 0.53mm x 10μm), with helium as a reference and carrier gas. Faradaic efficiencies for gas-phase products were calculated according to **Eq. 2.3**.

$$FE(\%) = \frac{nFXV_i}{V_m Q_{tot}} \quad (\text{Eq. 2.3})$$

where n = # of electrons transferred per product molecule

F = Faraday's constant

X = Mole fraction of product gas in cell headspace

V_i = Volume of headspace injected

V_m = Molar volume of gas at ambient conditions

Q_{tot} = Total charge passed

Aliquots of cell headspace were collected in a gas-tight syringe following each CPE experiment and were manually injected into the GC immediately upon completion of the experiment in order to quantify gas with minimal opportunity for product loss over time.

Multiple trials were performed at each applied potential and for each target molecule investigated in order to reveal the reproducibility of product formation over the catalysts studied and all plotted numerical data related to electrochemical activity and efficiency are plotted with corresponding error bars that reflect a single standard deviation. Faradaic efficiencies as plotted in **Fig. S2.9** were calculated after at least three trials at each potential according to **Eq. 2.2** and **Eq. 2.3**, depending on the physical state of the product.

Computational Details:

Periodic density functional theory (DFT) calculations were performed using the Vienna ab-initio simulation package (VASP) with the PBE functional (planewave cutoff = 520 eV, k-points = (5,5,5), force threshold = 0.03 eV/Å, Gaussian smearing width = 0.05 eV). Initial unit cell optimization (planewave cutoff = 700 eV) yields $a = 6.48 \text{ \AA}$ and $\alpha = 91.18^\circ$, in agreement with experimental measurements. Density of states was obtained using the hybrid HSE06 functional.

Binding energy calculations illustrated in **Fig. S2.10** and **Fig. S2.11** were performed using a 1x1x2 slab model of the un-promoted (formula $(\text{Mo}_6\text{S}_8)_2$) and Cu-Chevrel phase (formula $(\text{Cu}_2\text{Mo}_6\text{S}_8)_2$) for the stable [100] facets. A 3x3x1 K-point sampling was used according to the Monkhorst-Pack scheme. Multiple potential CO binding configurations were explored for Mo, Cu, and S sites in the structure.

Results and Discussion

Synthesis:

The rapid, microwave-assisted solid-state synthetic method implemented in this work has proven capable of yielding highly phase-pure polycrystalline CP materials, including $\text{Ni}_2\text{Mo}_6\text{S}_8$, $\text{Cr}_{1.73}\text{Mo}_6\text{S}_8$, and $\text{Cu}_2\text{Mo}_6\text{S}_8$. In order to observe changes to local and electronic structure with and without a ternary metal promoter atom, the un-promoted Mo_6S_8 CP was also synthesized according to a chemical etching process described in the experimental section. Catalyst morphology can be seen for $\text{Cu}_2\text{Mo}_6\text{S}_8$ in **Fig. 2.3**, while

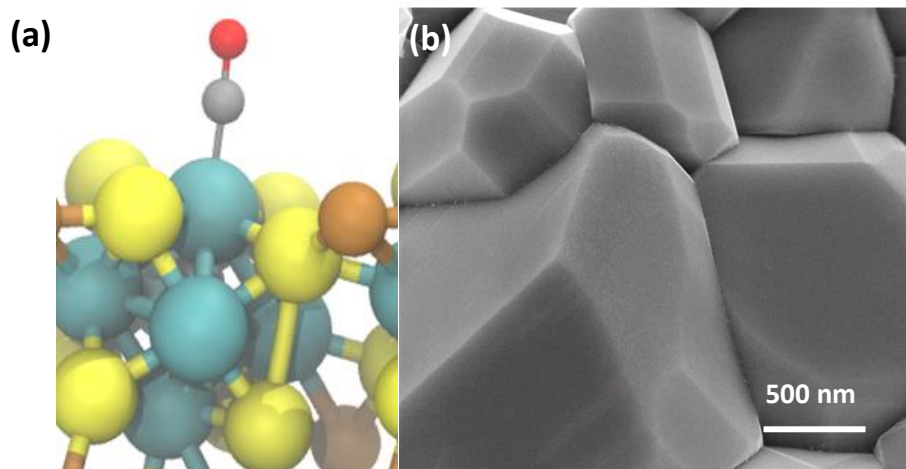


Figure 2.3. Computationally confirmed interaction between CO and a ternary CP active site ensemble (a). This illustrates that preferential binding of CO on a $\text{Cu}_2\text{Mo}_6\text{S}_8$ CP surface occurs at Mo (blue) active sites, while the proximity of Cu (brown) to S sites (yellow) encourages promoter-to-chalcogen charge transfer. Scanning electron micrograph detailing the faceted morphology of polycrystalline $\text{Cu}_2\text{Mo}_6\text{S}_8$ (b).

composition can be observed in the EDX scans shown in **Fig. 2.4**. Pawley refinement of synchrotron PXRD information has yielded lattice parameters of $a=b=9.6328 \text{ \AA}$, $c=10.2229 \text{ \AA}$ with a unit cell volume of 821.502 \AA^3 for the $\text{Cu}_2\text{Mo}_6\text{S}_8$ CP of interest in this study. These values are all in close agreement with literature values for the R-3H unit cell.^{16, 35} Results of XRD analysis are shown in **Table S2.1**.

Local and Electronic Structure:

$\text{Cu}_2\text{Mo}_6\text{S}_8$ and Mo_6S_8 CPs were analyzed at the Mo K-edge (20KeV), Cu K-edge (8.9KeV), and S K-edge (2.4KeV) XANES in order to elucidate spectral transitions that yield valuable information regarding frontier orbital population, oxidation state, coordination geometry, as well as charge transfer between species that constitute catalyst active site ensembles. **Fig. 2.5** shows normalized $\mu(E)$ in the K-edge XANES regions for Mo, Cu, and S. **Fig. 2.5a** shows the Cu K-edge spectra for $\text{Cu}_2\text{Mo}_6\text{S}_8$, with a Cu^0 foil for reference. By measuring the position of the most intense peak in the 1st derivative (inflection point) of the spectra compared to the reference foil, we see that the Cu K-edge in $\text{Cu}_2\text{Mo}_6\text{S}_8$ is shifted 2.5 eV higher than the reference. This indicates an oxidized Cu species in $\text{Cu}_2\text{Mo}_6\text{S}_8$ as has been previously determined in literature^{16, 30} as well as confirmed in this study by XPS analysis as shown in **Fig. 2.6**. Mo K-edge data is displayed in **Fig. 2.5b** for Mo_6S_8 and $\text{Cu}_2\text{Mo}_6\text{S}_8$ along with a Mo^0 foil for reference. The spectra show near

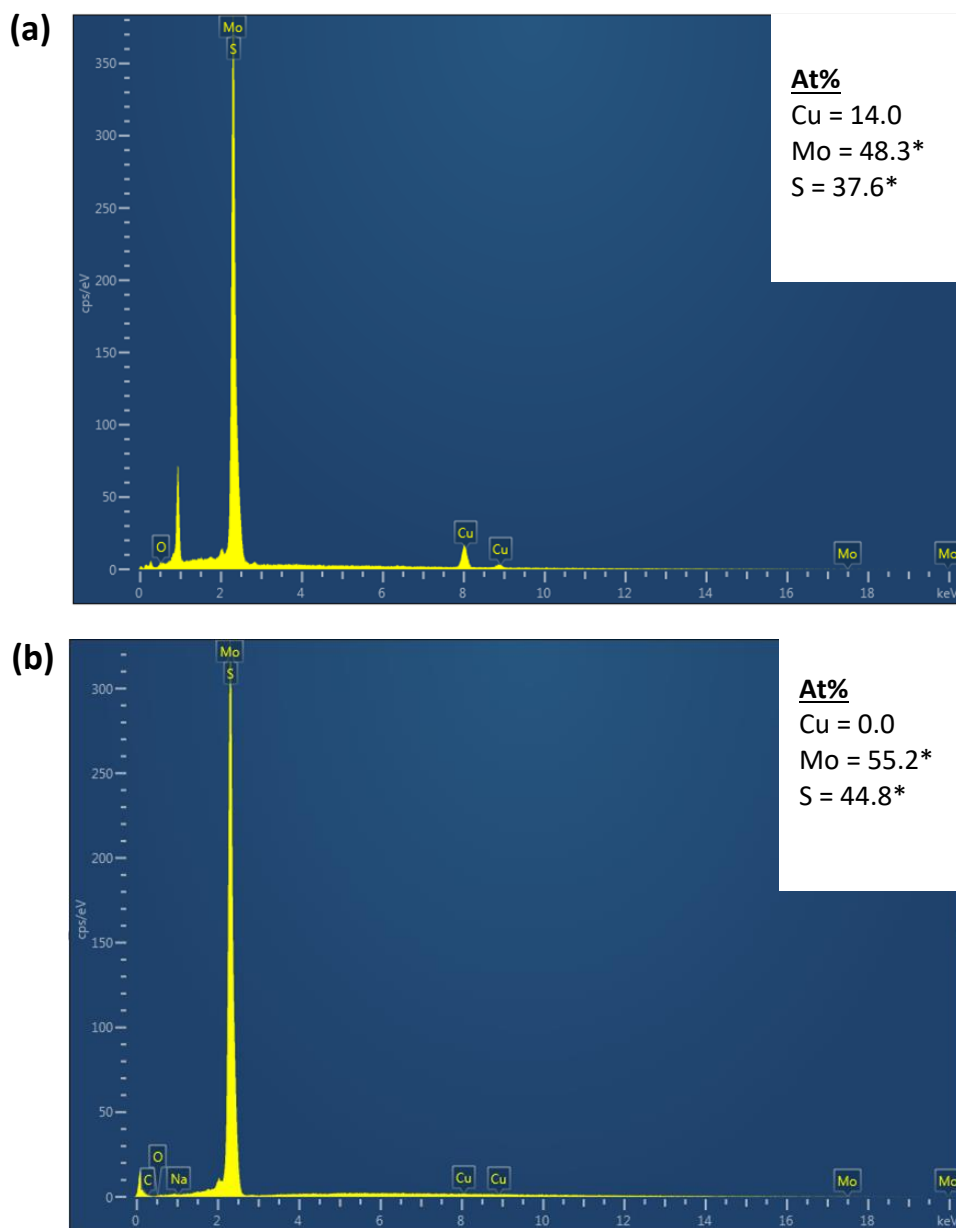


Figure 2.4. EDX spectra for $\text{Cu}_2\text{Mo}_6\text{S}_8$ (a), and Mo_6S_8 (b) indicating that copper has been removed from the bulk $\text{Cu}_2\text{Mo}_6\text{S}_8$ structure upon chemical etching. Signal at ~1 keV represents the Cu L edge, and is unlabeled because it was not required for quantification. Label for oxygen was included to illustrate lack of bulk oxidation in the samples.

*Mo L and S K edge overlap convolute quantitative determination of Mo and S, hence reported At% are only accurate for Cu.

overlap at the edge jump between $\text{Cu}_2\text{Mo}_6\text{S}_8$ and Mo_6S_8 (~ $\Delta 1$ eV), indicating a negligible change in Mo oxidation state when Cu is introduced to the structure. **Fig. 2.5c** shows the S K-edge data for $\text{Cu}_2\text{Mo}_6\text{S}_8$ and

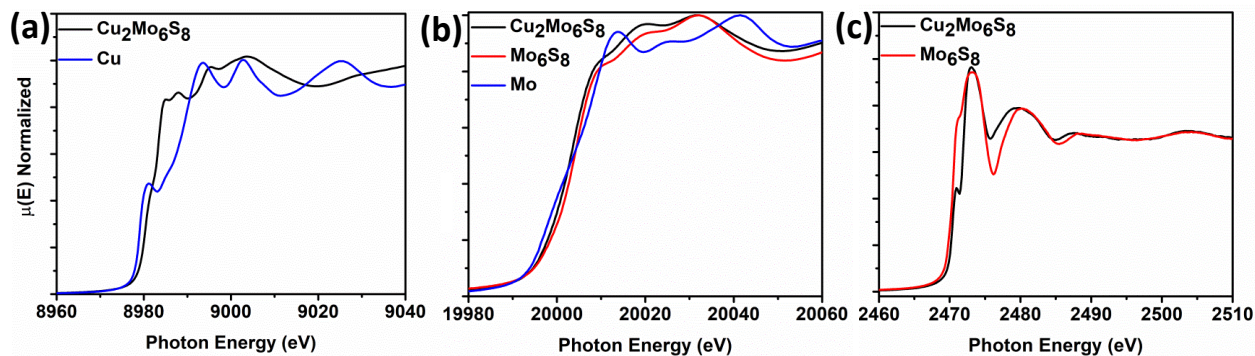


Figure 2.5. K-edge XANES for Cu in $\text{Cu}_2\text{Mo}_6\text{S}_8$ with a Cu^0 foil for reference (a), K-edge XANES for Mo in $\text{Cu}_2\text{Mo}_6\text{S}_8$ and Mo_6S_8 , with a Mo^0 foil for reference (b), and K-edge XANES for S in $\text{Cu}_2\text{Mo}_6\text{S}_8$ and Mo_6S_8 (c). A reference scan using $\text{Na}_2\text{S}_2\text{O}_3$ is shown in Fig. S2.12 of the SI.

Mo_6S_8 ; a scan for the $\text{Na}_2\text{S}_2\text{O}_3$ reference can be seen in Fig. S2.3. There are clear changes to the S electronic structure due to incorporation of the Cu promoter, as will be discussed further later.

After multiple scans of the EXAFS region for all elemental components of $\text{Cu}_2\text{Mo}_6\text{S}_8$ and unpromoted Mo_6S_8 it has been determined that all observed bond lengths are similar to expected values based upon the unit cells as described by the CIF file for each structure which includes its structural parameters. Furthermore, these established values are within the uncertainties of the EXAFS fits. EXAFS information and theoretical fittings plotted in magnitude and real space for Mo and Cu are shown in Fig. 2.7(a-d) where we observe qualitatively different local Mo coordination when promoting species are present compared to unpromoted Mo_6S_8 . Quantitative bond length information extracted from the EXAFS analysis shown in Fig. 2.7 is discussed in detail below.

Catalyst Evaluation:

$\text{Cu}_2\text{Mo}_6\text{S}_8$ was tested in neutral-pH controlled-potential electrolysis experiments with CO_2 dissolved in solution under applied potentials ranging from -1.0 V vs the reversible hydrogen electrode (RHE) to -0.4 V vs RHE, as maximum CO_2RR efficiency occurred within this potential window. We have confirmed that in this potential window, only two liquid-phase CO_2 reduction products are formed after electrolysis; namely, formate and methanol. Proton nuclear magnetic resonance (NMR) spectra for these CO_2RR products after electrolysis at -1.0 V vs RHE are given in Fig. 2.8(a,d).

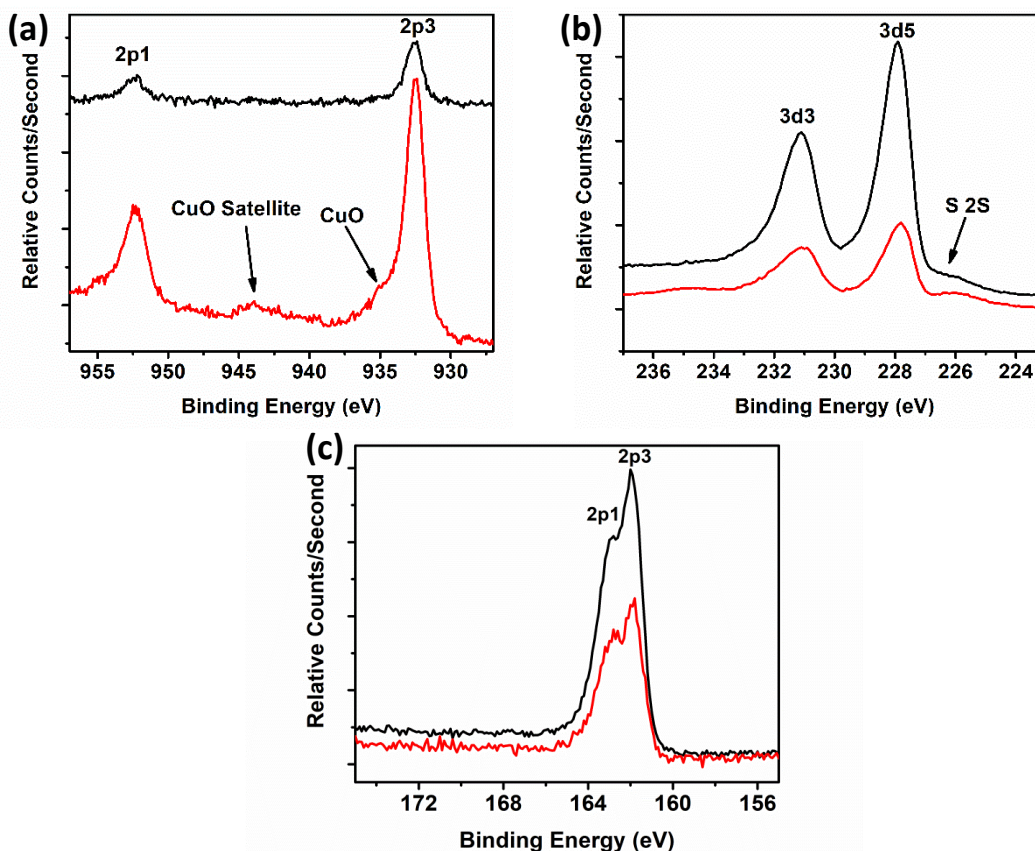


Figure 2.6. High-resolution XPS spectra for Cu (a), Mo (b), and S (c) before electrolysis (black) which are in reasonable agreement with expected oxidation states in $\text{Cu}_2\text{Mo}_6\text{S}_8$ of +1, +2.33, and -2, respectively, and after electrolysis (red) which indicates slight oxidation of Cu and Mo as a result of exposure to moisture and oxygen following electrolysis. It is not expected that either species is oxidized during electrolysis. Values were determined using the Perkin-Elmer handbook of XPS.

When the target molecule was changed from CO_2 to CO in a 0.1 M NaHCO_3 solution, an NMR signal for formate was no longer observed, but the signal for methanol remained. This is evidence that the undesirable formate pathway was entirely suppressed upon removal of CO_2 from the electrochemical cell. This observation is consistent with multiple accounts from literature that report a general lack of formate production when CO is implemented as a reduction feedstock, likely due to the impracticality of switching adsorbate-electrode coordination from C to O, as well as the required insertion of an additional oxygen atom.³⁶ **Fig. 2.8(b,e)** details this result by providing the insets required to visualize formate and methanol production or lack thereof when the electrochemical cell was purged with CO prior to electrolysis. To confirm that observed product formation in this study was the result of CO_2 or CO reduction and not electrolyte interactions, N_2 was purged into a near-neutral pH, 0.1 M NaHCO_3 solution and controlled

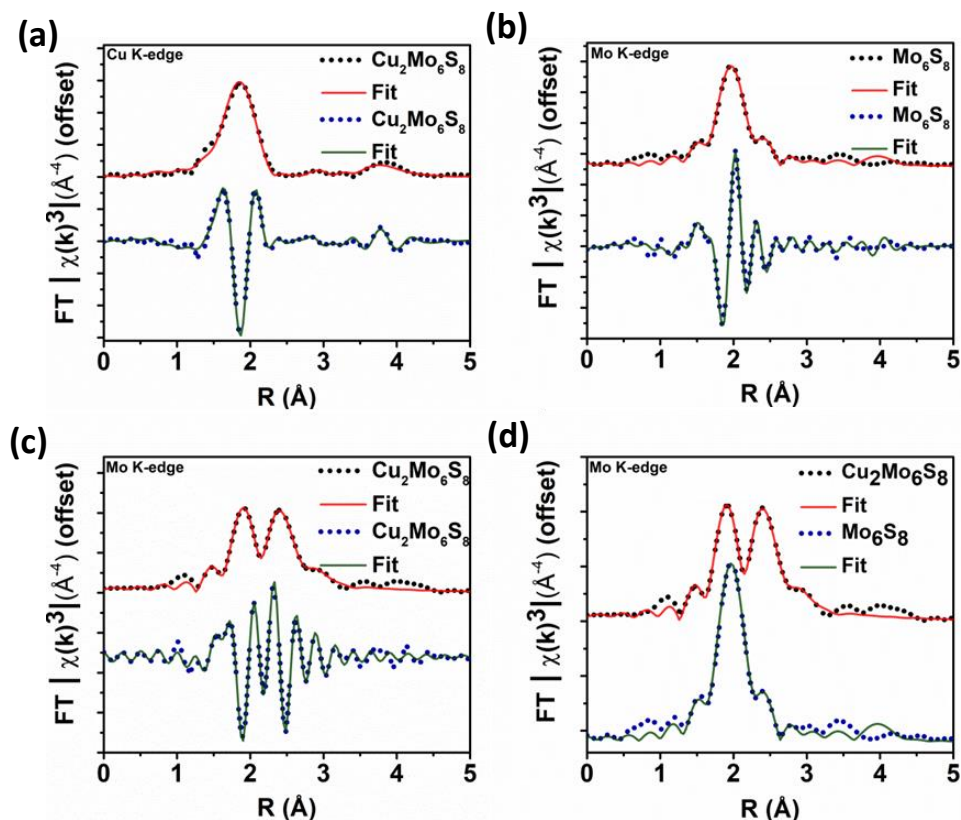


Figure 2.7. Processed EXAFS information plotted in magnitude and in real space for Cu in $\text{Cu}_2\text{Mo}_6\text{S}_8$ (a), Mo in Mo_6S_8 (b), Mo in $\text{Cu}_2\text{Mo}_6\text{S}_8$ (c), and for Mo in $\text{Cu}_2\text{Mo}_6\text{S}_8$ overlaid with Mo in Mo_6S_8 to compare Mo-S and Mo-Mo signals (d). Qualitative differences in local Mo coordination as presented here are discussed quantitatively in the results and discussion sections.

potential electrolysis was again performed at -1.0 V vs RHE. Notably, during these N_2 control experiments, neither formate nor methanol was observed, as shown in **Fig. 2.8(c,f)**.

As seen in **Fig. 2.9**, it was found that reductive current was dominated by hydrogen evolution. This is evidenced by large geometric current densities for hydrogen evolution compared to those for CO_2RR products. It is worth noting however, that no systematic attempts were made to minimize hydrogen evolution on these CP catalysts through modifications to operating conditions (e.g. ionic liquid electrolyte,³⁷ gas-diffusion methodologies³⁸) or electrochemical cell constructs. In addition to inhibition of the parasitic formate pathway when CO_2 is not present in solution, we see in **Fig. S2.9** a general trend that faradaic efficiencies for methanol conversion from CO increase relative to those from CO_2 at the same potentials. That is, despite lower solubility in water than CO_2 , CO is more efficiently converted to methanol on the

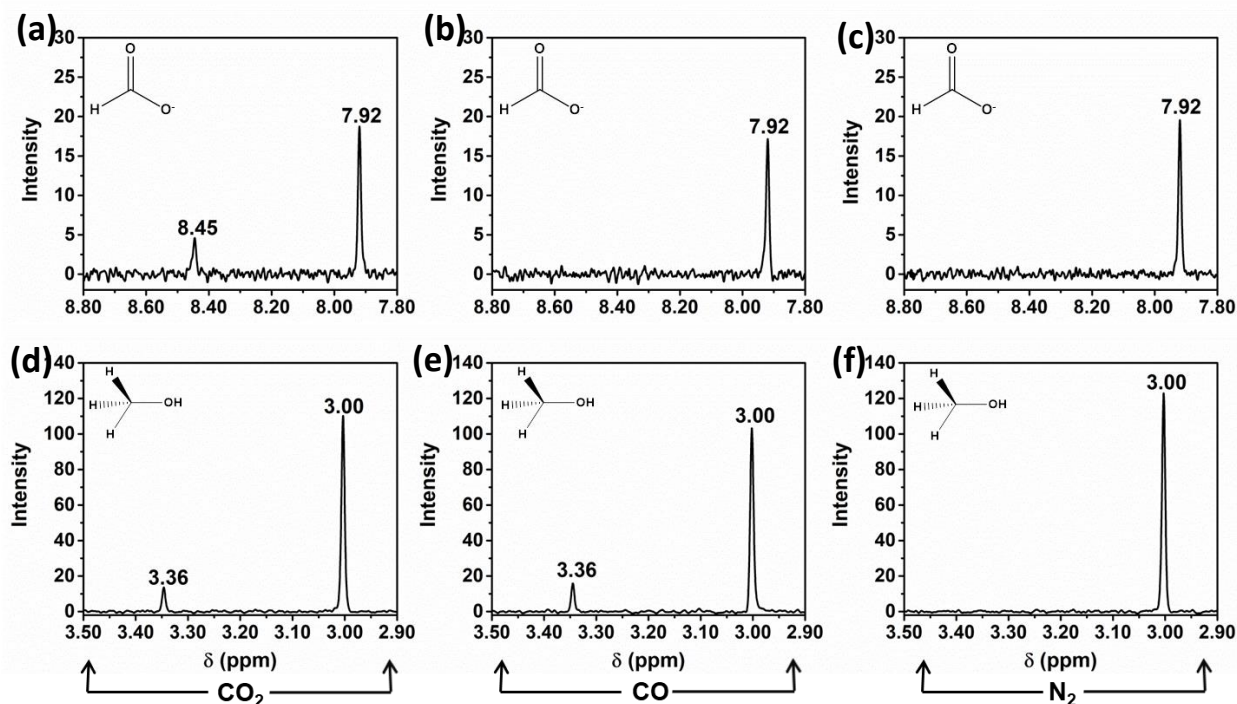


Figure 2.8. NMR signals for formate at 8.45 ppm (a)-(c) and for methanol at 3.36 ppm (d)-(e) detected after electrolysis under CO_2 (a),(d), CO (b), (e), and N_2 (c),(f). Signals at 3.00 ppm and 7.92 ppm both correspond to the internal standard, N,N -dimethylformamide. All displayed NMR spectra are the result of electrolysis at -1.0 V vs RHE in either 0.1M Na_2CO_3 purged with CO_2 or N_2 or 0.1M NaHCO_3 purged with CO .

$\text{Cu}_2\text{Mo}_6\text{S}_8$ surface although geometric current densities are not entirely dissimilar between CO_2 and CO reduction, indicative that hydrogen evolution remains the predominant reaction over these surfaces.

It was observed that $\text{Cu}_2\text{Mo}_6\text{S}_8$ maintained its electrocatalytic performance over the course of multiple hours of electrolysis, even at the most negative potentials applied. This is evident in **Fig. S2.6** by the stability of the reductive current over time. Further, catalyst stability is evidenced by high-resolution XPS spectra presented in **Fig 2.6** and **Fig. S2.14** which indicate no significant changes to the catalyst surface aside from slight oxidation following exposure to moisture and oxygen after the completion of chronoamperometry experiments, illustrated by the evolution of a Mo^{6+} signal in **Fig. S2.14**. **Fig. S2.15** also shows survey scans of the catalyst surface before and after electrolysis which indicate no plating of foreign metals that could yield false positives of product formation. Lastly, to confirm product formation was not the result of chemical degradation, NMR and GC-TCD analyses were completed on a CO_2 -purged Na_2CO_3 electrolyte after $\text{Cu}_2\text{Mo}_6\text{S}_8$ was left in solution at open circuit for 12 hours. Shown in **Fig. 2.10**, no

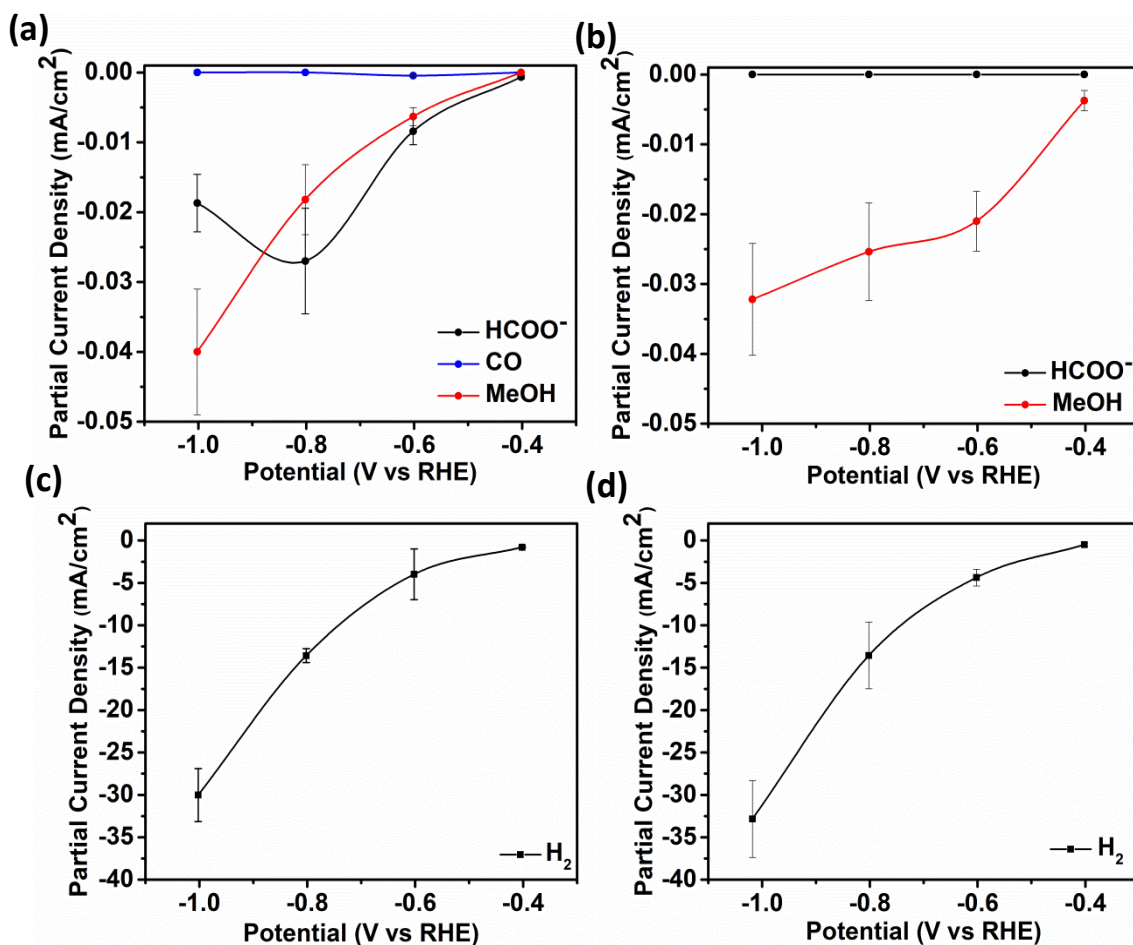


Figure 2.9. Potential-dependent geometric current density after electrolysis for CO₂ reduction products (a), for hydrogen evolution under CO₂ headspace (b), for CO reduction products (c), and for hydrogen evolution under CO headspace (d). Experiments for (a) and (b) were carried out in a pH 6.8 electrolyte where 0.1 M Na₂CO₃ was purged for 1 hr with CO₂, while experiments for (c) and (d) were carried out in pH 6.8 electrolyte where 0.1 M NaHCO₃ was purged for 1 hr with CO. Current densities were calculated using the product of the Faradaic efficiency (Fig. S2.9) and the steady-state geometric current density (Fig S2.13) during electrolysis at each potential, and standard deviations are shown. Note that connecting lines are included to aid in the visualization of partial current density trends, although these plots represent a collection of discrete fixed-potential experiments at -0.4 V, -0.6 V, -0.8 V, and -1.0V. Representative CPE data can be found in Fig. S2.13.

products were detected after this experiment. Furthermore, H₂S production which would indicate surface degradation during electrolysis was monitored via GC-MS. As shown in Fig. S2.16, no H₂S production (m/z = 34) was observed. H₂S was also un-detected qualitatively.

Local Coordination and Electronic Structure:

CPs have a general structure that includes Mo₆ octahedral clusters surrounded by cubes of S₈, where S atoms lie at each face of the Mo₆ octahedra as depicted in Fig. 2.11. These metal-sulfide units extend in a

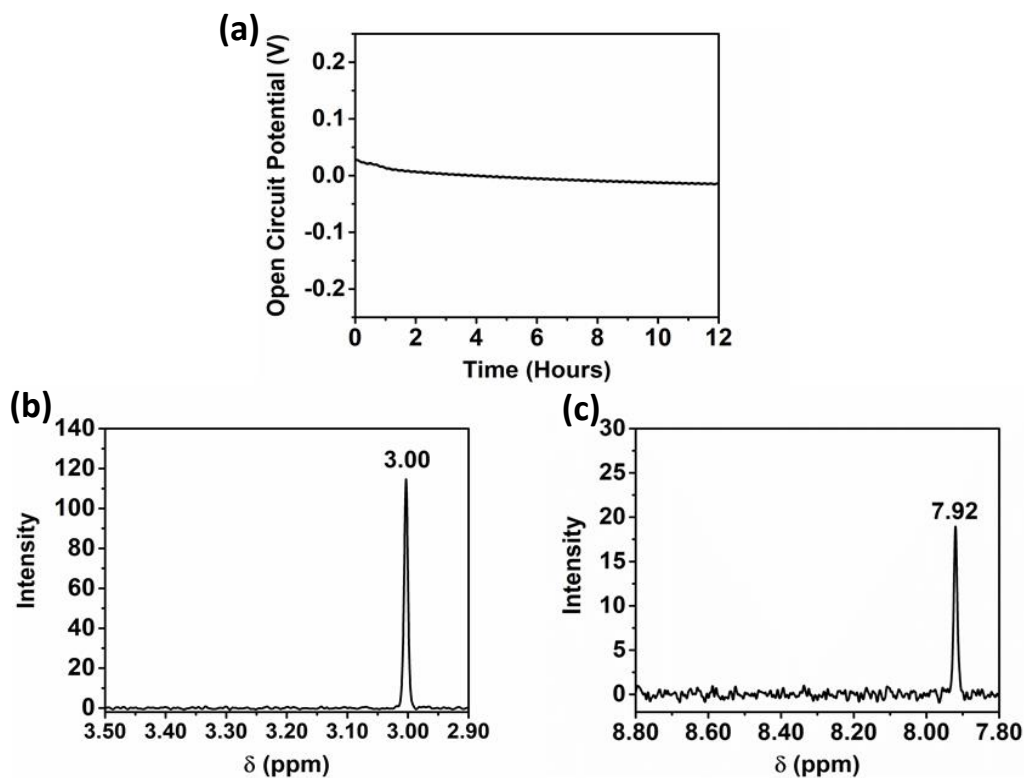


Figure 2.10. Plot of the open circuit potential over time with $\text{Cu}_2\text{Mo}_6\text{S}_8$ as a working electrode in 0.1 M Na_2CO_3 , purged with CO_2 to achieve neutral pH (a); NMR spectrum showing absence of methanol production, with a DMF standard signal at 3.00 ppm (b); NMR spectrum showing absence of formate production, with a DMF standard signal at 7.92 ppm (c).

three-dimensional network to form a hexagonal lattice structure. Mo_6S_8 clusters in CPs are tilted in alignment along the ternary axis, with axial S atoms that connect Mo_6S_8 units together in offset chains through relatively short Mo – S bonds. This gives each Mo atom in the bulk network a square pyramidal pseudo-coordination, while Mo atoms exposed on the surface are relatively under-coordinated and exhibit square planar pseudo-coordination.^{19, 39-41} Furthermore, as a result of this arrangement, large cavities exist between cluster units that are well-suited for occupation by various promoter cations of interest.

The absence of pre-edge features in the Mo K-edge XANES data shown in **Fig. 2.5b**, a signature of $s \rightarrow d$ -orbital transitions, suggested that the d-orbitals are fully occupied and/or there is little to no orbital mixing between p and d orbitals which indicates octahedral symmetry. The minimal shift in absorption onset and lack of alteration in the features of the near-edge spectra for $\text{Cu}_2\text{Mo}_6\text{S}_8$ and Mo_6S_8 indicate insignificant change in the electronic structure of the Mo species.⁴² Mo K-edge EXAFS signals and modeling for Mo_6S_8 and $\text{Cu}_2\text{Mo}_6\text{S}_8$ indicate a dramatic difference in local Mo coordination after Cu

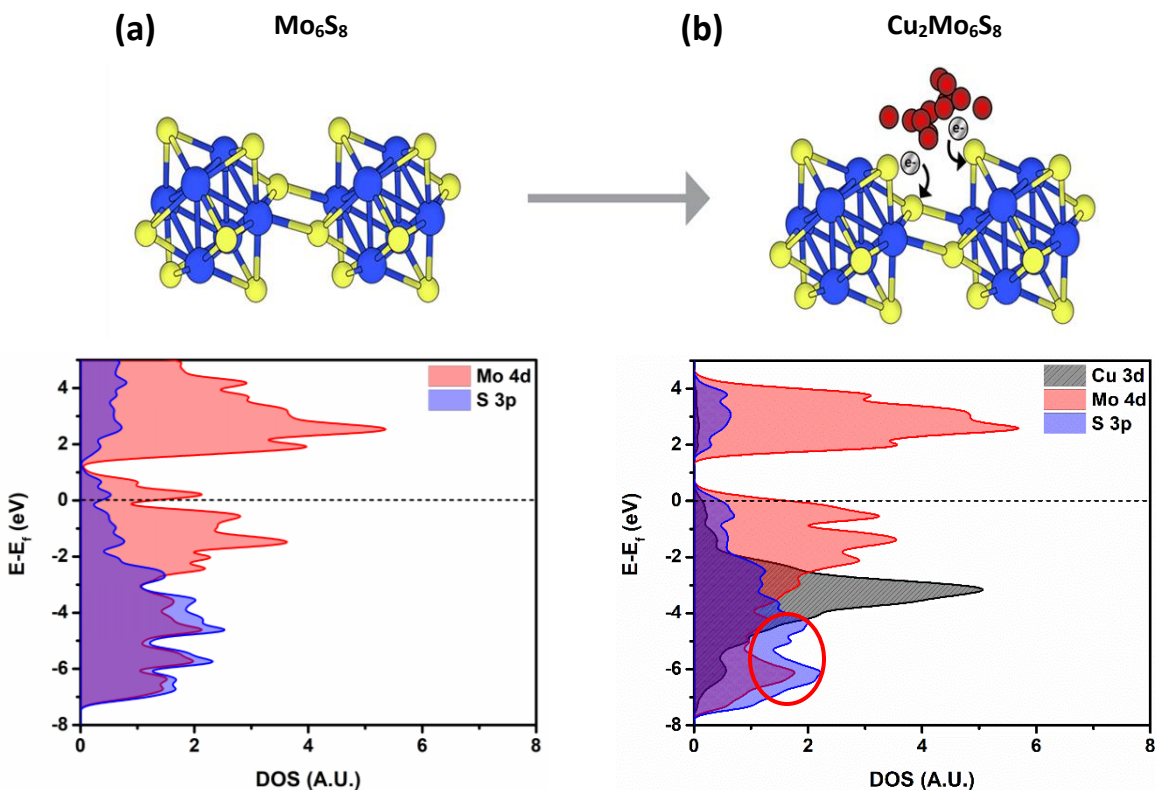


Figure 2.11. Density of states for Mo_6S_8 (a) and $\text{Cu}_2\text{Mo}_6\text{S}_8$ (b) calculated using the HSE06 functional. A noticeable DOS increase at more negative energies indicates charge transfer to the S atoms as evidenced by XAS. The grey region shows the d10 electronic configuration of Cu(I). Respective structures are represented above where Mo are blue spheres, S are yellow spheres, and Cu are red spheres. Further confirmation of charge transfer to S atoms can be seen in Fig. S2.17 which shows the result of Bader charge analysis.

incorporation. The Mo_6S_8 has a lone peak (**Fig. 2.7b**) centered around 2.0 \AA that originates from Mo – S nearest-neighbor scatterers with an additional small shoulder feature near 2.5 \AA . The diminished peak results from a shift in the Mo – S bond distances with axial Mo – S distances increasing to 2.57 \AA . Upon Cu incorporation, Mo – Mo bond distances contract towards uniform distances (2.67 \AA and 2.73 \AA) and constructively interfere to form a new peak. Fitting parameters are included in **Table S2.2-S2.4**, while aforementioned bond lengths for dominant/degenerate scatterers are shown in **Table S2.5**. The fitted bond lengths support small shifts in scattering distances that correlate between the Mo K-edge and Cu K-edge EXAFS modelling in $\text{Cu}_2\text{Mo}_6\text{S}_8$. These results match closely with those corresponding to a series of magnesiated $\text{Mg}_x\text{Mo}_6\text{S}_8$ compounds that was recently published.⁴³ This previous work by Prendergast *et al* showed that charge compensation during the introduction of an electron donating species actually proceeds

through chalcogen atoms—this phenomenon is intriguing because charge compensation during intercalation usually results in monotonic oxidation of transition metal species, although in this case the delocalized electronic nature of the Mo_6 cluster creates low-lying d-orbitals in CPs hence such behavior was not observed for the CP sulfides studied here.⁴⁴⁻⁴⁶

The Mo_6S_8 cluster is deficient by four electrons and is metastable, requiring donation of at least two additional electrons in order for an extended structure to be directly synthesized.⁴⁷ The oxidation state of Cu in $\text{Cu}_2\text{Mo}_6\text{S}_8$ was verified as Cu (I) in earlier studies of the phase, and XPS results (**Fig. 2.6**) closely match those of Cu_2S .^{32, 48} Hence, incorporation of Cu_2 into Mo_6S_8 induces the donation of two electrons, serving the dual purpose of rendering the framework thermodynamically stable while simultaneously filling available S 3p orbitals and thereby raising the potential reactivity of the S p-band²³ toward stabilizing bridging hydride intermediates that can facilitate hydrogenation steps in the CO_2R and COR pathways.^{26, 27} This filling of the S p-orbitals can clearly be seen in the S K-edge comparison at 2471 eV between $\text{Cu}_2\text{Mo}_6\text{S}_8$ and Mo_6S_8 in **Fig. 2.5c**, and is further exemplified graphically in the partial density of states (PDOS) calculations shown in **Fig. 2.11b** where a clear increase in S 3p PDOS at more negative energies indicates that charge is in fact transferred to S atoms in the structure upon ternary metal incorporation.

X-Ray absorption by S will cause core electrons to excite from 1s \rightarrow 3p orbitals that mix to some degree with Mo 4d orbitals, giving rise to a small pre-edge shoulder that can be clearly seen in the S K-edge XANES spectra at approximately 2471 eV in **Fig. 2.5c**. As Cu donates electrons to the metal-sulfide cluster, these S orbitals are filled and the pre-edge feature diminishes in magnitude.⁴¹ The feature also appears to sharpen, as fewer transitions are left available for core S electrons. Interestingly, the aforementioned $\text{Mg}_x\text{Mo}_6\text{S}_8$ study shows experimental data that indicates a completely masked pre-edge shoulder for $\text{Mg}_2\text{Mo}_6\text{S}_8$ S K-edge XANES.⁴³ This is because two Mg atoms would donate a total of four electrons, completing the ideal electron configuration of Mo_6S_8 and eliminating available pre-edge transitions.^{40, 43} In contrast, $\text{Cu}_2\text{Mo}_6\text{S}_8$ only yields two donated electrons (from two Cu^+), hence the shoulder feature is still present and available S 3p orbitals are not completely filled.

To interpret the observed reactivity of CP sulfides in this work, we correlate potentially increased reactivity of the chalcogen species to this filling of 3p orbitals, as shown in the PDOS included in **Fig. 2.11b**. It is hypothesized that CO hydrogenation will be the rate-limiting step in the CO₂RR to liquid fuels, hence surmounting the energy barrier associated with this step will rely strongly on the ability of the catalyst to facilitate hydrogenation. Thus, increasing the population of the S p states should increase the reactivity of the chalcogen atoms that are thought to play a key role in hydrogenation, as it is thought that H* is stabilized at Mo-S bridging sites in close enough proximity to CH_xO* to facilitate hydrogenation kinetics in the CO₂R and COR pathways.^{26, 27}

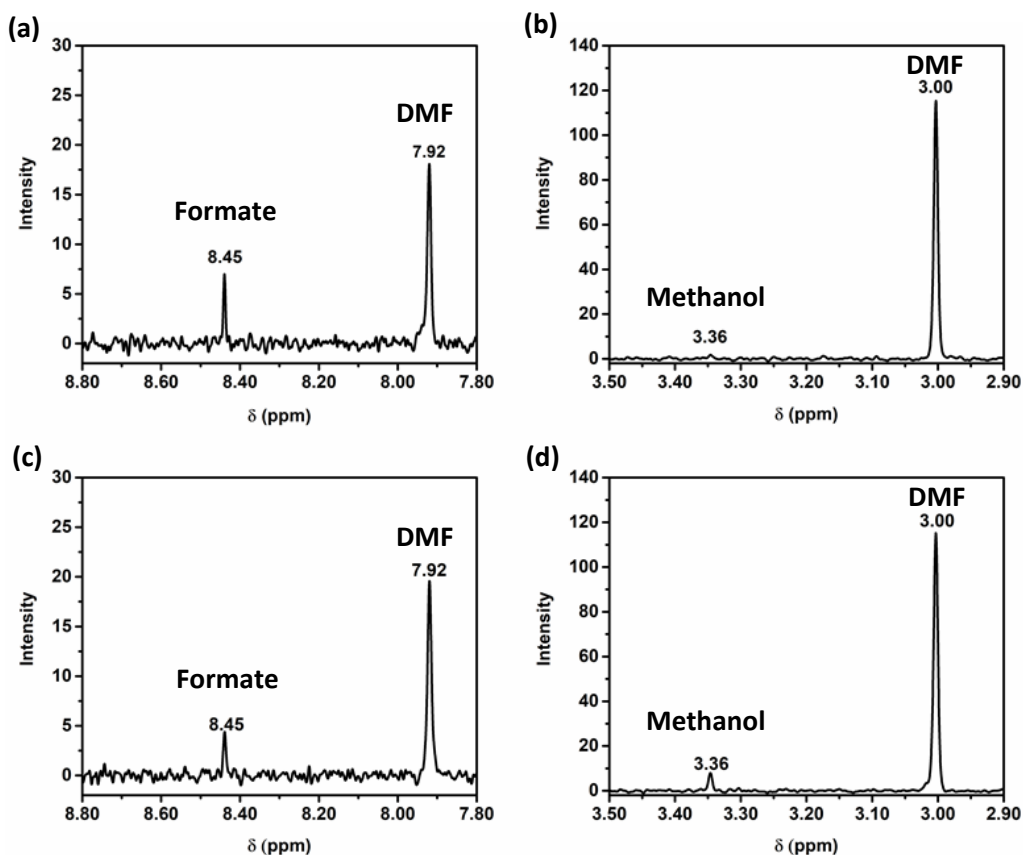


Figure 2.12. NMR spectra showing production of formate (8.45 ppm) (a) and methanol (3.36 ppm) (b) on Cr_{1.73}Mo₆S₈ as well as formate (8.45 ppm) (c) and methanol (3.36 ppm) (d) on Ni₂Mo₆S₈. Both formate and methanol were produced in significant quantities over Ni₂Mo₆S₈, while methanol was only produced in trace levels over Cr_{1.73}Mo₆S₈ while formate was the dominant CO₂RR liquid product. Raw data from CPE experiments for these phases is included in Fig. S2.18

Effect of Active Site Ensemble on Reactivity:

We observed that the $\text{Cu}_2\text{Mo}_6\text{S}_8$ can reduce CO_2 to methanol in aqueous electrolyte at low overpotentials and with only formate production as a competing CO_2RR pathway. Such activity is unique to this particular sulfide catalyst, as no known metal chalcogenides produce methanol in aqueous electrolyte. Interestingly, while copper is one of few transition metals known to reduce CO_2 to methanol (although methane is the preferred C_1 fuel product over copper surfaces),⁴⁹⁻⁵¹ it is not believed that its presence in $\text{Cu}_2\text{Mo}_6\text{S}_8$ is the source of observed catalytic activity. Rather, it is thought that copper merely acts as an electron donor to the catalytically active Mo_6S_8 cluster, rendering the cluster electronically stable and allowing for a direct, high-temperature synthesis of a ternary active-site ensemble similar to the one illustrated in the bottom panel of **Fig. 2.1**.⁴⁷ In fact, we were able to compute CO binding affinity at Cu sites in the extended structure as being -0.91eV , which is more likely to result in dissociation than prolonged residence on Cu sites for further electroreduction. In contrast, binding energies for CO at Mo sites in $\text{Cu}_2\text{Mo}_6\text{S}_8$ and Mo_6S_8 are much stronger at -1.61eV and -1.50eV , respectively. Additional support for this assertion that copper species do not contribute to observed product formation can be found in **Fig. 2.12**, where NMR spectra indicate the production of formate and methanol during controlled potential electrolysis of $\text{Ni}_2\text{Mo}_6\text{S}_8$ and $\text{Cr}_{1.73}\text{Mo}_6\text{S}_8$ (see **Fig. S2.19** for corresponding PXRD patterns for these CPs) at -0.8 V vs RHE . Lastly, chronoamperometry was performed for un-promoted Mo_6S_8 to obtain a baseline for CO_2 reduction activity, as shown in **Fig. 2.13**, where methanol is produced at -0.8V vs RHE only when catalyst is present on the carbon paper. It has yet to be determined quantitatively whether the identity and stoichiometry of the metal promoter in a CP lattice has a significant effect on activity or selectivity, although such a phenomenon has been predicted by Liu *et al.*²⁶

Although faradaic yields to CO_2RR products are low as a result of competing hydrogen evolution and mass transport limitations, methanol production efficiency as much as doubled at some potentials when CO was introduced as the target for reduction (**Fig. S2.9**). This is a strong indicator that the pathway for methanol production on CP catalysts does proceed via CO hydrogenation as expected, and further indicates either that the interaction between CO_2 and the Mo_6S_8 units is weaker than between CO and Mo_6S_8 , or that

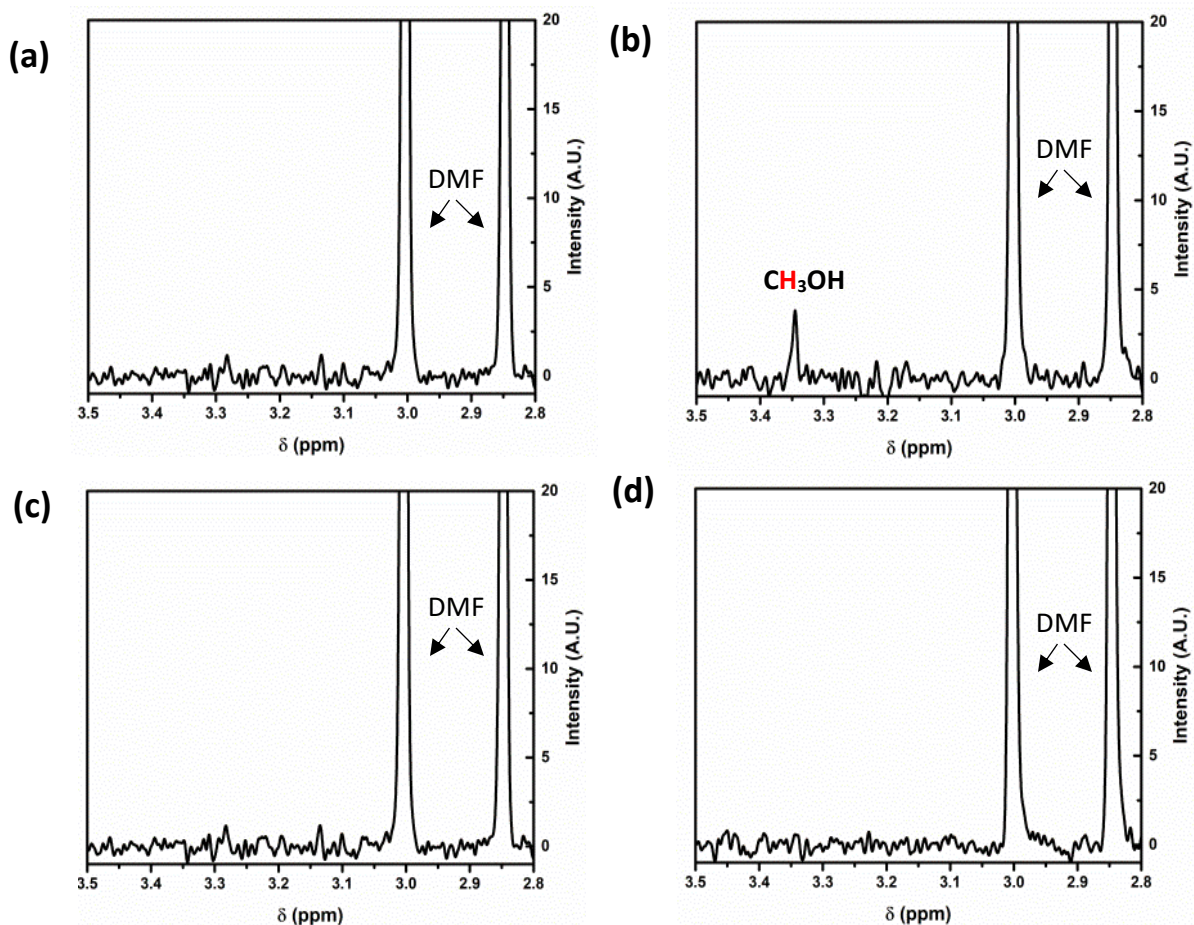


Figure 2.13. ^1H NMR spectra showing signals for methanol at 3.36ppm before electrolysis over a $\text{Mo}_6\text{S}_8@\text{C}$ working electrode (a) after electrolysis at 50 coulombs over the same $\text{Mo}_6\text{S}_8@\text{C}$ electrode (b), before electrolysis of PTFE@C working electrode (c), and after electrolysis at 50 coulombs over the same PTFE@C working electrode (d). Experiments were performed in CO_2 -saturated 0.1M Na_2CO_3 electrolyte at -0.8V vs RHE. We observe the evolution of a signal for methanol only when Mo_6S_8 is present on the electrode, indicating that the intrinsic activity of Mo_6S_8 yields methanol from CO_2 in aqueous environments. The same experiments also yield formate when Mo_6S_8 is present, where observed faradaic efficiencies for methanol and formate are 0.09% and 0.05%, respectively.

non-polar and sparingly soluble CO_2 does not readily diffuse to the polarized electrode/electrolyte interface during electrolysis—either (or both) situation may be the case.

The $\text{Cu}_2\text{Mo}_6\text{S}_8$ catalyst investigated here displays among the lowest reported overpotentials for electrochemical methanol production in aqueous media.⁵² Based upon the results of this work, it is hypothesized that CP sulfides promote a reaction pathway that involves CO hydrogenation to methanol, and in order to reach the CO^* intermediate of the CO_2RR , it has been calculated that an associative mechanism occurs which involves the formation of an HOCO^* intermediate as shown in **Fig. 2.14**, followed by an $\text{H}_2\text{O}^*\text{CO}^*$ intermediate. Formation of water through the reverse water-gas shift reaction may improve

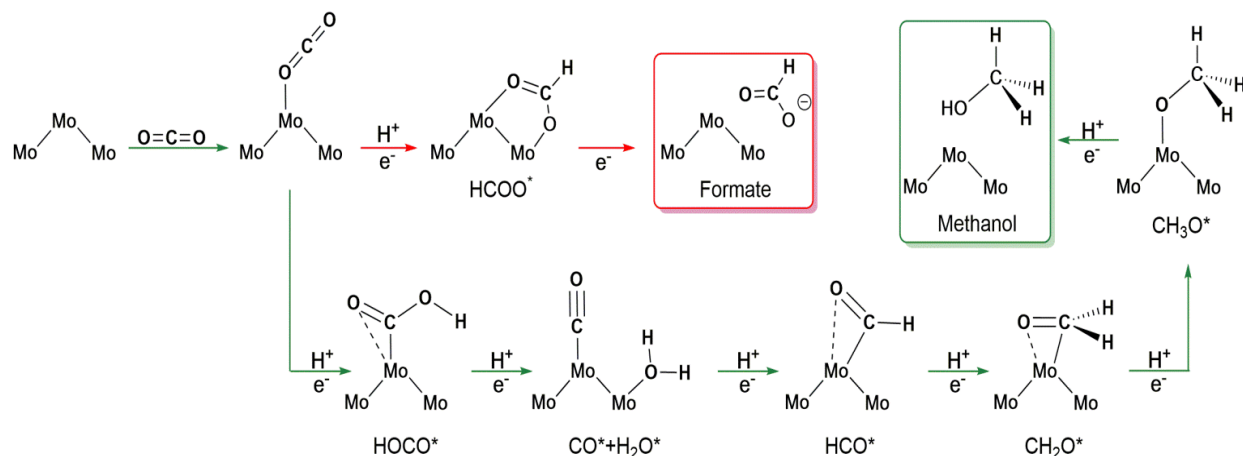


Figure 2.14. Proposed reaction pathway over a simplified CP surface for the carbophilic reduction of CO₂ to methanol (highlighted in green), with as well as the competitive oxophilic reaction pathway leading to formate (highlighted in red).

the energetics associated with a C=O cleavage that is inevitably required for methanol production from CO₂. This hypothesis seems reasonable, as the Mo d-band center is relatively low-lying with respect to the Fermi level, and is therefore not prone to directly break a C=O bond;^{23, 27} the PDOS results presented here for Mo₆S₈ and Cu₂Mo₆S₈ also support this Mo d-band positioning which can also be seen in **Fig. 2.11**. This hypothesis is supported by the production of methanol rather than methane by Cu₂Mo₆S₈ in CO₂ and CO saturated solutions.

Kinetic Limitations:

It is widely acknowledged that competitive hydrogen evolution often contributes to low overall current efficiencies for the CO₂RR in aqueous electrolytes. Hydrogen evolution in the electrolysis experiments presented here was vigorous enough that nucleation and de-nucleation of H₂ gas may have induced mass-transport difficulties during electrolysis, as the CO₂ target molecule—with intrinsically low solubility in water of ~35 mM for a saturated solution at 1 atm—may have been unable to diffuse to the electrode-electrolyte interface against such intense gas evolution. To confirm such an assertion, further experimentation utilizing a rotating disk electrode or vapor-fed cell architecture may be required. It is also postulated that a Butler-Volmer trend for product formation was not observed in this study as a result of large currents for competitive hydrogen evolution at more negative applied potentials. This may explain the decrease in Faradaic efficiency for both formate and methanol at more negative potentials.

To further confound the electrochemical reduction of CO₂ to methanol, production of methanol on a CP catalyst likely proceeds through the previously discussed CO hydrogenation pathway in multiple steps. The suspected rate-limiting CO hydrogenation step is likely to involve a large activation energy barrier owing to the high transition state energy required to yield the HCO* intermediate.^{26, 27} While extensive intermediate studies have yet to be performed for Cu₂Mo₆S₈, the relatively significant increase in FE towards methanol production when the target CO₂ molecule was replaced by CO suggests that the reaction does proceed via CO hydrogenation, and that the reaction rate is inherently limited by weak adsorption interactions between catalyst active sites and CO₂. Moreover, we believe that the simultaneous production of formate over CP surfaces when CO₂ is the target molecule for reduction is the result of insufficient stabilization of the HOCO* intermediate (predicted by theory) relative to the HCOO* intermediate that follows proton-coupled electron-transfer to CO₂*.^{26, 27}

To increase faradaic yields for CO₂RR products compared with the HER, implementation of an electrolyte cation with a greater specific adsorptivity to the electrode surface may serve to tune the electric potential at the outer Helmholtz plane such that proton migration may be suppressed and partially negative atoms within CO₂RR intermediate species may be further stabilized.^{53, 54} Additionally, implementation of a gas-diffusion electrode architecture could mitigate proton reduction by operating the cathode in a CO₂ membrane electrode assembly (MEA) configuration that negates the need for an aqueous electrolyte.

Conclusions

Using local probe *ex-situ* XAS, we have observed tuning of the S electronic structure of Mo₆S₈, potentially towards stronger activity for CO hydrogenation. We have also shown through DFT bonding analysis that metal promotion in CP frameworks leads directly to modular stabilization of reaction intermediates such as CO as evidenced by milder binding of CO to Mo active sites in Cu₂Mo₆S₈ than in Mo₆S₈, ostensibly through synergistic interactions that include coulombic stabilization by ternary active-site ensembles. This idea has been emphasized in theoretical work by Liu *et al.* for CP systems, and we now have experimental evidence that these hypotheses are valid.

We have demonstrated that $\text{Cu}_2\text{Mo}_6\text{S}_8$, although previously unexplored as a CO_2 reduction electrocatalyst, is capable of producing methanol—albeit at low partial current densities and low overall efficiency relative to hydrogen evolution. However, this reactivity was observed in aqueous electrolyte, at low overpotentials, and with a unique degree of selectivity relative to many existing electrocatalysts.^{49, 52, 55} Only two liquid-phase CO_2 reduction products, formate and methanol, were formed during electrolysis on the investigated catalysts. Further, the competing formate pathway was successfully suppressed by the alternative implementation of a CO target molecule, which yielded methanol as the lone liquid-phase product.

It will be of significant fundamental value to incorporate advanced spectroscopic analyses that allow for identification of adsorbed reaction intermediates as a function of applied potential. This avenue of future exploration, in tandem with an *operando* investigation of catalyst surfaces, will allow for reliable determination and rationalization of CO_2 and CO reduction mechanisms. Promising *operando* techniques such as grazing incidence XAS and XPS will yield necessary mechanistic information by elucidating changes to active-site local coordination and electronic configuration upon application of an applied potential and while in the presence of reduction target molecules dissolved in electrolyte.^{56, 57}

Future work is still required to establish the mechanism by which the investigated Chevrel-phase material reduces CO_2 to methanol. This knowledge will necessarily lead to an increased understanding of the role of active site multifunctionality on reaction efficiency, as many state-of-the-art CO_2R catalysts have shown CO_2R selectivity to formate exceeding 80%^{58, 59} and to CO exceeding 95%³⁷, although similar selectivity to methanol over heterogeneous catalysts has yet to be achieved in aqueous conditions without additives and irradiation. To develop a catalyst system whose tunable local and electronic structure can affect reactivity and selectivity could be a significant step forward in developing fundamental knowledge in energy conversion and storage research. The unique reactivity displayed by this metal-promoted Mo_6S_8 catalyst family warrants detailed investigation into the precise role of metal promotion in encouraging desirable reaction trajectories over promising energy-conversion catalysts. Hence, future work will

elucidate the effect of tunable metal promotion on electronic structure of catalytically active sites such that control over reaction kinetics may be achieved.

Supporting Information

Electrode preparation procedure, electrochemical analysis methods, electrochemical cell depiction, product analysis discussion and equations, computational details, synthesis diagram, crystal structures, PXRD patterns and refinement results, EDX spectra, XPS analysis before and after electrochemistry, raw XAS data, control experiment results, GC-MS analysis, GC-TCD analysis, NMR analysis, proposed reaction mechanism, Bader charge analysis results, electrolyte pH experimental results, modeled CO binding geometries, EXAFS and XANES discussion and fitting parameters.

Acknowledgements

We would like to acknowledge the University of California, Davis for start-up funding for this work. JTP thanks Chevron Corporation for funding through the UC Davis Institute of Transportation Chevron fellowship program, as well as the UC Davis Bradford Borge Graduate Student Fellowship and the Fred P Corson/Dow Chemical Graduate Student Fellowship. We also acknowledge funding support from the NSF through UC Davis ChemEnergy REU program, grant #1560479. Part of this work was performed at the Stanford Nano Shared Facilities (SNSF), supported by the National Science Foundation under award ECCS-1542152. This research used resources of the National Energy Research Scientific Computing Center, a DOE Office of Science User Facility supported by the Office of Science of the U.S. Department of Energy under Contract No. DE-AC02-05CH11231 (Project ID: 60905). Use of the Stanford Synchrotron Radiation Lightsource, SLAC National Accelerator Laboratory, is supported by the U.S. Department of Energy, Office of Science, Office of Basic Energy Sciences under Contract No. DE-AC02-76SF00515. The SSRL Structural Molecular Biology Program is supported by the DOE Office of Biological and Environmental Research, and by the National Institutes of Health, National Institute of General Medical Sciences (including P41GM103393). The contents of this publication are solely the responsibility of the authors and do not necessarily represent the official views of NIGMS of NIH.

Publication Information, Copyright, and Author Acknowledgements

This chapter forms the basis for the following publication:

Perryman, J. T.; Ortiz-Rodríguez, J. O.; Jude, J. W.; Hyler, F. P.; Davis, R. C.; Mehta, A.; Kulkarni, A. R.; Patridge, C. J.; Velázquez, J. M., Metal-Promoted Mo₆S₈ Clusters: A platform for probing ensemble effects on the electrochemical conversion of CO₂ and CO to methanol. *Materials Horizons* **2020**, *7*, 193-202.

Joseph T. Perryman conducted material synthesis, electrochemistry experiments, XAS, PXRD, SEM, EDX, XPS, GC, and NMR. JOR conducted material synthesis. JWJ, FPH, RCD, AM, and CJP contributed to XAS acquisition and processing. ARK performed DFT.

This chapter was adapted with permission from Perryman, J. T.; Ortiz-Rodríguez, J. O.; Jude, J. W.; Hyler, F. P.; Davis, R. C.; Mehta, A.; Kulkarni, A. R.; Patridge, C. J.; Velázquez, J. M., Metal-Promoted Mo₆S₈ Clusters: A platform for probing ensemble effects on the electrochemical conversion of CO₂ and CO to methanol. *Materials Horizons* **2020**, *7*, 193-202. © Copyright 2020 Royal Society of Chemistry

References

1. G. A. Olah, *Angewandte Chemie International Edition*, 2005, **44**, 2636-2639.
2. J. John-Paul, P. G. K. Surya and G. A. Olah, *Israel Journal of Chemistry*, 2014, **54**, 1451-1466.
3. S. J. Davis, N. S. Lewis, M. Shaner, S. Aggarwal, D. Arent, I. L. Azevedo, S. M. Benson, T. Bradley, J. Brouwer, Y.-M. Chiang, C. T. M. Clack, A. Cohen, S. Doig, J. Edmonds, P. Fennell, C. B. Field, B. Hannegan, B.-M. Hodge, M. I. Hoffert, E. Ingersoll, P. Jaramillo, K. S. Lackner, K. J. Mach, M. Mastrandrea, J. Ogden, P. F. Peterson, D. L. Sanchez, D. Sperling, J. Stagner, J. E. Trancik, C.-J. Yang and K. Caldeira, *Science*, 2018, **360**.
4. N. S. Lewis, *Science*, 2016, **351**.
5. N. S. Lewis and D. G. Nocera, *Proceedings of the National Academy of Sciences*, 2006, **103**, 15729.
6. D. D. Zhu, J. L. Liu and S. Z. Qiao, *Advanced Materials*, 2016, **28**, 3423-3452.
7. J. D. Wiensch, J. John, J. M. Velázquez, D. A. Torelli, A. P. Pieterick, M. T. McDowell, K. Sun, X. Zhao, B. S. Brunschwig and N. S. Lewis, *ACS Energy Letters*, 2017, **2**, 2234-2238.
8. J. Jun, G. Minrui, S. Wenchao and Y. Yushan, *Angewandte Chemie International Edition*, 2016, **55**, 15240-15245.
9. T. F. Jaramillo, K. P. Jørgensen, J. Bonde, J. H. Nielsen, S. Horch and I. Chorkendorff, *Science*, 2007, **317**, 100.
10. D. Lembke, S. Bertolazzi and A. Kis, *Accounts of Chemical Research*, 2015, **48**, 100-110.
11. Y. Yu, S.-Y. Huang, Y. Li, S. N. Steinmann, W. Yang and L. Cao, *Nano Letters*, 2014, **14**, 553-558.

12. T. Heine, *Accounts of Chemical Research*, 2015, **48**, 65-72.
13. S. A. Francis, J. M. Velázquez, I. M. Ferrer, D. A. Torelli, D. Guevarra, M. T. McDowell, K. Sun, X. Zhou, F. H. Saadi, J. John, M. H. Richter, F. P. Hyler, K. M. Papadantonakis, B. S. Brunshwig and N. S. Lewis, *Chemistry of Materials*, 2018, **30**, 15, 4902-4908.
14. N. Alonso-Vante, *Handbook of Fuel Cells*, 2010.
15. Ø. Fischer, *Applied physics*, 1978, **16**, 1-28.
16. R. Chevrel, M. Hirrien and M. Sergent, *Polyhedron*, 1986, **5**, 87-94.
17. D. Aurbach, Z. Lu, A. Schechter, Y. Gofer, H. Gizbar, R. Turgeman, Y. Cohen, M. Moshkovich and E. Levi, *Nature*, 2000, **407**, 724.
18. S. J. Hilsenbeck, R. E. McCarley, A. I. Goldman and G. L. Schrader, *Chemistry of Materials*, 1998, **10**, 125-134.
19. K. F. McCarty and G. L. Schrader, *Industrial & Engineering Chemistry Product Research and Development*, 1984, **23**, 519-524.
20. N. Alonso-Vante, B. Schubert and H. Tributsch, *Materials Chemistry and Physics*, 1989, **22**, 281-307.
21. P. Liu and J. K. Nørskov, *Physical Chemistry Chemical Physics*, 2001, **3**, 3814-3818.
22. T. Bligaard and J. K. Nørskov, *Electrochimica Acta*, 2007, **52**, 5512-5516.
23. B. Hammer and J. K. Nørskov, *Surface Science*, 1995, **343**, 211-220.
24. A. Nilsson, L. Pettersson, B. Hammer, T. Bligaard, C. H. Christensen and J. K. Nørskov, *Catalysis Letters*, 2005, **100**, 111-114.
25. X. Hong, K. Chan, C. Tsai and J. K. Nørskov, *ACS Catalysis*, 2016, **6**, 4428-4437.
26. C. Liu and P. Liu, *ACS Catalysis*, 2015, **5**, 1004-1012.
27. P. Liu, Y. Choi, Y. Yang and M. G. White, *J Phys Chem A*, 2010, **114**, 3888-3895.
28. K. Chan, C. Tsai, H. A. Hansen and J. K. Nørskov, *ChemCatChem*, 2014, **6**, 1899-1905.
29. F. Murgia, P. Antitomaso, L. Stievano, L. Monconduit and R. Berthelot, *Journal of Solid State Chemistry*, 2016, **242**, 151-154.
30. E. Lancry, E. Levi, Y. Gofer, M. Levi, G. Salitra and D. Aurbach, *Chemistry of Materials*, 2004, **16**, 2832-2838.
31. B. Ravel and M. Newville, *Journal of Synchrotron Radiation*, 2005, **12**, 537-541.
32. E. Levi, Y. Gofer, Y. Vestfried, E. Lancry and D. Aurbach, *Chemistry of Materials*, 2002, **14**, 2767-2773.

33. E. Levi, E. Lancry, A. Mitelman, D. Aurbach, G. Ceder, D. Morgan and O. Isnard, *Chemistry of Materials*, 2006, **18**, 5492-5503.
34. J. J. Rehr, J. J. Kas, F. D. Vila, M. P. Prange and K. Jorissen, *Physical Chemistry Chemical Physics*, 2010, **12**, 5503-5513.
35. A. M. Umarji, G. V. S. Rao, M. P. Janawadkar and T. S. Radhakrishnan, *Journal of Physics and Chemistry of Solids*, 1980, **41**, 421-429.
36. R. Kortlever, J. Shen, K. J. P. Schouten, F. Calle-Vallejo and M. T. M. Koper, *The Journal of Physical Chemistry Letters*, 2015, **6**, 4073-4082.
37. M. Asadi, B. Kumar, A. Behranginia, B. A. Rosen, A. Baskin, N. Reppin, D. Pisasale, P. Phillips, W. Zhu, R. Haasch, R. F. Klie, P. Král, J. Abiade and A. Salehi-Khojin, *Nature Communications*, 2014, **5**, 4470.
38. D. Higgins, C. Hahn, C. Xiang, T. F. Jaramillo and A. Z. Weber, *ACS Energy Letters*, 2019, **4**, 317-324.
39. T. Hughbanks and R. Hoffmann, *Journal of the American Chemical Society*, 1983, **105**, 1150-1162.
40. F. Thole, L. F. Wan and D. Prendergast, *Physical Chemistry Chemical Physics*, 2015, **17**, 22548-22551.
41. J. T. Perryman, F. P. Hyler, J. C. Ortiz-Rodríguez, A. Mehta, A. R. Kulkarni and J. M. Velázquez, *Journal of Coordination Chemistry*, 2019, **72**, 1322-1335.
42. V. Kunzl, *Collection of Czechoslovak Chemical Communications*, 1932, **4**, 213-224.
43. L. F. Wan, J. Wright, B. R. Perdue, T. T. Fister, S. Kim, C. A. Appleby and D. Prendergast, *Physical Chemistry Chemical Physics*, 2016, **18**, 17326-17329.
44. C. J. Patridge, C. T. Love, K. E. Swider-Lyons, M. E. Twigg and D. E. Ramaker, *Journal of Solid State Chemistry*, 2013, **203**, 134-144.
45. C. T. Love, A. Korovina, C. J. Patridge, K. E. Swider-Lyons, M. E. Twigg and D. E. Ramaker, *Journal of The Electrochemical Society*, 2013, **160**, A3153-A3161.
46. C. J. Patridge, C. Jaye, T. A. Abteu, B. Ravel, D. A. Fischer, A. C. Marschilok, P. Zhang, K. J. Takeuchi, E. S. Takeuchi and S. Banerjee, *The Journal of Physical Chemistry C*, 2011, **115**, 14437-14447.
47. R. Chevrel and M. Sergent, *Superconductivity in Ternary Compounds I*, 1982.
48. J. F. Moulder, W. F. Stickle, P. E. Sobol and K. D. Bomben, *Handbook of X-Ray Photoelectron Spectroscopy*, 1993.
49. K. P. Kuhl, E. R. Cave, D. N. Abram and T. F. Jaramillo, *Energy & Environmental Science*, 2012, **5**, 7050-7059.

50. Y. Hori, *Modern Aspects of Electrochemistry*, 2008.
51. Y. Hori, *Handbook of Fuel Cells*, 2010.
52. G. Seshadri, C. Lin and A. B. Bocarsly, *Journal of Electroanalytical Chemistry*, 1994, **372**, 145-150.
53. B. N. Kabanov, I. I. Astakhov and I. G. Kiseleva, *Russian Chemical Reviews*, 1965, **34**, 775.
54. A. Murata and Y. Hori, *Bulletin of the Chemical Society of Japan*, 1991, **64**, 123-127.
55. K. P. Kuhl, T. Hatsukade, E. R. Cave, D. N. Abram, J. Kibsgaard and T. F. Jaramillo, *Journal of the American Chemical Society*, 2014, **136**, 14107-14113.
56. A. D. Handoko, F. Wei, Jenndy, B. S. Yeo and Z. W. Seh, *Nature Catalysis*, 2018, **1**, 922-934.
57. S. Yamamoto, H. Bluhm, K. Andersson, G. Ketteler, H. Ogasawara, M. Salmeron and A. Nilsson, *Journal of Physics: Condensed Matter*, 2008, **20**, 184025.
58. J. He, X. Liu, H. Liu, Z. Zhao, Y. Ding and J. Luo, *Journal of Catalysis*, 2018, **364**, 125-130.
59. Y. Zhang, F. Li, X. Zhang, T. Williams, C. D. Easton, A. M. Bond and J. Zhang, *Journal of Materials Chemistry A*, 2018, **11**, 4714-4720.
60. E. Sanville, S. D. Kenny, R. Smith and G. Henkelman, *Journal of Computational Chemistry*, 2007, **28**, 899-908.

Supporting Information

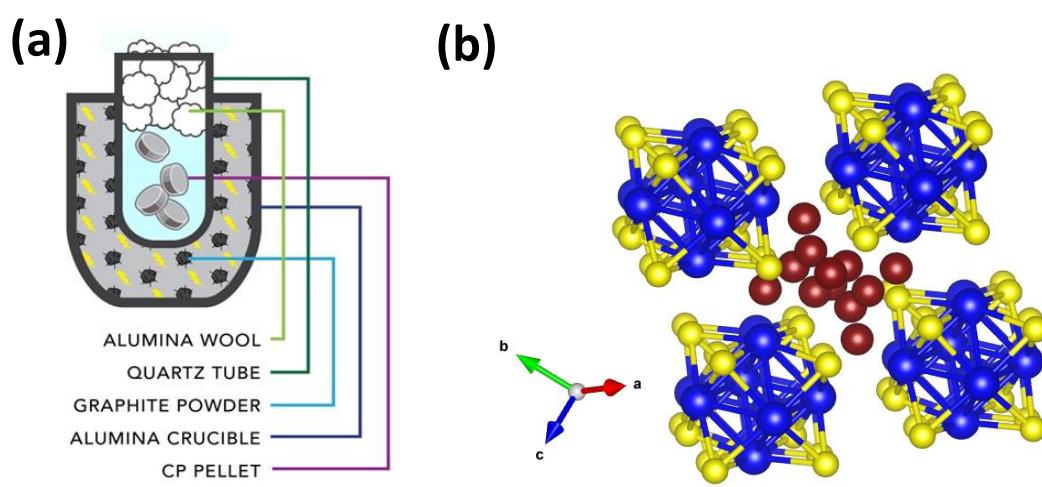


Figure S2.1. Diagram showing experimental set-up for microwave-assisted synthesis method (a) and Crystal structure for $\text{Cu}_2\text{Mo}_6\text{S}_8$ (b) where Cu = red spheres*, Mo = blue spheres, and S = yellow spheres.

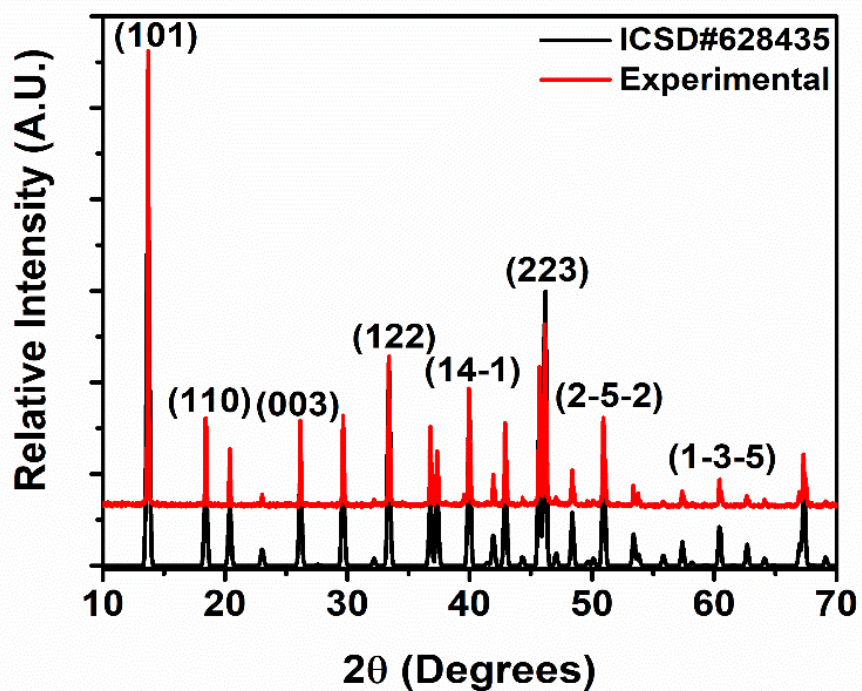


Figure S2.2. Indexed PXRD pattern for as-synthesized $\text{Cu}_2\text{Mo}_6\text{S}_8$ (red) overlaid with pattern expected from literature (black).

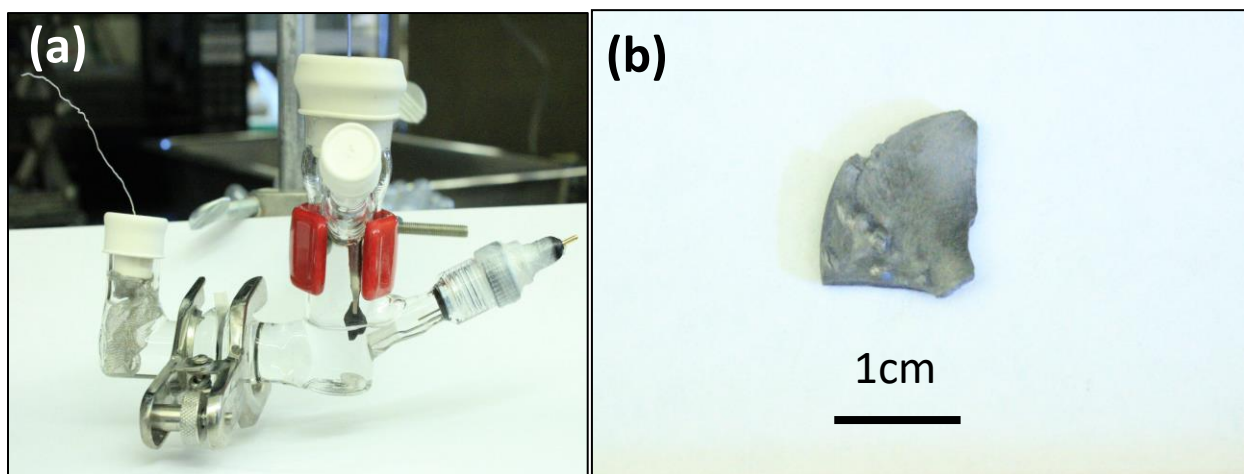


Figure S2.3. Images depicting a custom-blown H-cell configured electrolysis cell with working, reference, and counter electrodes sealed under CO_2 by precision seal rubber septa (a) and a piece of as-synthesized CP prior to electrolysis (b).

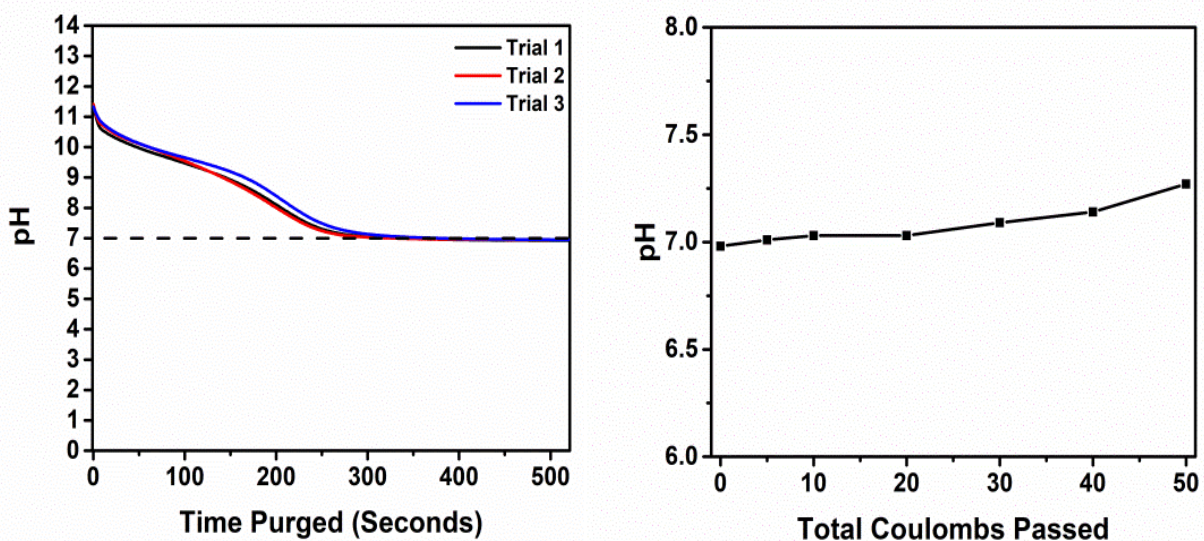


Figure S2.4. Experimental validation that carbonate electrolyte bulk pH is reduced to near-neutral values over the course of CO₂ sparging (left) and that bulk pH does not increase significantly in the static cells implemented in this study over the course of electrolysis where 50 coulombs of charge are passed through a Cu₂Mo₆S₈ working electrode (right).

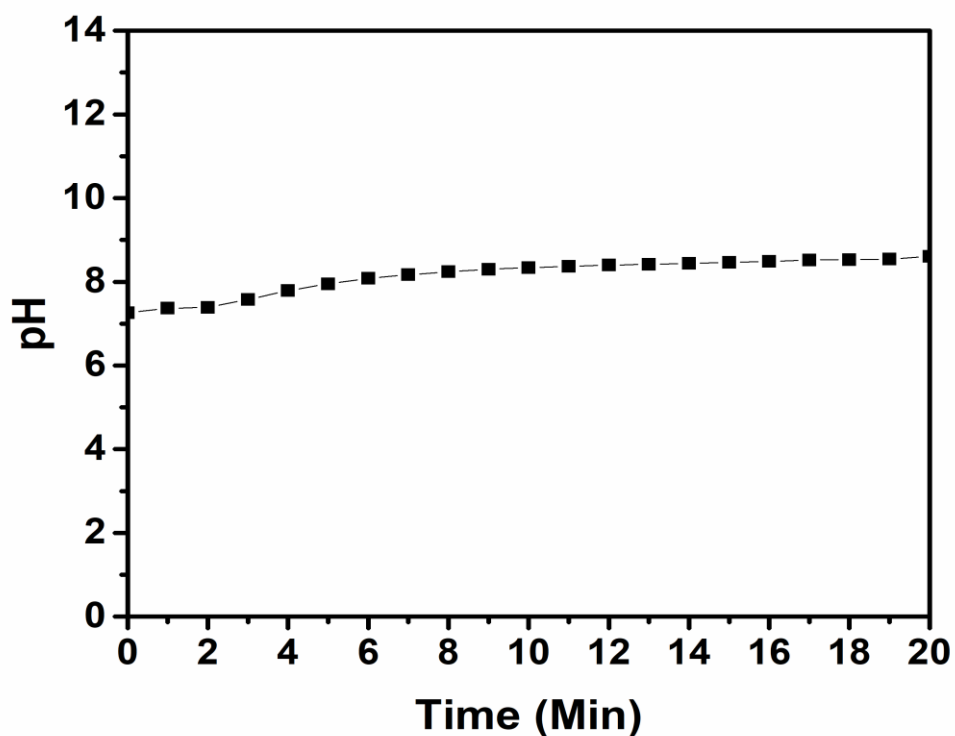


Figure S2.5. Monitoring pH over time for a CO-purged 0.1M NaHCO₃ electrolyte, showing slight increases to bulk electrolyte pH of less than one pH unit. Effects of increasing bulk pH do not necessarily reflect inherently high pH at the electrode-electrolyte interface, and as such the effect of bulk pH increase over time on CO₂ reduction catalysis are not systematically studied here.

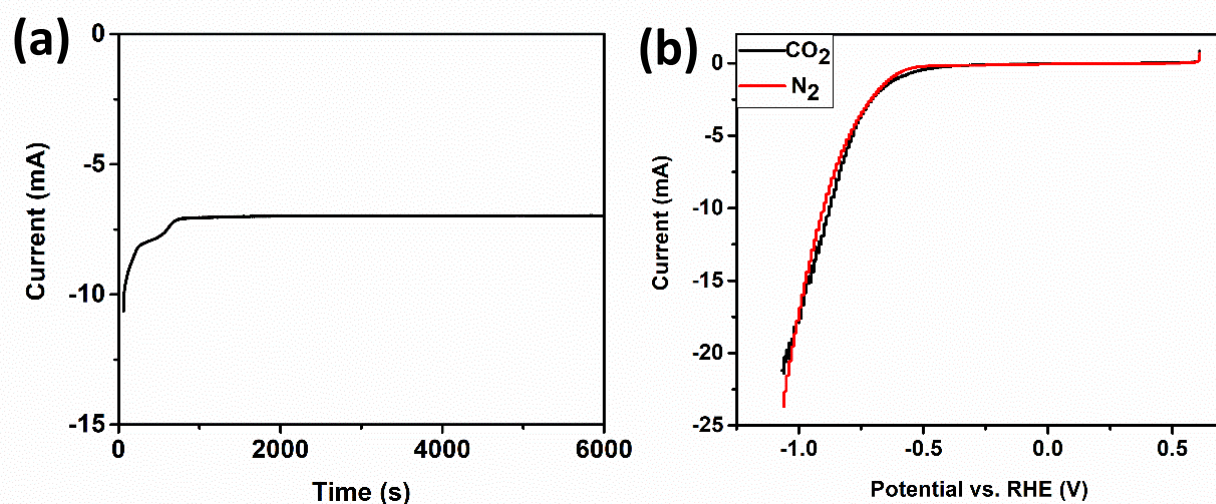


Figure S2.6. Current stability over the course of electrolysis at -1.0 V vs RHE and pH 6.8 in a 0.1 M Na₂CO₃ electrolyte purged with CO₂ (a). Linear sweep voltammograms in pH 6.8 electrolytes at constant scan rates of 50 mV/sec, showing an identical onset potential for reductive current under both CO₂ (black) and N₂ (red) (b). This indicates that HER dominates observed current densities and there is no observable contribution to current density from CO₂ reduction, as confirmed by the values seen in Figure S2.9. Linear sweep voltammograms were observed for pellets of identical exposed surface area.

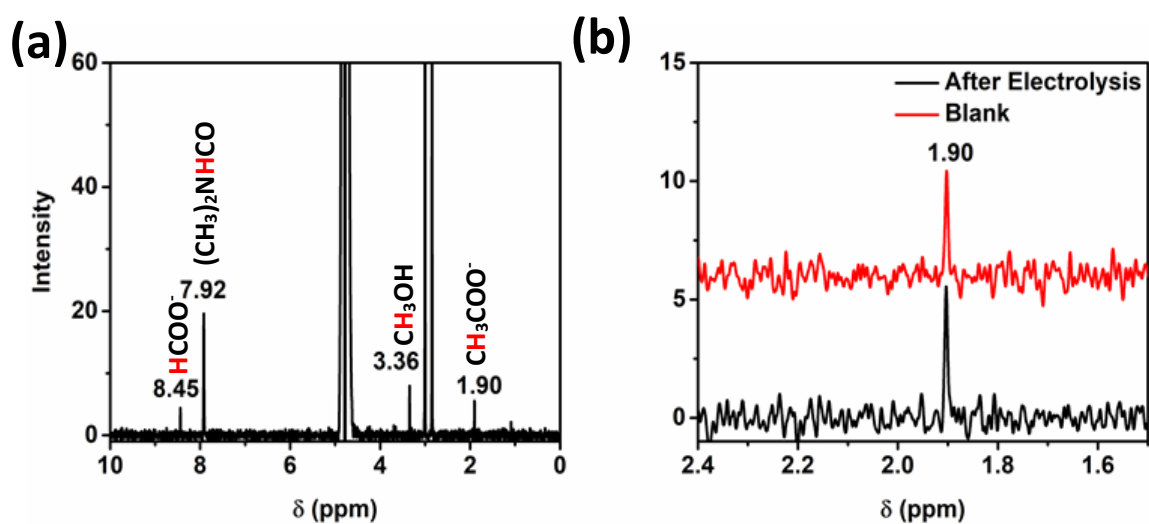


Figure S2.7. Complete NMR spectrum after electrolysis at -1.002V vs RHE at $\text{Cu}_2\text{Mo}_6\text{S}_8$ showing a large, suppressed H_2O signal at ~ 4.7 ppm (a)*, and NMR inset showing the peak at 1.90 ppm that corresponds to acetate in both the electrolysis product aliquot, as well as in a blank prior to electrolysis (b). Acetate was not observed as a product at any point in this study.

*Signals at 3.00 and 2.85 ppm correspond to methyl hydrogen atoms from DMF

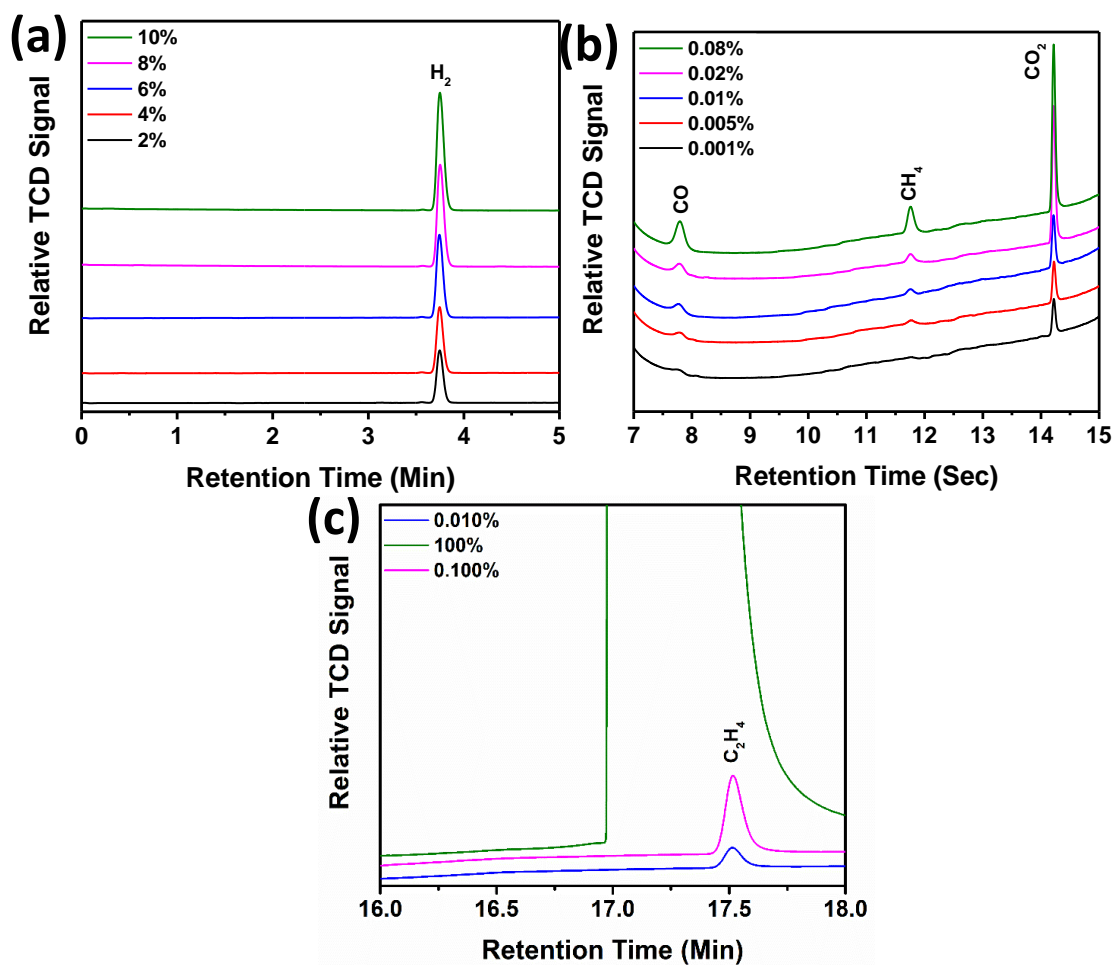


Figure S2.8. GC-TCD chromatographs illustrating the test injections used for calibration of H₂, CO, and CH₄ (a-b) as well as test injections to ensure sufficient detection of C₂H₄. 100% C₂H₄ resulted in fronting of the eluent, and the detection limit on the order of 0.01% percent was sufficient in detecting trace quantities of ethylene given the electrochemical cell construct implemented in this study. Methane and ethylene were undetected in all electrolysis experiments involving M_xMo₆S₈ catalysts.

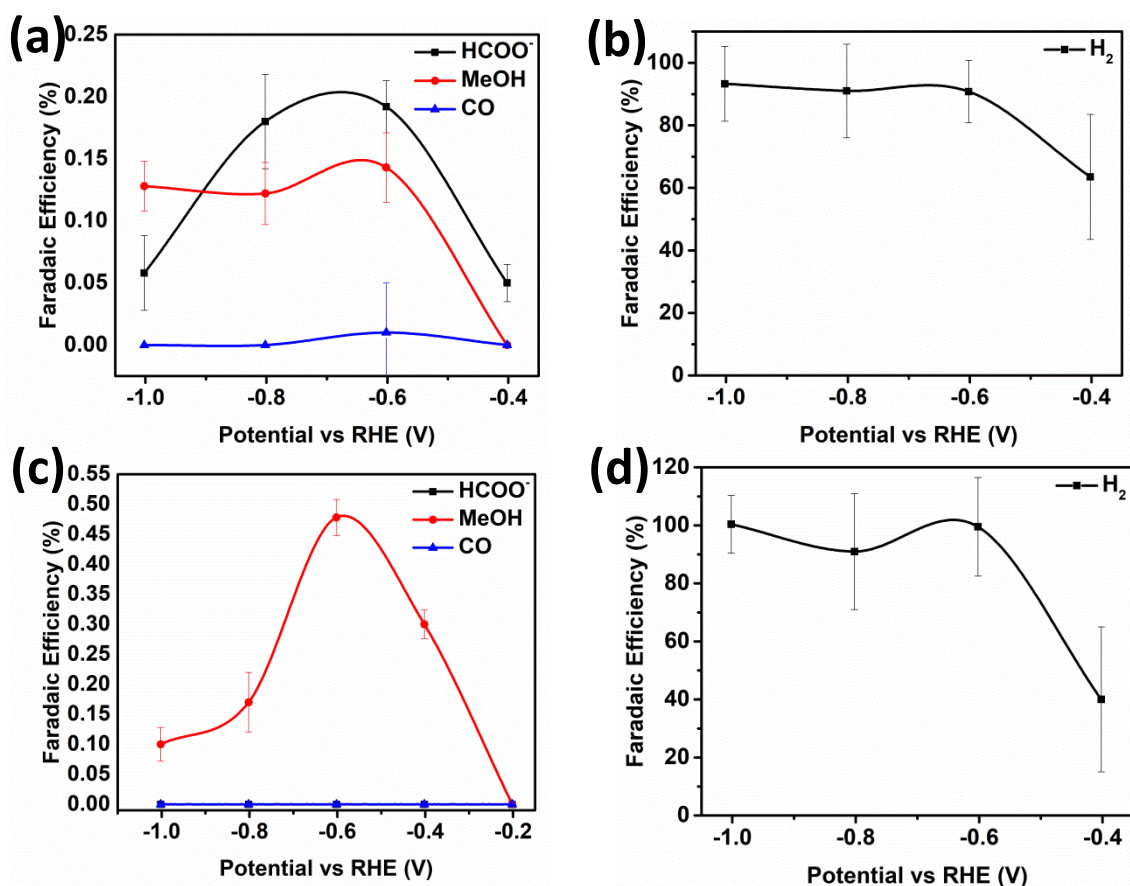


Figure S2.9. Potential-dependent Faradaic efficiency for CO₂ reduction products (a), for hydrogen evolution under CO₂ headspace (b), for CO reduction products (c), and for hydrogen evolution under CO headspace (d). Experiments for (a) and (b) were carried out in a pH 6.8 electrolyte where 0.1 M Na₂CO₃ was purged for 1 hr with CO₂, while experiments for (c) and (d) were carried out in pH 6.8 electrolyte where 0.1 M NaHCO₃ was purged for 1 hr with CO. Error bars reflect one standard deviation.

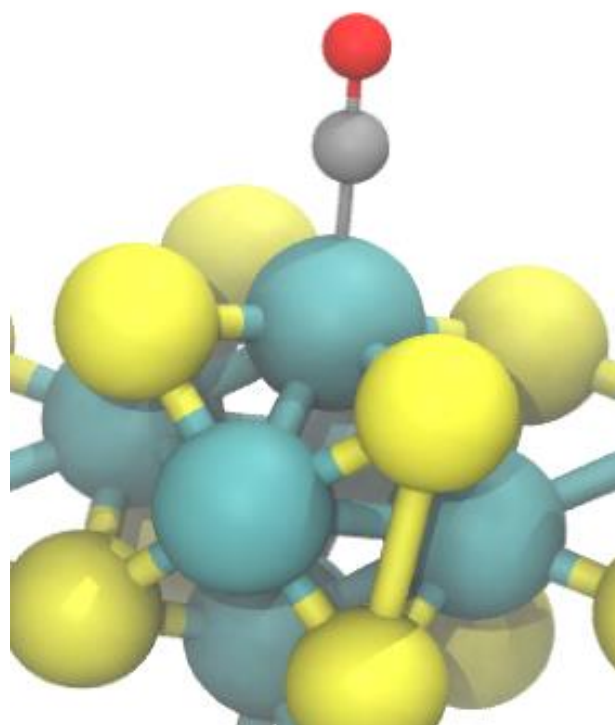


Figure S2.10. Most stable binding geometry for CO on Mo₆S₈. Multiple CO binding configurations at the Mo and atoms were explored and binding to Mo was determined to be most favorable in all cases. CO binding results in a stable octahedral coordination of the active Mo atom.

Color scheme: Mo (blue), S (yellow), C (grey) and O (red).

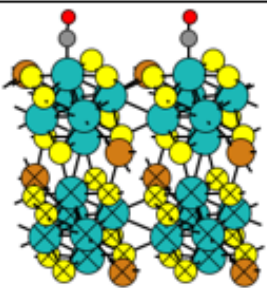
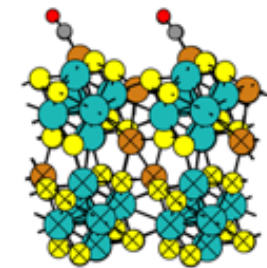
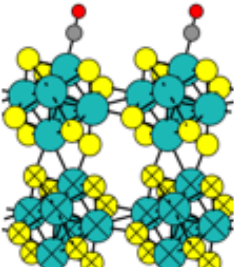
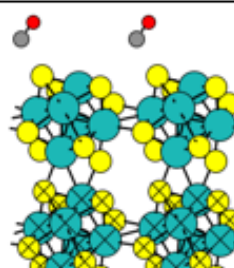
Geometry	CO Binding Energy (eV)	Binding Interaction
	-1.50	Strong CO Binding to Mo Sites
	-0.91	Weak CO Binding to Cu Sites
Geometry	CO Binding Energy (eV)	Binding Interaction
	-1.61	Strong CO Binding to Mo Sites
	-0.25	Weak Van der Waals Interaction at S sites

Figure S2.11. Calculated binding energies for CO at relevant binding sites in Mo_6S_8 (a), and at the most favorable Cu and Mo sites in $\text{Cu}_2\text{Mo}_6\text{S}_8$ (b). S interactions are not presented for $\text{Cu}_2\text{Mo}_6\text{S}_8$ because only very weak VdW forces were calculated, as was the case for Mo_6S_8 .

Color scheme: Mo (blue), S (yellow), Cu (brown), C (grey) and O (red).

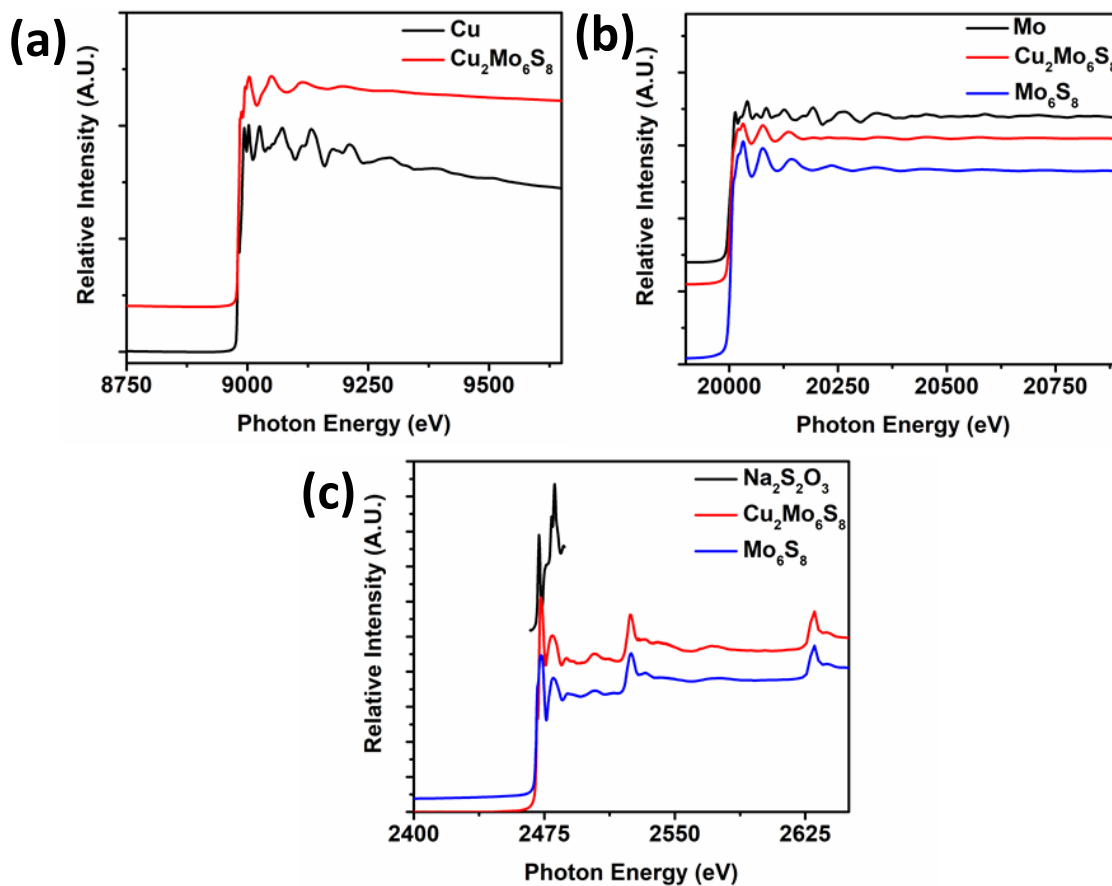


Figure S2.12. Full XAS spectra for (a) Cu-CP with a Cu^0 foil reference; (b) Cu-CP and bare-CP with a Mo^0 foil reference; (c) Cu-CP and bare-CP with a $\text{Na}_2\text{S}_2\text{O}_3$ reference. Scans for the $\text{Na}_2\text{S}_2\text{O}_3$ reference (black) in (c) were only carried out in the immediate energy range around the S K-edge because reference spectra were not collected simultaneously with CP spectra, as was the case for CPs.

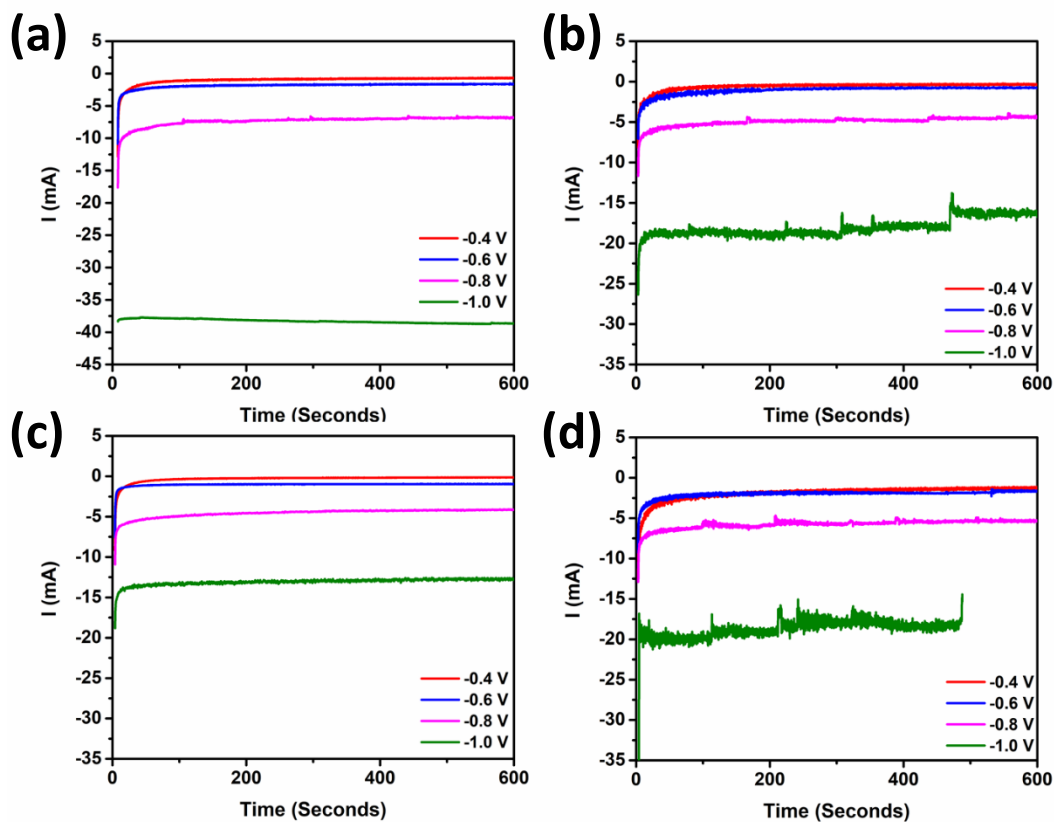


Figure S2.13. Raw data from controlled potential electrolysis experiments that show steady-state reduction currents over $\text{Cu}_2\text{Mo}_6\text{S}_8$ that were then normalized with respect to electrode surface area and then multiplied by Faradaic efficiency for each product that was detected via NMR and GC following each experiment in order to obtain partial current density values presented in Figure 2.9. These scans are representative of the raw current over time for each of the four potentials tested in this work (-0.4 V vs RHE (red), -0.6 V vs RHE (blue), -0.8 V vs RHE (pink), and -1.0 V vs RHE (green)), and are therefore not shown in their surface-area normalized forms. A notable increase in noise due to vigorous formation of H_2 under stirring is observable for the -1.0 V experiments in panels (b) and (d). All experiments were performed in CO_2 -saturated 0.1M Na_2CO_3 at pH 6.8 under vigorous magnetic stirring.

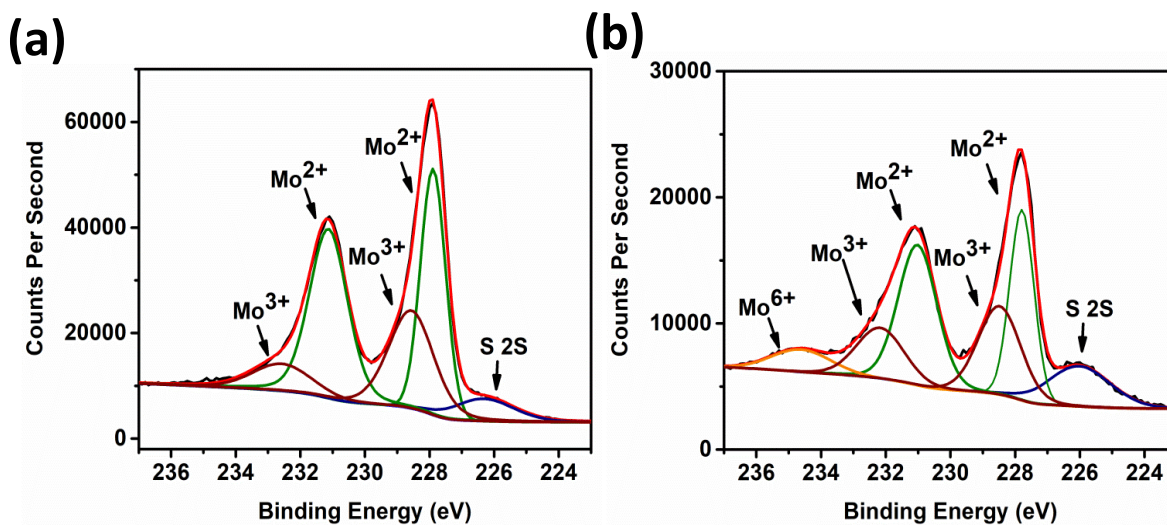


Figure S2.14. Mo 3d XPS spectra for $\text{Cu}_2\text{Mo}_6\text{S}_8$ catalyst before electrolysis (a), and after electrolysis (b), indicating slight oxidation of Mo following exposure to moisture and oxygen. It is not believed that catalyst oxidation occurs during electrolysis.

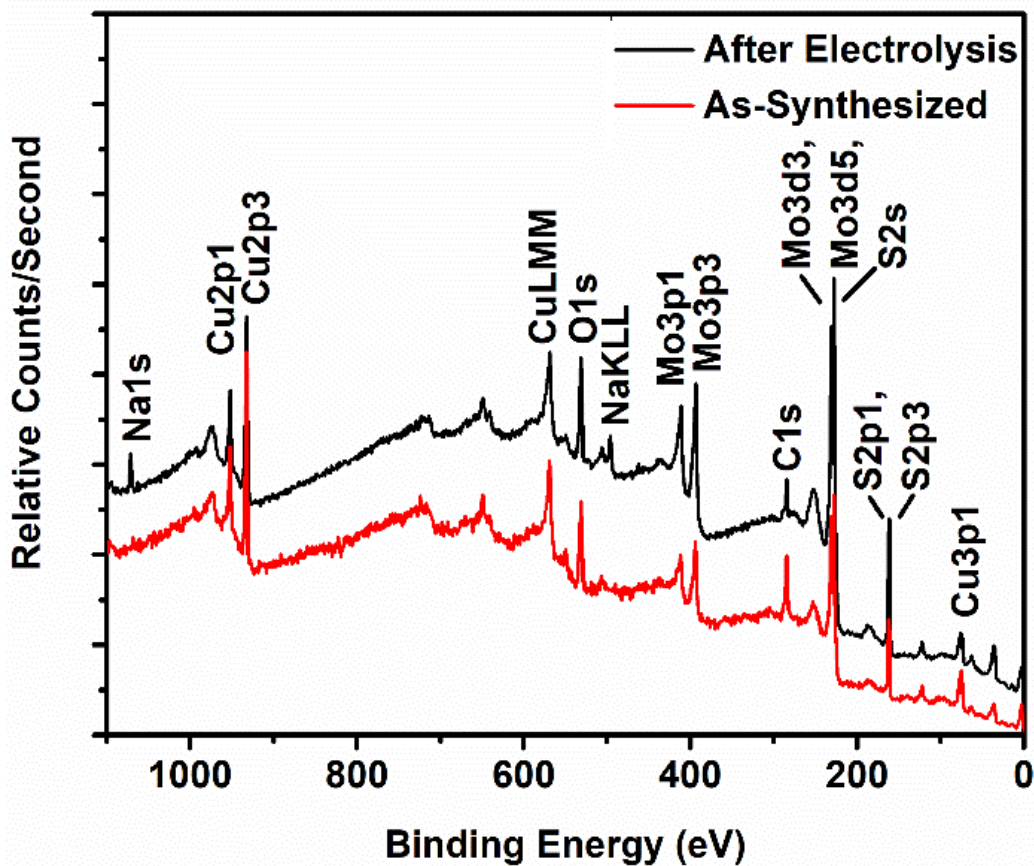


Figure S2.15. XPS survey scan of $\text{Cu}_2\text{Mo}_6\text{S}_8$ CP both before (black) and after (red) electrolysis. Peaks to note are the O1s and C1s signals that arise from a native oxide layer as well as surface carbon. Both species diminished over the course of successive surface-sputtering depth-profile scans, hence the only signal that evolved as the result of electrolysis is that of Na, a principle electrolyte component.

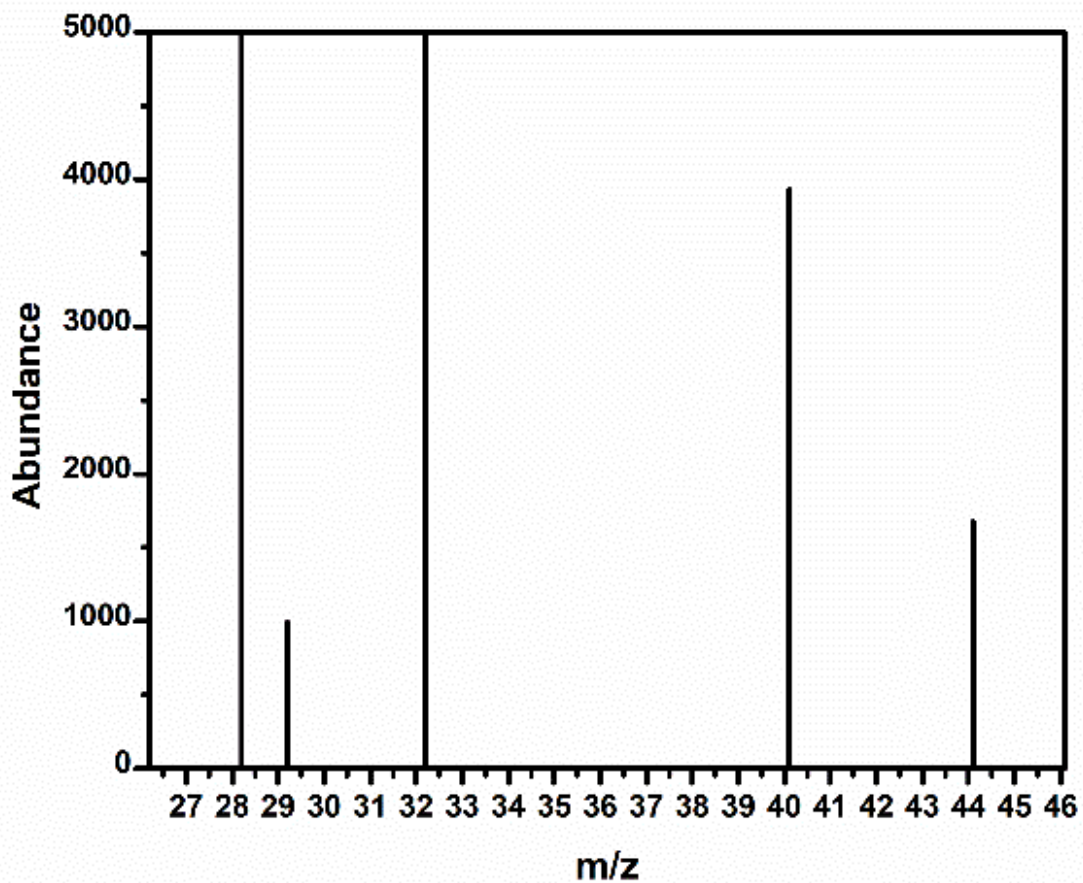
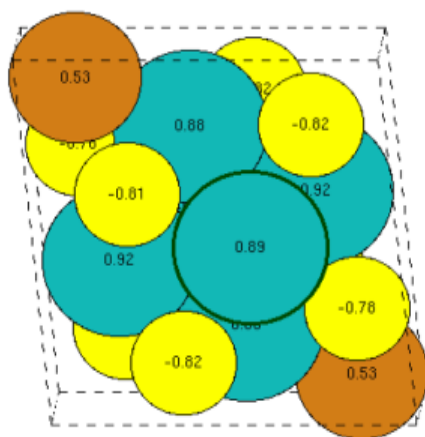
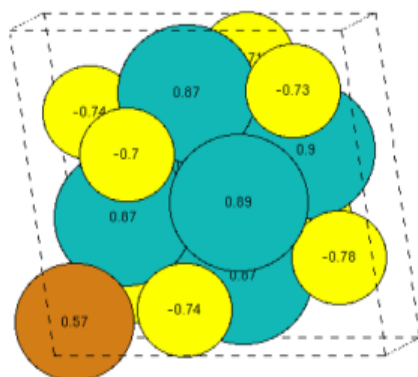


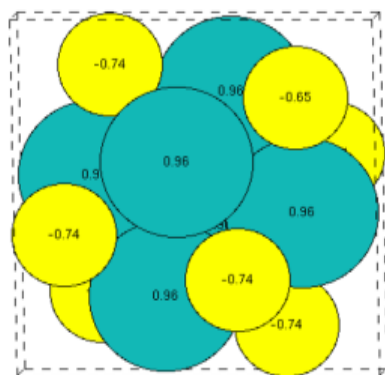
Figure S2.16. Mass-spectrum following injection of the cell headspace following electrolysis over $\text{Cu}_2\text{Mo}_6\text{S}_8$ at -1.0 V vs RHE in a $0.1\text{M Na}_2\text{C O}_3$ electrolyte saturated with CO_2 at 1 atm. Prominent signals for N_2 and O_2 resulted from the ambient gas in the needle of the injection syringe.



Cu₂Mo₆S₈
Cu (avg) = 0.53



Cu₁Mo₆S₈
Cu = 0.57



Mo₆S₈
S = -0.74
Mo = 0.96

Figure S2.17. Results of Bader charge analysis for Mo₆S₈, CuMo₆S₈ and Cu₂Mo₆S₈ which shows a notable increase in electron localization on S atoms upon introduction of Cu. Bader charge analysis operates on the principle that atoms within a structure can be divided based upon their charge density according to discrete volumes that form from zero-flux surfaces that are two-dimensional planes on which charge density for an atom is at a minimum perpendicular to the plane. Hence charge density within the volume made up by these zero-flux surfaces is a good approximation of the relative charge each atom within a structure.⁶⁰

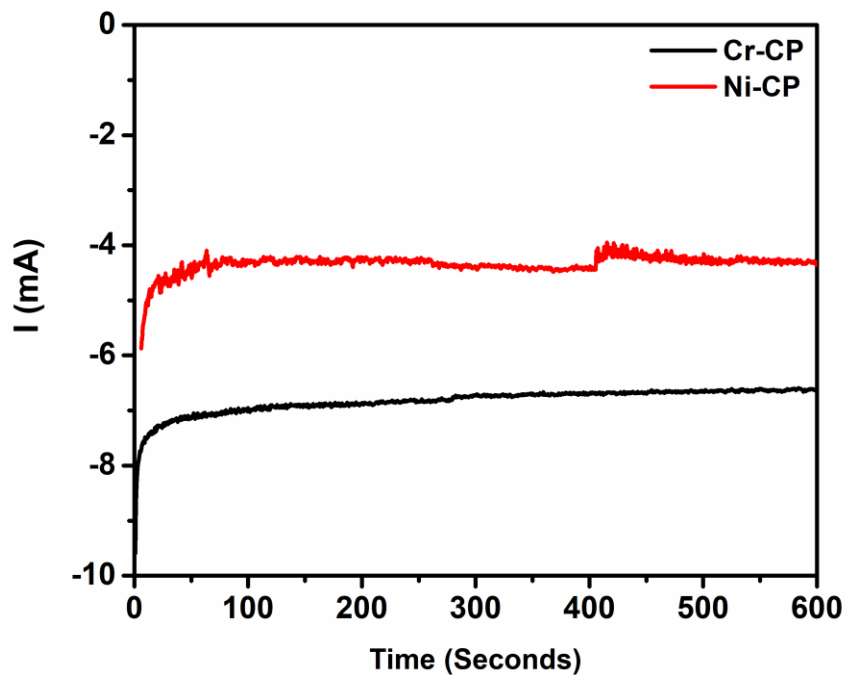


Figure S2.18. Raw data from controlled potential electrolysis experiments that show steady-state reduction currents over $\text{Cr}_{1.73}\text{Mo}_6\text{S}_8$ (black) and $\text{Ni}_2\text{Mo}_6\text{S}_8$ (red) that yielded the product distributions shown in Fig. 2.12. These experiments were performed in aqueous CO_2 -saturated 0.1 M Na_2CO_3 electrolyte at pH 6.8 at -0.8 V vs RHE under vigorous mechanical stirring.

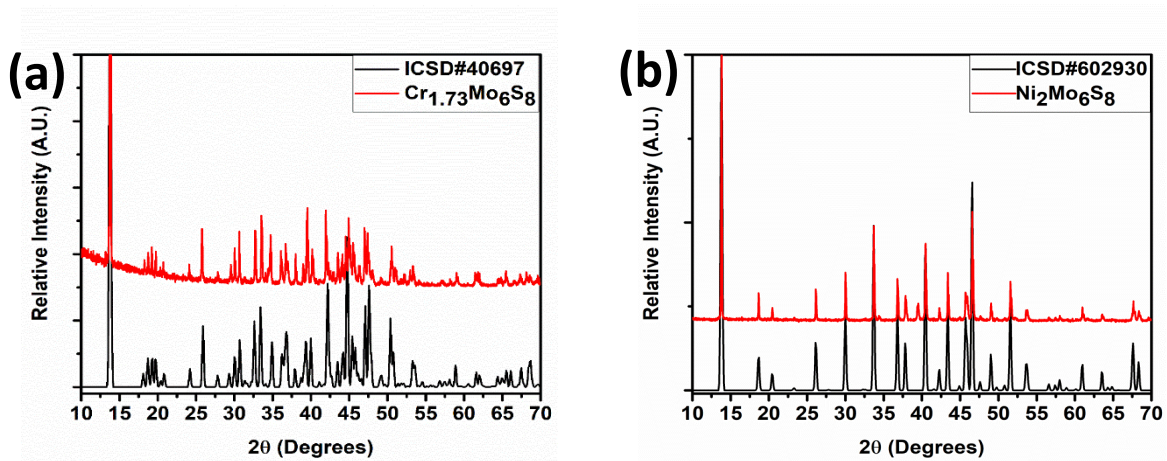


Figure S2.19. XRD patterns overlaid with published patterns for $\text{Cr}_{1.73}\text{Mo}_6\text{S}_8$ (a) and $\text{Ni}_2\text{Mo}_6\text{S}_8$ (b) that were used in control experiments.

Table S2.1 Result of Pawley refinement for all Chevrel-phase structures studied in this work.

Material	Unit Cell Parameter	Experimental Value	Literature Value	% Difference ³
Mo ₆ S ₈ (R-3H)	a	9.1932Å	9.1910Å	0.02
	b	9.1932Å	9.1910Å	0.02
	c	10.8891Å	10.2290Å	6.45
	α	90°	90°	0.00
	β	90°	90°	0.00
	γ	120°	120°	0.00
	Volume	797.006 Å ³	795.84Å ³	0.15
Cr _{1.73} Mo ₆ S ₈ (P1)	a	6.5035Å	6.5170Å	-0.21
	b	6.4795Å	6.4959Å	-0.25
	c	6.4562Å	6.4480Å	0.13
	α	94.5190°	94.70°	-0.19
	β	96.9590°	90.72°	6.88
	γ	97.0100°	97.87°	-0.88
	Volume	269.4447Å ³	269.41Å ³	0.01
Ni ₂ Mo ₆ S ₈ (R-3H)	a	9.5002Å	9.511Å	-0.11
	b	9.5002Å	9.511Å	-0.11
	c	10.2185Å	10.229Å	-0.10
	α	90°	90°	0.00
	β	90°	90°	0.00
	γ	120°	120°	0.00
	Volume	798.699Å ³	801.34Å ³	-0.33
Cu ₂ Mo ₆ S ₈ (R-3H)	a	9.6328Å	9.63Å	0.03
	b	9.6328Å	9.63Å	0.03
	c	10.2229Å	10.22Å	0.03
	α	90°	90°	0.00
	β	90°	90°	0.00
	γ	120°	120°	0.00
	Volume	821.502Å ³	820.79Å ³	0.09

EXAFS and XANES:

X-ray absorption spectroscopy is an element-specific tool for probing the local electronic and coordination environment in materials. This local probe nature originates from the underlying principles of the absorption event in which monochromatic x-rays eject core level electrons from elements of interest. The brief lifetime of the core-hole and its decay process limits information to less than 1 nm surrounding the absorbing atoms. Post-edge energies beyond the initial core level produce a photoelectron that is self-modulated by scattering with the surrounding environment. These modulations (EXAFS) provide bond length and scatterer information.

No observable pre-edge features at the Mo *K*-edge indicate that the Mo₆ octahedra in both Cu₂Mo₆S₈ and Mo₆S₈ are relatively symmetric (O_h). This is because transitions that would give rise to pre-edge features, in this case, would generally been seen only for more distorted geometries. The empty phase is dominated by a single peak centered around 1.95 Å with a small shoulder at longer distances—in strong agreement with previous EXAFS analyses of Mo₆S₈. This peak represents Mo – S interactions with 3 distinct types of S atom— the ternary (axial) S, and two slightly different S positions that form a pseudo-square planar geometry around Mo. The small shoulder at longer distances results from Mo – Mo interactions; the Mo₆ cluster is somewhat distorted in the empty Mo₆S₈ and variability in the scattering distance causes destructive interference and hence a weak signal. In the Cu-promoted CP, there is a dramatic change in the signal at the above distances. The Mo – S region is diminished and the Mo – Mo distances increase. Fitting reveals changes in the local cluster with an elongation of the ternary axial Mo – S to 2.58 Å from 2.44 Å. The Mo₆ cluster also shrank slightly to 2.69 from 2.72 Å in the case of empty Mo₆S₈. These shifts distort Mo – S distances and cause interference, while Mo – Mo bond lengths in the cluster become more uniform, and scattering signals become additive for the intense peak seen around 2.4 Å.

Cu EXAFS is consistent with a decrease in the fitted Cu – S bond of 0.12 Å, closely matching the shift in the Mo – S bond and increased separation between Cu absorbers and Mo₆ clusters. Of note, the Debye-Waller factor for Mo in the Cu fit is rather high but may be explained by the thermal and positional variability of the Cu absorber inside the cavity.

No EXAFS analysis on S K edge was performed due to the nice overlap between S K edge and Mo L_{3/2} and L_{5/2}-edges that appear approximately 100 eV past the S K edge.

Table S2.2 Fitting parameters for Mo K-edge of Cu₂Mo₆S₈

Parameter	Value		R-Factor
S02	0.85	set	0.029
enot	-2.88	+/- 0.94	
drS1	-0.04	+/- 0.005	
drS2	0.11	+/- 0.04	
drMo1	-0.05	+/- 0.004	
dCu1	0.07	+/- 0.03	
ssMo	0.004	+/- 0.001	
ssS	0.006	+/- 0.002	
ssCu	0.008	+/-0.005	

Table S2.3 Fitting parameters for Mo K-edge of Mo₆S₈

Parameter	Value		R-Factor
S02	0.85	set	0.015
enot	-0.8	+/- 0.98	
drS1	-0.017	+/- 0.009	
drS2	-0.04	+/- 0.008	
drMo1	-0.07	+/- 0.03	
ssMo	0.017	+/- 0.002	
ssS	0.009	+/- 0.003	

Table S2.4 Fitting parameters for Cu K-edge of Cu₂Mo₆S₈

Parameter	Value		R-Factor
S02	0.82	set	0.022
enot	1.26	+/- 0.89	
drS1	0.11	+/- 0.03	
drS2	-0.12	+/- 0.02	
drMo1	-0.08	+/- 0.05	
ssS	0.009	+/- 0.003	
ssMo	0.018	+/- 0.004	

Table S2.5 Extracted bond lengths from EXAFS fittings

	Absorber	Scatterer	N	Fitted R (Å)
Mo₆S₈	Mo	S	5	2.44
		Mo	2	2.67
		Mo	2	2.76
		Mo	1	3.24
Cu₂Mo₆S₈	Mo	S	1	2.58
		S	4	2.45
		Mo	2	2.69
		Mo	2	2.75
		Mo	1	3.25
		Cu	1	3.21
	Cu	S	1	2.23
		S	4	2.30
		Mo	3	3.16

3. Chapter 3: Spectroscopic, Calorimetric, and Computational Study of the Electronic Structure, Local Coordination, and Thermodynamic Stability of 1st Row Transition Metal-Intercalated Chevrel-Phase Sulfides

Abstract

The electronic structures of S and Mo, as well as the local coordination of Mo are investigated as a function of metal intercalation into Chevrel-phase sulfide structures. The effect of intercalant-based electron donation into the stoichiometric range $M_yMo_6S_8$ ($M=Fe, Ni, Cu; y=0-2$) is observed via X-ray absorption near-edge structure (XANES) analysis, as well as the effect of charge donation on the bonding environment of Mo_6 metal centers which is monitored using extended X-ray absorption fine structure (EXAFS) analysis. Expansion and contraction of Mo_6 octahedra is observed depending on the number of electrons populating bonding-like versus antibonding-like states, as is predicted by Hückel molecular orbital theory. Marked tunability is observed in the electronic structure of sulfur depending on charge transfer magnitude between intercalant species and Mo_6S_8 units. Average Mo_6 octahedron Mo-Mo bond contraction from 2.76Å to as short as 2.69Å was observed upon incorporation of metal intercalants, while intercluster separation displays a pronounced increase for intercalant-host lattices compared to de-intercalated Mo_6S_8 . To corroborate spectroscopically observed phenomena, we performed computational analyses of spin-polarized densities of state (DOS) for the Chevrel-phase materials investigated herein, where a detectable increase in sulfur-based frontier orbital population is observed in accordance with experimentally validated orbital filling. Further, experimentally measured and computationally verified local and electronic structure are used to build a holistic picture of thermodynamic stability in the Chevrel-phase sulfide family of materials, and framework ionicity and covalency are identified as competing drivers of thermodynamics. We implement a tandem calorimetric and computational approach to establishing quantifiable descriptors for formation enthalpy which can inform future strategies for accessing synthesizable multinary compositions.

Introduction

Designing and understanding efficient energy storage and conversion systems is an imperative that may prove critical for the sustenance of current population growth and resultant energy demands.^{1,2} Promising avenues in these two fields of study include heterogeneous catalysis as a means of energy conversion, as well as the development of multivalent battery technology as a means of efficient energy storage.^{3,4} An interesting family of materials with applications in both energy conversion catalysis and in multivalent ion intercalation are the ternary Chevrel-phase (CP) chalcogenides. These materials are known to be high-temperature superconductors as well as stable hydrogen evolution electrocatalysts owing to their favorable frontier orbital landscapes. They also comprise some of the first functional multivalent battery cathode architectures as a result of their structural flexibility and ability to facilitate ion migration during charging/discharging cycles.^{5,6} Finally, it is noteworthy that CPs show promise as selective CO₂ reduction catalysts resulting from synergistic interactions between chalcogen and metal sites which give rise to tunable electronic environments.⁷⁻¹⁰

The Chevrel-phase family has a general composition of $M_yMo_6X_8$ (M = transition or alkali metal, $y = 0-4$, $X = S, Se, Te$) and exhibits exceptional compositional flexibility.¹⁰⁻¹³ Perhaps more importantly, the CP family provides a framework for investigating the role that metal intercalation plays in determining local coordination and electronic structure within multinary materials. The generic CP structure as depicted

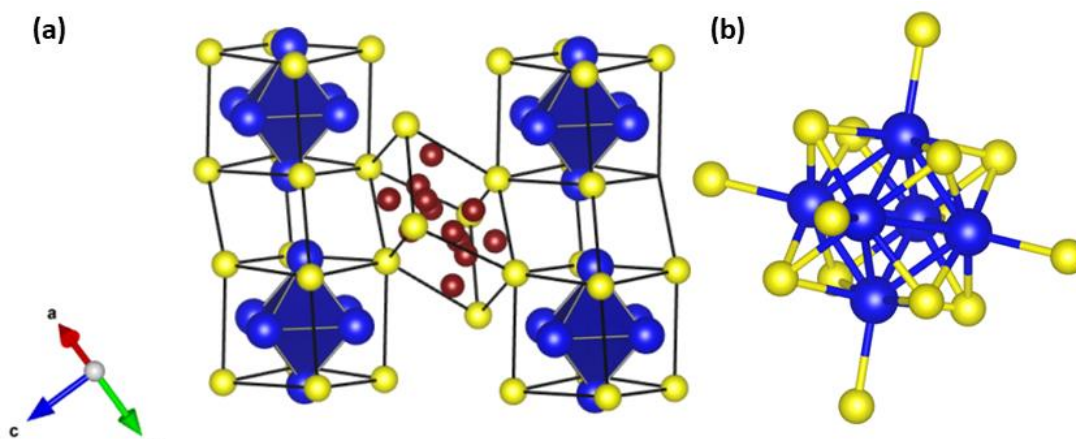


Figure 3.1. Crystal structure showing connectivity in $Cu_2Mo_6S_8$ where Cu ions (red) are found inside the cavity formed by adjacent Mo_6S_8 units (a), and an Mo_6S_8 cluster unit showing six additional axial bonds between Mo (blue) and S (yellow) that link adjacent clusters together (b).

in **Fig. 3.1** consists of Mo_6X_8 units where a slightly distorted Mo_6 octahedron lies in the center of eight face-sitting chalcogen atoms, forming a pseudo cubic environment around the Mo_6 (**Fig. 3.1a**). Individual Mo_6X_8 units are connected via intercluster Mo-X linkages such that axial, linking Mo-X bonds cap the pseudo square planar coordination environment formed by four surrounding face-sitting chalcogens (**Fig 3.1b**). This capping by an adjacent cluster chalcogen ultimately results in a pseudo square pyramidal coordination environment around Mo atoms. In the most common rhombohedral crystal structure, Mo_6X_8 cluster units extend via Mo-X linkages to form cavities and channels between clusters, inside which small metal intercalant ions reside indiscriminately in any of 6 crystallographically equivalent positions (**Fig. 3.1a**), whereas larger metal intercalants (e.g. K, Pb) tend to reside directly in the cavity center.^{11,14}

Given the importance of elucidating the electronic structure of promising compounds, it is of great interest to investigate materials for which there are reasons to believe desired catalytic activity may be achievable. In the case of CO_2 reduction to liquid fuels, Density Functional Theory (DFT) evaluations of the CP sulfide cluster system has revealed potentially favorable binding interactions for multiple intermediates along the CO_2 reduction pathway to methanol.^{9,15} In addition, previous work by Tributsch¹⁶ and Hoffman¹⁷ indicates that the band structure of the Chevrel-phase may indicate suitability for a variety of electrocatalytic processes such as hydrogen evolution and oxygen reduction, owing to the position of the Mo d-band with respect to the fermi level. Hence, in this work we experimentally investigate the electronic structure of a stoichiometric range of $\text{M}_y\text{Mo}_6\text{S}_8$ ($\text{M} = \text{Fe, Ni, Cu } y=0-2$), and further determine the degree to which structural modulation can affect the electronics of this known class of high-temperature superconductors and multi-valent battery intercalant hosts.^{12, 14, 18, 19} Previous work on CPs by Yvon et al. that explored structural modulation of the Mo_6 octahedron in CPs intercalated by Cu, Ag, Sn, and In is a valuable reference point for explanations of intercalant-induced structure changes in CPs.²⁰ We have expanded their X-ray diffraction (XRD)-based investigation to a series of transition metal-intercalated CPs, implementing highly structurally sensitive X-ray absorption techniques to monitor variations in the local coordination of CP Mo atoms,²¹⁻²⁴ with added insight regarding the electronic make-up of constituent elements in the structure that serves to guide our rationalization of bonding phenomena.

To thoroughly investigate coordination and electronic structure in intercalated CPs, we implement X-ray absorption spectroscopy (XAS) which utilizes tender and hard X-rays for core-level electron excitation into lowest unoccupied molecular orbitals (LUMO) as well as into continuum states as depicted graphically in **Fig S3.1**. These excitation processes are highly dependent on the nuclear charge, electronic structure, and local coordination environment of the absorbing atoms. Furthermore, elements have discrete energy ranges for excitation of electrons from various shells. Interpretation of observed excitation energies facilitates evaluation of absorber atom oxidation state, and in some cases yields valuable information regarding specific frontier orbital characteristics. In this manuscript, electronic information is extracted from features of the K and L edges of studied materials, corresponding to ejection of 1st and 2nd shell electrons, respectively. In short this spectroscopic technique gives our investigation a high degree of elemental specificity and, through data processing methods which have developed considerably in the years following the conception of X-ray absorption spectroscopy, we are able to discuss specific, individually observed and structurally dependent scattering events for the CP structures of interest.²⁵⁻²⁷ As such, we use aforementioned spectroscopic methods to investigate local Mo coordination in CPs intercalated by Fe, Ni, and Cu, as well as for a Mo₆S₈ structure that lacks a promoting species. We further explore the degree of cluster separation that is potentially induced by electron donation from various 1st row transition metals. Finally, we analyze the electronic structures of constituent atoms in the previously listed CP structures. This investigation compares the effect on Mo coordination and electronic structure of both intercalant identity and stoichiometry, and experimental results are corroborated by theoretical calculations that aim to rationalize interesting charge localization phenomena that have been observed for various metal-intercalated CP sulfides.^{18, 20}

Experimental Methods

3.1 Materials:

MoS₂ powder (>99.5%, ~325 mesh), Fe powder (99.998%, ~22 mesh), Cu powder (99.995%, ~100 mesh), Ni powder (99.8%, ~325 mesh), were used as purchased from Alfa Aesar. Mo powder (99.99%, ~100 mesh)

was used as purchased from Sigma Aldrich. Fused quartz tubes (2 mm thick) were purchased from Technical Glass Inc. and made into round-bottom tubes with an in-house oxy-hydrogen torch.

3.2 Synthesis:

All CPs studied were synthesized via solid-state methods adapted from literature.²⁸ For this method, appropriate elemental powders for each ternary metal, Mo powder, and MoS₂ powder as a S source weighed under N₂ to within +/- 0.0002 g of their target masses (**Table 3.1**). All precursor powders were then mixed in a ball mill under N₂ atmosphere for 24 hrs. Mixed powders were then transferred into a N₂ glovebox and pressed together under 25 metric tons over an area of 20mm². These pellets were then placed into round-bottom fused quartz tubes inside a glovebox. A protecting layer of tightly packed aluminum oxide microfiber was placed over samples to prevent diffusion of oxygen into the sample environment, and the tube was removed from N₂ and placed into graphite powder as shown in **Fig. S3.2**. The reaction vessels as seen in the SI were then transferred inside graphite baths to a conventional microwave oven outfitted with an Ar gas inlet to maintain inert atmosphere during the reaction. Samples achieved maximum phase conversion upon irradiating with 1200W for 10 minutes, where graphite powder acts as a microwave susceptor material capable of rapidly converting microwave radiation to thermal energy. The high temperature microwave heating step was followed by immediate quenching in room temperature water. In order to synthesize the binary Mo₆S₈ structure, an acidic leaching procedure was used according to literature methods in which Cu₂Mo₆S₈ was added to 6M HCl and bubbled with O₂ overnight.⁶ The synthesized binary product was isolated from the leachate by vacuum filtration followed by 5 sequential washes with ~10 mL of ultra-pure deionized (UPDI) water to ensure complete removal of residual acid and CuCl₄²⁻ complex that was formed through the leaching process.

Table 3.1. Reagent masses used to obtain 500 mg precursor mixtures for microwave heating.

Composition	Molar Mass (g/mol)	M _x Mass (g)	Mo Mass (g)	MoS ₂ Mass (g)
FeMo ₆ S ₈	888.073	0.0314	0.1080	0.3605
Fe ₂ Mo ₆ S ₈	943.918	0.0592	0.1017	0.3392

Ni ₂ Mo ₆ S ₈	949.614	0.0618	0.1010	0.3372
Cu ₂ Mo ₆ S ₈	959.320	0.0662	0.1000	0.3337

3.3 Structural and Electronic Characterization:

Phase purity of as-synthesized CPs was analyzed via powder XRD using a Bruker D8 Advance diffractometer with Cu K-alpha radiation (1.5406 Å) as well as at Stanford Synchrotron Radiation Lightsource (SSRL) BL 2-1 (0.728068 Å). XRD experiments at BL 2-1 were performed under He atmosphere with a 1.3 Tesla bend magnet and a Si (111) monochromator where energy resolution ($\Delta E/E$) was 5×10^{-4} . Refinement and powder pattern indexing such as that shown in **Table S3.1**, **Fig. 3.2a**, and **Fig. S3.3** were completed using the TOPAS analysis software by Bruker.

CP morphology as shown in **Fig. 3.2b** was analyzed using an FEI (Hillsboro, OR) 430 Nano Scanning Electron Microscope (SEM). SEM samples were prepared in their pelletized forms for all ternary phases and in the powdered form for the binary phase; pelletized samples were mounted in place on conductive SEM stages using metallic screws while powdered samples were adhered to conductive double-sided carbon tape followed by gentle blowing of loose particulates with high-purity nitrogen prior to introduction into the microscope chamber. Structural and electronic information was acquired via ex-situ XAS at SSRL beam lines 4-1 and 4-3 using hard and soft/tender X-rays, respectively, in order to observe

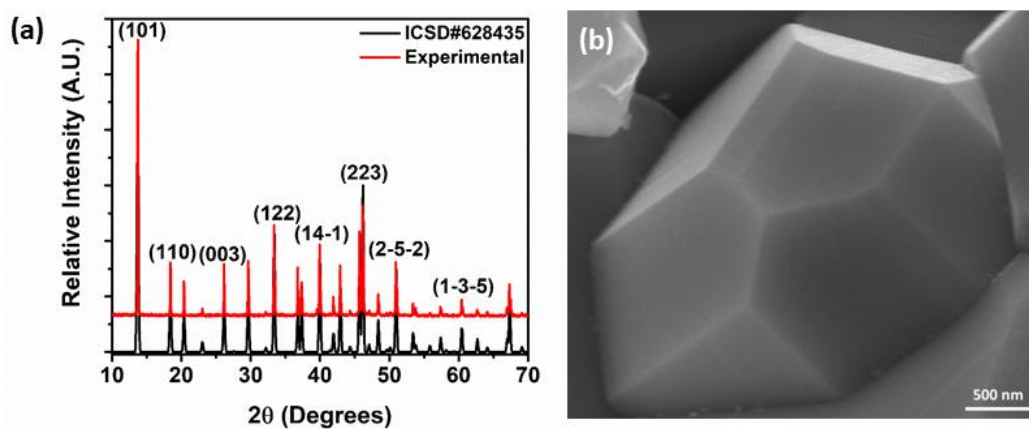


Figure 3.2. Indexed PXRD pattern for as-synthesized Cu₂Mo₆S₈ overlaid with an ICSD reference pattern (a) and a scanning electron micrograph showing faceted Cu₂Mo₆S₈ crystal which forms under microwave irradiation (b).

X-Ray Absorption Near-Edge Structure (XANES) and Extended X-Ray Absorption Fine Structure (EXAFS) information for Fe, Ni, Cu, Mo, and S. Samples were prepared for XAS analysis by pulverizing all samples and filtering size using a solvent (isopropanol) method with a mortar and pestle where the pestle would agitate particles suspended in solution within the mortar and would adhere only the smallest particles which were then briefly transferred to a glass slide to dry. Once dried these small particles were scraped into a thin and even layer over Kapton (polyimide) tape which exhibits high transmittance to X-rays, and this particle-coated Kapton was then fastened to the XAS beamline sample holders. Further elemental and electronic structure analysis was performed via X-ray photoelectron spectroscopy (XPS) using a PHI Versaprobe 3 spectrometer, where CP surface composition and oxidation states were verified. XPS sample preparation was identical to that of SEM.

3.4 X-ray Absorption Experiments and Analysis:

Mo_6S_8 , FeMo_6S_8 , $\text{Fe}_2\text{Mo}_6\text{S}_8$, $\text{Ni}_2\text{Mo}_6\text{S}_8$ and $\text{Cu}_2\text{Mo}_6\text{S}_8$ were all screened at their respective metal intercalant K-edge, Mo K-edge, and S K-edge. S K-edge and Mo L-edge scans were completed simultaneously at beam line 4-3 at SLAC national accelerator laboratory, while Mo K-edge, Cu K-edge, Ni K-edge, and Fe K-edge scans were all completed on beam line 4-1 at SLAC. During each scan at beamline 4-1, a reference foil composed of an appropriate metal was analyzed in tandem with the sample to calibrate the incident beam energy, while a $\text{Na}_2\text{S}_2\text{O}_3$ reference powder was used for energy calibration at beamline 4-3. This method of reference data collection allowed for the mitigation of any shifts in beam energy or monochromator position that could have occurred over the course of repeated scans.

Each edge scan performed with the exception of the S K-edge and Mo L-edge was performed under atmospheric conditions, while the S K-edge and Mo L-edge scans were performed under He with a chamber O_2 content $<0.04\%$ in order to avoid interactions between oxygen and the beam. For each edge scan, transmittance and fluorescence data were simultaneously collected at least 3 times per sample edge and then averaged to improve the signal to noise ratio. Fluorescence signal was collected using a Lytle detector, and the results presented herein are based exclusively on the averaged fluorescence data.

3.5 XAS Data Analysis:

Full X-ray absorption spectra (**Fig. S3.4** and **Fig. S3.5**) for each element edge in all five CPs studied here were first averaged using SixPack, then imported for further processing into Athena version 0.9.26 and Artemis version 0.9.26.²⁵ Both Athena and Artemis use IFEFFIT²⁵ for any numerical calculations based on the data. Spectra were normalized in Athena as shown in the supplementary information, based on ascribed pre- and post-edge regions for each element. As the S XAS spectra is interrupted by Mo L-edges, S K-edge scans were normalized following truncation of obstructive Mo signal. Normalized scans were fit in real-space where k-weighting was fixed according to the absorbing atom. The corresponding real-space data was then Fourier transformed and fit with a theoretical model based on established structural information from the International Crystallographic Structure Database (ICSD).²⁹ The amplitude reduction factor (S02) that accounts for potential signal contribution by multi-electron excitation events was calculated using an appropriate metal reference. The Debye-Waller factor (σ^2) that is based on bond vibration was defined as being identical for any species that has a similar bonding environment.

3.6 High-Temperature Oxide-Melt Calorimetry

High-temperature drop-solution calorimetry was performed using a Tian Calvet twin calorimeter AlexSYS (Setaram, France) at 1073 K.³⁰⁻³² Small temperature differences between the sample and its constant surroundings, namely a large metal block heat sink, registered by a thermopile, is proportional to the heat flow. The integral of the thermopile electromotive force (e.m.f.) in a calorimetric peak generated by a chemical reaction, relative to an established baseline, is proportional to the heat effect, and, with appropriate calibration, gives the enthalpy of reaction. In the experiments reported here, the powdered samples were pressed into pellets and dropped into a platinum crucible containing molten sodium molybdate $3\text{Na}_2\text{O}\cdot_4\text{MoO}_3$ solvent. Pure oxygen gas was flushed over the solvent at 90 ml/min and bubbled through it at 5 ml/min. The bubbling gas brings the samples into much more direct contact with an oxidizing environment, speeds oxidation and stirs the solvent. The calorimeter was calibrated against the heat of combustion of 5 mg pellets of benzoic acid ($\text{C}_7\text{H}_6\text{O}_2$, Parr Instruments).

The measured drop solution enthalpy represents the sum of heat content of the sample from room temperature to 1073 K, its heat of solution in the sodium molybdate melt and its heat of oxidation. Because the heat of oxidation is the largest contribution to the drop solution enthalpy, all values are expected to be negative. The drop solution enthalpy is then used to calculate the enthalpies of formation from components or from elements. To ensure validity of each calculation, initial states of the oxides immediately prior to dissolution were confirmed and their final state in the melt was well defined and reproducible.

3.7 Computational Details:

Spin-Polarized Densities of State: Periodic density functional theory (DFT) calculations were performed using the Vienna ab-initio simulation package (VASP)³³ with the PBE functional (planewave cutoff = 520 eV, k-points = (5,5,5), force threshold = 0.03 eV/Å, Gaussian smearing width = 0.2 eV). Initial unit cell optimization (planewave cutoff = 700 eV) yields $a = 6.48$ Å and $\alpha = 91.18^\circ$ for bare Mo₆S₈, in agreement with experimental measurements. Density of states was obtained using the hybrid HSE06 functional using a lower (3,3,3) k-point mesh.

Stability Descriptors and Charge Density: DFT calculations were performed using VASP. The Strongly Constrained and Appropriately Normed (SCAN)³⁴ semilocal density functional was used to compute ground state structures, total energies and densities of state (DOS) for the compounds and elements. Calculations were performed with a plane wave cutoff of 520 eV and a Γ -centered Monkhorst-Pack k-point grid. Charge densities were calculated using DDEC6 atomic population analysis,³⁵ and Madelung energies were computed from these charges using the Ewald summation method implemented in Pymatgen. Crystal orbital overlap populations (COOPs) were calculated using LOBSTER.³⁶

Results and Discussion

3.1 Electronic Structure

All CPs were probed at both the Mo K- and L₂- edges, thereby providing insight into coordination geometry, oxidation state and electronic structure of Mo. Shown in **Fig 3.3** are the Mo L₂-edge scans for all measured CPs that show direct edge jump overlap beginning at approximately 2626 eV and reaching a maximum at

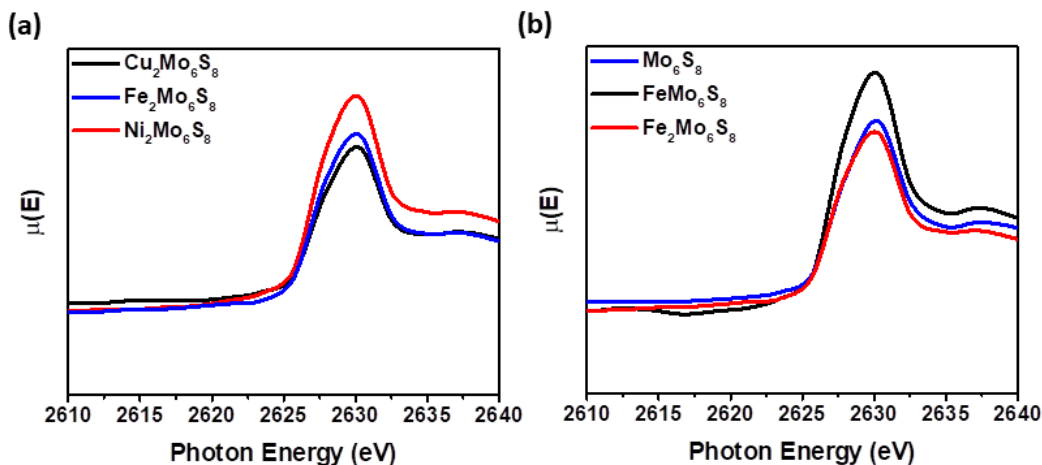


Figure 3.3. Mo L₂-edge XANES for M₂Mo₆S₈ (M = Fe, Ni, Cu) (a) and for Fe_xMo₆S₈ (x = 0-2) (b) showing consistent edge overlap irrespective of transition metal identity or stoichiometry. This overlap indicates consistent oxidation state between Mo in different CP species. Overlaid spectra are insets of normalized S K-edge EXAFS regions where the Mo L-edges arise and are therefore not normalized for the Mo L₂-region. Mo, S, and Mo K-edge XAS spectra in their entirety can be found in Fig. S3.4-S3.6.

approximately 2630 eV, regardless of intercalant identity and/or stoichiometry. According to Kunzli's law of linearly scaling edge jump positions with respect to absorber oxidation state, this overlap indicates that the apparent oxidation state of Mo is effectively unchanged regardless of the ternary cation that has been incorporated into the lattice. This observation is consistent with the interesting charge-transfer phenomenon that has been observed for Mo₆S₈ acting as a multivalent battery intercalant host, wherein CP chalcogen atoms are more susceptible than Mo to changes in electronic structure.^{18, 19} While it is unusual that charge transfer in transition metal-based compounds would not involve the metal center (a Mo₆ octahedron in the CP case), this observation of overlapping Mo L₂ edges is consistent with the overlap of Mo K-edges in **Fig. S3.6**, as well as the overlap in Mo 3p_{1/2}/3p_{3/2} and Mo 3d_{3/2}/3d_{5/2} XPS spectra in **Fig. 3.4**.

While Mo electronic structure appears relatively unchanged regardless of intercalant identity or stoichiometry, there is a marked difference in the S K-edge XANES region from one metal intercalant to another, as can be seen in **Fig. 3.5**. The existence of a pre-edge feature in the S XANES—the result of S 1s → 3p excitation—is indicative of relatively strong mixing between S 3p orbitals and Mo d-orbitals.³⁷ The prominence of said feature is believed to be dependent on the population of S 3p orbitals which constitute frontier CP electronic levels. As observed in literature, the intensity of this pre-edge feature is diminished

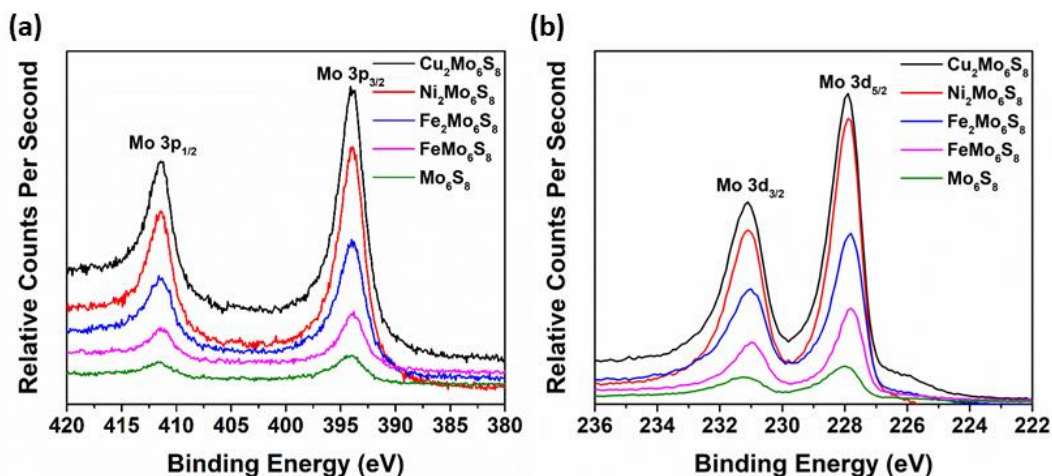


Figure 3.4. Mo 3p (a) and 3d (b) XPS spectra overlaid for all CPs studied, detailing similar oxidation states and chemical environments for Mo in each CP species.

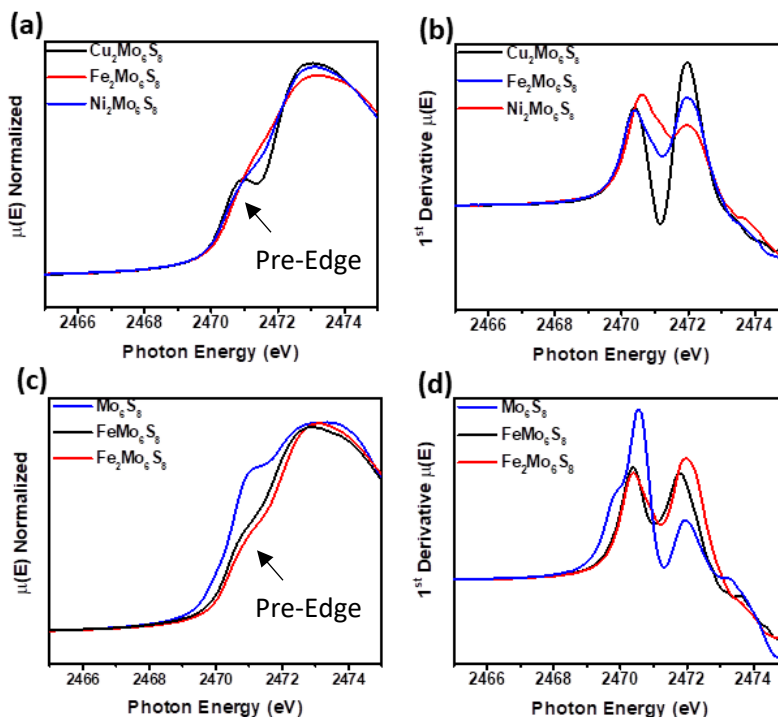


Figure 3.5. Overlaid S K-edge XAS spectra for $M_2Mo_6S_8$ ($M = Fe, Ni, Cu$) (a) and the corresponding 1st derivative plot for the same scans (b), along with overlaid S K-edge XAS spectra for $Fe_xMo_6S_8$ ($x = 0-2$) (c) and the corresponding 1st derivative plot for the same scans (d). Notably, the pre-edge centroid overlaps at 2471 eV for all phases, with a slight ($< \sim 0.25$ eV) shift in the white line position.

as electron density is donated from metal intercalants into Mo_6S_8 clusters.¹⁸ Mo_6 clusters are metastable 20-electron species and become stable at a valence electron count of 22 electrons.¹⁷ As clusters would have a complete valence shell at 24-electrons, the pre-edge that arises from electron transitions into slightly mixing

S 3p orbitals will diminish as up to four intercalant-derived electrons occupy frontier orbitals and render such pre-edge transitions forbidden. Hence, we can qualitatively determine the degree to which intercalant electron density is transferred to the Mo_6S_8 unit via observation of the position and intensity of this S pre-edge. We can further evaluate the effect of metal promotion by examining the calculated DOS of Mo and S where an overall shift is observed in the DOS of either Mo, S, or both near the Fermi energy when metal intercalants are present compared to when they are absent. This observation can be validated in **Fig. S3.7-S3.11** and may have important implications for catalysis, as accessible metal d-orbitals near the Fermi level often yield appropriate intermediate binding affinity to reaction intermediates during chemical reactions,³⁸³⁹ and the reactivity of chalcogen species in the Chevrel-phase is thought to play a significant role in hydrogenation and hydrodesulfurization reactions.^{15, 40} From the calculated DOS for the $\text{M}_2\text{Mo}_6\text{S}_8$ CPs, it appears that the materials should be antiferromagnetic, although this has not been experimentally validated to the best of our knowledge, and we further observe the evolution of a semiconducting band structure in the case of $\text{Fe}_2\text{Mo}_6\text{S}_8$ as evidenced by the observable DOS gap in **Fig. S3.9**.

Qualitative pre-edge analysis may be sufficient in discussing the degree of intercalation or de-intercalation of a cation species with fixed charge into the CP lattice, however 1st row transition metal cations convolute this analysis since their charge is not fixed, as can be seen in **Fig. S3.12** where the Fe K-edge jump for FeMo_6S_8 is noticeably blue shifted by more than 1eV compared to the edge jump for $\text{Fe}_2\text{Mo}_6\text{S}_8$, indicating an Fe species with a slightly higher average oxidation state in FeMo_6S_8 than in $\text{Fe}_2\text{Mo}_6\text{S}_8$. This phenomenon is also observed computationally, as can be seen in **Table S3.2** where the higher Bader charge for Fe in FeMo_6S_8 than in $\text{Fe}_2\text{Mo}_6\text{S}_8$ indicates that based upon the structure of the Fe-intercalated CPs, FeMo_6S_8 will possess a slightly more oxidized Fe species. This is also evident in the overlaid XPS spectra (**Fig 3.6**) highlighting the Fe 2p3 signal of FeMo_6S_8 compared to $\text{Fe}_2\text{Mo}_6\text{S}_8$ where a slight red-shift is observed in the onset of photoelectron ejection from ~706 eV to ~705 eV indicates a less oxidized Fe species in $\text{Fe}_2\text{Mo}_6\text{S}_8$. This change in oxidation may also explain similarities between the observed S pre-edge intensities for the two Fe-intercalated CPs, as it is apparent that increasing stoichiometry does not linearly increase electron donation in the case of transition metal intercalants. Had

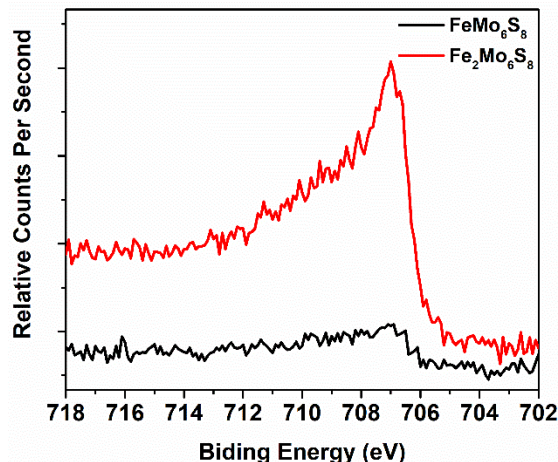


Figure 3.6. Fe 2p₃ XPS spectra overlaid for FeMo₆S₈ and Fe₂Mo₆S₈, illustrating a red-shift in the onset energy of photoelectron ejection from a moderately less oxidized Fe species in Fe₂Mo₆S₈.

stoichiometry scaled linearly with total electron donation into the cluster, one would expect significantly more masking of the S pre-edge feature owing to the increased donation of electron density in the case of Fe₂Mo₆S₈. As a result of the variable Fe oxidation state in FeMo₆S₈ and Fe₂Mo₆S₈, we are unable to directly correlate structural and electronic changes simply to increased or decreased stoichiometry of a metal cation. Instead, we restrict our comparison to Fe₂Mo₆S₈, Ni₂Mo₆S₈, and Cu₂Mo₆S₈ where intercalant stoichiometry is constant. In this case it was observed that despite a stark contrast in feature sharpness, the S pre-edge intensity as shown in **Fig. 3.5a** is roughly the same for all three CPs, as would be expected if similar electron density had been donated to the Mo₆S₈ cluster in each case.

3.2 Structure and Local Coordination

It should be noted that the rhombohedral CP crystal structure mentioned previously is unique to small cationic species within a certain stoichiometric range which is generally constrained between $y=0$ and $y=2$, or for large cation species with a single molar equivalent (e.g. K, Pb, La),¹¹ as larger metal cations such as Pb would form a crystal structure in which a single ternary atom sits directly in the center of the cavities;¹⁴ we are concerned only with the former case involving small cations in this study. Furthermore, in the case of Fe₂Mo₆S₈, clusters arrange in a triclinically distorted lattice with a primitive unit cell (space group P-1)

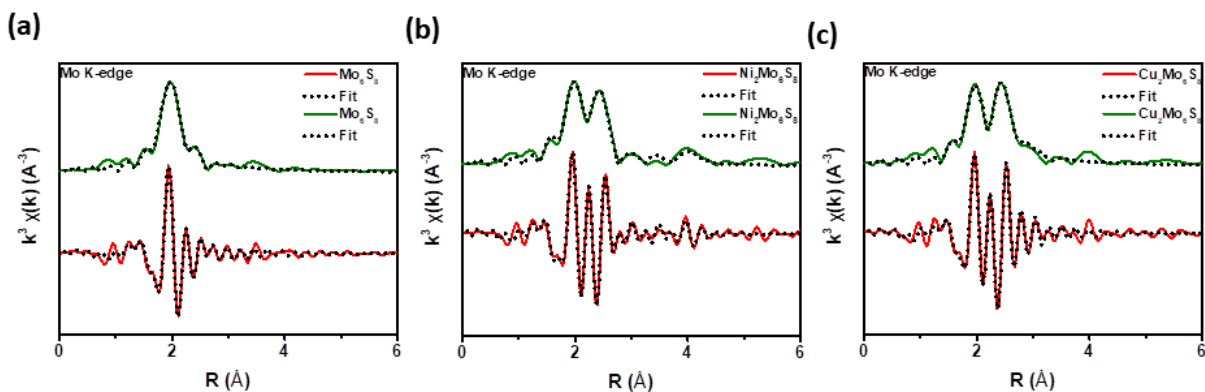


Figure 3.7. Processed EXAFS information plotted in magnitude (top line) and in real space (bottom line) for un-promoted Mo_6S_8 (a), $\text{Ni}_2\text{Mo}_6\text{S}_8$ (b), and $\text{Cu}_2\text{Mo}_6\text{S}_8$ (c), qualitatively indicating different local Mo coordination in the three CP structures. EXAFs fitting parameters can be found in Tables S3.3-S3.5.

as a result of the high Fe content.¹² As such, Fe cations occupy each of only two equivalent positions inside cavities between Mo_6S_8 units as shown in **Fig. S3.13**, hence no direct comparisons can be made between the structures of $\text{Fe}_2\text{Mo}_6\text{S}_8$, $\text{Ni}_2\text{Mo}_6\text{S}_8$, and $\text{Cu}_2\text{Mo}_6\text{S}_8$. Our discussion of local coordination is therefore limited to Mo_6S_8 , $\text{Ni}_2\text{Mo}_6\text{S}_8$, and $\text{Cu}_2\text{Mo}_6\text{S}_8$ —all of which share the same rhombohedral (R-3H) space group.

Fig. 3.7(a-c) shows the real magnitude of Fourier-transformed EXAFS data in R-space for Mo_6S_8 , $\text{Ni}_2\text{Mo}_6\text{S}_8$, and $\text{Cu}_2\text{Mo}_6\text{S}_8$, along with fitted lines calculated using appropriate ICSD structural information, while **Table 3.2** presents the results of these EXAFS fittings for Mo_6S_8 , $\text{Ni}_2\text{Mo}_6\text{S}_8$, and $\text{Cu}_2\text{Mo}_6\text{S}_8$, including scattering paths for absorber atoms, degeneracies of said scattering paths denoted by N in the table, as well as the effective length of the scattering interaction. Data plotted in k-space are also provided, shown in **Fig. S3.14**, where the oscillations shown are background-subtracted and k-weighted (normalized based on correction for systematic magnitude reduction at larger k values) oscillations in the raw XAS data. These results detail the local coordination of Mo in each of the three aforementioned CPs, and we observe changes

in bond distances when various metal intercalants are present in the lattice compared to the case for Mo_6S_8 where no intercalant is present.

From the Fourier-transformed data shown in **Fig. 3.7**, scattering paths were extracted that correspond to specific Mo-Mo and Mo-S bond distances. From this analysis, an interesting trend arises in intra-cluster Mo-Mo distances which can be visualized as **1** and **2** in **Fig. 3.8**. Average Mo-Mo bond lengths, as calculated by averaging the distance of the longer scattering interaction with the shorter scattering interaction for the binary, Ni_2 , and Cu_2 CPs are 2.76\AA , 2.72\AA , and 2.69\AA , respectively. In addition to the average Mo-Mo distance being larger for Ni_2 than Cu_2 CP, the longer Mo-Mo path for Ni_2 (2.76\AA) is longer than the longest Mo-Mo path for Cu_2 (2.73\AA). The same is true for the shorter paths for each structure (**Table 3.2**). This is in good agreement with the idea that, as electron density is donated to the Mo_6S_8 cluster and into orbitals with partially Mo-Mo bonding character, the Mo_6 center should contract. This trend may also explain the pre-edge sharpening in the S K-edge spectrum of $\text{Cu}_2\text{Mo}_6\text{S}_8$ because it appears (based on the degree of Mo_6 contraction) that slightly more electron density has filled the Mo_6S_8 cluster, thereby limiting previously accessible S $1s \rightarrow 3p$ transitions.

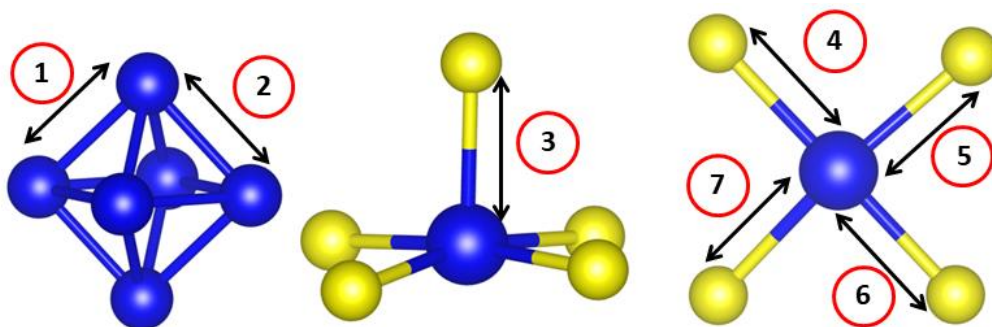


Figure 3.8. Relevant fragments of the CP structure including all scattering paths as discussed in **Table 3.2**, numbered as follows: intracuster Mo-Mo paths (**1**, **2**), axial Mo-S path (**3**), and intracuster Mo-S paths (**4-7**). Intuitively, in a distorted octahedron with 2 distinct Mo-Mo scattering paths for a given Mo absorber, each path (**1** and **2**) will have a degeneracy (N) of 2 which indicates that two of each such paths exist for each Mo absorber.

In addition to the contraction of Mo₆ centers in both metal-intercalated CPs for which EXAFS information was processed, the intercluster distance—that is, the distance between adjacent Mo₆S₈ units—was observed as a function of the axial Mo-S bond length represented by **3** in **Fig. 3.8**. This correlation is useful because axial Mo-S bonds form the linkages between adjacent clusters and are therefore a good approximation of intercluster distance. Rather unsurprisingly, it can be seen in **Table 3.2** that axial (intercluster) Mo-S distances increase drastically when metal intercalants are introduced into the cavities of a CP lattice. This is evidenced by the inter-cluster Mo-S bond distances in Mo₆S₈ of about 2.31Å compared to those for the Ni- intercalated and Cu- intercalated CPs which are 2.46Å and 2.51Å, respectively. This phenomenon is explained by lattice expansion that results upon incorporation of an intercalant species between clusters.^{41, 42}

Table 3.2. Results of EXAFS fittings sorted by structure, absorbing atom, and scattering atom.

Material	Absorber	Scatterer	N	R _{eff} (Å)
Mo ₆ S ₈	Mo	Mo	2	2.76
		S	1	2.31
			2	2.42
			1	2.58
			1	2.48
Ni ₂ Mo ₆ S ₈	Mo	Mo	2	2.76
			2	2.68
		S	1	2.32
			1	2.40
			3	2.46

Cu ₂ Mo ₆ S ₈	Mo	Mo	2	2.65
			2	2.73
		S	1	2.34
			2	2.42
			2	2.51

The last pertinent scattering path extracted from this fitted EXAFS information is between Mo centers and close-proximity face-sitting chalcogens. These scattering paths are enumerated as **4**, **5**, **6**, and **7** in **Fig. 3.8**, and essentially detail the size of the S₈ cubes that surround Mo₆ centers. While the coordination of Mo by these face-sitting chalcogens has been considered as pseudo-square planar, four distinct scattering paths are observable for Mo₆S₈, suggesting that local Mo coordination is noticeably distorted from this simplified model. Despite the non-uniformity in face-sitting Mo-S distances in the binary CP, only two distinct paths are observed for Ni₂Mo₆S₈ at 2.40Å and 2.32Å, as well as two paths for Cu₂Mo₆S₈ at 2.42Å and 2.34Å, indicating a slightly more symmetric pseudo square-planar coordination environment for the metal- intercalated CPs. Although slight distortions from perfect square-planar coordination have been observed, for the purpose of comparing Mo₆S₈, Ni₂Mo₆S₈, and Cu₂Mo₆S₈, scattering paths were addressed as though they are degenerate, and an average scattering distance was used as a result. In performing the analysis in this way, it becomes apparent that the presence or absence of metal cations inside the cavity has a more profound effect on intracuster Mo-S distances than does the identity of that cation. Without a full cavity, Mo₆S₈ average intracuster Mo-S distances—calculated by averaging all Mo-S scattering paths except the intercluster Mo-S path—are 2.48Å, compared to Ni- intercalated and Cu intercalated CPs where

average intracluster Mo-S distances shrink to 2.41Å and 2.42Å, respectively. There is little difference in the size of the S₈ cube in the cases of Ni₂Mo₆S₈ and Cu₂Mo₆S₈, although both are noticeably contracted relative to Mo₆S₈. It is possible that this discrepancy is the product of an empty intercluster cavity that allows more structural flexibility for Mo₆S₈ than for either of the intercalated CPs with partially occupied intercluster cavities.

3.3 Stability Analysis

Drop solution enthalpies and experimental enthalpies of formation from components ($\Delta H_{f(2)}$ and $\Delta H_{f(3)}$) and elements (ΔH_{el}) of all compounds are reported in **Table 3.3** and **Fig. 3.9**. All values have been calculated per gram atom. Experimental enthalpies of formation from components and elements were calculated at 298 K from the thermodynamic cycles shown in **Table S3.6** and **Table S3.7**, respectively. We note that because all ternary Chevrel phases have similar structures, their entropies can be assumed to be similar in magnitude, i.e. trends in thermodynamic stability are dictated by the enthalpies of formation.

Table 3.3. Drop solution enthalpies of the binary and ternary sulfides, enthalpies of formation calculated from reactions (3.1) and (3.2) and enthalpies of formation from elements.

Compound/element	ΔH_{ds} , kJ/gat	ΔH_{el} , kJ/gat	$\Delta H_{f(2)}$, kJ/gat	$\Delta H_{f(3)}$, kJ/gat
Fe ₂ Mo ₆ S ₈	-552.23 ± 2.63	-71.50 ± 3.18	-5.46 ± 3.78	-6.88 ± 2.70
FeMo ₆ S ₈	-562.93 ± 8.99	-77.27 ± 9.19	-6.83 ± 9.45	-8.34 ± 8.61
Ni ₂ Mo ₆ S ₈	-538.24 ± 2.91	-65.20 ± 3.49	0.93 ± 3.99	-0.48 ± 3.31
Cu ₂ Mo ₆ S ₈	-530.27 ± 4.29	-60.31 ± 4.66	6.35 ± 5.08	4.94 ± 4.64
Mo ₆ S ₈	-583.54 ± 3.10	-75.47 ± 3.66		
MoS ₂	-566.21 ± 2.27	-86.16 ± 2.22		
Mo	-698.77 ± 3.09(10) ^a			
Cu	-106.72 ± 2.38			
Fe	-376.83 ± 1.60			
Ni	-213.71 ± 1.97			
S	-629.18 ± 2.73			

^aNumber of experiments in (), uncertainty is two standard deviations of the mean.

The large errors originate from large heat effects obtained for all compounds and elements, and do not indicate a high uncertainty of the measurements.

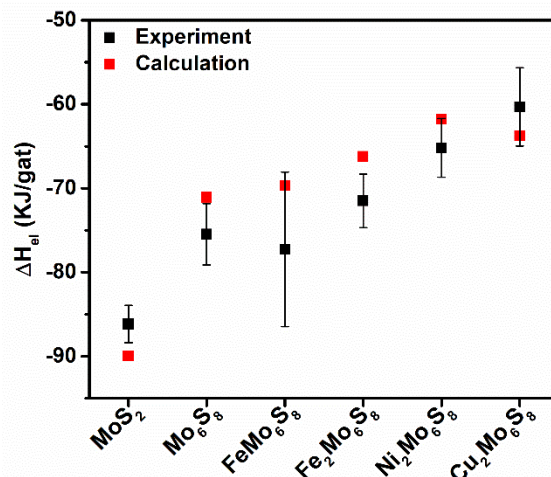
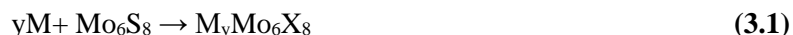
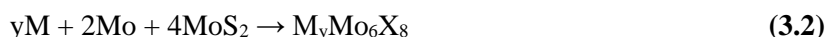


Figure 3.9. Experimental and computation enthalpies of formation from elements for $M_yMo_6S_8$ and MoS_2 , illustrating good agreement in the stability trend within the propagated error of the experimental enthalpy measurements.

Calorimetric measurements indicate that iron incorporation in the Mo_6S_8 structure promotes the thermodynamic stability of the ternary sulfides, i.e. the enthalpies of formation from pure elements, from sulfide components, and from Mo_6S_8 intercalation follows the trend: $FeMo_6S_8 < Fe_2Mo_6S_8 < Ni_2Mo_6S_8 < Cu_2Mo_6S_8$. The enthalpies of formation from elements are negative for all compounds (**Table 3.3**). The enthalpies of formation from the metal and the binary Mo_6S_8 according to the reaction:



are negative for both $Fe_2Mo_6S_8$ and $FeMo_6S_8$, while the values for $Ni_2Mo_6S_8$ and $Cu_2Mo_6S_8$ are slightly positive or approximately zero within the experimental error. The trend in the thermodynamic stability of the four CPs with respect to the cation incorporation in the Mo_6S_8 matrix can also be seen from the enthalpies of the synthesis reaction:



Because of the relatively large experimental error, the enthalpy of formation from the synthesis reaction (3.2) of $Cu_2Mo_6S_8$ can be considered close to zero, but probably still slightly positive.

The difference in the thermodynamic stability of these small-cation CPs can be attributed to the increased valency (i.e. increased charge donation) of the intercalated cations ($Fe > Cu > Ni$). Greater

electron donation (up to 4 e⁻ to Mo₆S₈) from cations with increased valency results in more pronounced contraction of the Mo₆ octahedron because the HOMO and LUMO of isolated Mo₆S₈ clusters are predominately Mo-Mo bonding in nature. EXAFS fitting, XRD, and DFT geometries indicate that the average Mo-Mo bond distance decreases (Fe₂Mo₆S₈ < Cu₂Mo₆S₈ < Ni₂Mo₆S₈) as cation valency increases (Fe > Cu > Ni). Furthermore, XAS analyses suggest that Fe is more oxidized in FeMo₆S₈ than in Fe₂Mo₆S₈ (**Fig. S3.12**), in good agreement with the calculated cation charge in each structure shown in **Table 3.4**. These results all indicate an increase in electron donation from the intercalated cation to the Mo₆S₈ cluster as valency increases, which stabilizes the structure.

ΔH_f values at 0 K computed using DFT (**Table S3.8**) match experimental results well, as illustrated in **Fig. 3.9**. Differences in the stability ordering between computation (0 K) and experiment (298 K) are attributed to temperature differences and the resolution of the different methods. DFT results indicate that the formation enthalpies of the studied ternary CPs decrease as the electropositivity and the stoichiometry of the intercalated cation increases (Fe₂Mo₆S₈ < FeMo₆S₈ < Cu₂Mo₆S₈ < Ni₂Mo₆S₈). This increase in electropositivity, and a corresponding increase in valency, leads to an increase in the Mo₆ cluster charge density which is observable by a decreasing average Mo oxidation state (2.00, 1.90, 1.77 for M_y = Ni₂, Cu₂, Fe₂, respectively), as shown in **Table 3.4**. The average Mo oxidation state for FeMo₆S₈ (2.00) is greater

Table 3.4. Computational bond distances, component charges, integrated COOP, and Madelung Energies for M_yMo₆S₈ (M = Fe, Ni, Cu; y = 0-2) and MoS₂.

Compound	Avg. Mo-Mo dist. (Å)	Avg. Mo-S dist. (Å)	Mo Charge ^a	S Charge ^a	M _y Cation Charge ^a	Sigma (eV) ^b	Madelung Energy (eV) ^b
Mo ₆ S ₈	2.77	2.43	+2.67	-2.00		0.98	-0.33
Fe ₂ Mo ₆ S ₈	2.67	2.47	+1.77	-2.00	+2.70	0.74	-0.56
FeMo ₆ S ₈	2.68	2.46	+2.00	-2.00	+3.98	0.81	-0.54
Cu ₂ Mo ₆ S ₈	2.69	2.46	+1.90	-2.00	+2.31	0.77	-0.51
Ni ₂ Mo ₆ S ₈	2.71	2.45	+2.00	-2.00	+1.96	0.78	-0.41
MoS ₂		2.40	+4.00	-2.00		0.95	-0.43

^aCharges here were normalized such that the oxidation state of sulfur is -2.

^bSigma and Madelung energies should not be directly compared (i.e. the values should not be combined to provide a quantitative descriptor for stability).

than for Fe₂Mo₆S₈ (1.77), matching the computational trend in stability. However, the oxidation state of Fe in FeMo₆S₈ (3.98) is greater than in Fe₂Mo₆S₈ (2.70 average) which indicates that the first Fe intercalated

into the Mo_6S_8 framework transfers more electron density to the Mo_6 cluster, and therefore yields a greater decrease in ΔH_f relative to the second Fe. This matches with the $\sim 1\text{eV}$ blue-shifted Fe K-edge XANES for FeMo_6S_8 versus $\text{Fe}_2\text{Mo}_6\text{S}_8$ in **Fig. S3.12**. Thus, both the electropositivity and the stoichiometry of the intercalated cation affect the electron donation to the Mo_6S_8 cluster and the resultant stabilizing contribution to the ternary CP.

It is apparent that the mechanism for ternary CP stabilization results from competing ionic and covalent contributions. To that end, the Madelung energy of a material is a measure of the interatomic electrostatic interactions (i.e. the ionicity). **Table 3.4** shows the negative Madelung energies of the studied materials, indicating a greater overall ionicity as electropositivity and stoichiometry of the intercalated cations increase ($\text{Fe}_2 > \text{Fe} > \text{Cu}_2 > \text{Ni}_2$). For the ternary CPs, a greater ionicity results in a lower computational ΔH_f . Similarly, the inherent stability of MoS_2 over Mo_6S_8 can be explained by the greater ionicity of MoS_2 . However, the Madelung energy alone would suggest greater ionicity, and thus stability, of $\text{Ni}_2\text{Mo}_6\text{S}_8$ over Mo_6S_8 and is therefore an incomplete descriptor for stability. Thus, covalent bonding must also be considered to provide a more complete understanding of material stability.

Fig. 3.10 shows the calculated electronic density of states (DOS) and COOP between Mo and S for the studied materials. Positive and negative COOP values indicate covalent bonding and antibonding states, respectively. The net covalent bonding (i.e. covalency) between Mo and S is indicated by Σ . For the CPs, Mo_6S_8 exhibits the greatest Σ , consistent with the shorter Mo-S bond distance in this material. Intercalating cations into the Mo_6S_8 framework increases the charge density on Mo, thereby decreasing the Mo-S bond strength and elongating the Mo-S bond, which leads to destabilization of the CP structure. As the ionic radii decrease ($0.92, 0.87, 0.83 \text{ \AA}$ for $\text{Fe}^{2+}, \text{Cu}^{2+}$ and Ni^{2+} , respectively) and stoichiometry of the intercalant cation increase, a greater decrease in Σ is observed computationally. For all the ternary CPs except $\text{Ni}_2\text{Mo}_6\text{S}_8$, the stabilization from an increase in ionicity is greater than the destabilization due to the loss of covalency at 0 K. Although all the materials have filled antibonding states, $\text{Fe}_2\text{Mo}_6\text{S}_8$ and $\text{Cu}_2\text{Mo}_6\text{S}_8$ have the lowest Σ values due to a greater filling of Mo-S antibonding states, which corresponds to electron donation from the

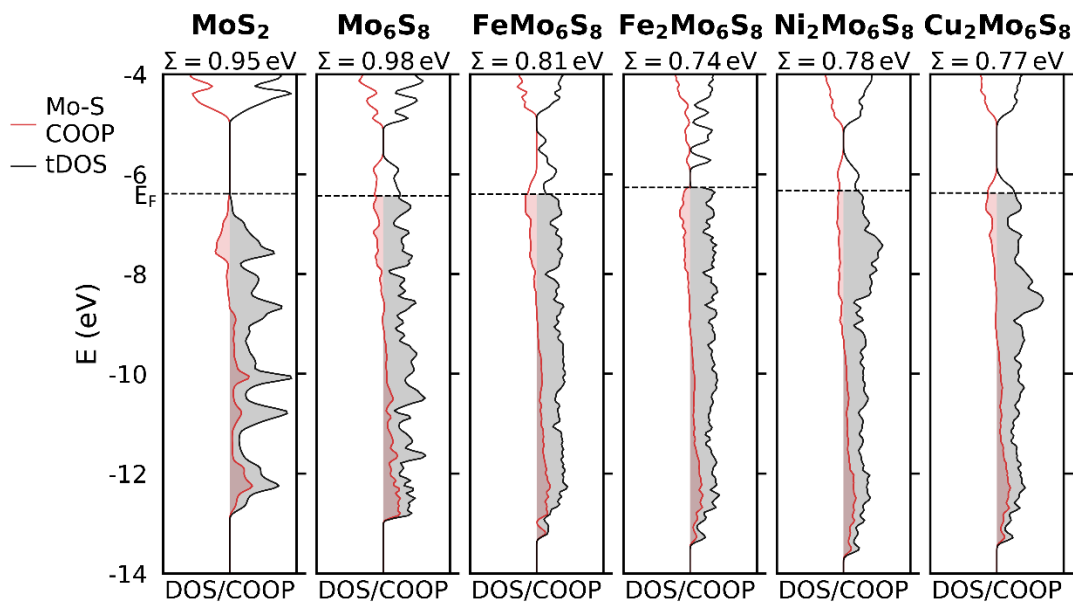


Figure 3.10. Total density of states (DOS, black line) and crystal orbital overlap population (COOP, red line) of Mo and S atoms for the five Chevrel structures and MoS₂. Positive COOP values indicate covalent bonding states and negative values indicate covalent anti-bonding states. Σ is the energy integrated COOP from -14 eV to the Fermi level (dashed line) which indicates the net covalent bonding between Mo and S in these structures.

intercalants to the Mo₆S₈ cluster that exceeds 4 electrons. The large Σ value of MoS₂ combined with its moderate Madelung energy explains the low computational ΔH_f of MoS₂ and the positive decomposition enthalpy to MoS₂ ($\Delta H_{f(3)}$) for the ternary CPs at 0 K which also indicates that elevated temperatures stabilize ternary CPs against MoS₂, in good agreement with experimental observations. No large variation in sulfur charge is predicted for any of the studied materials, and the innate instability of Mo₆S₈ is instead attributed to its relatively low ionicity without a ternary intercalant within cavities. This increase in ionicity and reduction of Mo-S covalency upon intercalation of a metallic species is represented in **Figure 3.11**.

Calorimetric analysis indicates that at 298 K, Fe₂Mo₆S₈ is metastable with respect to FeMo₆S₈. This also agrees well with Mo-Mo bond distances observed in X-ray diffraction analysis where average Mo-Mo distances in FeMo₆S₈ are approximately 2.679 Å as compared to 2.682 Å in Fe₂Mo₆S₈. This destabilization of Fe₂Mo₆S₈ may be the result of a slight degree of triclinic distortion in the Fe₂Mo₆S₈ structure where Mo₆S₈ cluster units are tilted with respect to the original rhombohedral axis (**Fig. 3.12**), thereby allowing more structural flexibility and slight deformation of the Mo₆ octahedral symmetry which is observed at 298

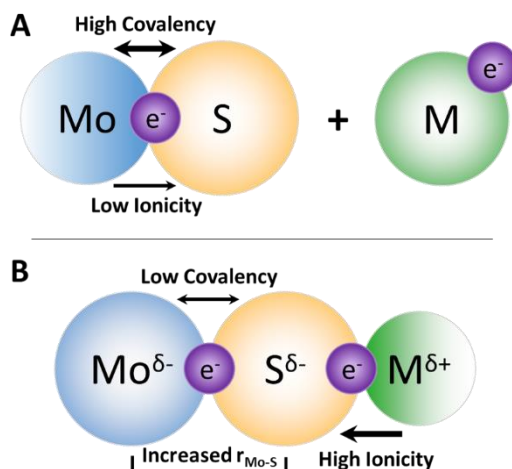


Figure 3.11. Reductive effects of M species intercalation into Mo_6S_8 decreases the covalency of the Mo-S interactions observed in binary Mo_6S_8 , and increases the relative charge on Mo and S to yield a net increase in ionic bonding character within the structure.

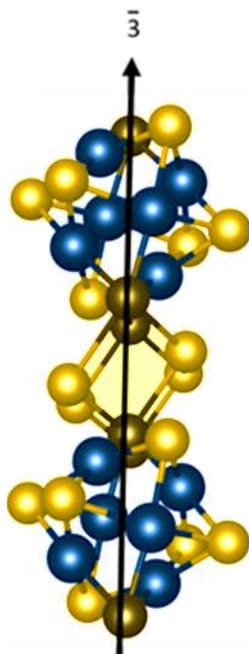


Figure 3.12. Orientation of linked Chevrel-Phase clusters showing the rhombohedral axis along which they possess three-fold rotation symmetry, and away from which clusters tilt in triclinic $\text{Fe}_2\text{Mo}_6\text{S}_8$.

K but not at 0 K. This also matches with our computational results that indicate greater filling of antibonding Mo-S states in $\text{Fe}_2\text{Mo}_6\text{S}_8$, which decreases covalency and destabilizes the structure. A similar destabilization is observed for MoS_2 where DFT predicts that this material is more stable than Mo_6S_8 and the ternary CPs at 0 K, in good agreement with published literature.^{6, 43-44} However, calorimetry indicates that Mo_6S_8 is

slightly more stable than MoS_2 at 298 K, although this is within the experimental error. The small formation enthalpy difference between these materials explains why Mo_6S_8 cannot be directly synthesized at 298 K but is persistently metastable at this temperature. Additionally, the propensity of Mo_6S_8 to decompose to Mo and MoS_2 at high temperatures is consistent with the observation that an intercalant such as Cu is required to stabilize the Mo_6S_8 structure at high temperature, despite $\text{Cu}_2\text{Mo}_6\text{S}_8$ having a slightly more positive formation enthalpy than Mo_6S_8 at 298K.

Conclusions

Comparative XAS and computational analyses for a range of 1st row transition metal-intercalated Chevrel-phase sulfides with unique stoichiometries and unique intercalant d-electron counts were completed; their electronic structure and local Mo coordination under varying degrees of transition metal promotion were also discussed. We observe potential tunability of Mo and S local structure through incorporation of metal intercalant species, and report the first theoretical evidence that Fe-intercalated CP species may be semiconducting—a property that can naturally facilitate material implementation in photocatalytic systems. Structural tunability of the Mo_6S_8 framework was observed after detailed EXAFS fitting, and we confirm here that the electronic properties of CP structures are largely based upon the interactions between metal intercalant and chalcogenide. Perhaps most importantly, the local coordination of Mo in a CP can be modulated such that it assumes a 5-coordinate pseudo square-pyramidal geometry, or that it assumes an axially elongated, 4-coordinate pseudo square-planar geometry—both scenarios depend on the presence and electronic configuration of the intercalated species. In addition, the thermodynamic stability of a series of binary and ternary CP sulfides was rigorously investigated, unraveling an interplay between the ionicity and covalency of the cluster frameworks that can be approximated by their Madelung energies and crystal orbital overlap populations, respectively, in order to accurately predict thermodynamic stability in good agreement with experimental calorimetry. These findings will pave the way for the development of a robust, system-specific mechanism for predicting composition-dependent stability in complex multinary

chalcogenides like CPs, thereby enabling a closed-loop approach where material synthesis is accelerated by experimentally verified computation.

Supporting Information

Core shell electron ejection diagram, synthesis reactor schematic, PXRD patterns, raw XAS spectra, spin-polarized DOS, k-space processed EXAFS, Pawley refinement results, Bader charge analysis results, XAS fitting parameter tables, thermochemical cycles, tabulated computational data.

Acknowledgments

I would like to thank Chevron Corporation for a graduate fellowship through the UC Davis Institute of Transportation, as well as the University of California, Davis for start-up funding for this work.

Use of the Stanford Synchrotron Radiation Lightsource, SLAC National Accelerator Laboratory, is supported by the U.S. Department of Energy, Office of Science, Office of Basic Energy Sciences under Contract No. DE-AC02-76SF00515. The SSRL Structural Molecular Biology Program is supported by the DOE Office of Biological and Environmental Research, and by the National Institutes of Health, National Institute of General Medical Sciences (including P41GM103393). The contents of this publication are solely the responsibility of the authors and do not necessarily represent the official views of NIGMS of NIH.

I would like to acknowledge Dr. Erik Nelson and Dr. Ryan Davis at SLAC National Accelerator lab in Palo Alto, CA for their insightful discussions regarding XAS experiments and results.

Publication Information, Copyright, and Author Acknowledgements

This chapter forms the basis for the following publications:

Perryman, J. T.; Hyler, F. P.; Ortiz-Rodríguez, J. C.; Mehta, A.; Kulkarni, A. R.; Velázquez, J. M., X-ray absorption spectroscopy study of the electronic structure and local coordination of 1st row transition metal-promoted Chevrel-phase sulfides. *Journal of Coordination Chemistry* **2019**, 72 (8), 1322-1335.

Lilova, K.*; Perryman, J. T.*; Singstock, N. R.*; Abramchuck, M.; Subramani, T.; Lam, A.; Yoo, R.; Ortiz-Rodríguez, J. C.; Musgrave, C. B.; Navrotsky, A.; Velázquez, J. M., A Synergistic Approach to Unraveling the Thermodynamic Stability of Binary and Ternary Chevrel Phase Sulfides. *Chemistry of Materials* **2020**, 32 (16), 7044-7051.

*- Joint first authors contributed equally to the manuscript

Joseph T Perryman performed material synthesis, PXRD, SEM, EDX, XPS, and XAS. JOR performed material synthesis. FPH and AM performed XAS. ARK performed DFT for DOS. NRS performed DFT for calorimetry. KL, MA, TS, AL, and RY performed calorimetry.

This chapter was adapted with permission from Perryman, J. T.; Hyler, F. P.; Ortiz-Rodríguez, J. C.; Mehta, A.; Kulkarni, A. R.; Velázquez, J. M., X-ray absorption spectroscopy study of the electronic structure and local coordination of 1st row transition metal-promoted Chevrel-phase sulfides. *Journal of Coordination Chemistry* **2019**, 72 (8), 1322-1335, © Copyright 2019 Taylor and Francis, as well as from Lilova, K.*; Perryman, J. T.*; Singstock, N. R.*; Abramchuck, M.; Subramani, T.; Lam, A.; Yoo, R.; Ortiz-Rodríguez, J. C.; Musgrave, C. B.; Navrotsky, A.; Velázquez, J. M., A Synergistic Approach to Unraveling the Thermodynamic Stability of Binary and Ternary Chevrel Phase Sulfides. *Chemistry of Materials* **2020**, 32 (16), 7044-7051, © Copyright 2020 American Chemical Society.

References

1. S.J. Davis, N.S. Lewis, M. Shaner, S. Aggarwal, D. Arent, I.L. Azevedo, S.M. Benson, T. Bradley, J. Brouwer, Y.-M. Chiang, C.T.M. Clack, A. Cohen, S. Doig, J. Edmonds, P. Fennell, C.B. Field, B. Hannegan, B.-M. Hodge, M.I. Hoffert, E. Ingersoll, P. Jaramillo, K.S. Lackner, K.J. Mach, M. Mastrandrea, J. Ogden, P.F. Peterson, D.L. Sanchez, D. Sperling, J. Stagner, J.E. Trancik, C.-J. Yang, K. Caldeira, *Science*, **360** (2018) 6396.
2. N.S. Lewis, D.G. Nocera, *Proceedings of the National Academy of Sciences*, **103** (2006) 15729.
3. J.H. Montoya, L.C. Seitz, P. Chakthranont, A. Vojvodic, T.F. Jaramillo, J.K. Nørskov, *Nature Materials*, **16** (2016) 70.
4. P. Canepa, G. Sai Gautam, D.C. Hannah, R. Malik, M. Liu, K.G. Gallagher, K.A. Persson, G. Ceder, *Chemical Reviews*, **117** (2017) 4287-4341.
5. L. Geng, J.P. Scheifers, J. Zhang, K.N. Bozhilov, B.P.T. Fokwa, J. Guo, *Chemistry of Materials*, **30** (2018) 8420-8425.
6. E. Lancry, E. Levi, Y. Gofer, M. Levi, G. Salitra, D. Aurbach, *Chemistry of Materials*, **16** (2004) 2832-2838.
7. J. Jun, G. Minrui, S. Wenchao, Y. Yushan, *Angewandte Chemie International Edition*, **55** (2016) 15240-15245.
8. E. Levi, Y. Gofer, Y. Vestfreed, E. Lancry, D. Aurbach, *Chemistry of Materials*, **14** (2002) 2767-2773.
9. P. Liu, Y. Choi, Y. Yang, M.G. White, *J Phys Chem A*, 114 (2010) 3888-3895.
10. R. Chevrel, M. Hirrien, M. Sergent, *Polyhedron*, **5** (1986) 87-94.
11. E. Levi, D. Aurbach, *Chemistry of Materials*, **22** (2010) 3678-3692.

12. R. Chevrel and M. Sergent, *Superconductivity in Ternary Compounds I*, Springer-Verlag Berlin Heidelberg, 1982.
13. S. Kondo, K. Takada, Y. Yamamura, H. Gyoten, S. Yoshida, *Solid State Ionics*, **57** (1992) 147-151.
14. Ø. Fischer, *Applied physics*, **16** (1978) 1-28.
15. C. Liu, P. Liu, *ACS Catalysis*, **5** (2015) 1004-1012.
16. N. Alonso-Vante, B. Schubert, H. Tributsch, *Materials Chemistry and Physics*, **22** (1989) 281-307.
17. T. Hughbanks, R. Hoffmann, *Journal of the American Chemical Society*, **105** (1983) 1150-1162.
18. L.F. Wan, J. Wright, B.R. Perdue, T.T. Fister, S. Kim, C.A. Appleby, D. Prendergast, *Physical Chemistry Chemical Physics*, **18** (2016) 17326-17329.
19. F. Thole, L.F. Wan, D. Prendergast, *Physical Chemistry Chemical Physics*, **17** (2015) 22548-22551.
20. K. Yvon, A. Paoli, *Solid State Communications*, **24** (1977) 41-45.
21. P.A. O'Day, J.J. Rehr, S.I. Zabinsky, G.E. Brown, Jr., *Journal of the American Chemical Society*, **116** (1994) 2938-2949.
22. S.J. Hilsenbeck, R.E. McCarley, A.I. Goldman, G.L. Schrader, *Chemistry of Materials*, **10** (1998) 125-134.
23. P.P. Vaishnava, C.W. Kimball, J.L. Matykiewicz, F.Y. Fradin, G.K. Shenoy, P.A. Montano, *Physical Review B*, **34** (1986) 4599-4603.
24. D.A. Holtman, B.K. Teo, J.M. Tarascon, B.A. Averill, *Inorganic Chemistry*, **26** (1987) 1669-1674.
25. B. Ravel and M. Newville, *Journal of Synchrotron Radiation*, **12** (2005) 537-541.
26. C.J. Patridge, C. Jaye, T.A. Abtew, B. Ravel, D.A. Fischer, A.C. Marschilok, P. Zhang, K.J. Takeuchi, E.S. Takeuchi, S. Banerjee, *The Journal of Physical Chemistry C*, **115** (2011) 14437-14447.
27. J.M. Velázquez, C. Jaye, D.A. Fischer, S. Banerjee, *The Journal of Physical Chemistry C*, **113** (2009) 7639-7645.
28. F. Murgia, P. Antitomaso, L. Stievano, L. Monconduit, R. Berthelot, *Journal of Solid State Chemistry*, **242** (2016) 151-154.
29. Inorganic Crystal Structure Database, *FIZ Karlsruhe*, www.iscd.fiz-karlsruhe.de
30. A. Navrotsky, *Physics and Chemistry of Minerals*, **3**, (1997) 222-241.
31. A. Navrotsky, *Physics and Chemistry of Minerals*, **1**, (1977) 89-104.
32. A. Navrotsky, *Journal of the American Ceramic Society*, **11**, (2014) 3349-3359
33. G. Kresse and J. Furthmüller, *Physical Review B*, **16**, (1996) 11169-11186.

34. J. Sun, A. Ruzsinszky and J. P. Perdew, *Physical Review Letters*, **3**, (2015) 036402.
35. A. T. Manz and N. G. Limas, *RSC Advances*, **53**, (2016) 47771-47801.
36. S. Maintz, V. L. Deringer, A. L. Tchougreef and R. Dronskowski, *Journal of Computational Chemistry*, **11**, (2016) 1030-1035.
37. K. Getty, M.U. Delgado-Jaime, P. Kennepohl, *Inorganica chimica acta*, **361** (2008) 1059-1059.
38. B. Hammer, J.K. Nørskov, *Surface Science*, **343** (1995) 211-220.
39. A. Nilsson, L. Pettersson, B. Hammer, T. Bligaard, C. H. Christensen, J. K. Nørskov, *The electronic structure effect in heterogeneous catalysis*, 2005.
40. K.F. McCarty, G.L. Schrader, *Industrial & Engineering Chemistry Product Research and Development*, **23** (1984) 519-524.
41. J. Xu, Y. Dou, Z. Wei, J. Ma, Y. Deng, Y. Li, H. Liu, S. Dou, *Advanced Science*, **4** (2017) 1700146.
42. M.S. Whittingham, A.H. Thompson, *The Journal of Chemical Physics*, **62** (1975) 1588-1588.
43. R. Chevrel, M. Sergent, J. Prigent, *Materials Research Bulletin*, **9** (1974) 1487-1498.
44. M. W. Chase, NIST-JANAF Thermochemical Tables. NIST Chemistry WebBook, SRD 69, 1998; Vol. J. Phys. Chem. Ref. Data, Monograph 9.

Supporting Information

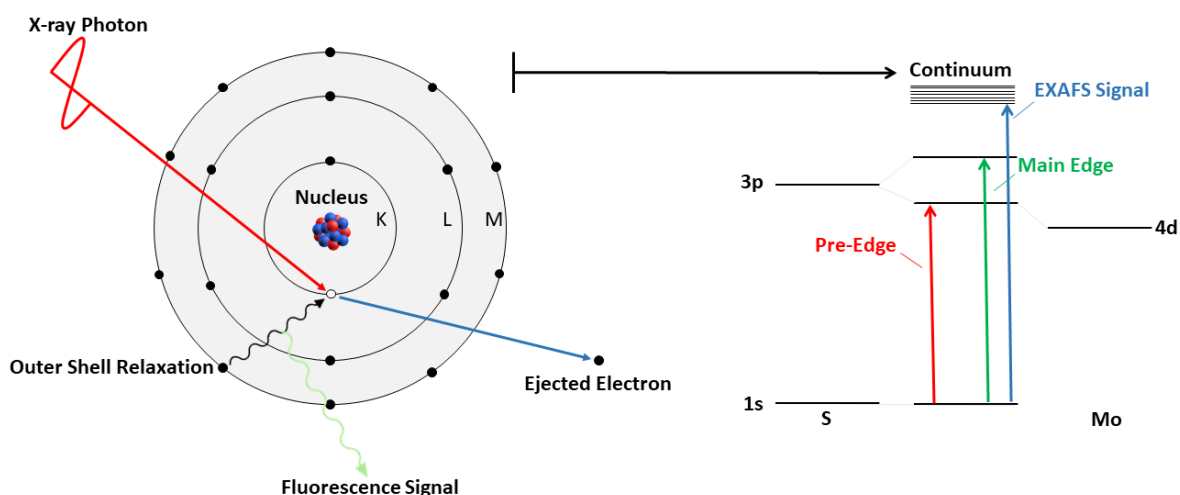


Figure S3.1. Graphic representation of the principle of core-shell electron ejection, followed by relaxation of outer-shell electrons to yield fluorescent radiation. Fluorescence signal was acquired in all of the experiments presented in this work. The diagram to the right represents a generalized view of S K-shell ejection mechanisms that would result in the evolution of a pre-edge feature (Laporte forbidden), as well as the excitations that result in the main edge (Laporte allowed). States higher in energy than the LUMO positions constitute the continuum.

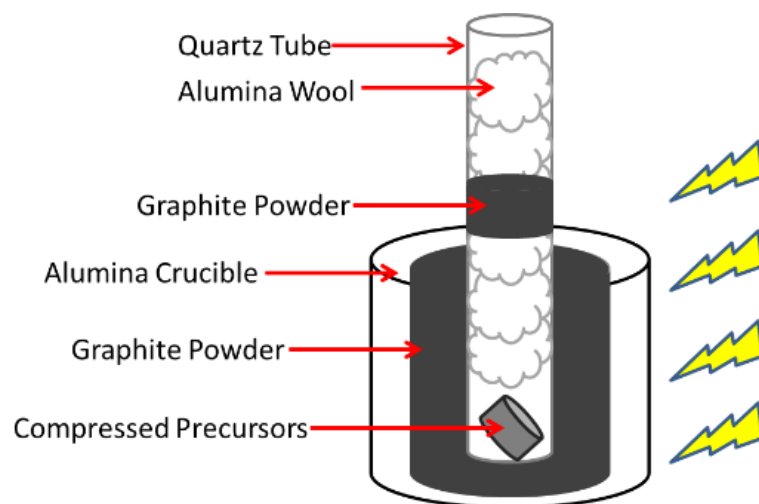


Figure S3.2. Schematic illustrating the experimental set-up adapted from ref. 28 implemented for microwave-assisted solid-state synthesis of Chevrel-phase materials.

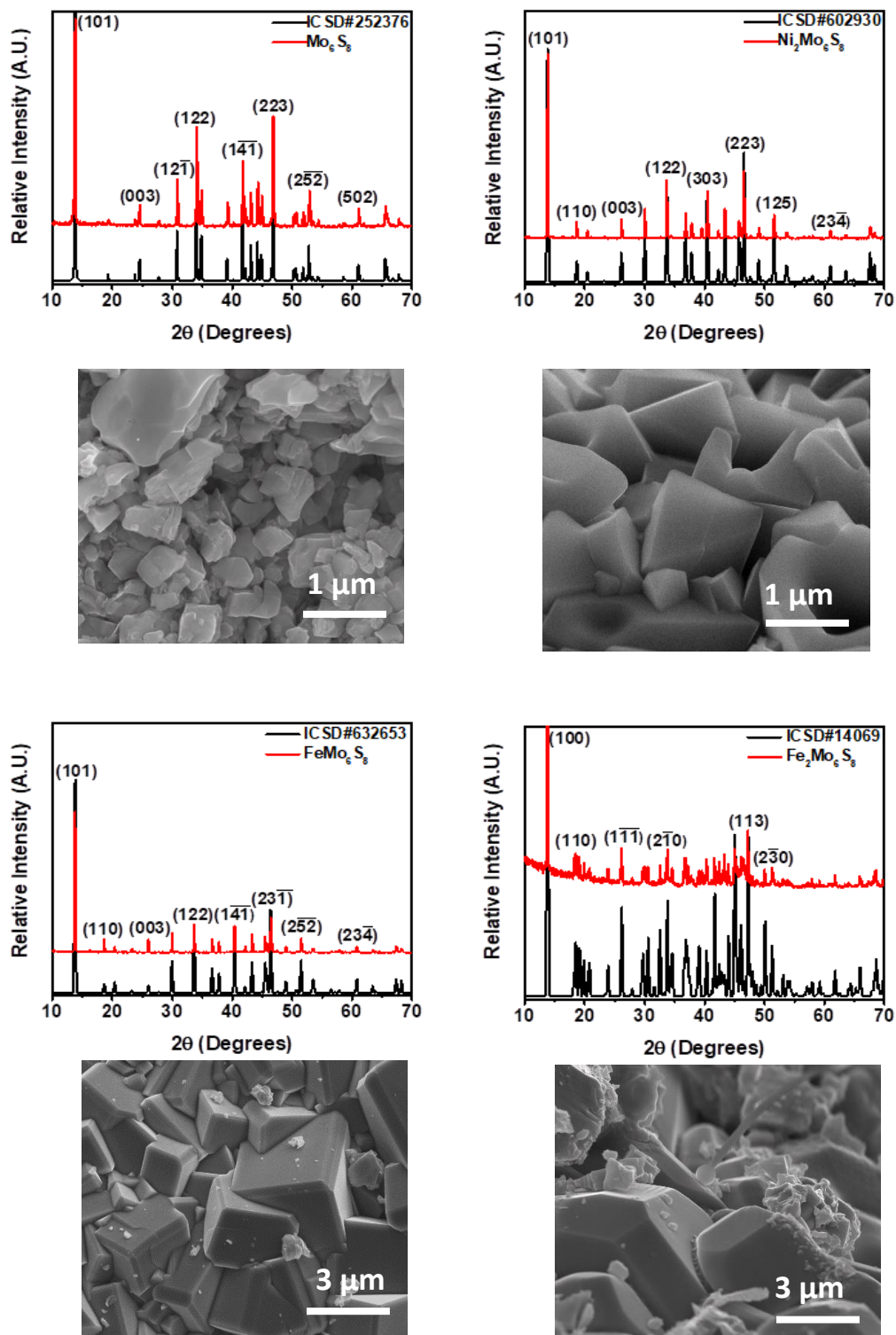


Figure S3.3. Powder XRD patterns for synthesized $M_x\text{Mo}_6\text{S}_8$ ($M = \text{Fe}, \text{Ni}; x = 0-2$) with major peaks indexed, showing ICSD reference patterns and collection codes, along with corresponding SEM images listed immediately below each pattern overlay.

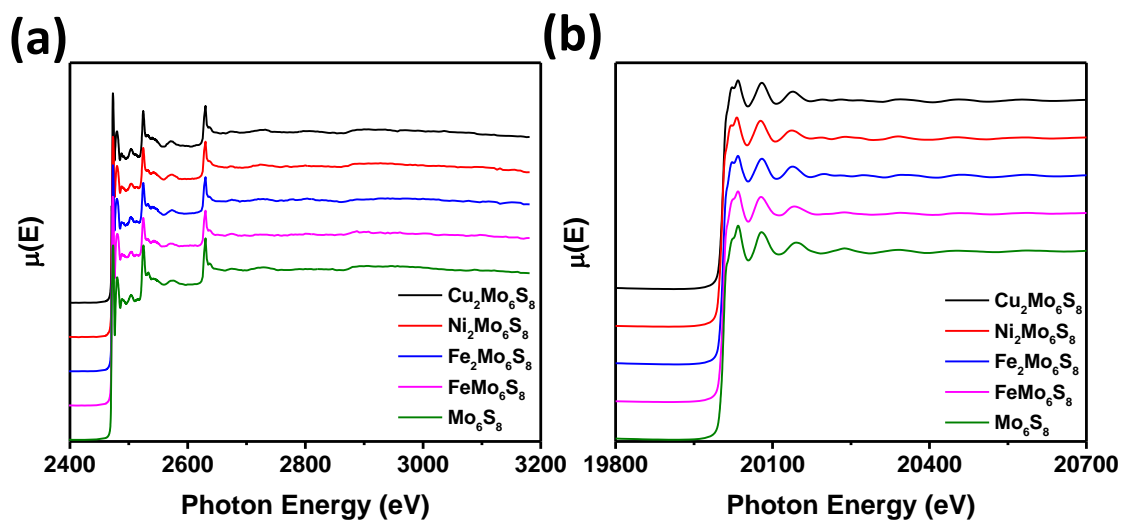


Figure S3.4. Overlaid raw XAS spectra showing raw fluorescence signal starting at the S K-edge (a) and the Mo K-edge (b) for all CPs studied.

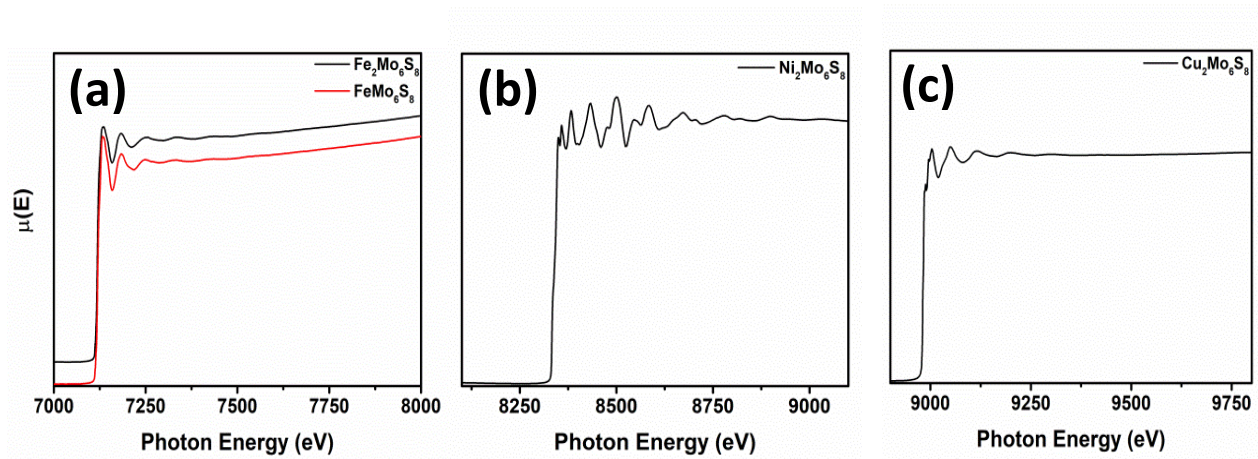


Figure S3.5. Raw XAS spectra for all metal intercalant K-edges, including raw fluorescence signal for the Fe K-edge in $\text{Fe}_2\text{Mo}_6\text{S}_8$ (black) and FeMo_6S_8 (red) (a), for the Ni K-edge in $\text{Ni}_2\text{Mo}_6\text{S}_8$ (b), and for the Cu K-edge in $\text{Cu}_2\text{Mo}_6\text{S}_8$ (c).

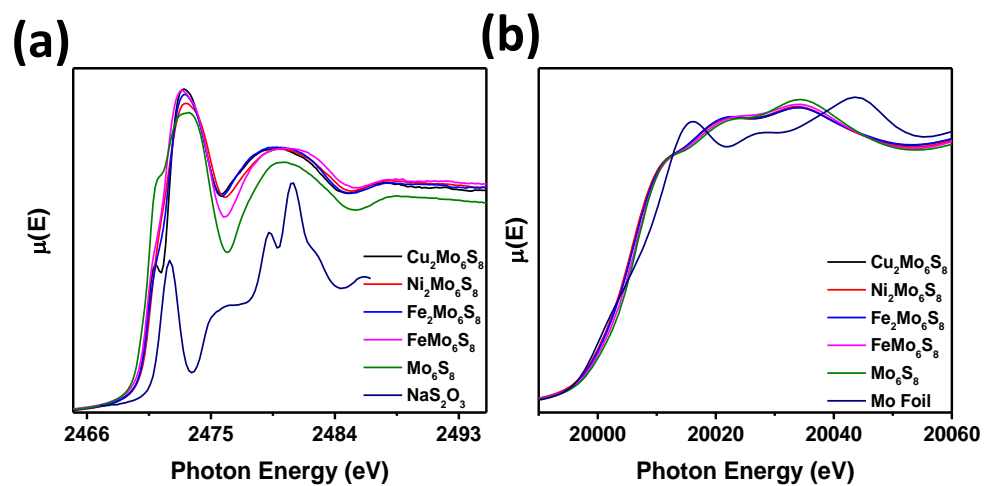


Figure S3.6. Zoomed and overlaid XAS spectra showing fluorescence signal for all Chevrel-phase S (a) and Mo (b) K-edge XANES regions.

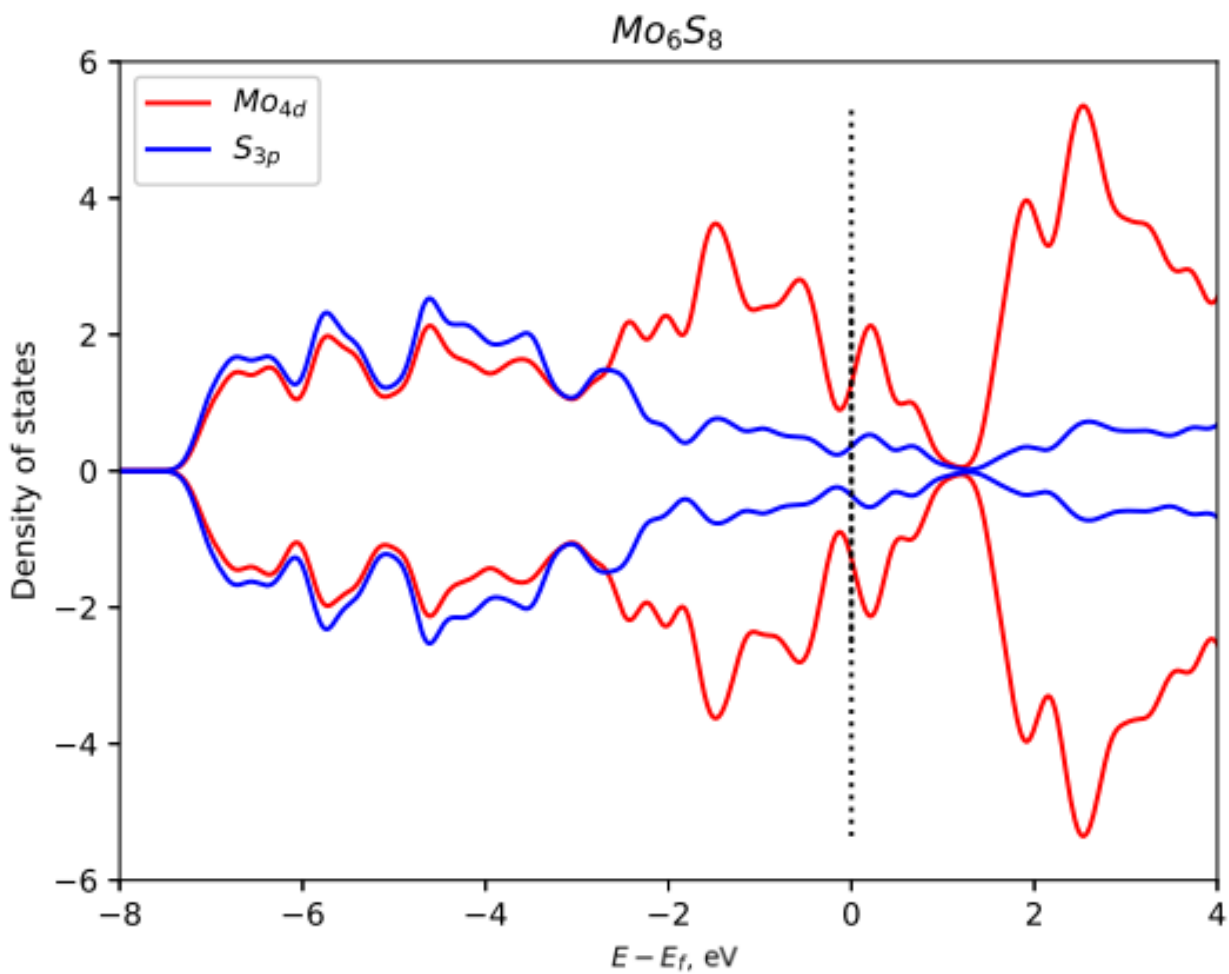


Figure S3.7. Spin-polarized densities of state calculated for Mo and S in Mo_6S_8 .

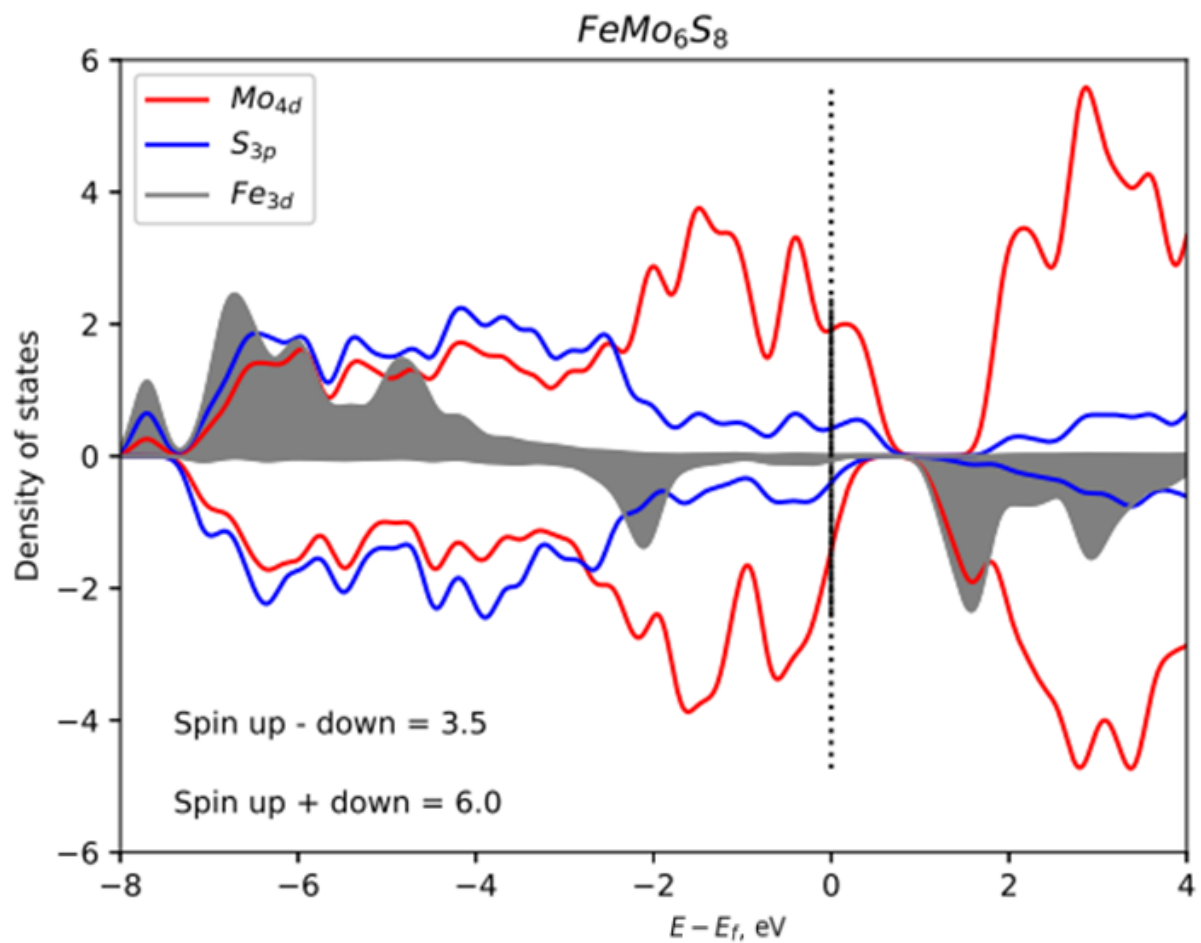


Figure S3.8. Spin-polarized densities of state calculated for Fe, Mo, and S in FeMo_6S_8 , indicative of a d^6 Fe(II) iron species.

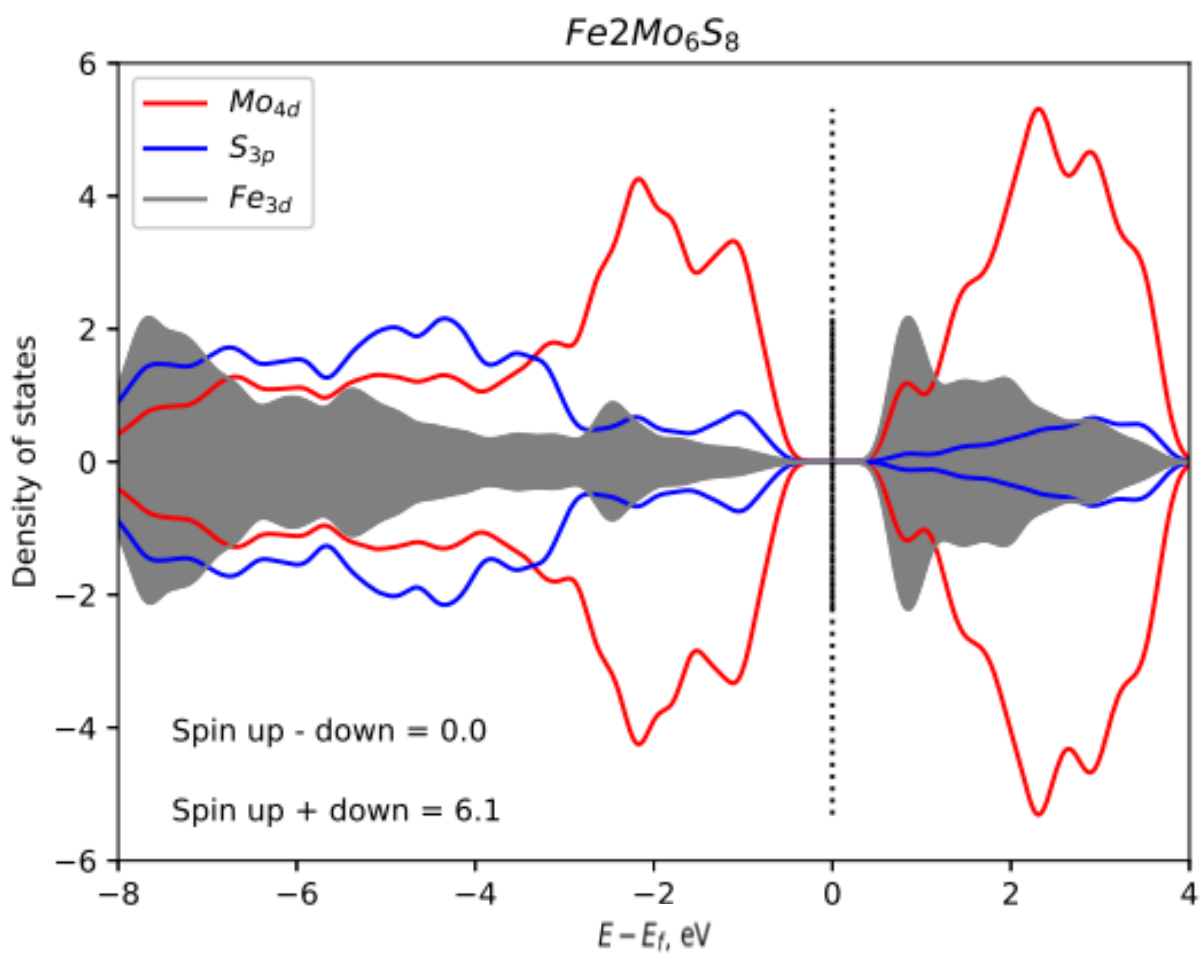


Figure S3.9. Spin-polarized densities of state calculated for $Fe_2Mo_6S_8$, indicative that the triclinic Fe-promoted CP may exhibit semiconducting properties.

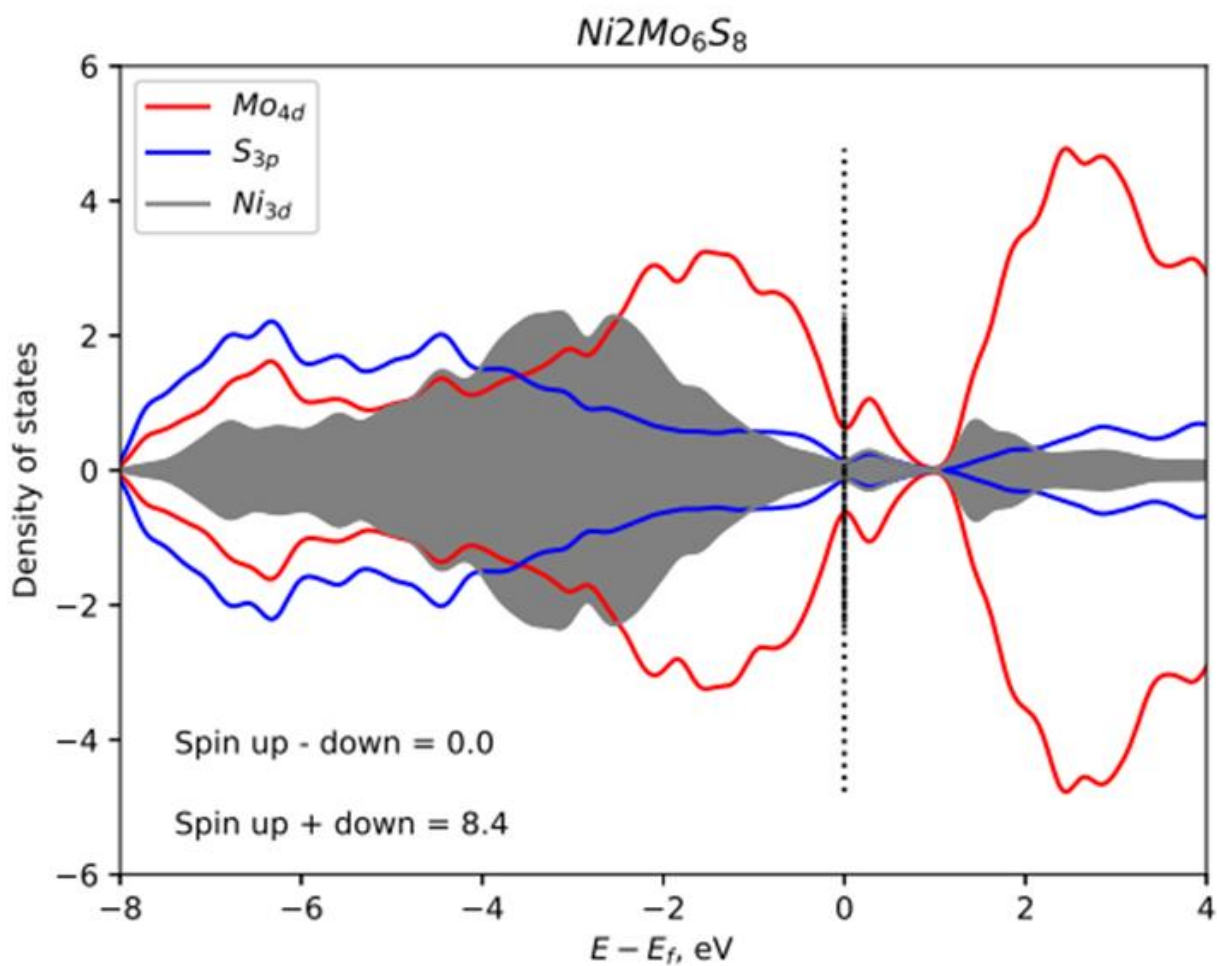


Figure S3.10. Spin-polarized densities of state calculated for Ni, Mo, and S in $Ni_2Mo_6S_8$, indicative of a d8 Ni(II) iron species.

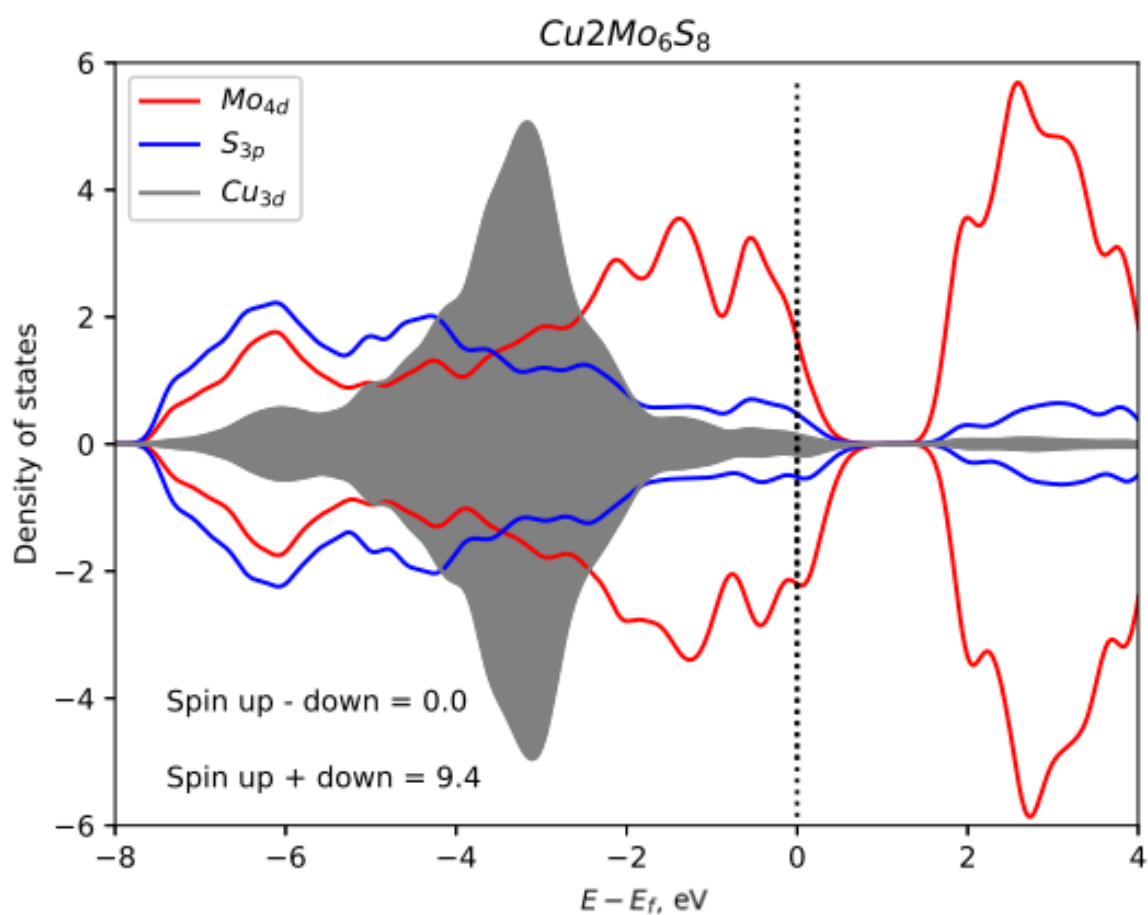


Figure S3.11. Spin-polarized densities of state calculated for Cu, Mo, and S in $\text{Cu}_2\text{Mo}_6\text{S}_8$, indicative of a d10 Cu(I) species.

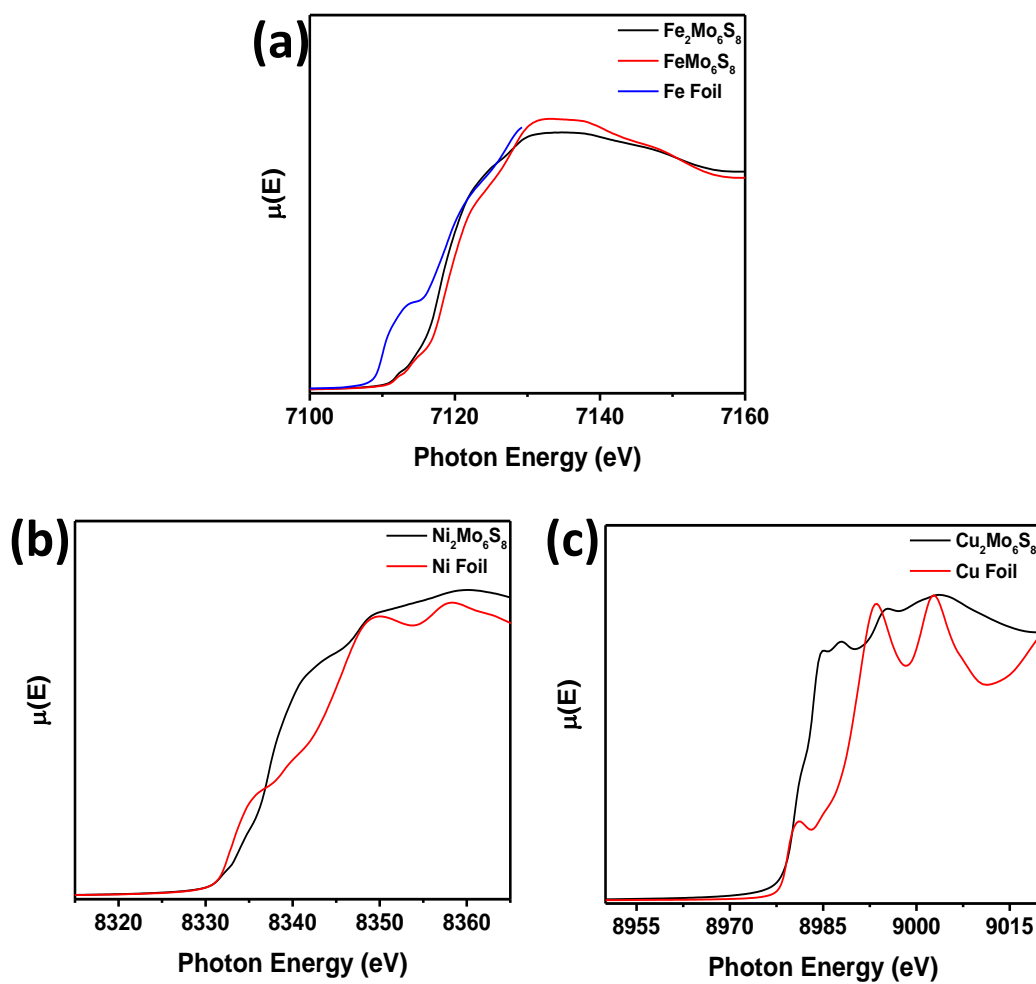


Figure S3.12. Zoomed and overlaid Chevrel-phase and reference foil XAS spectra, showing fluorescence signal for metal intercalant K-edges that include Fe (a), Ni (b), and Cu (c).

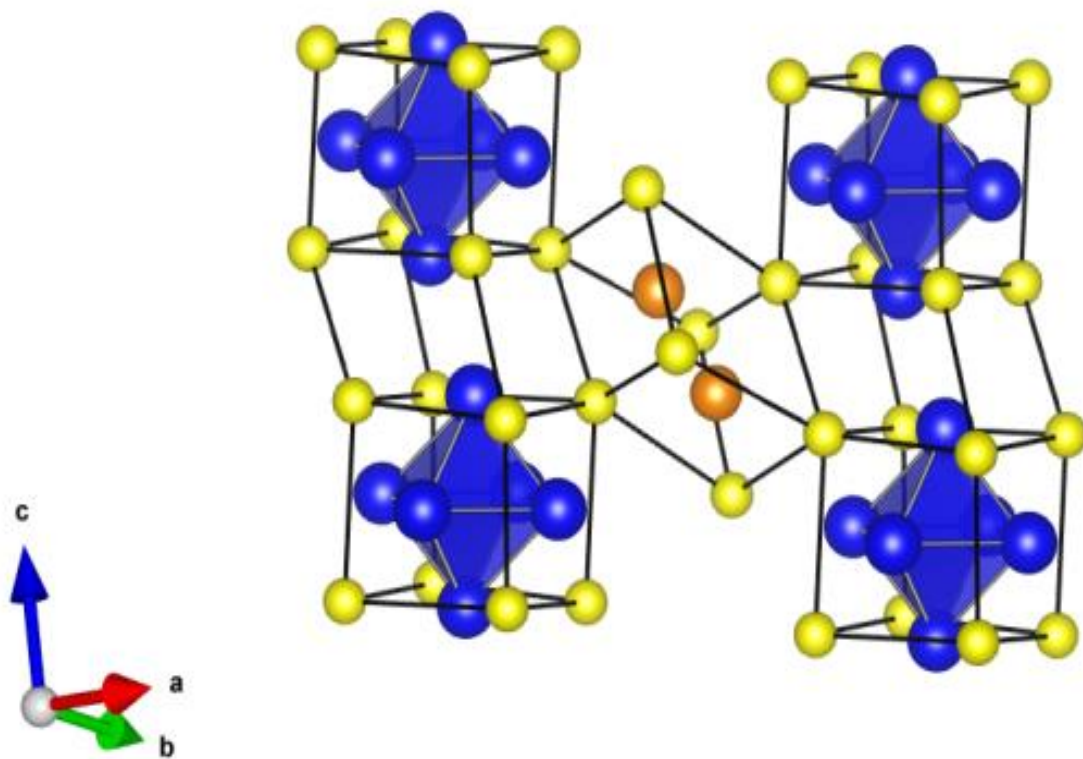


Figure S3.13. Wireframe representation of the triclinic $\text{Fe}_2\text{Mo}_6\text{S}_8$ crystal structure where Fe atoms (orange) reside in exactly two cavity positions.

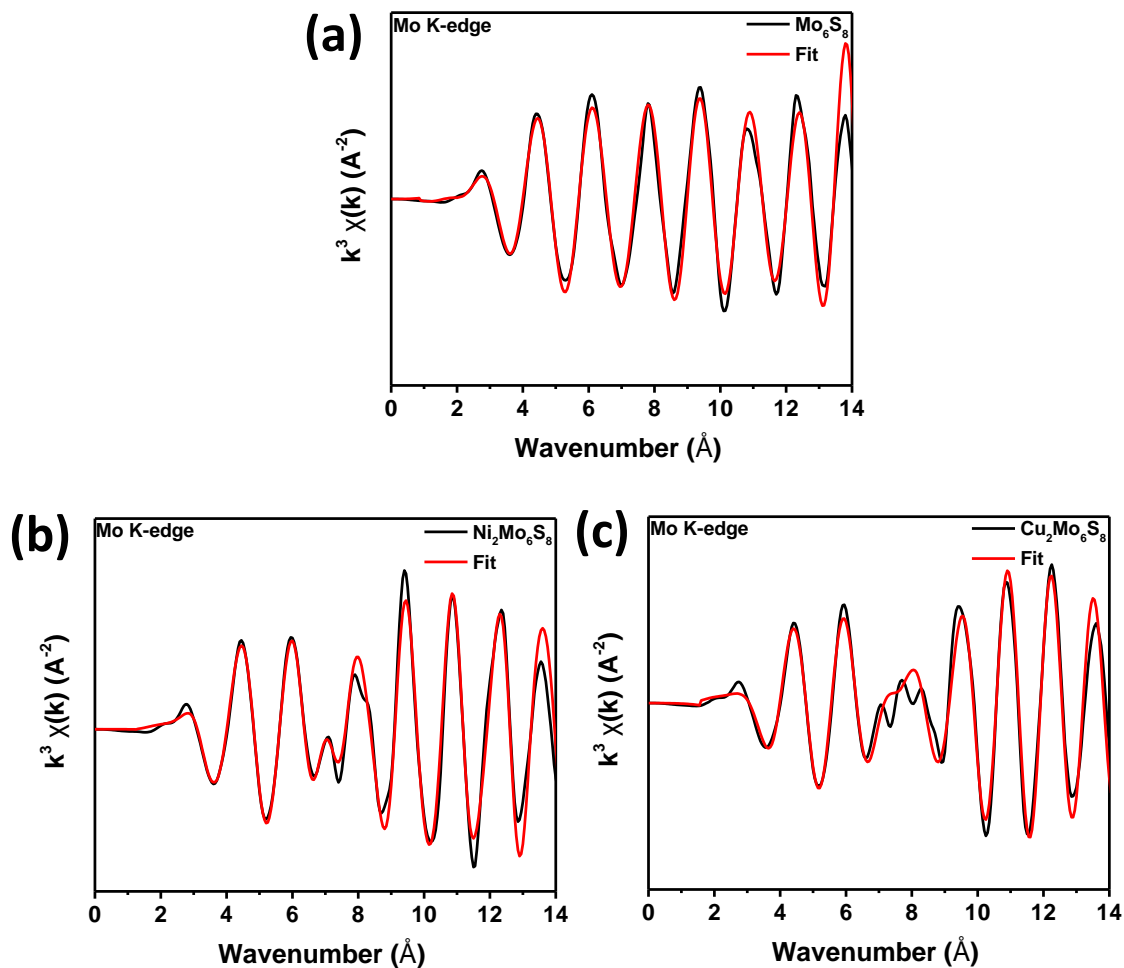


Figure S3.14. Processed EXAFS information plotted in k-space for un-promoted (a), Ni-promoted (b), and Cu-promoted (c) CPs. As is reflected by extracted scattering paths, oscillation magnitudes for both Ni and Cu-promoted Mo_6S_8 differ similarly from 6-9 wavenumbers in comparison to un-promoted Mo_6S_8 where weighted oscillation is comparatively more uniform. This qualitatively indicates that the changes in local coordination of Mo upon metal promotion are similar in nature, as is quantitatively observed following further processing of experimental data.

Table S3.1 Results of Pawley refinements on each Chevrel-phase investigated.

Sample	Space Group	Unit Cell Parameter	Parameter Value	% Difference From ICSD
Cu₂Mo₆S₈	R-3H (148)	a	9.6328 Å	0.03
		b	9.6328 Å	0.03
		c	10.2229 Å	0.03
		α	90°	0
		β	90°	0
		γ	120°	0
Ni₂Mo₆S₈	R-3H (148)	a	9.5075 Å	-0.04
		b	9.5075 Å	-0.04
		c	10.2315 Å	.02
		α	90°	0
		β	90°	0
		γ	120°	0
Fe₂Mo₆S₈	P-1 (002)	a	6.4875 Å	-0.22
		B	6.4771 Å	0.17
		c	6.4746 Å	-0.10
		α	95.4770°	-0.48
		β	88.3156°	-9.30
		γ	83.0060°	-9.11
FeMo₆S₈	R-3H (148)	a	9.5232 Å	-0.01
		b	9.5232 Å	-0.01
		c	10.2734 Å	-0.03
		α	90°	0
		β	90°	0
		γ	120°	0
Mo₆S₈	R-3H (148)	a	9.1853 Å	-0.06
		b	9.1853 Å	-0.06
		c	10.8857 Å	0.07
		α	90°	0
		β	90°	0
		γ	120°	0

Table S3.2 Results of Bader Charge analysis for Fe_yMo₆S₈ (y = 0-2).

	S	Mo	Intercalant
Mo ₆ S ₈	-0.74	0.96	N/A
FeMo ₆ S ₈	-0.82	0.90	1.15
Fe ₂ Mo ₆ S ₈	-0.91	0.86	1.06

Table S3.3 Fitting parameters for the Mo K-edge of Mo₆S₈.

Parameter	Value		R-Factor
S02	0.80	Fixed	0.0041
E0	2.96	+/- 1.19	
DrS1	0.03	+/- 0.45	
DrS2	-0.16	+/- 0.02	
DrS3	-0.16	+/- 0.47	
DrS4	-0.05	+/- 0.02	
DrS5	-0.07	+/- 0.02	
DrMo1	0.04	+/- 0.03	
SsMo	-0.010	+/- 0.001	
SsS	0.001	+/- 0.002	

Table S3.4 Fitting parameters for the Mo K-edge of Ni₂Mo₆S₈.

Parameter	Value		R-Factor
S02	0.85	Fixed	0.0096
E0	5.98	+/- 1.07	
DrS1	-0.09	+/- 0.03	
DrS2	0.00	+/- 0.02	
DrS3	-0.09	+/- 0.04	
DrMo1	-0.01	+/- 0.03	
DrMo2	-0.01	+/- 0.01	
DrMo3	-0.04	+/- 0.03	
DrMo4	-0.01	+/- 0.02	
DrNi1	-0.22	+/- 0.10	
DrNi2	0.32	+/- 0.12	
DrNi3	-0.24	+/- 0.05	
SsS	0.000	+/- 0.002	
SsMo	0.004	+/- 0.002	
SsNi	0.010	+/- 0.004	

Table S3.5 Fitting parameters for the Mo K-edge of Cu₂Mo₆S₈.

Parameter	Value		R-Factor
S02	0.80	Fixed	0.0117
E0	9.52	+/- 1.55	
DrS1	-0.06	+/- 0.03	
DrS2	-0.04	+/- 0.01	
DrS3	0.01	+/- 0.02	
DrMo1	-0.06	+/- 0.04	
DrMo2	-0.02	+/- 0.01	
DrCu	0.19	+/- 0.54	
SsS	-0.002	+/- 0.002	
SsMo	0.001	+/- 0.002	
SsCu	0.010	+/- 0.006	

Table S3.6. Thermodynamic cycles used to calculate the enthalpy of formation of Me_yMo₆S₈ from Me and Mo₆X₈ (Me = Fe, Ni, Cu).

$(\Delta H_{ds,1}) \text{ Me}_2\text{Mo}_6\text{S}_8 (s, 298 \text{ K}) + 22(22.5)\text{O}_2 (g, 1073 \text{ K}) \rightarrow 2\text{Me}^{2+} (\text{sln}, 1073\text{K}) + 6\text{Mo}^{6+} (\text{sln}, 1073 \text{ K}) + 8\text{SO}_4^{2-} (\text{sln}, 1073 \text{ K}) + 12(13)\text{O}^{2-} (\text{sln}, 1073)$
$(\Delta H_{ds,2}) \text{ Mo}_6\text{S}_8 (s, 298 \text{ K}) + 21\text{O}_2 (g, 1073 \text{ K}) \rightarrow 6\text{Mo}^{6+} (\text{sln}, 1073 \text{ K}) + 8\text{SO}_4^{2-} (\text{sln}, 1073 \text{ K}) + 10\text{O}^{2-} (\text{sln}, 1073 \text{ K})$
$(\Delta H_1) \text{ Me} (s, 298 \text{ K}) + 0.5\text{O}_2 (g, 1073 \text{ K}) \rightarrow \text{Me}^{2+} (\text{sln}, 1073\text{K}) + \text{O}^{2-} (\text{sln}, 1073 \text{ K})$
$(\Delta H_{f,\text{comp}}) y\text{Me} (s, 298 \text{ K}) + \text{Mo}_6\text{S}_8 (s, 298 \text{ K}) \rightarrow \text{Me}_y\text{Mo}_6\text{S}_8 (s, 298 \text{ K})$
$\Delta H_{f,\text{comp}} = -\Delta H_{ds,1} + \Delta H_{ds,2} + y\Delta H_1$

Table S3.7. Thermodynamic cycles used to calculate the enthalpy of formation from elements of Mo_6S_8 and $\text{Me}_y\text{Mo}_6\text{S}_8$ (Me = Fe, Ni, Cu).

<p>($\Delta H_{\text{ds},1}$) $\text{Me}_2\text{Mo}_6\text{S}_8$ (s, 298 K) + 22(22.5)O_2 (g, 1073 K) \rightarrow 2Me^{2+} (sln, 1073K) + 6Mo^{6+} (sln, 1073 K) + 8SO_4^{2-} (sln, 1073 K) + 12(13)O^{2-} (sln, 1073 K)</p> <p>(ΔH_1) Me (s, 298 K) + 0.5O_2 (g, 1073 K) \rightarrow Me^{2+} (sln, 1073K) + O^{2-} (sln, 1073 K)</p> <p>(ΔH_2) Mo (s, 298 K) + 1.5O_2 (g, 1073 K) \rightarrow Me^{6+} (sln, 1073K) + 3O^{2-} (sln, 1073 K)</p> <p>(ΔH_3) S (s, 298 K) + 2O_2 (g, 1073 K) \rightarrow SO_4^{2-} (sln, 1073 K)</p> <p>($\Delta H_{\text{f,el}}$) 2Me (s, 298 K) + 6Mo (s, 298 K) + 8X (s, 298 K) \rightarrow $\text{Me}_2\text{Mo}_6\text{S}_8$ (s, 298 K)</p> <p>$\Delta H_{\text{f,el}} = -\Delta H_{\text{ds},1} + 2*\Delta H_1 + 6*\Delta H_2 + 8*\Delta H_3$</p> <p>($\Delta H_{\text{ds},2}$) Mo_6S_8 (s, 298 K) + 21O_2 (g, 1073 K) \rightarrow 6Mo^{6+} (sln, 1073 K) + 8SO_4^{2-} (sln, 1073 K) + 10O^{2-} (sln, 1073 K)</p> <p>($\Delta H_{\text{f,el}}$) 6Mo (s, 298 K) + 8S (s, 298 K) \rightarrow $\text{Me}_2\text{Mo}_6\text{S}_8$ (s, 298 K)</p> <p>$\Delta H_{\text{f,el}} = -\Delta H_{\text{ds},2} + 6*\Delta H_2 + 8*\Delta H_3$</p>

Table S3.8. Computational enthalpies of formation from elements, from intercalation of M_y into Mo_6S_8 , and from synthetic conditions for $\text{Me}_y\text{Mo}_6\text{S}_8$ (Me = Fe, Ni, Cu).

Compound	ΔH_{f} (kJ/gat)	$\Delta H_{\text{f,(3.1)}}$ (kJ/gat)	$\Delta H_{\text{f,(3.2)}}$ (kJ/gat)
Mo_6S_8	-71.09		6.01
$\text{Fe}_2\text{Mo}_6\text{S}_8$	-66.22	-4.02	1.24
FeMo_6S_8	-69.65	-3.29	2.32
$\text{Cu}_2\text{Mo}_6\text{S}_8$	-63.75	-1.54	3.72
$\text{Ni}_2\text{Mo}_6\text{S}_8$	-61.75	0.46	5.72
MoS_2	-89.96		

4. Chapter 4: Direct Solid-State Nucleation and Charge Transport

Dynamics of Alkali Metal-Intercalated $M_2Mo_6S_6$ ($M = K, Rb, Cs$)

Nanorods

Abstract

Microwave-assisted solid-state heating has been employed to control anisotropic growth of $M_2Mo_6S_6$ ($M = K, Rb, Cs$) pseudo-Chevrel phase nanorods without a growth template for the first time. Pronounced preferential crystal nucleation along the hexagonal axis is observed, and electrochemical methods are implemented to elucidate viability for employment of these materials in energy storage and energy conversion systems. It is observed that these nanomaterials exhibit capacitive behavior with charge storage capabilities ranging from 2–8 F/g in strongly acidic aqueous electrolyte, as well as promising electrochemical performance, evolving hydrogen gas at 10 mA/cm² under an applied bias of less than 300 mV vs. RHE.

Introduction

Molybdenum chalcogenides have attracted much attention over the years, owing to their compositional and dimensional tunability that engenders a wide range of favorable chemical and physical properties. Two dimensional molybdenum chalcogenides in the MX_2 family ($M = Mo, W$; $X = S, Se, Te$) have attracted immense focus due to their composition-dependent electronic structure,^{1,2} as well as the plethora of available synthetic methods with which researchers can achieve precise control of dopant density,^{3,4} heterostructure growth,^{5–7} and layer-dependent properties like indirect-to-direct band-gap transitions.^{8,9} Three-dimensional molybdenum chalcogenides such as the $M_yMo_6X_8$ ($M = \text{alkali, alkaline earth, transition, or post-transition metals}$; $y = 0–4$; $X = S, Se, Te$) Chevrel-Phases (CPs) have been widely investigated as a result of their electronic and structural properties that lead to favorable performance in interfacial electron-transfer reactions like CO_2 , CO , and H^+ reduction.^{10,11} In previous work, much promise has been attributed

to CP chalcogenides owing to their favorably positioned Mo d-band and chalcogen p-band,^{10,12} which may enable tunable small-molecule reduction reactivity and charge-transfer kinetics.¹³ CPs have also been successfully integrated in energy storage devices where multivalent cations are intercalated and de-intercalated from the crystal lattice with impressively low coulombic restriction.^{14–16} Furthermore, these ternary chalcogenides have found use in electronic devices where their thermoelectric and superconducting properties can be exploited.^{17–19} With this work we introduce a facile synthetic method which yields an analogous one-dimensional class of ternary chalcogenides with the composition $M_2Mo_6S_6$ ($M = K, Rb, Cs$) (M_2 -PCP) that boasts intrinsically large surface areas as well as controllable interfacial electron-transfer as a function of ternary element composition. The so called pseudo-Chevrel-Phases (PCPs) synthesized in this work are of great interest, as they have strikingly similar compositions and electronic structures compared to their cluster analogues as has been highlighted by Kibsgaard et al. and Vilfan et al. in earlier work on these phases.^{20,21} Unlike their cluster analogues, however, PCPs are comprised of infinite one-dimensional arrays of condensed molybdenum sulfide clusters as is shown in **Fig. 4.1**. These arrays are separated by a metallic intercalant species that affords additional control over electronic structure and may allow for

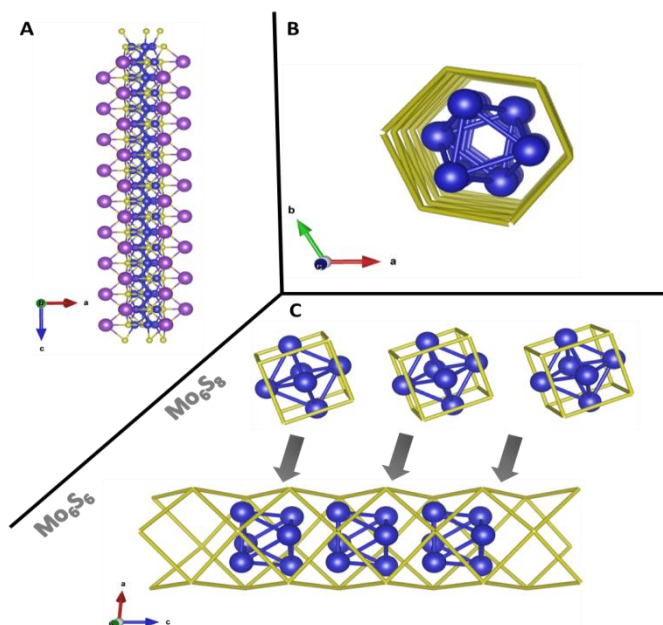


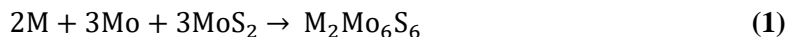
Figure 4.1. (A) 1-dimensional structure of $M_2Mo_6S_6$ (Alkali = Purple, Mo = Blue, S = Yellow) as viewed perpendicular to the principle hexagonal axis with alkali intercalants surrounding Mo_6S_6 wires, (B) Mo_6S_6 wire as viewed along the hexagonal axis, and (C) crystal structure representations of the Chevrel parent phase where Mo_6 clusters are significantly separated via S_8 encapsulation, while Mo_6 units form a continuous chain surrounded by an S_6 “sleeve” in the PCP framework.

similar control over PCP performance in various types of electronic device components.²⁰ The ability to intercalate multiple different ternary species into these 1-dimensional materials opens the door for modulation of their anisotropic electrical and optical conductivity,²¹ which is of potential importance for nano-scale device integration that requires dimensionally controlled components that can enable topological charge-transport and spatially resolved exciton separation.^{22,23} To date, synthetic routes for ternary chalcogenide heterostructure growth are scarce, despite promise of these materials as integral components in electronic and optical devices.²⁴ Previous reports of PCP synthesis involve traditional solid-state synthesis, including direct synthesis from the constituent elements or from thiomolybdate precursors,²⁵ as well as ion-exchange from indium-intercalated precursors to form alkali intercalated PCPs.²⁵ These methods can be impractically time and energy intensive, and generally do not allow for scalable material production. Herein we report the first instance of a template-free synthetic route toward nanorod PCPs, wherein rapid microwave heating affords pure-phase, alkali metal-intercalated PCP materials with a high degree of anisotropic crystal growth. To evaluate PCP compatibility with integrated, nano-scale electronic devices which hinges on their unique 1-dimensional electronic properties,^{20,21,26} in this work capacitive charge storage and inner-sphere electron-transfer properties are evaluated electrochemically as ternary M intercalant composition changes. Investigating electron transport properties in these chalcogenide materials may be an important step in understanding functionality in monolithic device schemes.²⁷

Experimental Methods

Materials: Rb (99.999% purity, elemental), Cs (99.999% purity, elemental), MoS₂ (95% purity, 325 mesh), and graphite powder (99% purity, 125 mesh) were all used as purchased from Alfa Aesar. Mo powder (99.995%, 250 mesh) and H₂SO₄ were used as purchased from Sigma Aldrich. K₂S (95%) was used as purchased from Pfaltz and Bauer. Al₂O₃ microfiber was used as purchased from Thermo Fisher Scientific. Fused quartz tubes were purchased from AdValue Technology and blown into round-bottom tubes using an in-house oxyhydrogen torch. Nano-pure H₂O (18.2 MΩ) was obtained with an in-house Barnstead E-Pure filtration system.

Synthesis: All PCPs were synthesized using microwave-assisted solid-state methods described in our previous work.^{10,28} Briefly, stoichiometric amounts of precursors were weighed to within +/- 0.0010 g of their target masses in a N₂ glovebox according to the balanced reaction



and ball-milled under N₂ until completely homogenized (8 h).

Table 4.1. Reagent masses used to obtain 250 mg precursor mixtures for microwave heating.

Composition	Molar Mass (g/mol)	M _x Mass (g)	Mo Mass (g)	MoS ₂ Mass (g)
K ₂ Mo ₆ S ₆	846.292	0.0326*	0.0992	0.1182
Rb ₂ Mo ₆ S ₆	939.032	0.0455	0.0766	0.1279
Cs ₂ Mo ₆ S ₆	1033.906	0.0643	0.0696	0.1161

*K₂S was used as the K source in K₂Mo₆S₆ and was mixed according to the balanced equation 2K₂S+7Mo+5MoS₂→2K₂Mo₆S₆, and the M₂ mass in this table highlights the mass of K₂S rather than K.

Samples were then cold-pressed under N₂ and sealed in 2 mm thick quartz round-bottom tubes under tightly packed Al₂O₃ microfiber and graphite as depicted in **Fig. S4.1** to prevent contamination by O₂ during heating. Samples were then removed from the glove box and placed in a graphite bath inside multiple layers of Al₂O₃ insulating foam inside an Ar-filled conventional microwave with inverter technology (Panasonic NN-SN651B) and irradiated at a power of 120–240 W for 10 minutes where a temperature of ~750 was held constant. In this reaction, graphite is acting as the microwave susceptor to rapidly yield large amounts of thermal energy.²⁹ Reactions were immediately quenched in a room temperature water bath. We note that handling of elemental Cs and Rb precursors can be hazardous even under inert N₂ atmosphere, and significant precautions were taken to ensure any materials introduced to the glove box had been sufficiently dried under vacuum prior to work with the alkalis. Moreover, due to the exothermicity of mixing with sulfide precursors, care was taken to limit batch sizes to <250 mg at a time and MoS₂ was used as a precursor rather than elemental S. To further circumvent issues arising from the particularly high exothermicity of mixing Cs with MoS₂, Cs and Mo precursors were first mixed under N₂ prior to addition

of MoS₂ and further mixing in order to dilute local concentrations of solid Cs in the ball mill cup. We also note that K₂S can be used as the potassium precursor for K-PCP synthesis owing to its ease of mixing.

Structural and Elemental Characterization: Crystal phase purity of as-synthesized PCPs was determined via powder X-ray diffraction (PXRD) using a Bruker D8 Eco Advance diffractometer with Cu K α radiation (1.432 Å), and powder diffraction patterns were compared with calculated patterns from the Inorganic Crystal Structure Database (ICSD). Experimental lattice parameters were extracted via Pawley refinement using the TOPAS suite from Bruker. High-resolution transmission electron microscopy (HRTEM) was performed using a JEOL JEM-2100F microscope. Morphology of synthesized PCPs was evaluated via scanning electron microscopy (SEM) using a FEI (Hillsboro, Or) Nova NanoSEM 430, while bulk composition was evaluated via energy-dispersive X-ray spectroscopy (EDX) using a FEI Scios Dual Beam FIB/SEM with an Oxford EDX detector.

Electrochemical Characterization: All electrochemical analyses were performed using a Bio-Logic VSP-300 potentiostat with custom three-electrode cells in an H-shaped configuration (**Fig. 4.2**) where Ag/AgCl reference electrodes and Pt mesh counter electrodes were used in all cases. Conductive inks of all synthesized PCPs were made by mixing each PCP with carbon black, polytetrafluoroethylene (PTFE) suspension, and isopropyl alcohol. A blank ink was also mixed for reference that contained no PCP. These inks were sonicated for 30 minutes prior to deposition onto conductive carbon substrates. 10 μ L of each ink was deposited on the bottom half of 1 x 2 cm pieces of conductive, micro-structured Toray carbon paper purchased from Fuel Cell Store, and was then dried under vacuum prior to introduction into an electrochemical cell. This method allowed for control over the exact mass of PCP that was deposited on each electrode. All experiments herein were performed using 0.5 M H₂SO₄ electrolyte in both the working

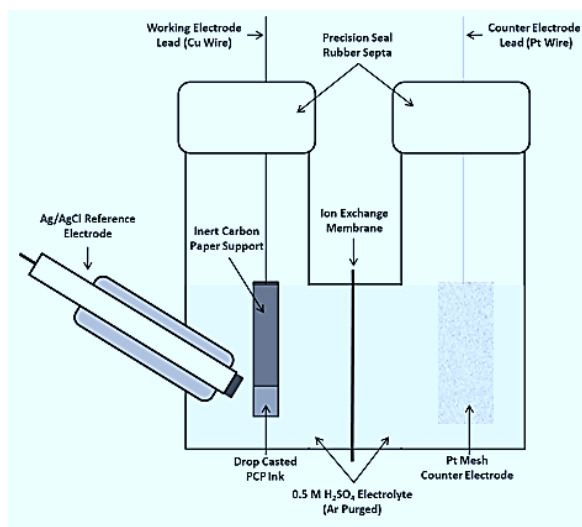


Figure 4.2. Schematic representation of the H-shaped three-electrode configuration that was implemented in all electrochemical experiments.

and counter electrode compartments. The electrolyte was de-oxygenated via purging with high-purity Ar for ~30 minutes prior to each experiment. The electrochemically active surface area and specific capacitance of all ink-deposited electrodes were both determined by observing the scan-rate dependence of the capacitive charging current in cyclic voltammetry experiments where scans were centered 0.1 V around the open circuit potential, as this was found to be a non-faradaic region for all of the electrodes. Resistance to charge transfer was determined via potentiostatic electrochemical impedance spectroscopy (PEIS) with an applied DC bias ranging from -0.5 V vs. RHE to -0.9 V vs. RHE and an AC bias with 10 mV sinus amplitude ranging from 1 MHz to 10 mHz. Nyquist plots relating imaginary and real components of observable impedance were analyzed with the simplification that interfacial charge-transfer proceeds according to a Randle circuit that involves a capacitive component, a solution/circuit resistance component, and a charge-transfer component. Hence, resistance to charge transfer was taken as the semi-circular diameter of the Nyquist plots. Hydrogen evolution behavior was observed via linear sweep voltammetry (LSV) where external potential was varied from 0.0 V vs. RHE down to -1.0 V vs. RHE for each ink, and current density normalized with respect to surface area was measured. Overpotential was taken as the potential required to achieve a current density of 10 mA/cm², while Tafel slopes were determined using the linear region of overpotential versus log(current density) plots.

Computational Methods: Density functional theory calculations (as implemented in the Vienna Ab initio Simulation Package (VASP))³⁰ were used to calculate the surface energies of relevant $M_2Mo_6S_6$ facets. Initially, the bulk lattice is optimized using the PBE-functional (using 700 eV plane-wave energy cut-off, $4 \times 4 \times 8$ K points);³¹ the predicted lattice constants are in good agreement with experimental values. Slab models for the $\langle 010 \rangle$, $\langle 110 \rangle$ and $\langle 001 \rangle$ facets are used to calculate the surface energy using the methods of Fiorentini and Methfessel.³² For these slab calculations, the reciprocal space was sampled using $3 \times 3 \times 1$, $6 \times 3 \times 1$ and $2 \times 6 \times 1$ K-points for $\langle 010 \rangle$, $\langle 110 \rangle$ and $\langle 001 \rangle$ facets, respectively. All surface calculations were performed using the PBE functional and 520 eV plane-wave energy cut-off. The structures were optimized until the forces on each atom were lower than 0.03 eV/\AA .

Results and Discussion

We have demonstrated that the synthetic method described herein is effective in yielding crystalline $M_2Mo_6S_6$ nanorods as shown in the electron micrographs in **Fig. 4.3a-c**. As shown in **Fig. 4.3d-f**, the PXRD patterns for each PCP are in close agreement with literature, illustrating a hexagonal crystal structure for each PCP. In addition, reaction times using this synthetic method have been reduced to 5-10 minutes owing to rapid conversion of microwave radiation into thermal energy, thereby drastically reducing required energy input in comparison to traditional solid-state methods.³³ Hence this work offers the first account of direct nucleation of nanostructured Pseudo-Chevrel Phase materials using high-temperature solid-state methods, and indeed represents one of the first known successes in direct solid-state formation of a ternary nanorod material. We speculate that the successful nucleation of these rods can be attributed to one of two potential crystal growth mechanisms: 1) strongly oriented crystal growth may be driven by an insurmountable difference in interfacial energy between “solid” and “liquid” PCP, and the volume energy which results upon changing from liquid to solid phase,³⁴ or 2) favorable surface free energies for the exposed $\langle 010 \rangle$ and $\langle 110 \rangle$ facets that drive self-propagating 1-dimensional growth.^{35, 36} Density Functional Theory calculated surface energies for the $\langle 010 \rangle$, $\langle 110 \rangle$, and $\langle 001 \rangle$ surfaces confirm the latter hypothesis,

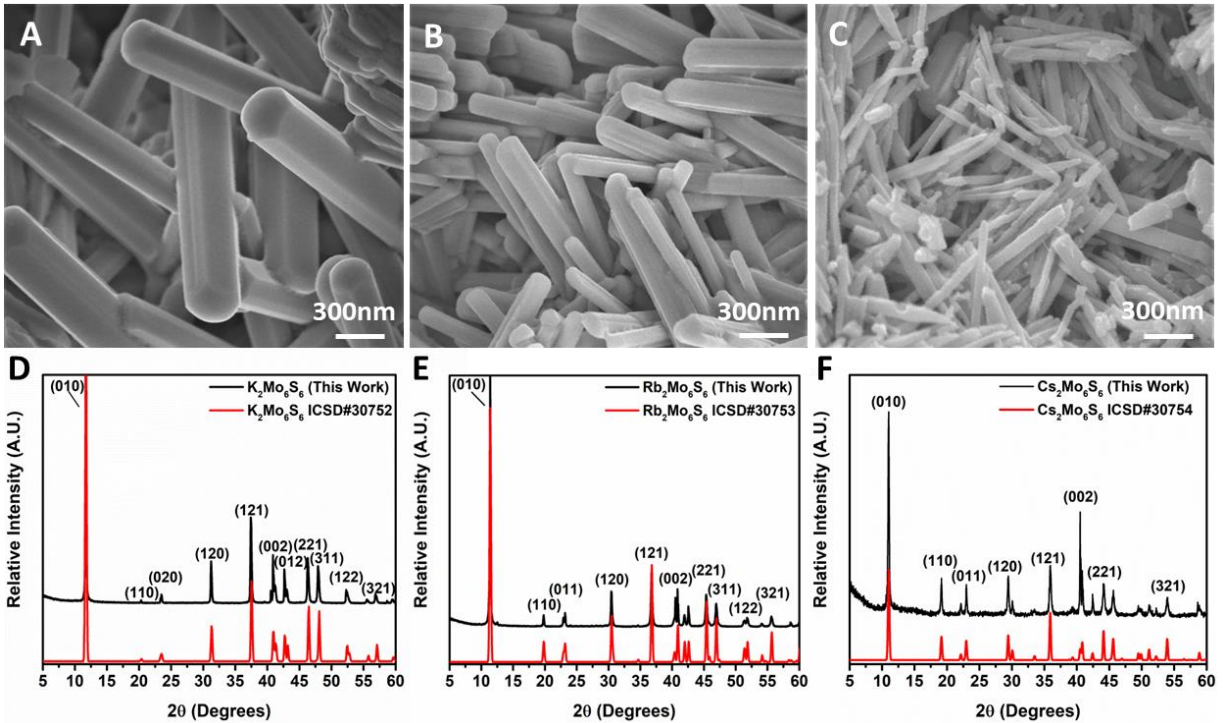


Figure 4.3. (A)-(C) SEM images for as-synthesized K-PCP (A), Rb-PCP (B), and Cs-PCP (C), (D)-(F) Indexed PXRD patterns overlaid with literature patterns from the International Crystal Structure Database (ICSD) for K-PCP (D), Rb-PCP (E), and Cs-PCP (C).

with the $\langle 010 \rangle$ and $\langle 110 \rangle$ surfaces exhibiting drastically lower surface energies at ~ 0.37 eV/formula unit and ~ 0.93 eV/formula unit, respectively. These surfaces that exist parallel to the observed one-dimensional growth direction are significantly lower than the $\langle 001 \rangle$ surface that exhibits a surface energy of ~ 4.19 eV/formula unit. This is illustrative that surface energy is indeed a strong driving force for the anisotropic nucleation observed for this solid-state reaction. The surfaces of interest can be seen in **Fig. 4.4**, where the

Table 4.2 Results of computational surface energy modeling for K_2 -PCP $\langle 010 \rangle$, $\langle 110 \rangle$, and $\langle 001 \rangle$ surfaces.

Facet	Surface energy (eV/ Formula Unit)
$\langle 010 \rangle$	0.37
$\langle 110 \rangle$	0.93
$\langle 001 \rangle$	4.19

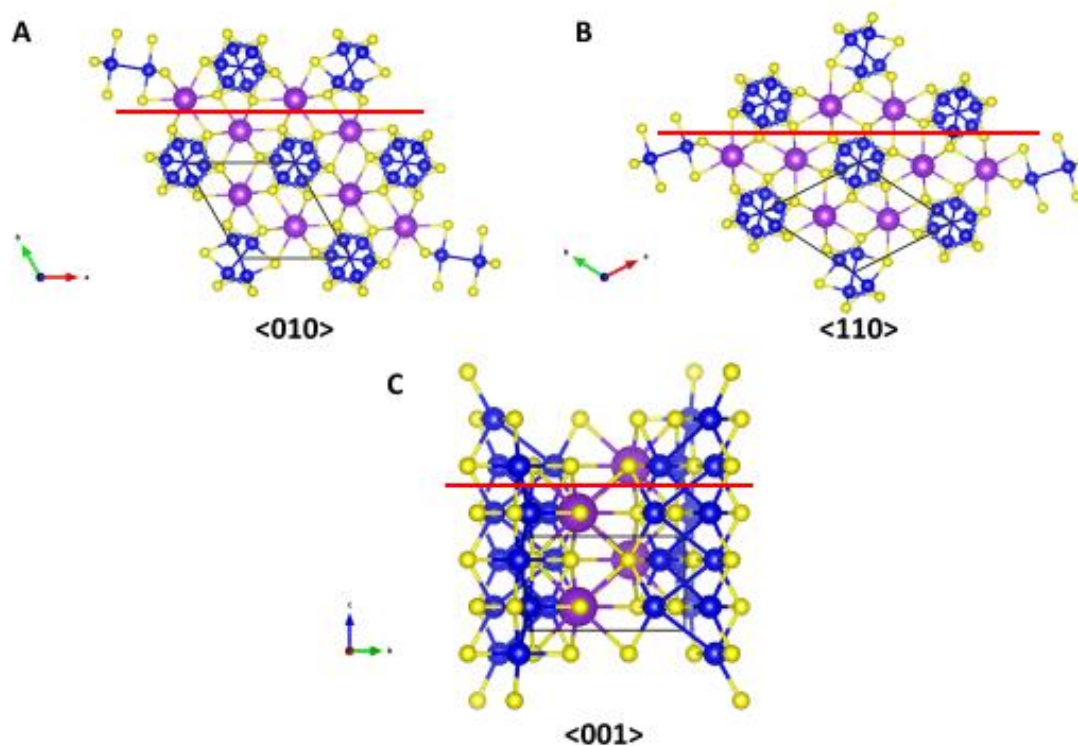


Figure 4.4. Crystal structure representations for each surface for which computational free energies were determined, illustrating an increasing number of broken bonds in moving from (A) $\langle 010 \rangle$, to (B) $\langle 110 \rangle$, and finally to (C) $\langle 001 \rangle$. In each case, the compass shows that the unit cell is oriented such that the lattice plane is parallel to the viewing perspective.

$\langle 010 \rangle$ (**Fig. 4.4a**) surface clearly requires bisection of fewer bonds than either $\langle 110 \rangle$ (**Fig. 4.4b**) or $\langle 001 \rangle$ (**Fig. 4.4c**) and yields a more coordinated, more stable interface. The results of this modelling are shown in **Table 4.2**.

From lattice parameters extracted via Pawley refinement (**Fig. S4.4**) and tabulated in the supporting information in **Table S4.1**, it is apparent that unit cell parameters for each of the hexagonal PCPs studied here are in good agreement with literature values, with lattice parameters for each of the P63/m (176) structures within 0.19% of expected values.³⁷ The highest error, belonging to the Cs-PCP, is attributed to the relatively poor R_{WP} of 16.21 that can be ascribed to the lower signal-to-noise ratio in the corresponding diffraction pattern—likely the result of a slightly lower degree of crystallinity. We observe via HRTEM as shown in **Fig. S4.3** that the $\langle 010 \rangle$ and $\langle 110 \rangle$ facets of Rb-PCP and Cs-PCP are exposed, although no lattice resolution was achieved for K-PCP owing to the increased rod thickness which prevented efficient transmission. Lastly, we do not observe that this method of heating introduces any bulk impurity, as

evidenced by the EDX point scan spectra in **Fig. S4.4** which indicate the presence of only Mo, S, and each respective alkali metal. Alkali composition was quantified via point scans at three distinct locations on rods of each PCP that were averaged together, yielding atomic percent compositions in a range from 13.12%-15.02%, as would be expected for the $M_2Mo_6S_6$ composition within instrumental error $\sim 1\%$. To confirm the uniformity of elemental distribution in as-synthesized nanorods, EDX line scans and two-dimensional EDX maps were acquired for isolated rods of each M_2 -PCP and the results are shown in **Fig. S4.5-S4.10**. These scans indicate that alkali metal distribution scales directly with Mo and S distribution in the rods, and there is no obvious deficiency in any constituent element at the tips or along the lengths of the rods.

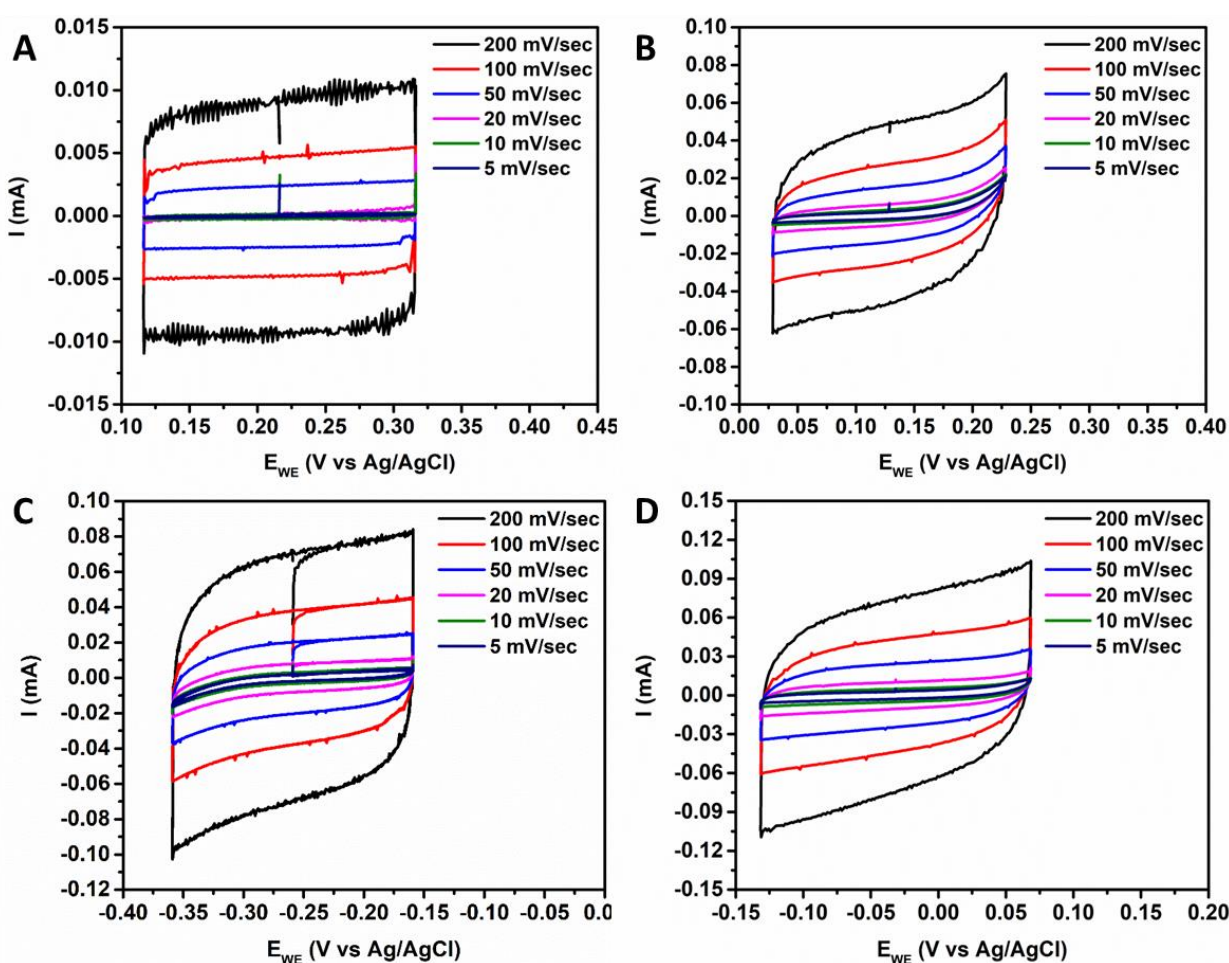


Figure 4.5. Scan-rate dependent cyclic voltammograms performed in 0.5M H₂SO₄ for (A) a blank ink without PCP, (B) K-PCP, (C) Rb-PCP, and (D) Cs-PCP. Voltammograms were collected in a region $\pm 0.1V$ from each electrode's open circuit potential, as this region is generally non-Faradaic and therefore measured currents accurately represent purely capacitive charging. To ensure reliable statistics, CVs similar to the ones shown here were repeated for at least 6 electrodes of each ink.

In the series of M_2 -PCPs, it was found that specific capacity measured via cyclic voltammetry as shown in **Fig. 4.5** and **Fig. 4.6** scaled well with alkali metal electro-positivity ($K < Rb < Cs$), as Cs-PCP exhibited significantly higher charge storage at 8.45 F/g, compared to Rb and K at 6.34 F/g and 1.48 F/g, respectively (**Fig. 4.7a**). Indeed, resistance to electrochemical charge transfer determined by EIS as shown in **Fig. S4.12** for the adsorption of H^+ and subsequent reductive evolution of H_2 gas was highest for Cs-PCP at 6.03Ω , followed by Rb and K at 5.88Ω and 4.18Ω , respectively (**Fig. 4.7b**). This indicates that in an electrochemical water splitting device where the reduction half-reaction is given by **Eq. 2**.

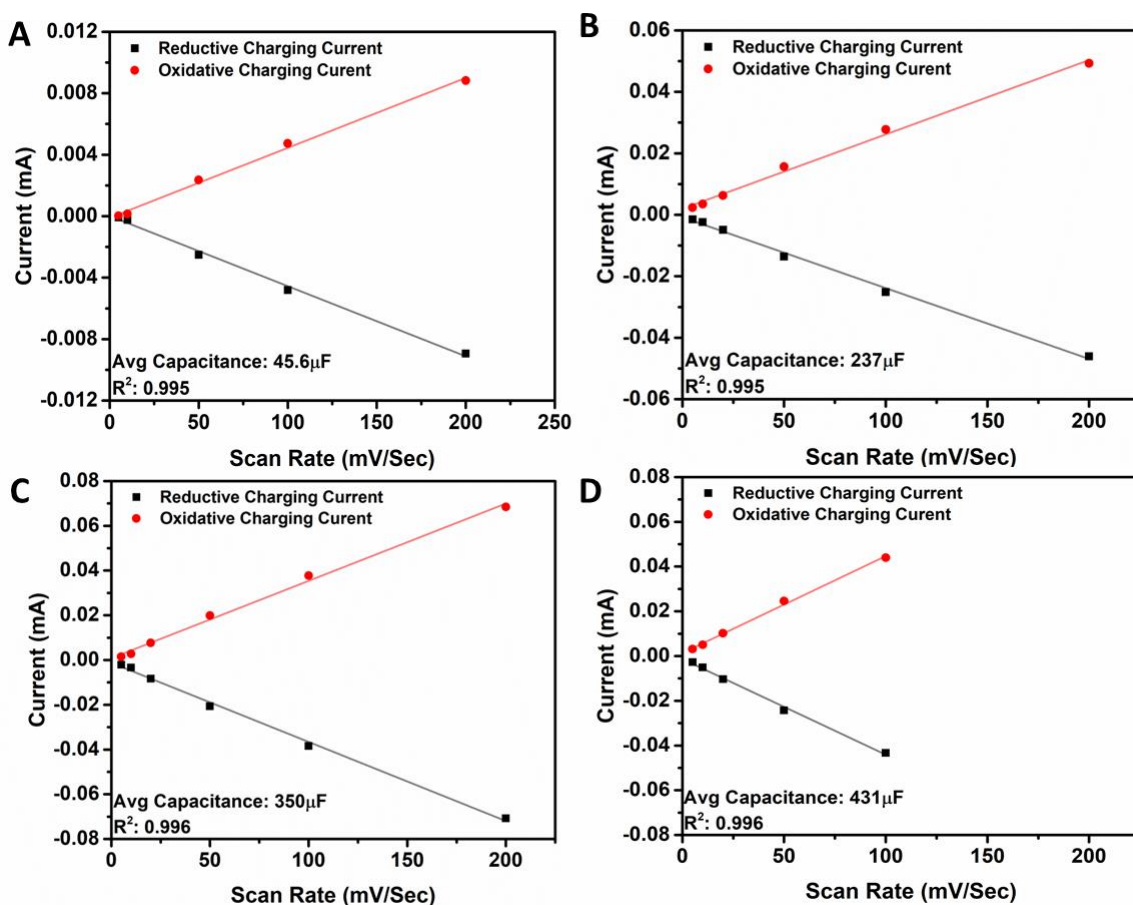


Figure 4.6. Examples of oxidative and reductive charging currents for (A) PCP-free blank ink, (B) K-PCP, (C) Rb-PCP, and (D) Cs-PCP. Capacitance is taken as the average of the absolute value for both positive and negative slopes in each case. In some experiments, 200mV/sec scans resulted in a large amount of noise, and are excluded on a case by case basis. Average capacitance values shown here represent the values for these specific scans, and are not the average values following replicated scans as reported in the main text. Average values for double layer capacitance are reported in Figure S3.11.

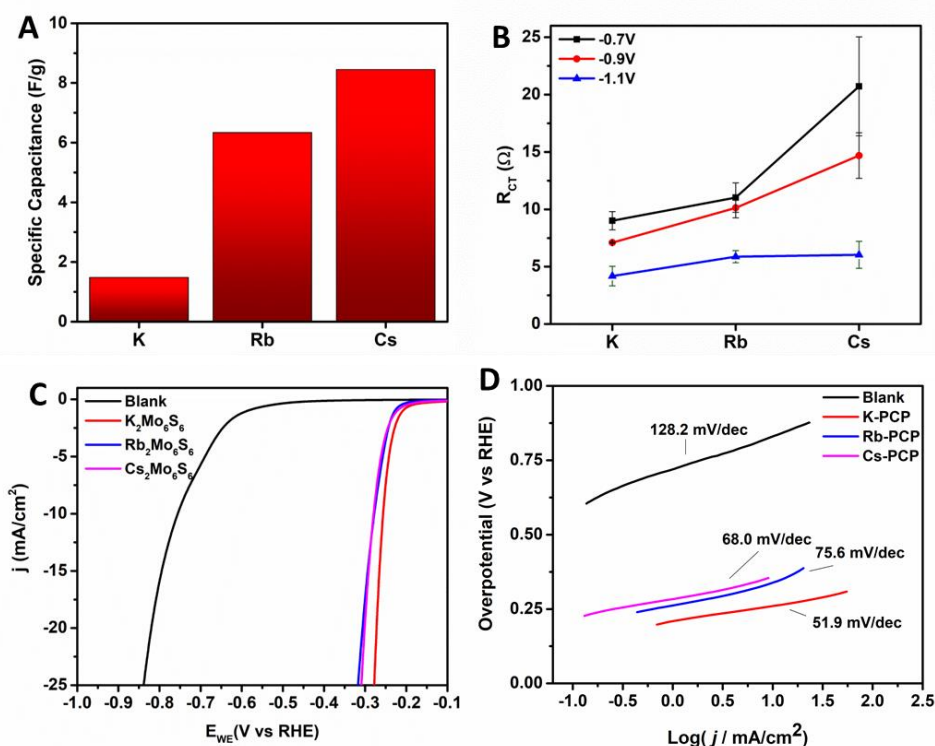


Figure 4.7. (A) Specific capacitance per gram of M_2PCP , calculated using double layer capacitance and known mass loading onto a conductive carbon substrate, (B) Resistance to electron-transfer of M_2PCP inks in a $0.5M H_2SO_4$ solution under multiple applied potentials vs RHE, (C) Polarization curves obtained via linear sweep voltammetry for M_2PCP inks as well as for a blank ink, all submerged in $0.5M H_2SO_4$, and (D) Tafel plots for M_2PCP inks along with a blank ink for reference, further illustrating the current-potential response of each ink acting as a catalyst for the Hydrogen Evolution Reaction (HER).



K-PCP is likely to be the most efficient material, owing to its lower tendency to resist charge transfer to H^+ to form H_2 (4.18Ω), while Cs-PCP would require unnecessarily high input voltages to maintain comparable rates of H_2 production, due to its higher barrier for inner-sphere electron transfer that is required for proton adsorption. However, the higher resistance to charge transfer for Cs-PCP (6.03Ω) in an electrolyte that is highly conducive to electron transfer is indicative that Cs-PCP can perform well as an aqueous capacitor. This is also in good agreement with the significantly higher specific capacitance ($8.45 F/g$) for Cs-PCP in comparison to K-PCP ($1.48 F/g$). In impeding interfacial charge transfer to H^+ in $0.5M H_2SO_4$, it can be inferred that Cs-PCP will preferentially mediate alternative small-molecule conversion reactions wherein

hydrogen gas evolution is an unwanted side reaction such as CO₂ reduction and N₂ reduction. This speculation warrants further investigation, although we do not explore such a possibility in the present work.

In addition to Nyquist plots that allow for direct extraction of charge-transfer resistance, **Fig. 4.8** and **Fig. 4.9** give the phase angle response and impedance magnitude response for each electrode, respectively, as functions of AC oscillatory frequency. These plots indicate that at mild applied DC bias and low frequency, ($\log(\omega) \sim 0-2$) a diffusion-controlled Warburg impedance element exists with a frequency dependence that can be expressed as

$$Z_W = \frac{\sigma(1-j)}{\sqrt{\omega}} \quad (3)$$

with

$$\sigma = \frac{RT}{n^2 F^2 A \sqrt{2}} \left(\frac{1}{C^{*o} \sqrt{D_o}} + \frac{1}{C^{*R} \sqrt{D_R}} \right) \quad (4)$$

where Z_W is the Warburg impedance, σ is the Warburg coefficient, j is the imaginary term, ω is the radial frequency, C^* and D represent concentrations and diffusion coefficients for oxidized and reduced species – H⁺ and H₂ in this case—and n represents the number of electrons associated with the electrochemical reaction. We observe from these plots that regardless of applied potential, current response during EIS measurements remains firmly controlled by diffusion for the blank electrode owing to the kinetically hindered electron-transfer that leads to poor mass-transport of H⁺ and H₂ to and from the electrode interface, respectively. However, we observe that upon application of an increasingly reductive DC bias, each of the PCP catalyst-loaded electrodes exhibits a drastically reduced impedance modulus at lower oscillatory frequencies, suggesting that neither adsorption/desorption kinetics nor oxidant/reductant diffusion are significantly limiting the observed current response.

In terms of reaction energetics, K-PCP is the most effective catalyst in its class for electrochemical H⁺ reduction, as the overpotential required to achieve a current density of 10mA/cm² is 270mV, whereas

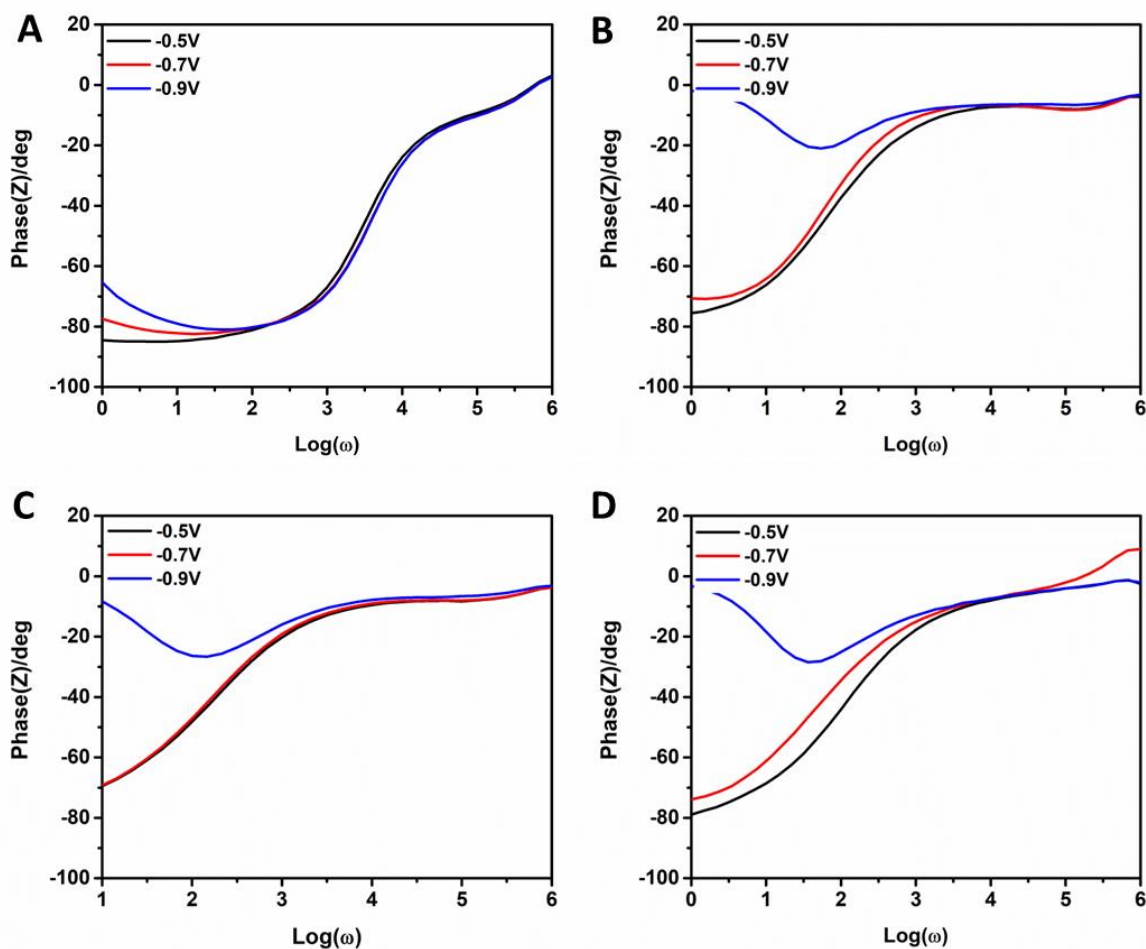


Figure 4.8. Phase angle response during potential-dependent EIS experiments for (A) PCP-free blank ink, (B) K-PCP, (C) Rb-PCP, and (D) Cs-PCP where ω is the AC bias frequency.

Rb-PCP and Cs-PCP require overpotentials of 349mV and 328mV, respectively, in order to achieve 10mA/cm² (Fig. 4.7c). While this result of Cs-PCP seemingly outperforming Rb-PCP is surprising owing to the higher charge transfer resistance of Cs-PCP in comparison to its Rb analogue, we note that these overpotential values are very close within experimental error as reported by a single standard deviation in Fig. S4.13a, and we do not therefore draw any conclusion that Cs-PCP mediates the HER at significantly milder operating voltages. We observe a strikingly similar trend in Tafel slope which relates applied potential to catalytic current on a logarithmic scale and is a widely accepted descriptor for catalytic activity. As shown in Fig. 4.7d and Fig. S4.13b, we observe that K-PCP is the most efficient mediator of H⁺ reduction, with a shallow Tafel slope of 51.9mV/dec, followed by Rb-PCP and Cs-PCP which exhibit

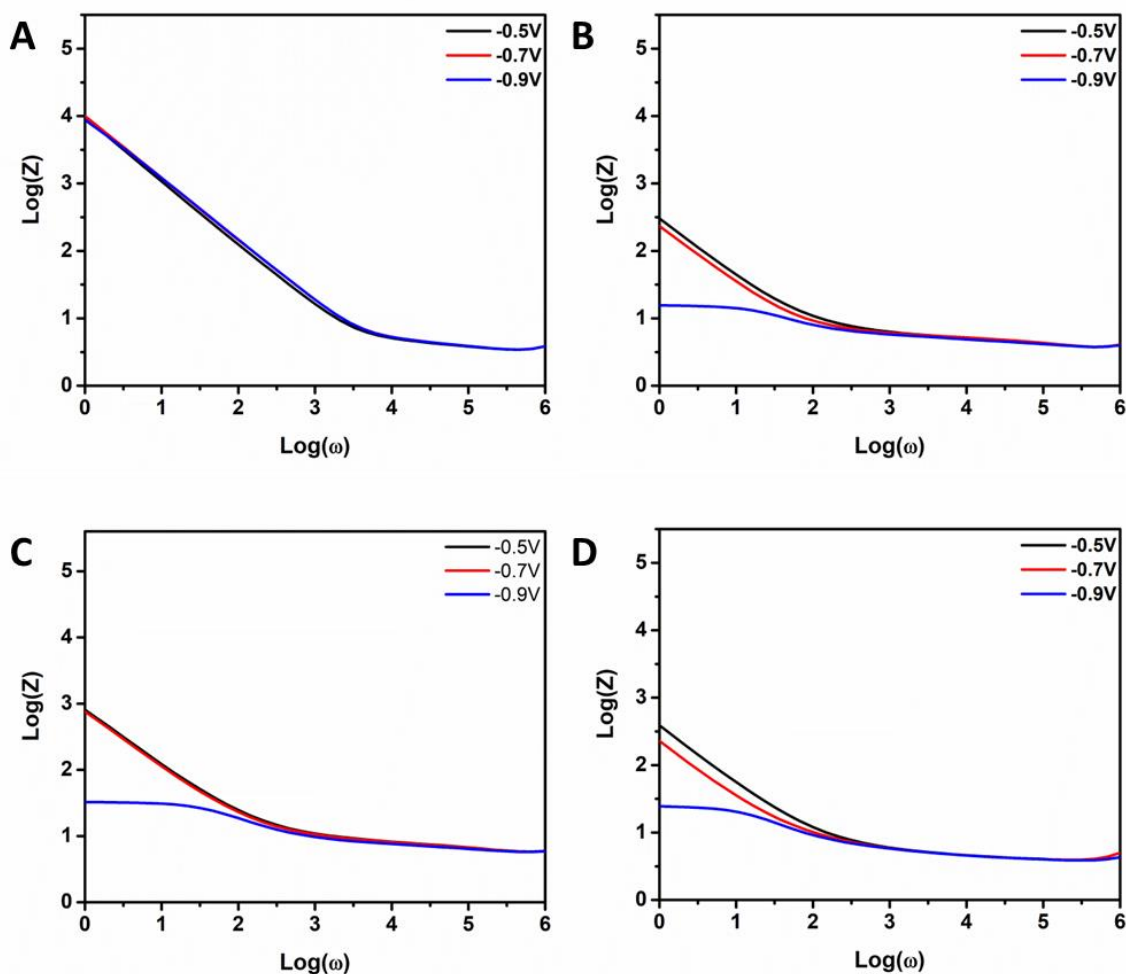


Figure 4.9. Impedance modulus response during potential-dependent EIS experiments for (A) PCP-free blank ink, (B) K-PCP, (C) Rb-PCP, and (D) Cs-PCP where ω is the AC bias frequency. Low frequency regions in all cases exhibit potential-dependent diffusion control, evidenced by the ~ 45 degree response of the impedance modulus.

steeper and therefore less desirable Tafel slopes of 75.6mV/dec and 68.0mV/dec, respectively. Again, Rb-PCP and Cs-PCP are similar within experimental error, which may be a result of presently unexplored surface-dependent thermodynamic and kinetic properties such as variable H^+ adsorption strength on sites in different facets of Rb-PCP versus Cs-PCP which can feasibly dictate the overall rate of reaction, although K-PCP is the clear outlier and consequently represents the more promising electrocatalytic composition of all three M_2 -PCPs studied.

Conclusions

We have achieved microwave-assisted solid-state synthesis of a ternary nanomaterial without a template or catalyst for anisotropic crystal nucleation. To the best of our knowledge, this is the first of such accounts. We have applied this time- and energy-efficient method to a promising chalcogenide composition wherein alkali metal intercalation can be controlled such that the charge storage and electron-transfer properties are directly affected. When intercalated by potassium, the 1-dimensional Mo_6S_6 structure readily allows interfacial electron-transfer to electrolytic protons through the hydrogen evolution reaction, while intercalation by Cs leads to a significant increase in charge storage capacity and a resulting high barrier toward charge transfer. In order to deconvolute intrinsic electronic structure versus morphological effects on charge storage capacity, fine control over average nanorod size must likely be coupled with computational and/or spectroscopic evaluation of the composition-dependent $\text{M}_2\text{Mo}_6\text{S}_6$ band structure. A more detailed quantification of the effect of alkali metal electropositivity on electronic structure will ultimately lead to the extraction of useful descriptors for material performance that can be applied to other electronics applications, and this type of elucidation will be a focus of future work related to this family of nanomaterials. For example, quantifying the effect of alkali metal on the currently unknown interfacial kinetics of hydrogen evolution reactivity is an important knowledge gap to address with further systematic evaluation. Further development of composition-structure-function relationships in the expansive transition metal chalcogenide space will elucidate new modalities in controlling charge-transport dynamics and potentially in controlling exciton localization in low-cost, dimensionally reduced, and environmentally benign frameworks.

Supporting Information

Reaction diagram, PXRD refinement results, TEM images, EDX line scans, Nyquist plots, figures of merit, PXRD lattice parameters.

Acknowledgments

We acknowledge the University of California, Davis for start-up funding for this work, as well as support from the Cottrell Scholar program supported by the Research Corporation for Science Advancement (RCSA Grant ID#26780). I would like to acknowledge support from the Chevron fellowship program through UC Davis Institute of Transportation Studies in coordination with Chevron Corporation, as well as support from the Bradford P. Borge fellowship and the Ernest E. Hill Memorial graduate student fellowship. Computational resources were provided by Extreme Science and Engineering Discovery Environment (XSEDE), which is supported by National Science Foundation grant number ACI-1548562.

Publication Information, Copyright, and Author Acknowledgements

This chapter forms the basis for the following publication:

Perryman, J. T.; Kulkarni, A. R.; Velázquez, J. M., Direct solid-state nucleation and charge-transport dynamics of alkali metal-intercalated $M_2Mo_6S_6$ ($M = K, Rb, Cs$) nanorods. *Journal of Materials Chemistry C* **2020**, 8, 10742-10748.

Joseph T. Perryman conducted material synthesis, electrochemistry experiments, PXRD, SEM, EDX. ARK performed DFT.

This chapter was adapted with permission from Perryman, J. T.; Kulkarni, A. R.; Velázquez, J. M., Direct solid-state nucleation and charge-transport dynamics of alkali metal-intercalated $M_2Mo_6S_6$ ($M = K, Rb, Cs$) nanorods. *Journal of Materials Chemistry C* **2020**, 8, 10742-10748. © Copyright 2020 Royal Society of Chemistry.

References

1. F. Xiong, H. Wang, X. Liu, J. Sun, M. Brongersma, E. Pop and Y. Cui, *Nano Letters*, 2015, **15**, 6777-6784.
2. X. Hong, K. Chan, C. Tsai and J. K. Nørskov, *ACS Catalysis*, 2016, **6**, 4428-4437.
3. D. M. Sim, M. Kim, S. Yim, M.-J. Choi, J. Choi, S. Yoo and Y. S. Jung, *ACS Nano*, 2015, **9**, 12115-12123.
4. A. A. Tedstone, D. J. Lewis and P. O'Brien, *Chemistry of Materials*, 2016, **28**, 1965-1974.
5. Y. Gong, J. Lin, X. Wang, G. Shi, S. Lei, Z. Lin, X. Zou, G. Ye, R. Vajtai, B. I. Yakobson, H. Terrones, M. Terrones, Beng K. Tay, J. Lou, S. T. Pantelides, Z. Liu, W. Zhou and P. M. Ajayan, *Nature Materials*, 2014, **13**, 1135.
6. Y. Jung, Y. Zhou and J. J. Cha, *Inorganic Chemistry Frontiers*, 2016, **3**, 452-463.

7. J. Etzkorn, H. A. Therese, F. Rocker, N. Zink, U. Kolb and W. Tremel, *Advanced Materials*, 2005, **17**, 2372-2375.
8. A. Splendiani, L. Sun, Y. Zhang, T. Li, J. Kim, C.-Y. Chim, G. Galli and F. Wang, *Nano Letters*, 2010, **10**, 1271-1275.
9. A. Ramasubramaniam, D. Naveh and E. Towe, *Physical Review B*, 2011, **84**, 205325.
10. J. T. Perryman, J. C. Ortiz-Rodríguez, J. W. Jude, F. P. Hyler, R. C. Davis, A. Mehta, A. R. Kulkarni, C. J. Patridge and J. M. Velázquez, *Materials Horizons*, 2020, **7**, 193-202.
11. J. Jun, G. Minrui, S. Wenchao and Y. Yushan, *Angewandte Chemie International Edition*, 2016, **55**, 15240-15245.
12. P. Liu, Y. Choi, Y. Yang and M. G. White, *J Phys Chem A*, 2010, **114**, 3888-3895.
13. C. Liu and P. Liu, *ACS Catalysis*, 2015, **5**, 1004-1012.
14. G. Gershinsky, O. Haik, G. Salitra, J. Grinblat, E. Levi, G. Daniel Nessim, E. Zinigrad and D. Aurbach, *Journal of Solid State Chemistry*, 2012, **188**, 50-58.
15. E. Levi, Y. Gofer, Y. Vestfreed, E. Lancry and D. Aurbach, *Chemistry of Materials*, 2002, **14**, 2767-2773.
16. P. Canepa, G. Sai Gautam, D. C. Hannah, R. Malik, M. Liu, K. G. Gallagher, K. A. Persson and G. Ceder, *Chemical Reviews*, 2017, **117**, 4287-4341.
17. R. Chevrel and M. Sergent, *Superconductivity in Ternary Compounds I*, Springer-Verlag Berlin Heidelberg, 1982.
18. Ø. Fischer, *Applied physics*, 1978, **16**, 1-28.
19. T. Caillat, J. P. Fleurial and G. J. Snyder, *Solid State Sciences*, 1999, **1**, 535-544.
20. J. Kibsgaard, A. Tuxen, M. Levisen, E. Lægsgaard, S. Gemming, G. Seifert, J. V. Lauritsen and F. Besenbacher, *Nano Letters*, 2008, **8**, 3928-3931.
21. I. Vilfan, *The European Physical Journal B - Condensed Matter and Complex Systems*, 2006, **51**, 277-284.
22. R. Ge, X. Wu, M. Kim, J. Shi, S. Sonde, L. Tao, Y. Zhang, J. C. Lee and D. Akinwande, *Nano Letters*, 2018, **18**, 434-441.
23. F. F. Wang, X. Y. Hu, X. X. Niu, J. Y. Xie, S. S. Chu and Q. H. Gong, *Journal of Materials Chemistry C*, 2018, **6**, 924-941.
24. K. Galatsis, P. Gargini, T. Hiramoto, D. Beernaert, R. DeKeersmaecker, J. Pelka and L. Pfitzner, *IEEE Technology and Society Magazine*, 2015, **34**, 21-30.
25. M. Potel, R. Chevrel, M. Sergent, J. C. Armici, M. Decroux and Ø. Fischer, *Journal of Solid State Chemistry*, 1980, **35**, 286-290.

26. S. Kasap, C. Koughia and H. E. Ruda, in *Springer Handbook of Electronic and Photonic Materials*, eds. S. Kasap and P. Capper, Springer International Publishing, Cham, 2017, DOI: 10.1007/978-3-319-48933-9_2, pp. 1-1.
27. L. Greene, T. O. M. Lubensky, M. Tirrell, P. Chaikin, H. Ding, K. Faber, P. Hammond, C. Heckle, K. Hemker, J. Heremans, B. Jones, N. Mason, T. Mason, T. Shahnaz Rahman, E. Reichmanis, J. Sarrao, S. Sinnott, S. Stemmer, S. Stupp, T. I. A. Benson Tolle, M. Weaver, T. Younkin and S. Zinkle, *Frontiers of Materials Research: A Decadal Survey*, United States, 2019.
28. J. T. Perryman, F. P. Hyler, J. C. Ortiz-Rodríguez, A. Mehta, A. R. Kulkarni and J. M. Velázquez, *Journal of Coordination Chemistry*, 2019, **72**, 1322-1335.
29. S. Chandrasekaran, T. Basak and R. Srinivasan, *International Communications in Heat and Mass Transfer*, 2013, **48**, 22-27.
30. J. Hafner, *Journal of Computational Chemistry*, 2008, **29**, 2044-2078.
31. J. P. Perdew, K. Burke and M. Ernzerhof, *Physical Review Letters*, 1997, **78**, 1396-1396.
32. V. Fiorentini and M. Methfessel, *Journal of Physics: Condensed Matter*, 1996, **8**, 6525-6529.
33. E. E. Levin, J. H. Grebenkemper, T. M. Pollock and R. Seshadri, *Chemistry of Materials*, 2019, **31**, 7151-7159.
34. A. Mariaux and M. Rappaz, *Acta Materialia*, 2011, **59**, 927-933.
35. S. J. Jung, T. Lutz, M. Boese, J. D. Holmes and J. J. Boland, *Nano Letters*, 2011, **11**, 1294-1299.
36. C. J. O'Kelly, S. J. Jung and J. J. Boland, *Crystal Growth & Design*, 2016, **16**, 7318-7324.
37. *Inorganic Crystal Structure Database (ICSD)* <https://www.fiz-karlsruhe.de/>.

Supporting Information

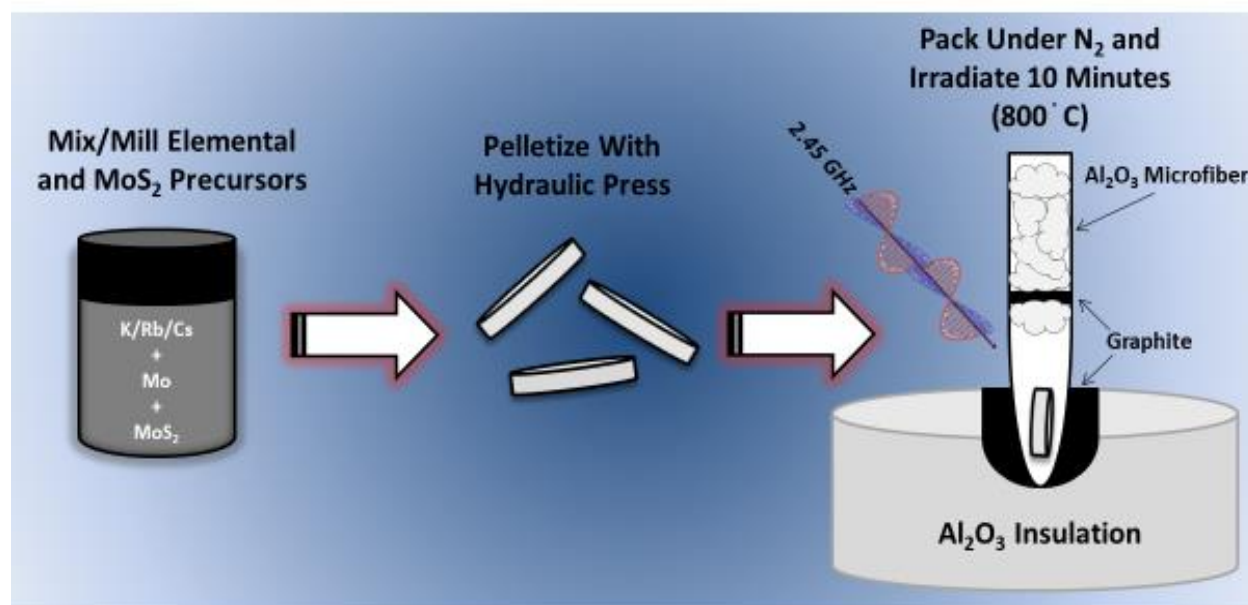


Figure S4.1. Schematic illustration of the synthetic method wherein the fused quartz reaction vessel is packed tightly with microfibrinous Al₂O₃ and a layer of sacrificial graphite in order to isolate compressed pellets with M₂Mo₆S₆ stoichiometry under an inert atmosphere during heating. The entirety of the far-right figure is placed in a microwave chamber under continuous flow of Ar.

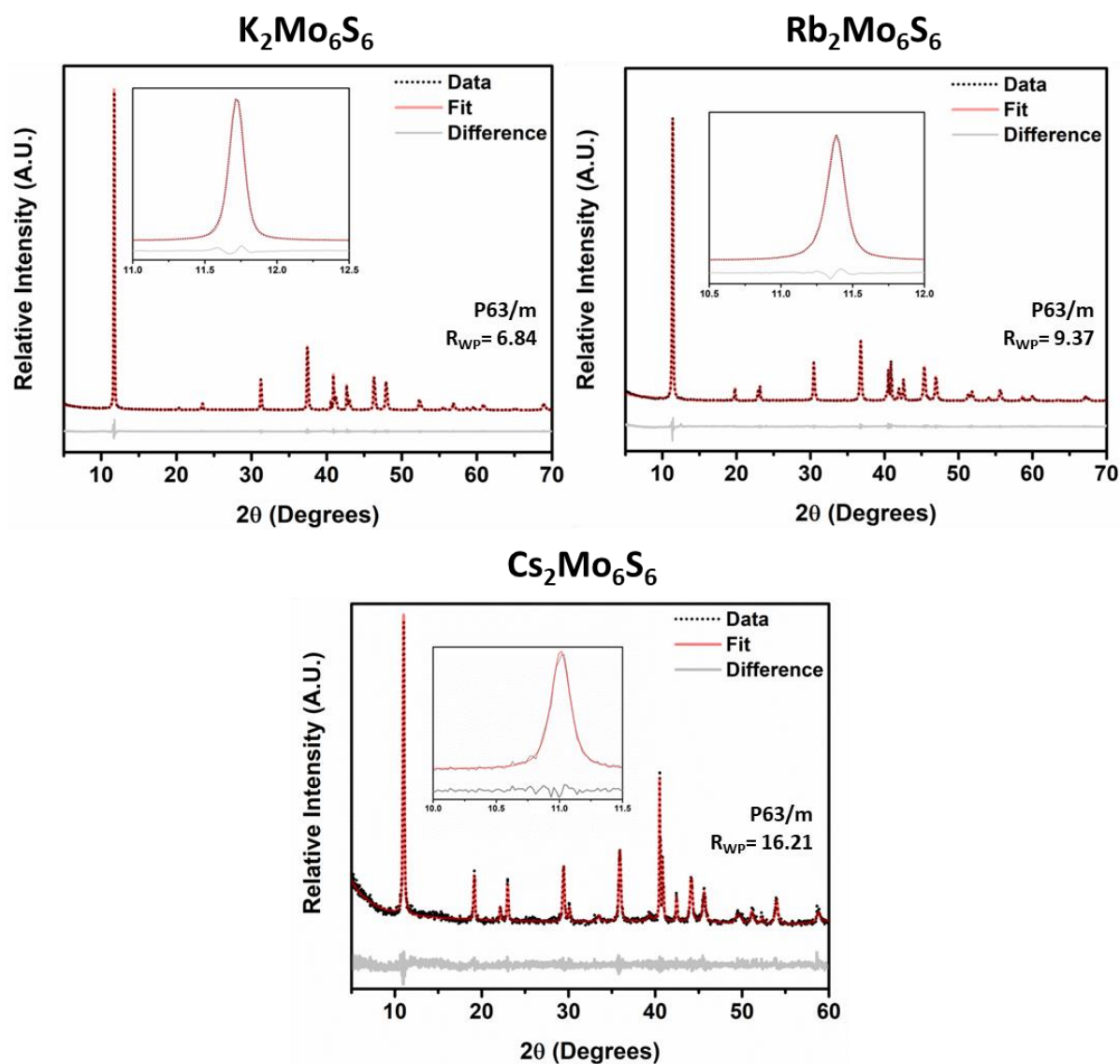


Figure S4.2. PXRD patterns used for Pawley refinement (black dots), along with their calculated patterns (red line) and the difference curve (grey line) for all three PCPs studied. Insets in each case contain the characteristic (010) peak of the PCP crystal system illustrating a relatively large degree of asymmetry, consistent with many low-angle diffraction peaks.

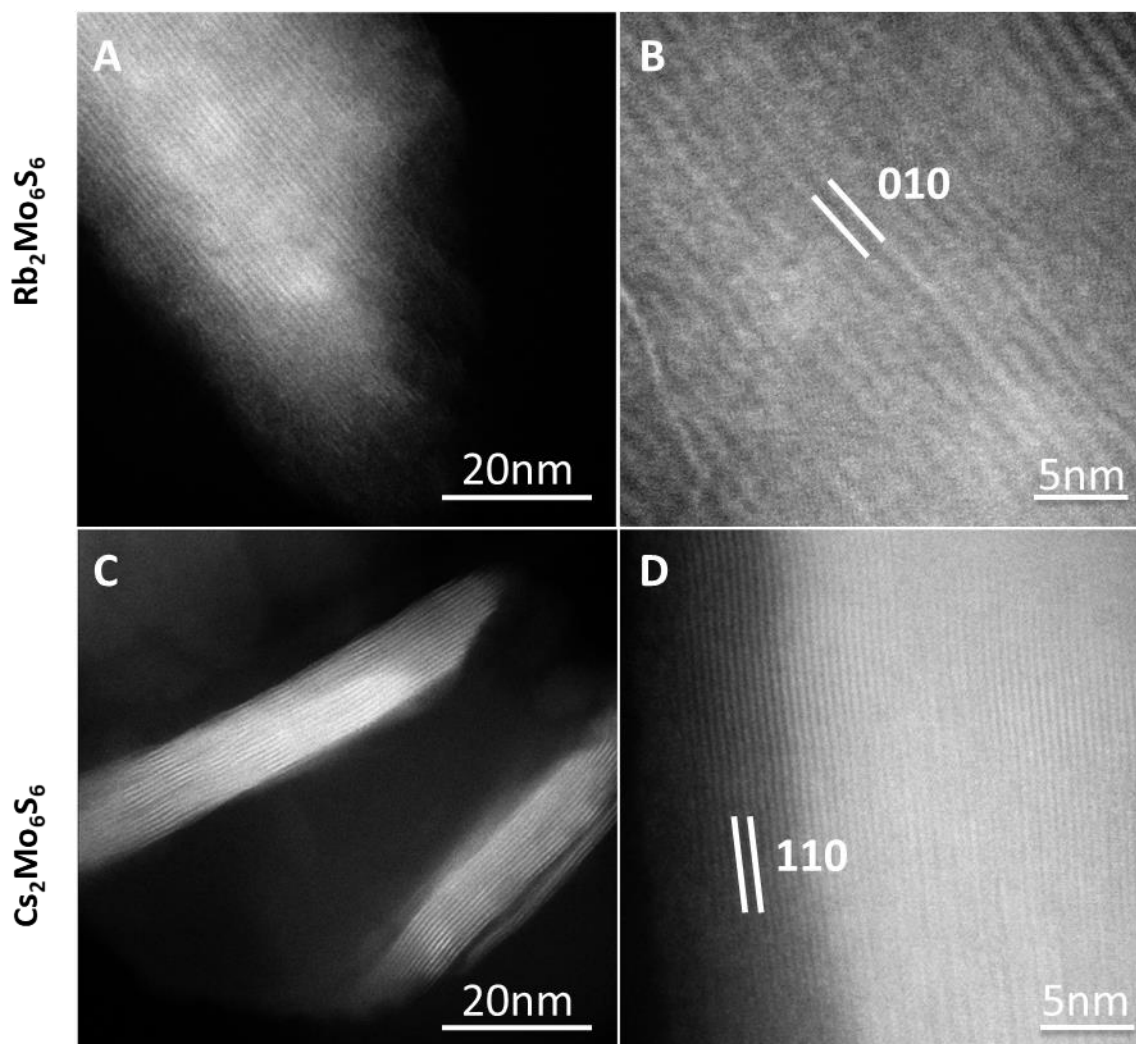


Figure S4.3. Lattice-resolved TEM images for Rb-PCP and Cs-PCP that illustrate the (010) and (110) directions, respectively. K-PCP was omitted owing to the thickness of K-PCP rods preventing required levels of transmission for lattice imaging.

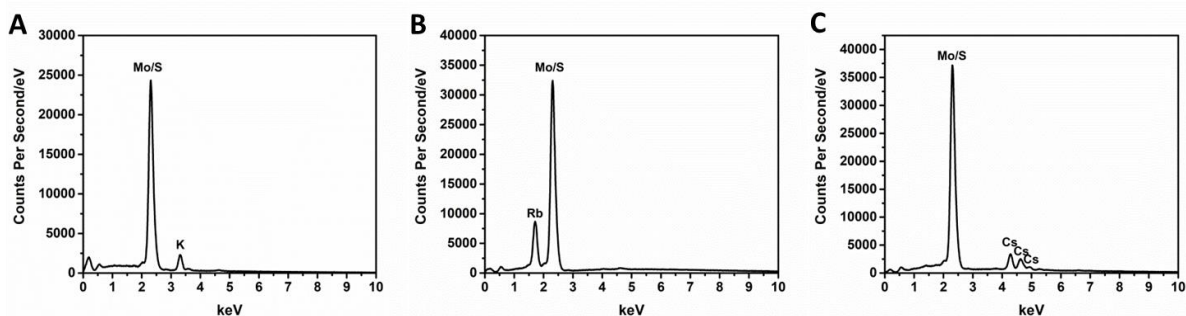


Figure S4.4. EDX spectra for (A) K-PCP, (B) Rb-PCP, and (C) Cs-PCP, illustrating no bulk elemental impurities for the rods synthesized here, and no significant evidence of bulk oxidation as might be expected from a nano-scale chalcogenide. Average alkali metal atomic percent compositions for each M_2 -PCP are listed and are in good agreement with expected values within the error of EDX quantification, although Mo/S composition is omitted owing to strong overlap between Mo $L\alpha_1$ and S $K\alpha_1$ lines which convolutes their quantification.

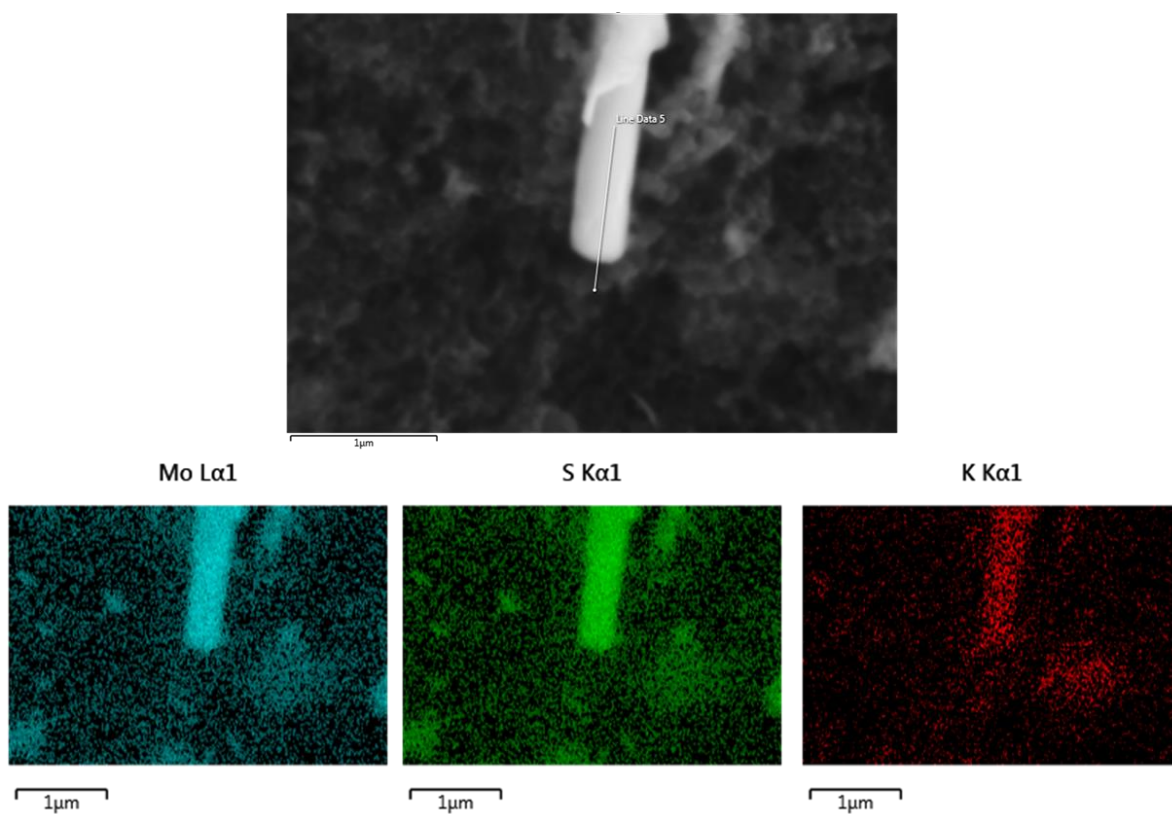


Figure S4.5. Result of EDX mapping of an individual K-PCP nanorod, performed with an accelerating voltage of 10 keV and beam current of 3.2 nA, illustrating uniform elemental distribution throughout the entirety of the rod. The corresponding line scan is shown in Figure S4.6.

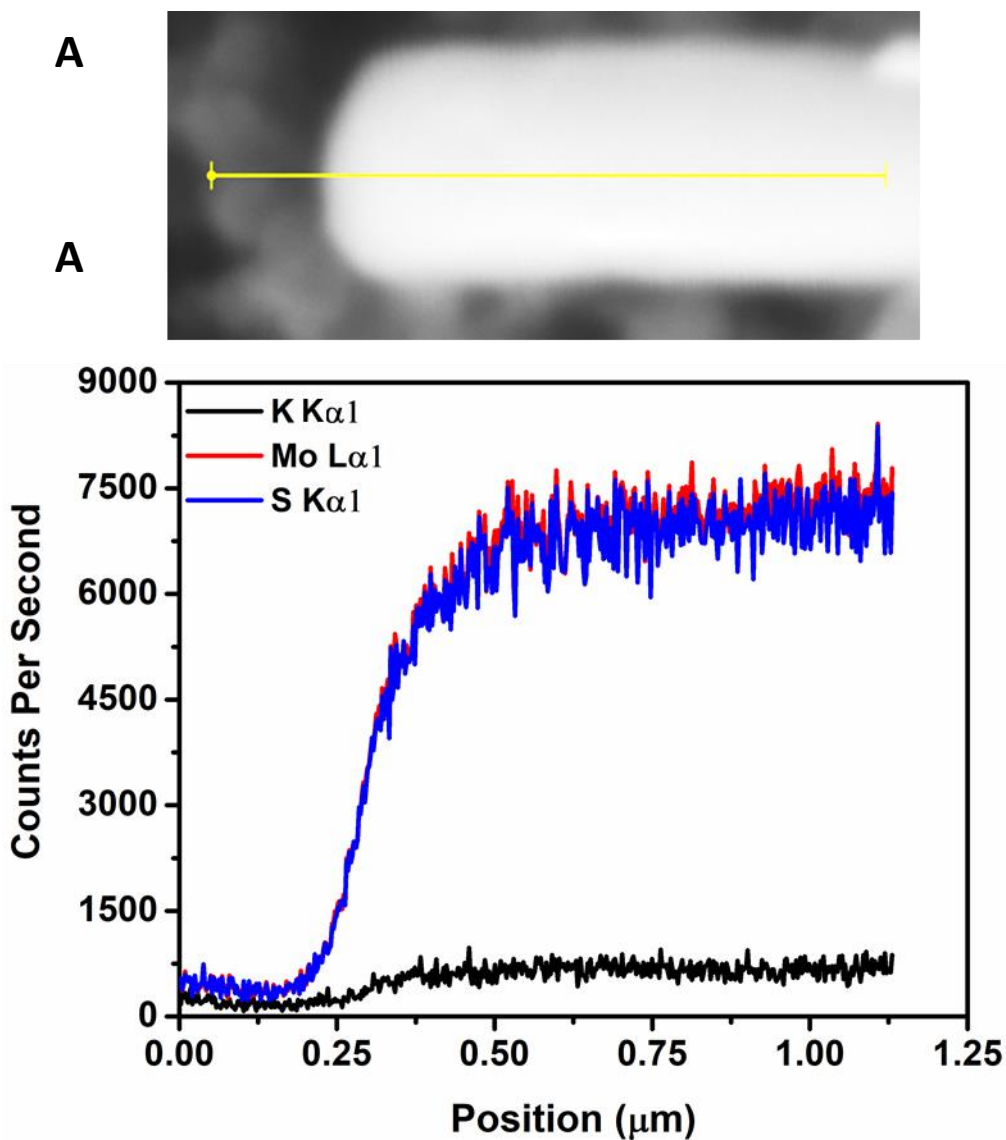


Figure S4.6. EDX line scan for the isolated K-PCP nanorod shown in Figure S4.5. Constituent element signals scale with sample thickness under the electron beam, and is uniform along the length of the rod. The scan position represented by a yellow line in the corresponding SEM (A) has been aligned to scale with the position axis in (B).

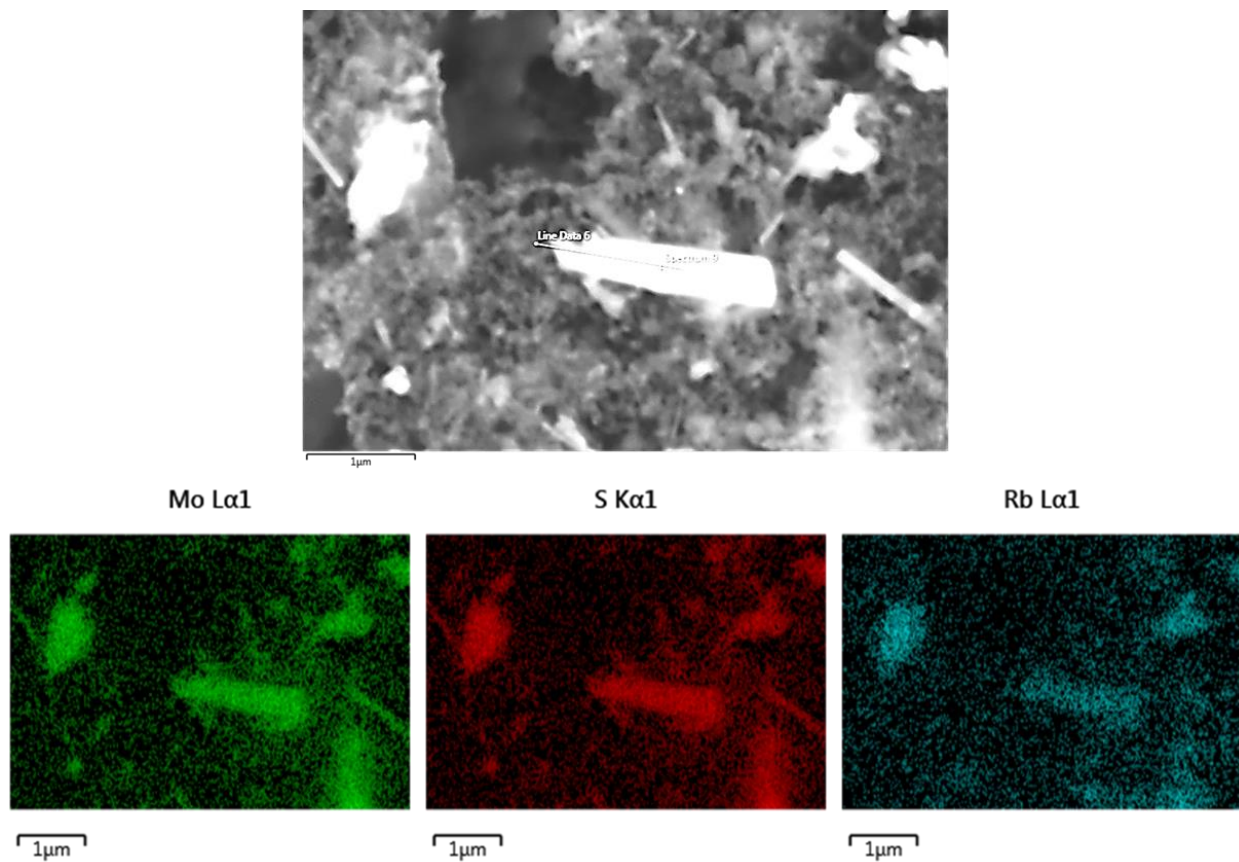


Figure S4.7. Result of EDX mapping of an individual Rb-PCP nanorod, performed with an accelerating voltage of 10 keV and beam current of 3.2 nA, illustrating uniform elemental distribution throughout the entirety of the rod. The corresponding line scan is shown in Figure S4.8.

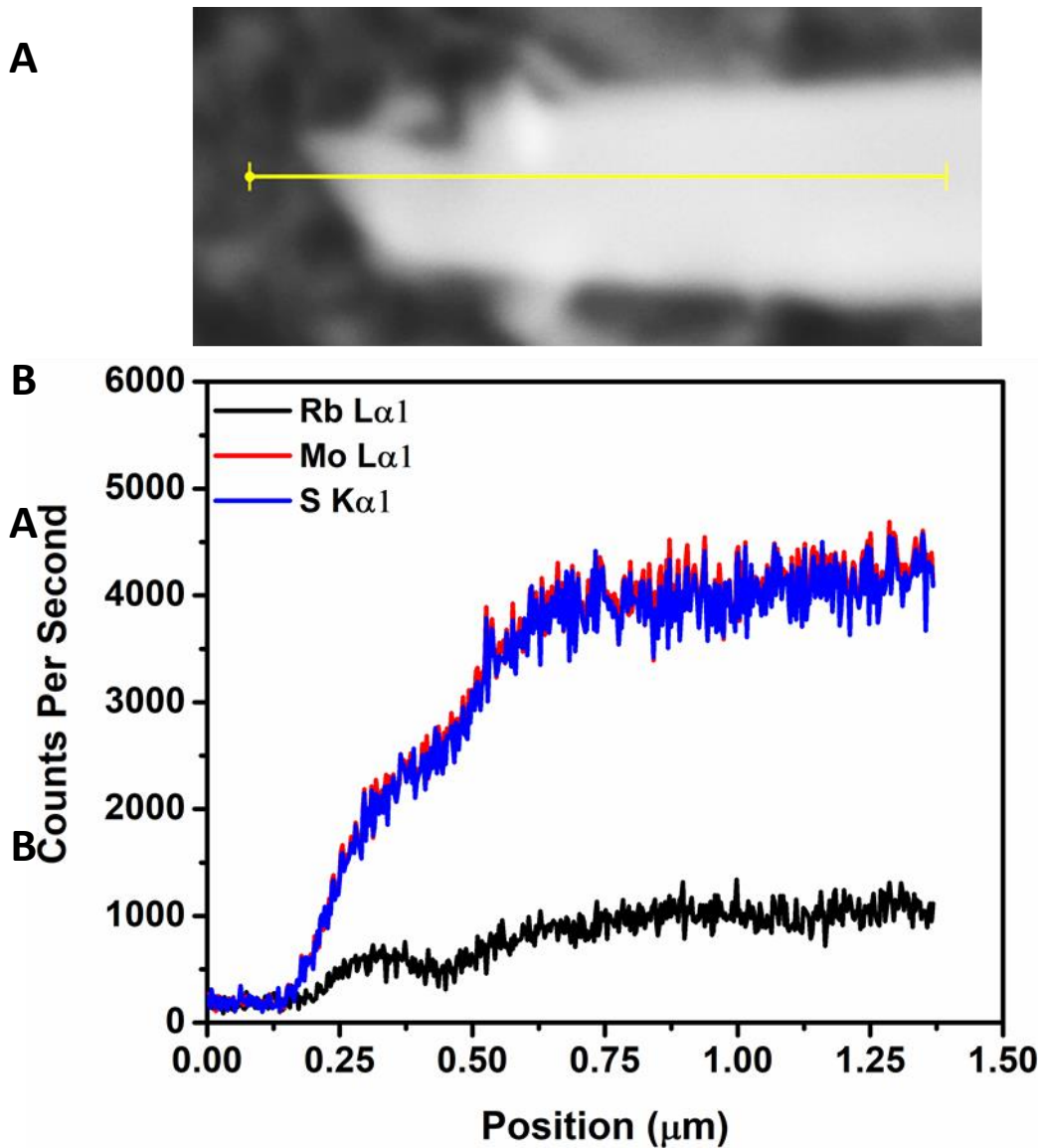


Figure S4.8. EDX line scan for the isolated Rb-PCP nanorod shown in Figure S4.7. Constituent element signals scale with sample thickness under the electron beam, and is uniform along the length of the rod. The scan position represented by a yellow line in the corresponding SEM (A) has been aligned to scale with the position axis in (B).

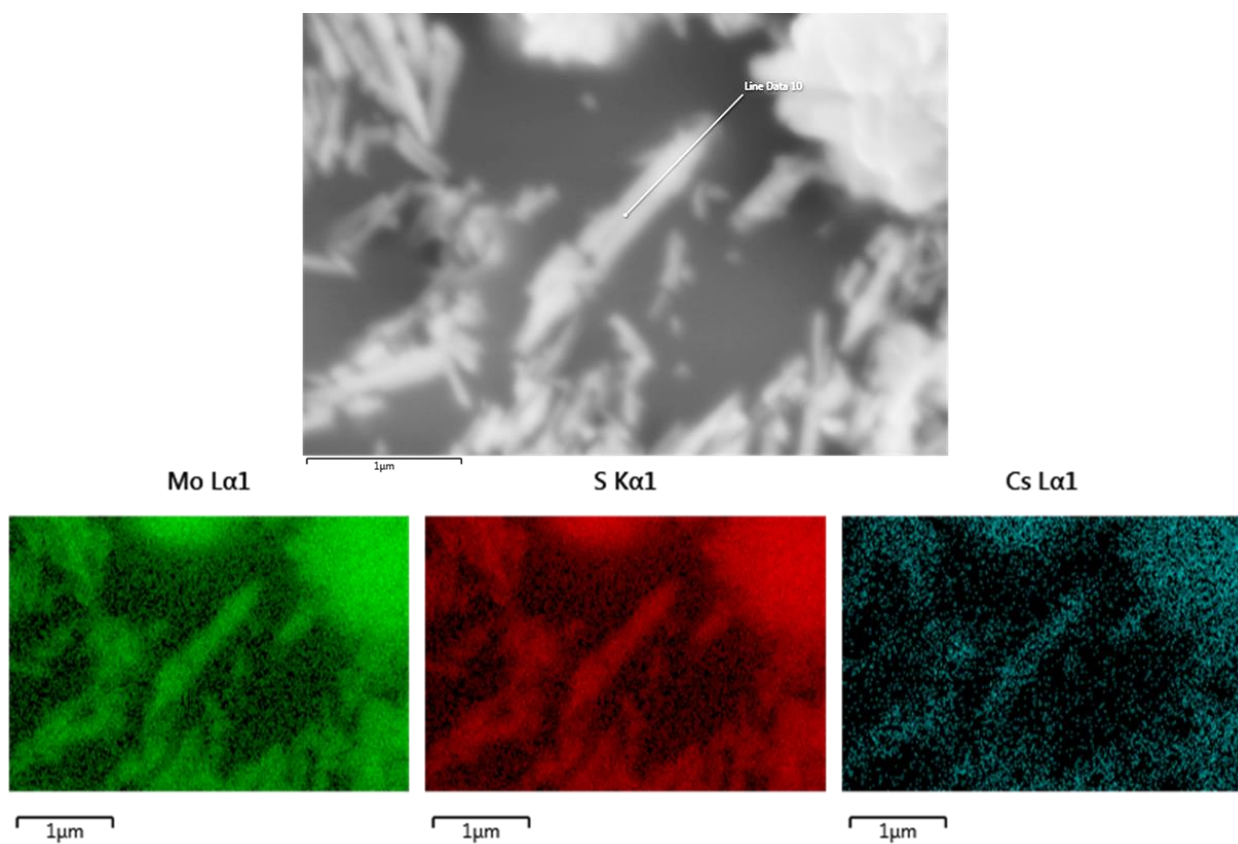


Figure S4.9. Result of EDX mapping of an individual Cs-PCP nanorod, performed with an accelerating voltage of 10 keV and beam current of 3.2 nA, illustrating uniform elemental distribution throughout the entirety of the rod. The corresponding line scan is shown in Figure S4.10.

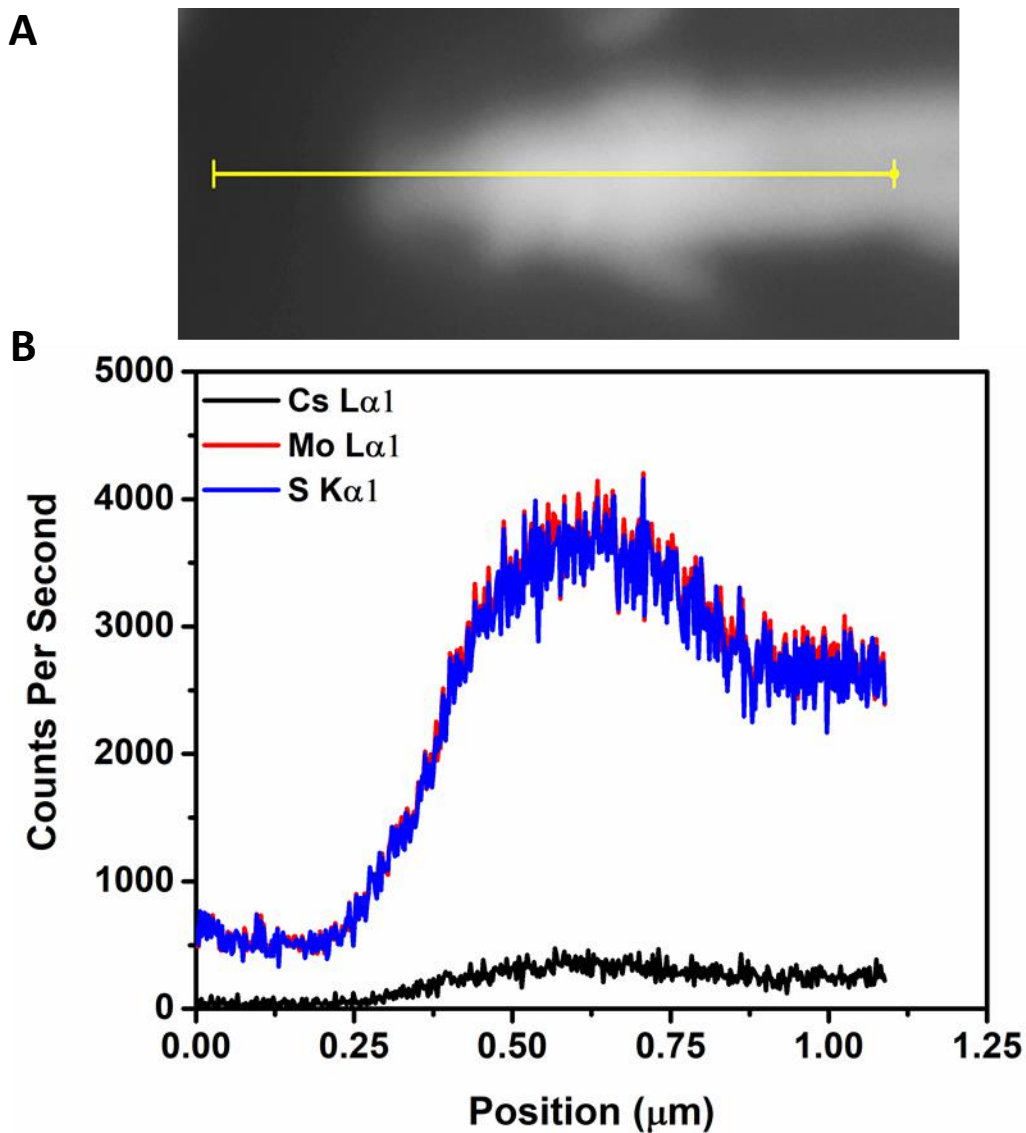


Figure S4.10. EDX line scan for the isolated Cs-PCP nanorod shown in Figure S4.9. Constituent element signals scale together with sample thickness under the electron beam. Intensity of each component decreases from $\sim 0.6 \mu\text{m}$ onward owing to decreased thickness of the rod. The scan position represented by a yellow line in the corresponding SEM (A) has been aligned to scale with the position axis in (B).

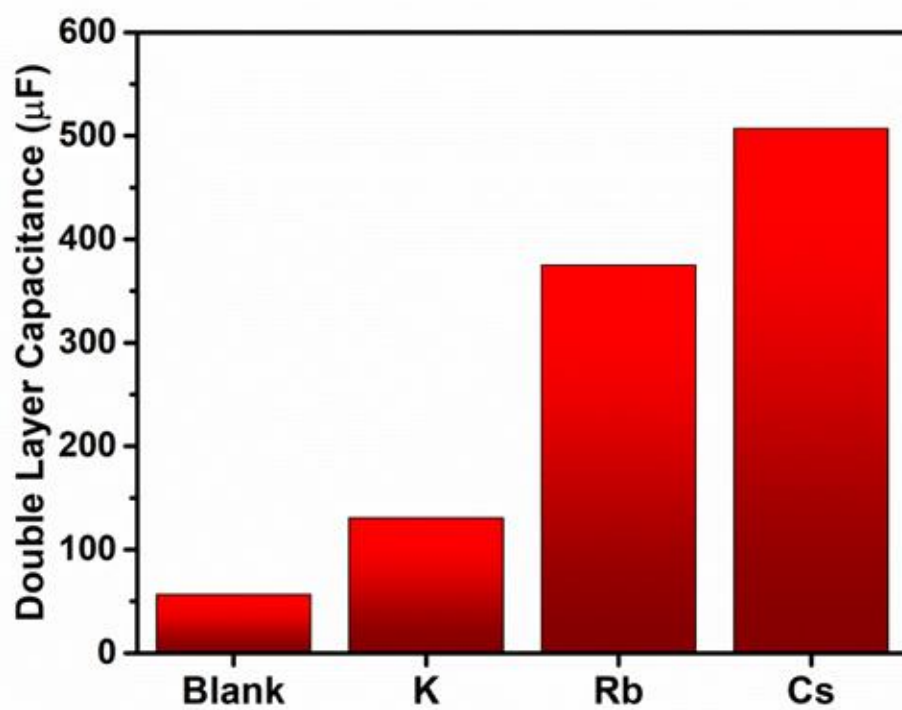


Figure S4.11. Double layer capacitance for each of the inks studied herein, taken as the average slope of all repeated current versus scan-rate plots.

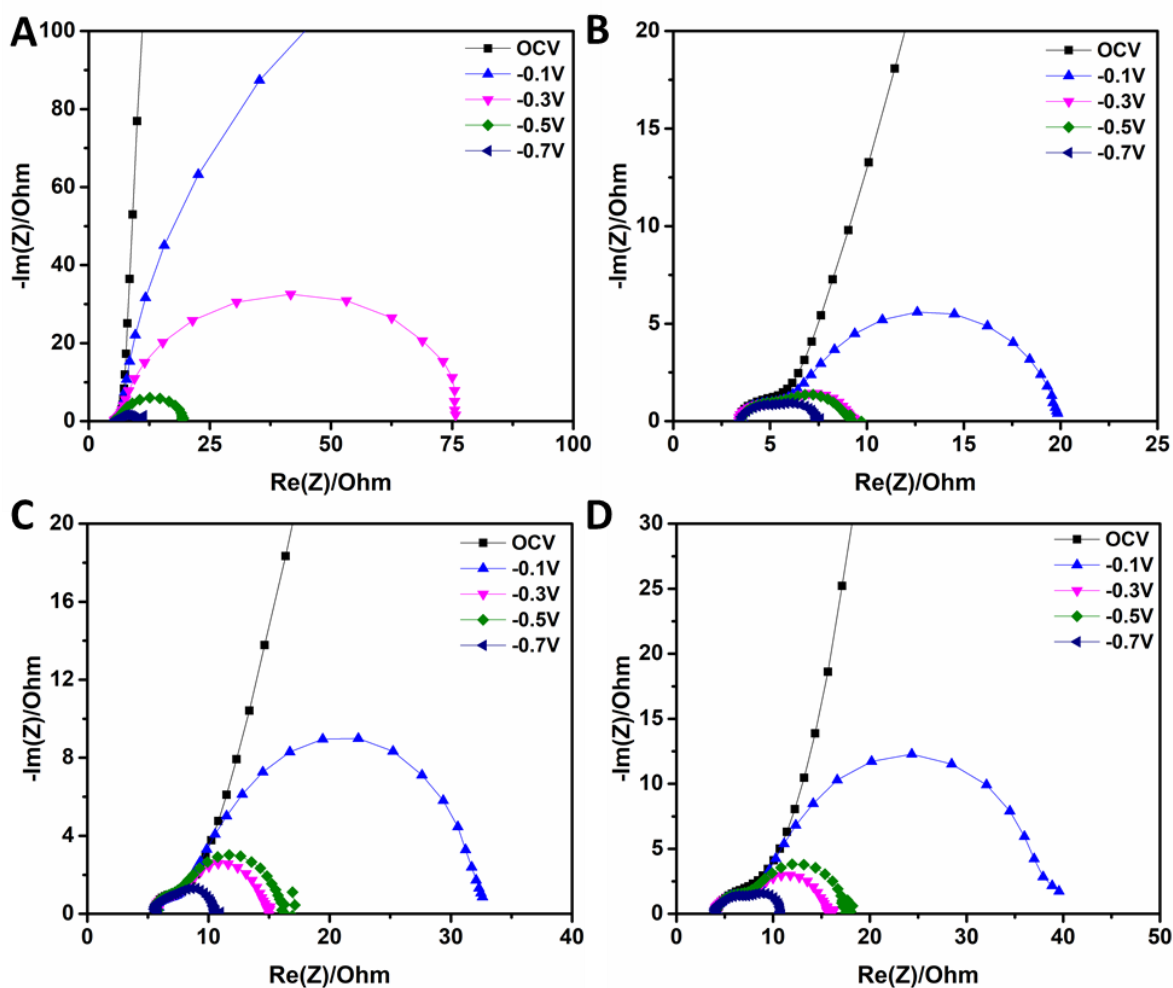


Figure S4.12. Examples of Nyquist plots for (A) PCP-free blank ink, (B) K-PCP, (C) Rb-PCP, and (D) Cs-PCP that were used to determine interfacial charge transfer resistance. Using a Randle circuit, resistance to charge transfer is taken as the difference between extrapolated x-intercepts at low AC frequency (right side) and at high frequency (left side).

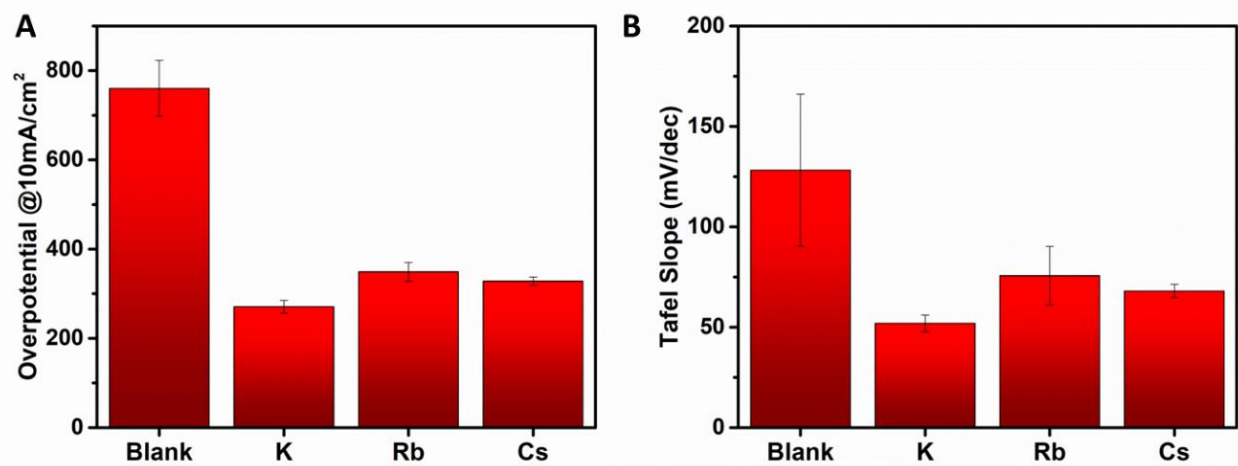


Figure S4.13. (A) Average overpotential required to achieve a current density of 10mA/cm² for all four inks, and (B) Average Tafel slope calculated for all four inks. In both figures, error bars represent a single standard deviation.

Table S4.1 Compiled lattice parameters extracted via Pawley refinement for $M_2Mo_6S_6$, compared with literature values.

Parameter	This Work	Literature	%Difference
$K_2Mo_6S_6$			
a	8.7346	8.7204	0.16%
b	8.7346	8.7204	0.16%
c	4.4136	4.4076	0.14%
α	90	90	0.00%
β	90	90	0.00%
γ	120	120	0.00%
Cell Volume	291.61	290.27	0.46%
$Rb_2Mo_6S_6$			
a	8.9553	8.9589	-0.04%
b	8.9553	8.9589	-0.04%
c	4.4046	4.4114	-0.15%
α	90	90	0.00%
β	90	90	0.00%
γ	120	120	0.00%
Cell Volume	305.912	306.63	-0.23%
$Cs_2Mo_6S_6$			
a	9.2518	9.269	-0.19%
b	9.2518	9.269	-0.19%
c	4.4114	4.419	-0.17%
α	90	90	0.00%
β	90	90	0.00%
γ	120	120	0.00%
Cell Volume	327.008	328.86	-0.56%